https://doi.org/10.25923/kykm-sn39

An Integrated Assessment of Oil and Gas Release into the Marine Environment at the Former Taylor Energy MC20 Site

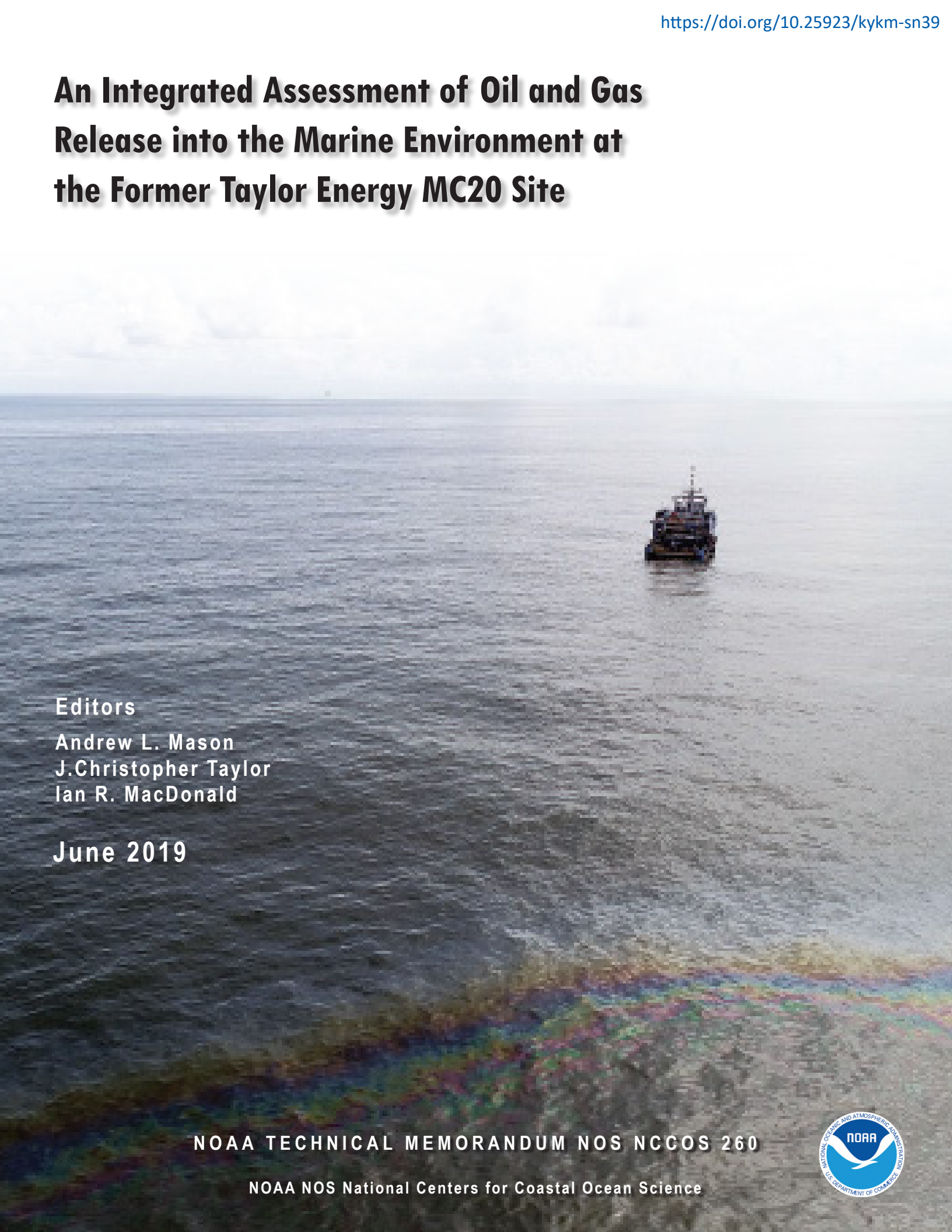

Editors

Andrew L. Mason
J.Christopher Taylor
Ian R. MacDonald

June 2019

NOAA TECHNICAL MEMORANDUM NOS NCCOS 260

NOAA NOS National Centers for Coastal Ocean Science

Suggested Citations

Full report citation:
Mason, A.L., J.C. Taylor, and I.R. MacDonald (eds.). 2019. An Integrated Assessment of Oil and Gas Release into the Marine Environment at the Former Taylor Energy MC20 Site. NOAA National Ocean Service, National Centers for Coastal Ocean Science. NOAA Technical Memorandum 260. Silver Spring, MD. 147 pp. doi: 10.25923/kykm-sn39

Chapter citation: example for Chapter 1
Mason, A.L., M.M. Rider, I.R. MacDonald, and J.C. Taylor. 2019. Chapter 1: Introduction and Background Conditions at the Former Taylor Energy MC20 Site in September 2018. pp. 1-6. In: A.L. Mason, J.C. Taylor, and I.R. MacDonald (eds.), An Integrated Assessment of Oil and Gas Release into the Marine Environment at the Former Taylor Energy MC20 Site. NOAA National Ocean Service, National Centers for Coastal Ocean Science. NOAA Technical Memorandum 260. Silver Spring, MD. 147 pp. doi: 10.25923/kykm-sn39

Acknowledgments
This survey was jointly funded by the U.S. Department of the Interior, Bureau of Safety and Environmental Enforcement and the U.S. Department of Commerce, National Oceanic and Atmospheric Administration through Interagency Agreement E18PG00016.

The authors wish to acknowledge the dedication and support of all their partners at TDI-Brooks International, Florida State University, and Florida International University. They would also like to thank Tom Weber and Scott Loranger of the University of New Hampshire for their input and participation in logistical mission planning and acoustic methods review, Lieutenant Commander Sam Greenaway of NOAA's Office of Marine and Aviation Operations and Chris Bassett of the University of Washington Applied Physics Laboratory for their assistance interpreting acoustic data. Eric Ebert and Kimani Kimbrough of NOAA's National Centers for Coastal Ocean Science (NCCOS) both also provided valuable input to this report. Sarah Hile of NCCOS (CSS, Inc.) for her indispensable assistance in getting this report together. Lisa DiPinto of NOAA's Office of Response and Restoration (ORR) provided immense assistance in multiple areas over the course of this project. David Fish, Glenn Degnitz, and T.J. Broussard of the Bureau of Safety and Environmental Enforcement each provided valuable logistical support during field operations for this mission as well as helped facilitate communication between government agencies. The authors would like to recognize SeaTrepid International and their outstanding crew Jason Hanagriff, Thomas Katzmire, and Zachary Lupo for their professionalism and ability to operate successfully under challenging conditions. The authors are extremely grateful to everyone who provided support and assistance in the completion of this project, especially NOAA leadership including both Steve Thur of NCCOS and Dave Westerholm of ORR.

Some of the chapter authors and people acknowledged for supporting this report were CSS, Inc. employees supported under NOAA contract Nos. EA133C-14-NC-1384 and EA133C-17-BA-0062. Analytical chemistry services were provided by TDI-Brooks International under NOAA contract Number EA133C-14-BA-0049.

Front and back cover images are provided by NOAA/NOS NCCOS.

Disclaimer
This report was prepared under an interagency agreement between the Department of the Interior, Bureau of Safety and Environmental Enforcement (BSEE) and the Department of Commerce, National Oceanic and Atmospheric Administration (NOAA). The opinions, findings, conclusions, and recommendations expressed in this report are those of the authors and they do not necessarily reflect the views or policies of BSEE or NOAA. Reference herein to any specific commercial product, process, or service by trade name, trademark, manufacturer, or otherwise, does not necessarily constitute or imply its endorsement, recommendation, or favoring by the United States Government or any agency thereof.

https://doi.org/10.25923/kykm-sn39

An Integrated Assessment of Oil and Gas Release into the Marine Environment at the Former Taylor Energy MC20 Site

Prepared by:
National Centers for Coastal Ocean Science (NCCOS)
NOAA National Ocean Service (NOS)
Silver Spring, MD
USA

June 2019

EDITORS

Andrew L. Mason
NOAA National Centers for Coastal Ocean Science

J. Christopher Taylor
NOAA National Centers for Coastal Ocean Science

Ian R. MacDonald
Florida State University

NOAA Technical Memorandum NOS NCCOS 260

About This Report

This report is the result of an expedited Interagency Agreement (E18PG0016) between the Department of Commerce (DOC), National Oceanic and Atmospheric Administration (NOAA), National Ocean Service's (NOS), National Centers for Coastal Ocean Science (NCCOS) and the Department of the Interior's (DOI), Bureau of Safety and Environmental Enforcement (BSEE). BSEE provided funding to NCCOS for the assessment detailed in the chapters included in this report. The overall goal was to quantify the sources, characteristics, and magnitudes of the hydrocarbon plumes present at the Former Taylor Energy Company's (TEC) MC20 site. The funding was specifically intended to aquire the scientific and technical services necessary to accomplish an independent, government led assessment.

A project of this scope typically includes three phases; 1) planning, 2) mission execution, and 3) data interpretation/reporting. These three (3) phases generally take 2-3 years combined. In light of ongoing release of oil and gas into the marine environment and the immediate need for an independent government assessment of the MC20 site to provide decision makers with complete information, the process for generating this report was compressed from 2-3 years down to less than one (1) year from the signing of the IAA to delivery of this final report.

NCCOS provides federal partners and coastal managers with the information and tools they need to balance society's environmental, social, and economic goals. NCCOS is the primary coastal science arm within NOAA's National Ocean Service (NOS). NCCOS works directly with managers, industry, regulators, and scientists to deliver relevant, timely, and accurate scientific information and tools.

For more information contact:
Andrew Mason
National Centers for Coastal Ocean Science
Monitoring and Assessment Branch
andrew.mason@noaa.gov

Table of Contents

Table of Contents

Table of Contents

Table of Contents

EXECUTIVE SUMMARY

R/V Brook McCall, *Gulf of Mexico. Credit: NOAA NOS/NCCOS*

In September of 2004, Hurricane Ivan, a Category 3 storm at the time, passed through the northern Gulf of Mexico. Severe wave action attributed to the storm triggered a subsea mudslide that toppled Taylor Energy Company's (TEC) Saratoga oil production platform A at Mississippi Canyon Block 20 (MC20). The superstructure, also known as the jacket, came to rest on the ocean floor approximately 210 m southeast of the original location. The collector bundle containing the original 28 well pipes was also dragged in the direction of the collapsed jacket, breaking and becoming buried by deposited sediment at the northwest corner of the final resting place of the structure.

The MC20 site has since been associated with persistent plumes of oil and gas and surface oil slicks. These slicks are visible on the ocean surface from ships and by aerial and satellite remote sensing and have been used as a means of measuring the output of hydrocarbons from the site. However, it was determined that these estimates needed to be compared to collections and measurements from within the water column along with sediment collection for chemical analysis. Additionally, because vigorous and persistent gas plumes have been observed at the site, the flux of hydrocarbon gas at the surface and into the atmosphere was assessed. In response to a request by the Bureau of Safety and Environmental Enforcement (BSEE), the National Oceanic and Atmospheric Administration's (NOAA) National Centers for Coastal Ocean Science (NCCOS), in cooperation with NOAA's Office of Response and Restoration (ORR) conducted a survey at the MC20 site.

NOAA's NCCOS along with its partners at Florida State University (FSU), Florida International University (FIU), and TDI Brooks International, and with funding from BSEE, conducted a series of integrated surveys from 1 to 7 September 2018 at the former Taylor Energy MC20 site in the northern Gulf of Mexico. These surveys included surface and subsurface acoustic measurements, mid-water column oil, gas, and water collections, surface water sample collections, mid-water column video bubble collections, surface methane collections, and marine sediment collections. Ancillary physical water column data was also collected including ocean current profiles and conductivity, temperature, and depth.

Executive Summary

The MC20 site currently sits in roughly 135 m of water and is dominated subsurface by the collapsed well jacket. At the time of this survey, surface waters above MC20 were characterized by persistent surface oil sheens. Acoustic measurements detected an erosional pit and at least four (potentially five) individual plume "mini-pit" features inside the erosional pit located at the northwest corner of the downed jacket. These plume features were able to be separated by those containing predominantly oil and those containing predominantly gas. The predominantly gas plumes are located to the north of the center of the erosional pit while the predominantly oil plumes were grouped closely together to the south of the center of the pit. The entire extent of the plume "mini-pit" features from north to south measured approximately 12.7 m and ranged from approximately 1.5-5.5 m distant from the edge of the collapsed jacket structure. A salinity anomaly of slightly fresh water was detected within the erosional pit in addition to oil and gas (Chapter 2).

Acoustic measurements of the combined plumes under both relatively high and low current conditions, combined with oil droplet and gas bubble densities determined from deployment of a new device called the "bubblometer", allowed for the calculation of flux rate estimates for oil and gas entering the water column at the northwest corner of the jacket. This acoustic flux rate is estimated by taking the measured backscatter volume of the combined oil and gas plumes and, using the measured rise rate of the plume from an ocean floor mounted Acoustic Doppler Current Profiler (ADCP) along with the measured American Petroleum Institute (API) gravity of the oil from laboratory chemistry analysis, calculating a range of modeled oil release required to account for the plume volumes observed. The range represents assumptions based on the ratio of oil to gas actually present within the plumes. We are confident in these range values based on measurements provided by the video bubble chamber and that methodology's statistical characterization of the oil to gas ratio and bubble size distributions. A detailed description of these results and related methodology can be found in Chapters 3, 4, and 8 of this Report.

Video bubble chamber, or bubblometer, measurements from this survey also provide a related, but independent flux rate estimate from those calculated by acoustic measurements. The bubblometer chamber consists of a rectangular frame of known dimensions. One face of the chamber is open and mounted with lights and a high-definition camera. Video captured during this survey yielded approximately 665 individual sample images of oil and gas located in subsurface plumes and represents combinations of predominantly oil, predominantly gas, and varying combinations of the two. Using methodology described in Chapter 4 of this document, gas and oil bubble volumes are estimated. Combining the volume estimates for each individual video "still" image sample with its three dimensional location within the plume measured by Ultra Short Base-Line (USBL) beacon locator along with the estimated plume size and density from acoustic backscatter and estimated oil rise rate from ADCP measurements allows for calculation of oil and gas flux.

The estimated oil flux rate calculated from the acoustic survey method is approximately 9 to 47 barrels of oil per day. The estimated oil flux rate calculated from the bubblometer survey method is approximately 19 to 108 barrels of oil per day. It is important to note that these are both estimates and while we are confident in the methods developed and calculations employed, these two ranges do not necessarily represent a final definitive government estimate of the flux of oil and gas being released at the MC20 site.

Gas flux rates, while not identified as a primary priority item, were also calculated as part of this survey by NOAA partners at FSU. Surface measured methane flux was estimated using a Picarro® cavity ring-down spectrometer and calibrated using a known release tracer mounted on a deployed raft (Chapter 5). The estimated flux rate of methane gas being released at the ocean surface at MC20 is 9 g per second or approximately 0.7 tons of methane per day. This equates to a volume of roughly 1,200 m^3 of methane at the ocean surface.

The chemical analysis of gas samples collected at the MC20 site are presented in detail in Chapter 6 of this

document. Gas samples were collected mid-water column within the combined plumes using the inverted funnel mounted on top of the bubblometer chamber and using the sediment box corer. All gas samples were analyzed by TDI Brooks International for C1 to C5 hydrocarbons from both mid-water and sediment samples. Carbon 13 isotopes were also analyzed as part of this survey. All laboratory analysis for MC20 gas samples confirm a thermogenic wet gas and not a primarily biogenic source. The gas samples were determined to be from Upper Jurassic Marine Carbonate source rock, very similar in geological time to the mid-Cretaceous Shale source rock determined by the petroleum biomarker results detailed in Chapter 7.

Bulk oil samples from the MC20 site were also collected mid-water column using the inverted funnel on the bubblometer chamber. The sample collection design ensured that mid-water column collection activities would not be biased by previous or concurrent interaction with marine sediments within or adjacent to the erosional pit. To that end, all sediment collection activities were conducted over the last two days of the survey after all mid-water column samples had been collected and multiple acoustic and video bubblometer surveys were completed. Bulk oil chemistry samples were analyzed by TDI Brooks and GeoMark for Polycyclic Aromatic Hydrocarbons (PAHs), Total Petroleum Hydrocarbons (TPH), saturated petroleum hydrocarbons, and biomarker Hydrocarbons (HCs). These same analyses were performed on sediment and water samples as well.

Concentrations of oil-related contaminants in surficial marine sediments decrease as distance from the release point(s) increases. This pattern is observed up to 500 m from the erosional pit after which background concentrations dominate sediments. Oil-related contaminants are an order of magnitude higher at the perimeter of the erosional pit than in any others measured in this study. Oil collected from the water column was found to be mildly biodegraded as compared to sediments at the perimeter of the erosional pit, which are severely biodegraded. This indicates that the sediments collected for this study cannot be the primary source of oil in the water column or the resulting surface sheen. Historic data from two different MC20 wells show that at least one of the original wells, well #9, produced oil that is degraded in the reservoir. The oil from well #9 resembles the oil characterized for this study in its pristane/C17 and phytane/C18 ratios though it is not possible to determine that the oil collected mid-water column specifically contains oil from well #9. The fact that at least one MC20 reservoir contained in-reservoir biodegraded oil helps explain the mild biodegradation observed in this study and others as “fresh” oil entering the marine environment could be arriving already degraded and therefore not significantly degraded before it reaches the ocean surface. Additionally, the variations observed between oil from well #9 and well #2 show that chemically different oils from the MC20 wells can be leaking concurrently and account for subtle oil heterogeneities observed in this study and others.

Our overall conclusion for the MC20 site is that there is ongoing release of reservoir oil and gas that enters the marine environment at the ocean floor and migrates up through the water column in a series of discrete and dense plumes. These plumes can separate into individual components or homogenize depending on the prevailing current conditions at the time the oil and gas enter the water column. Under relatively high current conditions, such as those observed on 2 September 2018, a portion of the predominantly oil plumes can become entrained by the currents and surface separately hundreds of meters away from the predominantly gas plumes. Certain portions of the oil partition out into the water column, either as microscopic droplets or through dissolution, or precipitate out onto the surrounding sediments where degradation continues. The oil that reaches the surface forms a surface sheen that continues to degrade through photolysis, evaporation, and further dissolution.

While it is feasible that the heavily oiled sediments in and around the erosional pit could be contributing to oil in the water column, the chemical nature and volume of oil and gas measured precludes sediments from currently being the major source of oil to the marine environment at the MC20 site.

Executive Summary

The detailed results of these combined surveys at the MC20 site are contained in this report which is organized into 8 chapters documenting in detail each correlated scientific focus area. Specifically, Chapter 1 presents background information about the study area and an overview of the project as a whole. Chapter 2 presents the physical water column characteristics measured at the site. Chapter 3 details the acoustic findings which resulted in multiple 3-dimensional models of the plumes under varying current profiles. Chapter 4 describes the physical characteristics of the bubbles of oil and gas observed using a unique tool called the bubblometer. Chapter 5 contains results for the surface methane measurements including spatial expression of measured values and an estimated methane flux rate. Chapter 6 presents the gas chemistry results from sediment and mid-water column captured gas samples. Chapter 7 documents the analytical chemistry results from oil, water, and sediment samples that were collected during the survey. And Chapter 8 presents calculated results from two different methods for measuring oil and gas flux estimates at the MC20 site.

Chapter 1 Introduction and Background Conditions at the Former Taylor Energy MC20 Site in September 2018

- Hurricane Ivan contributed to the destruction of seven drilling platforms in the Gulf of Mexico including Taylor Energy Company's MC20A.
- A subsurface mudslide toppled the MC20 platform, dragged and broke the conductor bundle designed to carry produced oil and gas, and buried the broken pipes under multiple meters of sediment.
- The destruction of MC20 by a subsurface mudslide was not the first instance of this occurring as mudslides triggered by Hurricane Camille in 1969 caused the destruction of a platform in South Pass Block 70.

Chapter 2 Characterization of the Observed Physical Characteristics of the Water Column at MC20

- Water column characteristics document the effects of persistent discharges of gas and fluids at MC20, which are focused in and above the erosional pit at the northwest corner of the well jacket.
- Negative salinity anomalies of about 3 PSU below ambient water column values were documented in the erosional pit.
- Sediments at this site are comprised of loosely consolidated material displaced by mudslides and therefore a groundwater source at this location is unlikely.

Chapter 3 Surface and ROV Acoustic Mapping of the MC20 Oil and Gas Leak in the Northern Gulf of Mexico

- Water column anomalies attributed to an oil and gas plume were consistently observed over the toppled jacket at the MC20 site.
- Observations under various ocean current regimes indicates several separate plume components with seabed origins of the plume in a defined erosional pit near the northeast corner of the toppled jacket, consistent with previous acoustic surveys.
- Relative acoustic backscatter intensity suggest components of the plume are comprised of separate oil and gas sources.
- Sonar observations at the seabed indicate finite and separate sources of 4 or 5 primary components of the plume comprised of two oil sources and two or three gas/mixed gas and oil sources.
- Each of the plume subcomponents were emanating from individual pits within the larger erosional pit at the northwest corner of the jacket.

- Acoustic backscatter properties from the plume can be used to estimate flux of oil and gas from the seabed to the surface.

Chapter 4 Quantitative Imaging of Oil and Gas Bubbles Discharged at MC20

- The visual samples from the bubblometer consistently showed dense assemblages of oil and gas bubbles in the hydrocarbon plume that originated from the erosional pit at the northwest corner of the well jacket.
- Computer vision algorithms were able to classify bubbles as gas or oil and to measure their major and minor axes so that estimates of volume could be calculated.
- Gas bubbles were found to contain a measurable fraction of oil by volume (35.6%), which means that the flux of gas bubbles must be included in the estimates of total flux.
- The three-dimensional distribution of bubbles in the image samples is consistent with the acoustic images of the plume obtained from the ROV and ship-mounted instruments.
- Vertical distribution of bubbles indicates three domains with different characteristics: crater, benthic layer, and midwater. Differences in size distribution and oil content indicate that fluxes should be calculated separately for oil, gas-oil, and depth domain.

Chapter 5 Surface Methane Measurements and Flux at the MC20 Oil and Gas Leak in the Northern Gulf of Mexico

- Atmospheric methane concentrations at the MC20 site were consistently higher than background methane concentrations detected in the air (>1.85 ppm).
- Higher atmospheric methane concentrations were detected 3 m above the ocean surface over the northwest corner of the toppled jacket, with values that exceeded 3.0 ppm of methane, and a peak concentration of 11.8 ppm.
- Dominant winds coming from the southeast (112° to 157°) with an average speed of 12.6 Kn dissipated the methane coming from the plume towards the northwest and upper atmosphere.
- Inverse Plume Modeling combined with atmospheric methane concentrations were used to estimate a methane flux rate from the hydrocarbon plume to the atmosphere. Preliminary estimates provide the methane flux rates of 9 g/s (>0.7 ton/per day).
- Inverse Plume Modeling results are influenced by wind speed and directional variability.

Chapter 6 Chemical Analysis of Gas Samples Collected from the MC20 Leak in the Northern Gulf of Mexico

- The abundances and ratios of the C1-C5 light hydrocarbons in the gas collected at the MC20 site are consistent with known thermogenic “wet” well gases and suggest that little to no biogenic contribution was observed.
- The carbon isotopic ratios ($^{13}C/^{12}C$) of the C1-C5 hydrocarbon gases are considered to be isotopically “heavy” and are consistent with thermogenic well gases according to models published in scientific literature.
- The isotopic ratios of the gas samples collected at MC20 suggest that the gas originated from a similar Upper Jurassic gas source like the gas produced from the MC252 Deepwater Horizon well.

Executive Summary

Chapter 7 An Assessment of Oil-related Chemical Contaminants in Sediment, Water, and Oil from the MC20 Site in the Northern Gulf of Mexico

- Concentrations of oil-related contaminants in surface sediments decrease as distance from the release point increases up to 500 m from the erosional pit. No direct evidence for MC20 oil was found in surface sediments >500 m from the erosional pit.
- Oil-related contaminants are an order of magnitude higher in sediments at the perimeter of the erosional pit as compared to all other sediment samples.
- Oil-related compounds measured in the sediments at the perimeter of the erosional pit are severely degraded as compared to oil collected mid-water column and at the surface indicating that oil in the water column and at the surface are not primarily sourced from sediment characterized at MC20.
- Mid-water column collected oil is mildly degraded and closely resembles historic reservoir degraded oil from MC20 well #9 in both its API oil gravity and its *n*-C17 and *n*-C18 relative ratio to their pristane and phytane counterparts.
- Subtle heterogeneities observed between mid-water column captured bulk oil, mid-water column captured water, and surface water sheen samples, along with the variations observed from three historic MC20 oils point toward current ongoing release from multiple wells at the MC20 site.

Chapter 8 Estimates of Oil Flux to the Ocean using Optical and Acoustical Methods

- Estimated oil flux numbers are conservative and do not account for portions of the plume that do not visibly rise through the water column or constitute oil droplet size and volume density below acoustic detection limits.
- Optical oil flux methods estimate a range of 19 to 108 barrels of oil per day.
- Acoustic backscatter oil flux methods estimate a range of 9 to 47 barrels of oil per day.
- Further development of these approaches could reduce uncertainties and lead to the creation of a standardized set of tools and procedures to measure current and future releases of hydrocarbons in the marine environment.

Chapter 1
Introduction and Background Conditions at the Former Taylor Energy MC20 Site in September 2018

Andrew L. Mason[1], Mary M. Rider[1,2], Ian R. MacDonald[3], and J. Christopher Taylor[4]

Sunrise in the Gulf of Mexico. Credit: NOAA NOS/NCCOS

ABSTRACT

In September of 2018 NOAA and its partners conducted seven days of field operations to collect data for an integrated survey of conditions at the former Taylor Energy MC20 site in the northern Gulf of Mexico. Data or environmental samples from eight surface pole mounted acoustic surveys, seven subsurface ROV mounted acoustic surveys, five video bubble size measurement collection efforts (comprising hundreds of samples), four direct oil/water/gas sample collection efforts (thirteen gas samples and eight water/oil samples), three CTD-rosette casts, two surface water collection efforts, fifteen sediment samples, and two gravity core samples were collected to allow a thorough characterization of the conditions at the site. These data are described in detail in the following chapters of this report. This chapter details how the MC20 site came to be in the condition it was in during September 2018 and why this integrated survey was conducted.

Citation for chapter
Mason, A.L., M.M. Rider, I.R. MacDonald, and J.C. Taylor. 2019. Chapter 1: Introduction and Background Conditions at the Former Taylor Energy MC20 Site in September 2018. pp. 1-6. In: A.L. Mason, J.C. Taylor, and I.R. MacDonald (eds.), An Integrated Assessment of Oil and Gas Release into the Marine Environment at the Former Taylor Energy MC20 Site. NOAA National Ocean Service, National Centers for Coastal Ocean Science. NOAA Technical Memorandum 260. Silver Spring, MD. 147 pp. doi: 10.25923/kykm-sn39

[1] *NOAA National Ocean Service, National Centers for Coastal Ocean Science, Stressor Detection and Impacts Division, Monitoring and Assessment Branch. Silver Spring, MD*
[2] *CSS, Inc., Fairfax, VA.*
[3] *Florida State University, Earth, Ocean, and Atmospheric Science, College of Arts and Sciences. Tallahassee, FL.*
[4] *NOAA National Ocean Service, National Centers for Coastal Ocean Science, Marine Spatial Ecology Division, Biogeography Branch. Silver Spring, MD*

Introduction

Chapter 1

1.1 BACKGROUND

The 2004 Atlantic hurricane season was a particularly active and destructive season resulting in over 3,200 deaths and more than $61 billion in damage (Franklin *et al*., 2006). One of the most destructive Atlantic hurricanes in 2004 was Hurricane Ivan, which swept through the Caribbean, Gulf of Mexico, and southern United States twice between 2 and 24 September. On 16 September 2004, when Hurricane Ivan reached the northern part of the Gulf of Mexico and made landfall on the U.S. mainland, it was a Category 3 Hurricane producing 200 km/h (125 mph) winds and 22 m (71 foot) waves. It completely destroyed seven drilling platforms, majorly damaged 12 large pipelines and six other platforms, disrupted the daily flow of 475,000 barrels of oil and 1.8 billion cubic feet of natural gas for more than four weeks, and produced over $20.5 billion in damages (Blake *et al*., 2011; Franklin *et al*., 2006; MMS, 2004).

One of the drilling platforms destroyed by Hurricane Ivan was the Taylor Energy Company's (TEC) Mississippi Canyon Block 20 Saratoga Platform A (MC20). MC20 is located about 16 km southeast of the mouth of the South Pass of the Mississippi River, approximately 100 km west from where the eye of Hurricane Ivan passed through the northern Gulf of Mexico. The fixed, 8-pile structure was installed in 1984 at a depth of 146 m and had 28 connected oil and gas wells reaching reservoirs as deep as 3.35 km. On 16 September 2004, an underwater mudslide triggered by large wave action toppled the MC20 superstructure, also known as the jacket, dragging it along the seafloor to its final resting position 210 m southeast and downslope of its original location and partially burying it in as much as 21 m of mud (MMS, 2004; Figure 1.1). The conductor bundle containing the 28 wells, which was attached to the jacket, was dragged along with the structure and buried under deposited sediment at its northwest corner. The site currently sits in approximately 135 m of water and is dominated by the collapsed jacket. There are three major bathymetric depression features currently present at the site, one resulting from removing the platform deck structure in 2011 from what was the top of the jacket, one at the former well bay location from initial attempts to dredge down to the conductor bundle for well intervention efforts, and an erosional pit at the northwest corner of the jacket formed by ongoing release of oil and gas from the leaking conductor bundle.

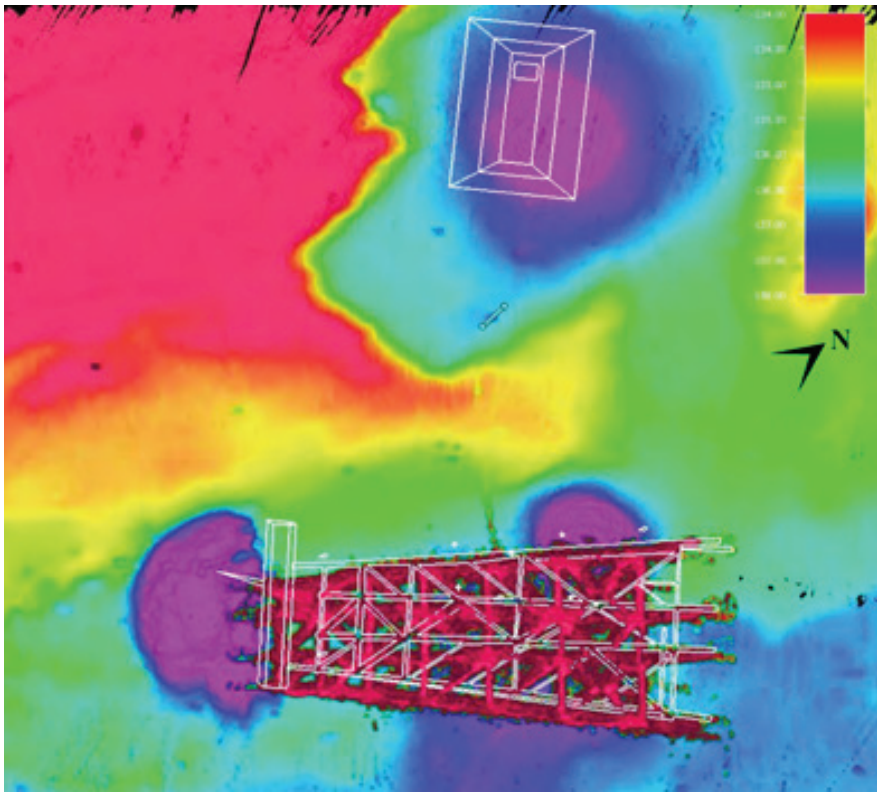

Figure 1.1. Bathymetric map of the Mississippi Canyon Block 20 Saratoga Platform A (MC20) study site with line drawings of the former well bay area and the toppled jacket platform showing the erosional pit on the northwest side of the toppled jacket. The depression at the left side of the image was created during removal operations of the superstructure on the jacket top. Source: Camilli et al.*, 2019*

The destruction of the MC20 platform was not the first time where wave action from a large hurricane in the Gulf of Mexico triggered a submarine slope failure resulting in an underwater mudslide that damaged an offshore oil platform. In 1969, during Hurricane Camille, a subsea mudslide destroyed one offshore platform and severely damaged at least one other in the South Pass Block 70 area of the Gulf of Mexico. Following this event, the offshore oil industry began dedicating considerable attention to developing numerical and analytical methods to predict when and where future mudslides might occur. In 1980, Coleman *et al*. (1980) produced a

report for the Department of the Interior's (DOI) Bureau of Land Management (BLM) which analyzed sediment instabilities in the offshore Mississippi Delta region. The area they identified as being mudslide susceptible included the South Pass Block 70 sites. After Hurricane Ivan, an assessment for the Minerals Management Service (MMS) assessing mudslides during Hurricane Ivan and the potential for future mudslides showed that MC20 is also within what Coleman *et al*. (1980) referred to as the mudflow lobe in the mudslide-prone area (Nodine *et al*., 2007). The difference between Hurricane Camille and Hurricane Ivan is that the longer wave period associated with Hurricane Ivan is thought to have triggered mudslides in deeper water than during Hurricane Camille.

Sea surface oil slicks were first reported around the MC20 site to the U.S. Coast Guard (USCG) on 17 September 2004 (USCG NRC, 2018; SEQNOS ID: 735409). On 28 September, the MODIS satellite captured a cloud-free color image of the northern Gulf of Mexico showing a black streak of oil emerging from the sediment laden coastal waters off the Mississippi Delta. Under the Oil Pollution Act of 1990 (OPA), when an oil spill occurs, the law designates a Responsible Party (RP) that is required to pay for the oil spill recovery and response costs. Because TEC owned MC20 at the time of the accident, they were designated as the RP and required to work with the USCG and other agencies comprising a Unified Command (UC) to determine any response efforts deemed necessary. In 2008, the USCG established a UC composed of TEC, USCG, and the MMS, now divided into the Bureau of Ocean Energy Management (BOEM) and the Bureau of Safety and Environmental Enforcement (BSEE), to respond to the ongoing release at the site.

Initial assessments identified oil and gas plumes originating from three discrete locations, two oil plumes near the site of the partially buried jacket and a gas plume near the original location of the platform. The oil plumes emanating from near the buried jacket were identified as originating from conductor bundle pipes buried under mud and sediment, making conventional plugging operations difficult. In response to the ongoing leak, TEC planned to drill intervention wells to plug nine of the wells and to place containment domes over three observed hydrocarbon plumes (Figure 1.2). In 2008, TEC began conducting twice-daily overflights to monitor oil slick sightings and reporting them to the USCG National Response Center (NRC; USCG NRC, 2018). TEC officials assert at the time of this publication that any ongoing source of oil at the site is from oil-soaked sediment, that any gas is biogenic in nature and that any current visible sheens represent an average volume

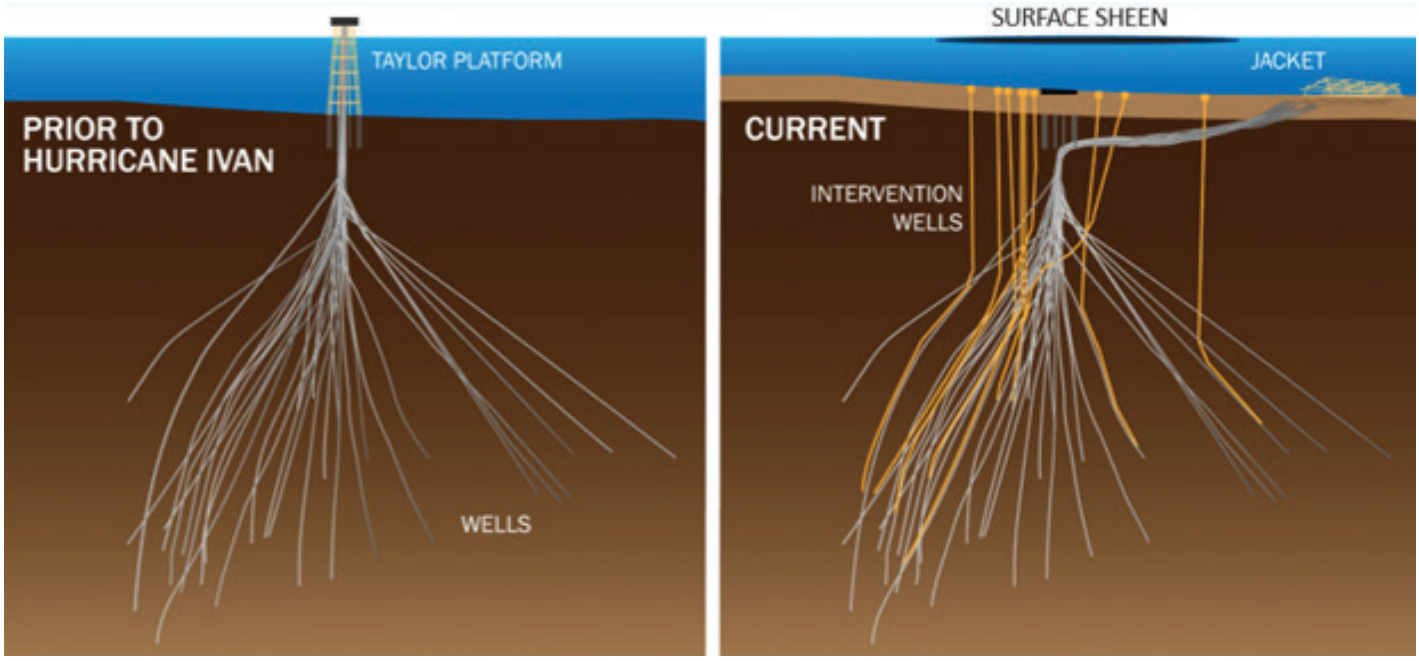

Figure 1.2. An approximate pictorial representation of the MC20 platform before Hurricane Ivan and under current conditions. (Reddy et al.*, 2018).*

Introduction

of 2.4 gallons of oil per day (Camilli and Reddy, 2018). They equate this to "approximately one drop of oil being released each minute from a two square foot area on the mud line", although acknowledge that occasional larger slicks do occur, attributing them to the lunar cycle and the influence of tidal movements (TEC, 2014). The results of this study contradict these conclusions by TEC and are described in detail in the following chapters.

Renewed attention was brought to the MC20 site following the Deepwater Horizon MC252 oil spill when persistent oil slicks that appeared unrelated to the 2010 spill were noticed by SkyTruth analysts (Amos, 2010). The oil slicks emanating from the MC20 site have been visible on the ocean surface from ships and by aerial and satellite remote sensing (Figure 1.3). These images, and other sources of remote sensing images, have been used by a number of researchers to estimate the output of hydrocarbons from the site, resulting in a wide range of calculations quantifying the oil leaking from the site. All of these estimates were higher than the amounts reported by TEC. Due to the persistent surface sheens and oil and gas plumes observed, it was determined that collections and measurements from the water column and sediments, as well as the possible flux of hydrocarbon gas into the atmosphere, needed to be analyzed to compliment previous observations.

Figure 1.3. Persistent oil slicks originating from the erosion pits under the platform jacket.

In response to a request by BSEE, the National Oceanic and Atmospheric Administration's (NOAA) National Centers for Coastal Ocean Science (NCCOS), in cooperation with NOAA's Office of Response and Restoration (ORR), conducted a survey at the MC20 site in September 2018 on the R/V *Brooks McCall.* The project goals were to better quantify the sources, characteristics, and magnitudes of hydrocarbon seep plumes at the MC20 site. The tasks were summarized as follows:

1. Collect data that will allow NOAA and its partners to support an accurate, and scientifically defensible flow rate at the former Taylor Energy MC20 site,

2. Collect and characterize viable gas samples from the plume sources coming from within the excavated depression at the former Taylor Energy MC20 site for isotopic and hydrocarbon analysis, and

3. Collect other relevant environmental data related to any oil and gas release at the former Taylor Energy site after priorities one and two have been achieved.

From 1-7 September 2018, NOAA and its partners conducted a series of combined surveys including surface and subsurface acoustic measurements, mid-water column oil, gas, and water collections, surface water sample collections, mid-water column video bubble collections, surface methane collections, and marine sediment collections. Ancillary physical water column data were also collected including ocean current profiles and conductivity, temperature, and depth. The results and conclusions from these surveys are included in detail in the subsequent chapters of this report.

1.2 SCIENTIFIC INTEGRITY AND PEER REVIEW

Scientific integrity is one of the core values of NOAA, all of its scientists, and required of its collaborators. To ensure the highest scientific standards are upheld, NOAA strictly adheres to the policies detailed in NAO 202-735D: Scientific Integrity. Of particular relevance is Section 4.01, which is quoted below:

> *"NOAA is an organization based upon science, scientific research, and providing and using scientific advice for decision-making. NOAA recognizes a clear distinction between the scientific process and the policy decisions made based on the results of science. NOAA's ability to achieve its strategic vision of "healthy ecosystems, communities, and economies that are resilient in the face of change" relies on transparency, traceability, and scientific integrity at all levels. Transparency, traceability, and integrity are, therefore, core values of our organization and the reason for issuing this Order."*

Toward the end of upholding the highest standards of scientific integrity and to provide the best possible scientific answers to complex environmental questions, the authors of the subsequent chapters undertook specific peer review steps for the publication of this NOAA Technical Memorandum. While these review steps varied between chapters, at a minimum each individual chapter's methods and conclusions were reviewed by at least three internal NOAA or external partner scientists not associated with the authoring of that chapter. Where possible, independent outside expert peer reviewers were utilized to confirm sound scientific processes and conclusions. The authors of this report fully stand behind their sample design, data analysis, methods and method development, and results and conclusions as part of this innovative and challenging integrated survey.

1.3 REFERENCES

Amos, J. 2010. Gulf of Mexico – Time To Get Serious About Routine Satellite Monitoring. SkyTruth, June 10, 2018. Online: https://skytruth.org/2010/06/gulf-of-mexico-time-to-get-serious/ (Accessed 24 May 2019)

Blake, E.S., C. Landsea, and E.J. Gibney. 2011. The Deadliest, Costliest and Most Intense U.S. Tropical Cyclones: Costliest U.S. tropical cyclones tables updated (2018). NOAA National Weather Service, National Hurricane Center. NOAA Technical Memorandum NWS NHC-6. Miami, FL. 49 pp. Online: https://www.nhc.noaa.gov/news/UpdatedCostliest.pdf (Accessed 24 May 2018)

Camilli, R., A. Mallios, C. Reddy, and W. Bryant. 2019. Two Decades of *In-Situ* Observation Guiding MC20 Response Operations: What We Have Learned and Why It Matters. Paper presented at the Gulf of Mexico Oil Spill and Ecosystem Science Conference (GoMOSES), New Orleans, LA. Retrieved from MC-20 Response Information Center. Online: https://mc20response.com/wp-content/uploads/2019/02/Camilli-GOMOSES-for-TEC.pdf (Accessed 24 May 2019)

Camilli, R., and C. Reddy. 2018. Rum-Punch: Time series petroleum biomarker testing of the scenario that an actively leaking oil well is contributing to the MC20 sea surface sheen. Prepared for Unified Command, February 10, 2018. Retrieved from MC-20 Response Information Center. Online: https://mc20response.com/wp-content/uploads/2019/01/2018.02.10-Rum-Punch-Analysis-Drs-Camilli-and-Reddy.pdf (Accessed 24 May 2019)

Coleman, J.M., D.B. Prior, and L.E. Garrison. 1980. Subaqueous Sediment Instabilities in the Offshore Mississippi River Delta. A final report by Louisiana State University and the U.S. Department of the Interior, U.S. Geological Survey for the U.S. Department of the Interior, Bureau of Land Management Gulf of Mexico OCS Office. New Orleans, LA. NTIS No. PB80-224629. BLM Open File Report 80-01. Contract No. AA551-MU9-10. 60 pp.

Introduction

Franklin, J.L., R.J. Pasch, L.A. Avila, J.L. Beven II, M.B. Lawrence, S.R. Stewart, and E.S. Blake. 2006. Atlantic Hurricane Season of 2004. Monthly Weather Review 134(3): 981-1025. doi: https://doi.org/10.1175/MWR3096.1

MMS. 2004. MMS Updates Damage Assessment from Hurricane Ivan [Press release]. Release: #3164, October 8, 2004. U.S. Department of the Interior, Minerals Management Service. Online: https://www.boem.gov/boem-newsroom/press-releases/2004/press1008a.aspx (Accessed 24 May 2019)

Nodine, M.C., J.Y. Cheon, S.G. Wright, and R.B. Gilbert. 2007. Mudslides during Hurricane Ivan and an Assessment of the Potential for Future Mudslides in the Gulf of Mexico. Phase II Project Report, Prepared for the Minerals Management Service, Under the MMS/OTRC Cooperative Research Agreement 1435-01-04-CA-35515, Task Order 39239, MMS Project Number 552. 192 pp. Online: https://www.bsee.gov/research-record/tap-552-mudslides-during-hurricane-ivan-and-assessment-potential-future-mudslides (Accessed 24 May 2019)

Reddy, C.M., E. Overton, R. Camilli, W. Bryant, D Valentine. 2018. Surface sheens at the Taylor Energy site at MC20: Historical and recent data. Paper presented at the Society of Environmental Toxicology and Chemistry (SETAC), Sacramento, CA. Retrieved from MC-20 Response Information Center. Online: https://mc20response.com/wp-content/uploads/2019/01/REDDY-SETAC-Nov-7-2018-uploaded-final.pdf (Accessed 24 May 2019)

TEC. 2014. Final Risk Assessment and Cost Estimate (FRACE): Executive Summary. Taylor Energy Group. Retrieved from MC-20 Response Information Center. Online: https://mc20response.com/wp-content/uploads/2019/01/FRACE-Executive-Summary.pdf (Accessed 24 April 2019)

USCG NRC. 2018. 2004 Reports. U.S. Coast Guard, National Response Center. SEQNOS ID: 735409. Online: http://nrc.uscg.mil/ (Accessed 24 May 2019)

Chapter 2
Characterization of the Observed Physical Characteristics of the Water Column at the MC20 Site in the Northern Gulf of Mexico

Ian R. MacDonald[1], Mauricio Silva[1], Carrie O'Reilly[1], Bernie B. Bernard[2], and Les Bender[2]

Sunset in the Gulf of Mexico. Credit: NOAA NOS/NCCOS

ABSTRACT

The MC20 site displayed profiles of salinity, temperature, and dissolved oxygen that are typical for coastal Gulf of Mexico regions in late summer. Temperature profiles indicated that the site is within the upper portion of the thermocline. Some freshening of the surface layer salinity was noted in response to Mississippi River outflow. Dissolved oxygen was variable with the transient appearance of a borderline hypoxic layer centered around 60 m depth. Distinct salinity anomalies were found above an erosional pit near the fallen well jacket. An acoustic Doppler current profiler deployed near the erosional pit recorded vertical velocities of 20-25 cm s^{-1} when the rising plume of gas and oil was deflected over the instrument. A cavity ring-down spectrometer recorded atmospheric methane anomalies as high as 11 ppm over the erosional pit and well jacket.

Citation for chapter
MacDonald, I.R., M. Silva, C. O'Reilly, B.B. Bernard, and L. Bender. 2019. Chapter 2. Characterization of the Observed Physical Characteristics of the Water Column at the MC20 Site in the Northern Gulf of Mexico. pp. 7-18. In: A.L. Mason, J.C. Taylor, and I.R. MacDonald (eds.), An Integrated Assessment of Oil and Gas Release into the Marine Environment at the Former Taylor Energy MC20 Site. NOAA National Ocean Service, National Centers for Coastal Ocean Science. NOAA Technical Memorandum 260. Silver Spring, MD. 147 pp. doi: 10.25923/kykm-sn39

[1] *Florida State University, Earth , Ocean, and Atmospheric Science, College of Arts and Sciences. Tallahassee, FL.*
[2] *TDI-Brooks International, Inc. College Station, TX.*

Physical Characteristics

Chapter 2

2.1 INTRODUCTION

This chapter documents physical measurements of the water column and atmosphere undertaken from 1-7 September 2018 to establish background conditions for interpreting and characterizing the source, shape, and trajectory of the oil and gas plume at the MC20 site and to document concentration anomalies that could lead to calculations of discharge and flux rates. Measurements were based on instruments mounted on the R/V *Brooks McCall,* on the SeaTrepid remotely operated vehicle (ROV) Comanche, or mounted on the seafloor. Additional reference data are drawn from public sources.

2.2 METHODS

2.2.1 Research Vessel

The MC20 sampling operations were carried out on the R/V *Brooks McCall* (BMCC hereafter). This is a 49.4 m ship home-ported in Freeport, Texas. The BMCC is equipped with winches, sediment coring devices, water column samplers, and laboratory space. The scientific party included 29 scientists, technicians, ROV operators, and government observers.

2.2.2 Navigation and Ship Log

The position of the BMCC was continuously recorded based on output from a ship-mounted differential GPS receiver and digital compass system. Wind speed and direction were recorded from output of a ship-mounted anemometer. Location of the ROV was estimated with the use of a HiPAP ultrashort baseline (USBL) transponder system that measured the vehicle offset from a pole-mounted transponder and calculated regular fixes based on the ship position. All navigation inputs were logged with use of WinFrog™ navigation software. All times were based on GPS, UTC time (universal time code, central standard time plus 6), which made it possible to estimate the location of the ship or ROV during any sampling event based on the UTC time index. On-demand fixes entered in WinFrog™ were also used to record events such as instrument lowerings or other discrete observations. The WinFrog™ event logs are provided as Appendix A to this report. All times are reported in UTC and all sampling dates were recorded between 1 and 7 September 2018.

Metadata for sampling operations were additionally recorded with the use of the Deep-C CRUISE WORKBOOK spreadsheet program maintained by the Florida State University team. This software generates unique event codes for all sampling operations, as well as paper log-sheets that the cruise personnel could fill in with specific information regarding sampling operations while they were underway. The written data were then transferred to digital spreadsheets when operations were completed. The project thus maintains paper records of all operations, as well as a digital record.

2.2.3 Study Site

All sampling operations undertaken for this project, with the exception of sediment reference sites, took place in the Mississippi Canyon 20 (MC20) lease block, located approximately 18 km southeast from Port Eads, Louisiana, which is the approximate southernmost point of land on the Birdfoot Delta of the Mississippi River (Figure 2.1). Sonar returns in the center of the bathymetric map in Figure 2.1 indicate the location of the well jacket. Bathymetric depressions exist at the original well head from dredging operations that removed sediments from the area immediately north of the jacket. A second bathymetric depression southwest of the jacket was created during the removal of the platform decking. A third smaller bathymetric depression is located at the northwest corner of the jacket, attributed to an erosional pit caused by emission of gas and oil through the seafloor sediment (Figure 2.1). This region of the continental shelf is characterized by extensive deposition of poorly consolidated silt and clay that were displaced from the delta marshlands in mudslides generated by Hurricane Ivan in the 2004 event that destroyed the MC20A platform (Nodine *et al*., 2007).

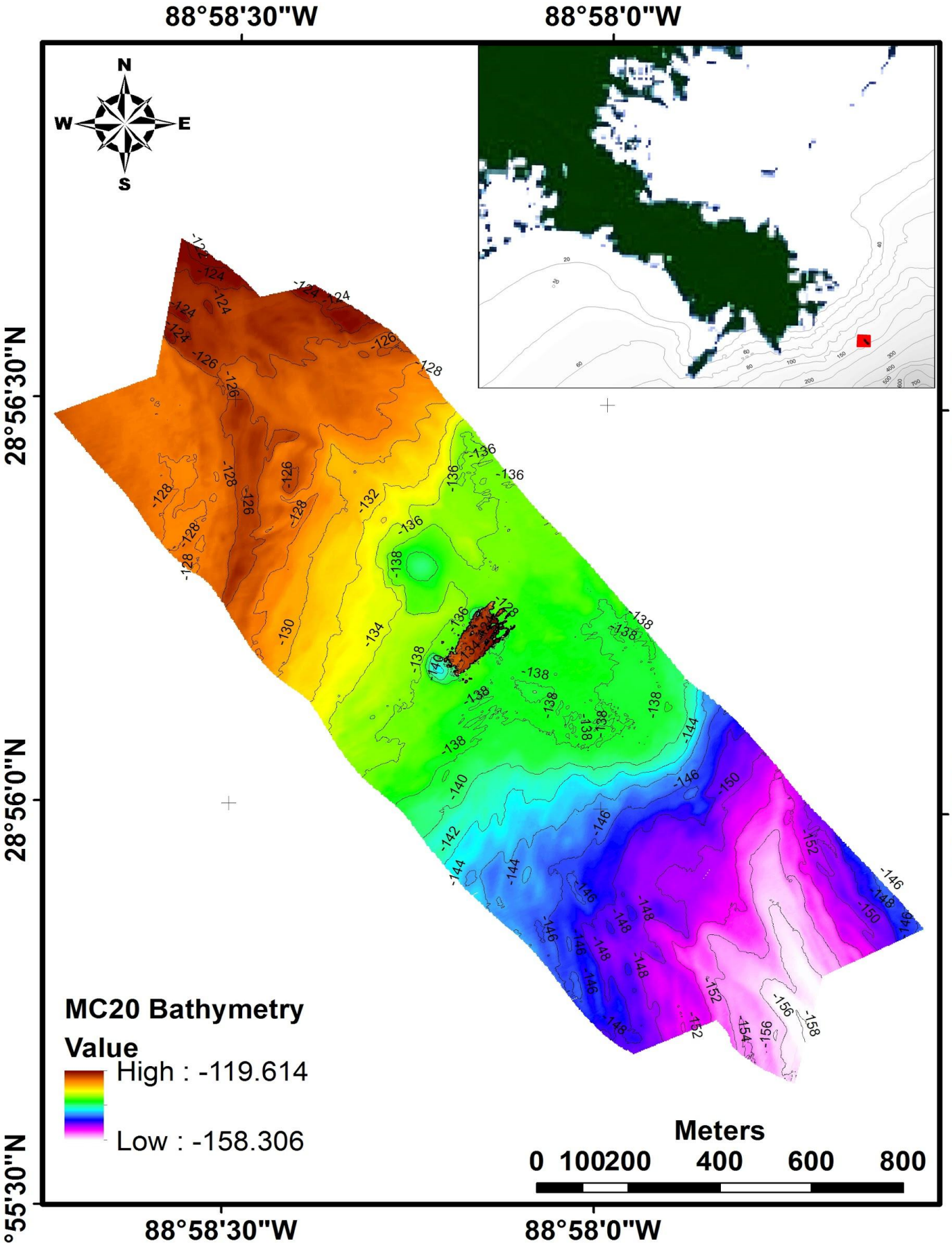

Figure 2.1. General location of the MC20 lease block (inset) and local bathymetry of the site. Source data: Baldwin et al., 2018.

Physical Characteristics

Operations were confined within a 2 km radius surrounding the former location of the MC20A production platform (known as the "well template") and were largely focused on or around the northwest corner of the platform's fallen legs (known as the "well jacket"), where discharging gas and fluids have excavated distinctive craters in the seabed (Figure 2.2, Figure 2.3). The seabed slopes gradually to the southeast in this area. Considerable sediments were removed by dredging operations undertaken by the Responsible Party (RP) in 2005 and the faint outline of the removal area is evident in the fine-scale bathymetry of the site (Figure 2.1).

2.2.4 Data Acquisition

Water column variables were recorded with conductivity-temperature-depth (CTD) instruments (Sea-Bird Electronics (SBE), Inc.). Two CTDs were used, a SBE18-SBE43 and an SBE 19plus. The SBE18-SBE43 was deployed on a rosette sampler that was lowered over the side of the ship. It recorded profiles of the water column variables (salinity, temperature, depth, and oxygen) and collected discrete water samples from multiple depths. The water samples were analyzed for methane (CH_4) concentrations with the use of gas chromatography with flame-ionized detection (GC-FID). The rosette sampler was used to collect water samples from hydrocarbon plumes based on plume locations observed by the acoustic equipment (see Chapter 3 for methods). Lowerings with the rosette were terminated at a maximum depth of 110 m to avoid collision with the well jacket. A SBE 19plus CTD was mounted on the ROV and recorded water column variables while the ROV was operating (Table 2.1).

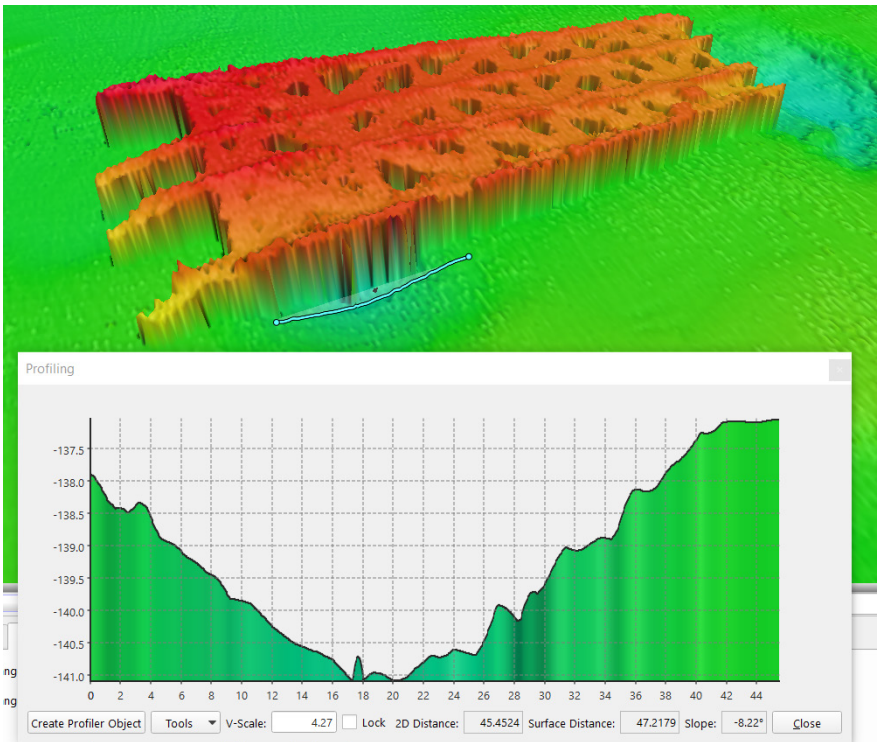

Figure 2.2. Profile of erosional pit at the northwest corner of the jacket. Upper panel is a view to the southeast. Profile shows the depression (front left) is at least 4 m deeper than the surrounding seabed. Source data on file: Camilli, 2017.

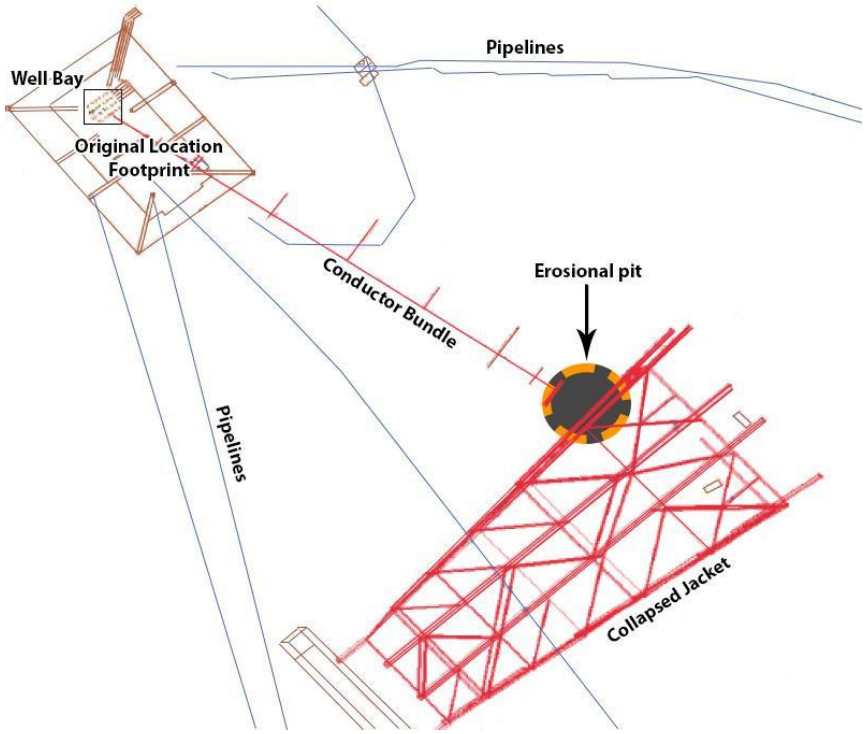

Figure 2.3. Sketch of how the remains of the MC20A platform are situated on the seabed. Sampling operations focused on the erosional pit and followed plumes of gas and liquid that emanated from this location. Image source: Adapted from BSEE documents on file.

Temperature and salinity anomalies were calculated by subtracting the average of all salinity or temperature readings in intervals of 10 m to each absolute temperature and salinity value. Salinity and temperature anomalies were also gridded and plotted in Ocean Data Viewer (ODV) as continuous profiles and surface maps using the same at intervals of 10 m.

2.2.5 ROV Dives

Measurements, collections, and observations in the water column were primarily carried out with the use of the Comanche ROV (simply ROV hereafter), which is homeported in Robert, Louisiana. The ROV was launched and recovered from a dedicated winch and A-Frame system mounted for the project on the starboard side of the BMCC main deck. Pilot functions were carried out in a deck-mounted control van. The data stream from the ROV sensors included three black and white video cameras that were overlaid with depth and compass read-outs; these were visible in the control van and also in the upper deck dry lab of the BMCC where the science party could observe operations and make piloting requests. Only two of the three video feeds could be recorded due to limitations of the audio/video hardware available during the cruise. All ROV video recordings collected during this survey are maintained by the National Oceanic and Atmospheric Administration (NOAA) in an unaltered state. The SBE 19plus CTD described above was mounted on the stern of the ROV and provided a real-time read-out of depth, temperature and salinity.

Dive operations with the ROV were carried out each day that the BMCC was on station in the MC20 area (Table 2.1). CTD data from five of the dive profiles were synchronized, georeferenced, and matched with ROV navigation data using the time and depth from the CTD clock and pressure sensor with time stamp and USBL depth from the ROV. The georeferenced CTD data was exported into ODV (version 5.1.5) in order to create continuous gridded profiles (from surface to bottom) and surface plots of water temperature, salinity, density, and dissolved oxygen each 10 m from surface to bottom.

Table 2.1. CTD measurements of the water column recorded from instruments on the ROV and on the rosette casts taken over the side. Note that date and time here are local and from the Deep-C CRUISE WORKBOOK while those from Appendix A are in UTC from the BMCC Event Log.

Event ID	Type	Date	Start Time	End Time	Instrument
SV6	ROV Dive	9/2/2018	18:33:14	22:36:50	SBE19Plus
SV11	ROV Dive	9/3/2018	14:21:25	16:44:01	SBE19Plus
SV13	ROV Dive	9/3/2018	19:08:39	20:51:02	SBE19Plus
SV16	ROV Dive	9/5/2018	18:51:21	16:47:24	SBE19Plus
SV23	ROV Dive	9/6/2018	14:16:03	17:14:36	SBE19Plus
CT2	Rosette Cast	9/1/2018	17:33:32	17:58:23	SBE18-SBE43
CT8	Rosette Cast	9/2/2018	21:39:08	22:56:36	SBE18-SBE43
CT18	Rosette Cast	9/6/2018	0:00:51	0:22:43	SBE18-SBE43
CT19	Rosette Cast	9/6/2018	1:43:00	2:01:54	SBE18-SBE43

2.2.6 Current Profiling

Profiles of the currents in the water column above the northwest corner of the collapsed jacket were recorded with the use of a Teledyne RDI Workhorse 300 kHz Acoustic Doppler Current Profiler (up-looking ADCP hereafter) that was deployed on the seabed and directed upward from a weighted frame. The up-looking ADCP was placed and recovered on the bottom by the ROV approximately 3 m northwest from the erosional pit. It recorded data from 21:21, 3 September until 23:11, 6 September 2018. From this position, the instrument was able to interrogate the oil and gas plume when lateral currents carried it directly above the instrument's location. Note that deployment was initially delayed to avoid disturbance of the bottom and any potential biasing of acoustic results detailed in Chapter 3 of this overall document. After the instrument was deployed, Tropical Storm Gordon forced the BMCC to vacate the area as it passed by the site at approximately 01:00 on 4 September 2018. Any possible disturbance of the bottom by placement of the up-looking (instrument sensors facing toward the ocean surface) ADCP would have been mitigated by passage of tropical storm waves across the site prior to resumption of sampling activities late on 4 September. Results from the up-looking ADCP are focused on the horizontal and vertical velocities that instrument recorded, in particular on times when the oil and gas plume was situated above the instrument.

A second Teledyne RDI Workhorse 300 kHz ADCP was mounted on the BMCC and recorded down-looking from the ship as it maneuvered across the study area. Interpretation of these data has required some special processing to remove the effects of vessel pitch and roll and only limited reporting of these results are within the scope of this report.

2.2.7 Atmospheric Methane Concentrations

The atmospheric concentration of methane (CH_4) was continuously measured with the use of a cavity ring-down spectrometer (CRDS) Picarro® G2203 Analyzer for CH_4/C_2H_2 that drew air samples (4 Hz) from an intake tube located on the starboard side of the ship, 3 m above the water surface and below the level of the exhaust stacks of the vessel. The length of the intake line introduced a 60 second lag between intake and measurement. Data were recorded during the entire time the BMCC was on-station. Sample readings were georeferenced in real-time using a Trimble® GPS antenna connected to the computer of the CRDS. On the final day of operations, a raft was deployed with a small tank of acetylene so that CH_4 fluxes to the atmosphere could be compared to the acetylene tracer.

2.3 RESULTS AND DISCUSSION

2.3.1 Water Column CH_4 Concentrations and CTD Profiles

A total of four CTD casts were completed during the sampling operation; water samples were taken with Niskin bottles on three of the lowerings (Figure 2.4). Salinity and temperature profiles were typical for coastal Gulf of Mexico, showing an upper mixed layer extending to about 15 m depth. The mixed layer indicated a slight freshening of the salinity values, which reflects the influence of the Mississippi River outflow in this locality, but not a direct reflection of the main outflow plume itself, which would typically show values of less than 30 PSU (practical salinity units; Androulidakis *et al.*, 2018). Therefore, the depth of the pycnocline likely reflects variation in river plume influence on different days. Decrease in water temperature below the mixed

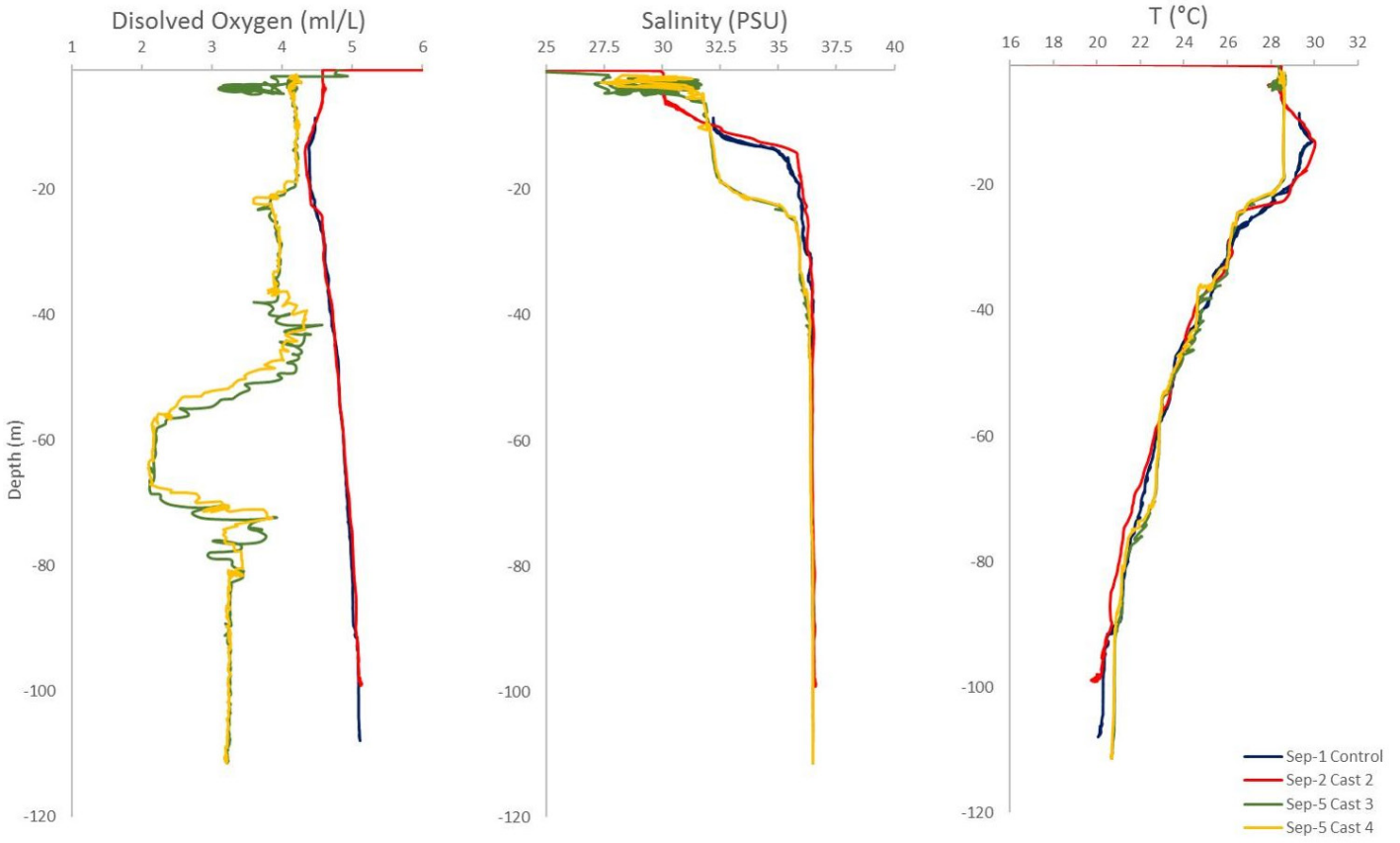

Figure 2.4. Oxygen, salinity, and temperature profiles from the MC20 site recorded during the project.

layer from about 30°C to 20°C indicates that the site remains in the upper portion of the thermocline. The water column was well-oxygenated prior to 6 September when a layer of borderline hypoxic water appears around 60 m. This anomaly does not correspond to elevated CH_4 concentrations.

The goal of the water collections was to sample the oil and gas plume as it was detected with the M3 sonar and other acoustic sensors (see Chapter 3 for details regarding this component of the project). Ambient methane concentrations in the Gulf of Mexico offshore areas have been reported to be about 0.002 µM/L (Lamontangne *et al*., 1973). The first cast (CT8) was completed at 21:39:08 2 September (28° 56.1501 N; 88° 58.2936 W; Figure 2.5). Ambient CH_4 concentrations in these samples were elevated relative to this baseline, which may reflect the influence of CH_4 released from the wells, or the influence of coastal waters. However, the influence of the oil and gas plume was evident at approximately 22 m depth, where CH_4 concentration showed an excursion of 7-fold above the values from the rest of the water column. The second and third casts (CT18 and CT19) were completed on 6 September at 00:00:51 (28° 56.2362 N; 88° 58.2110 W) and 01:43:00 (28° 56.2424 N; 88° 58.1653 W), respectively. The CT18 cast avoided the plume, whereas CT19 intersected the plume at a depth of 91 m. Results of the water sampling demonstrate that the plume produces very elevated CH_4 concentrations within discrete strata of the water column. As would be predicted, CH_4 concentration was greater at greater depths for the data recorded.

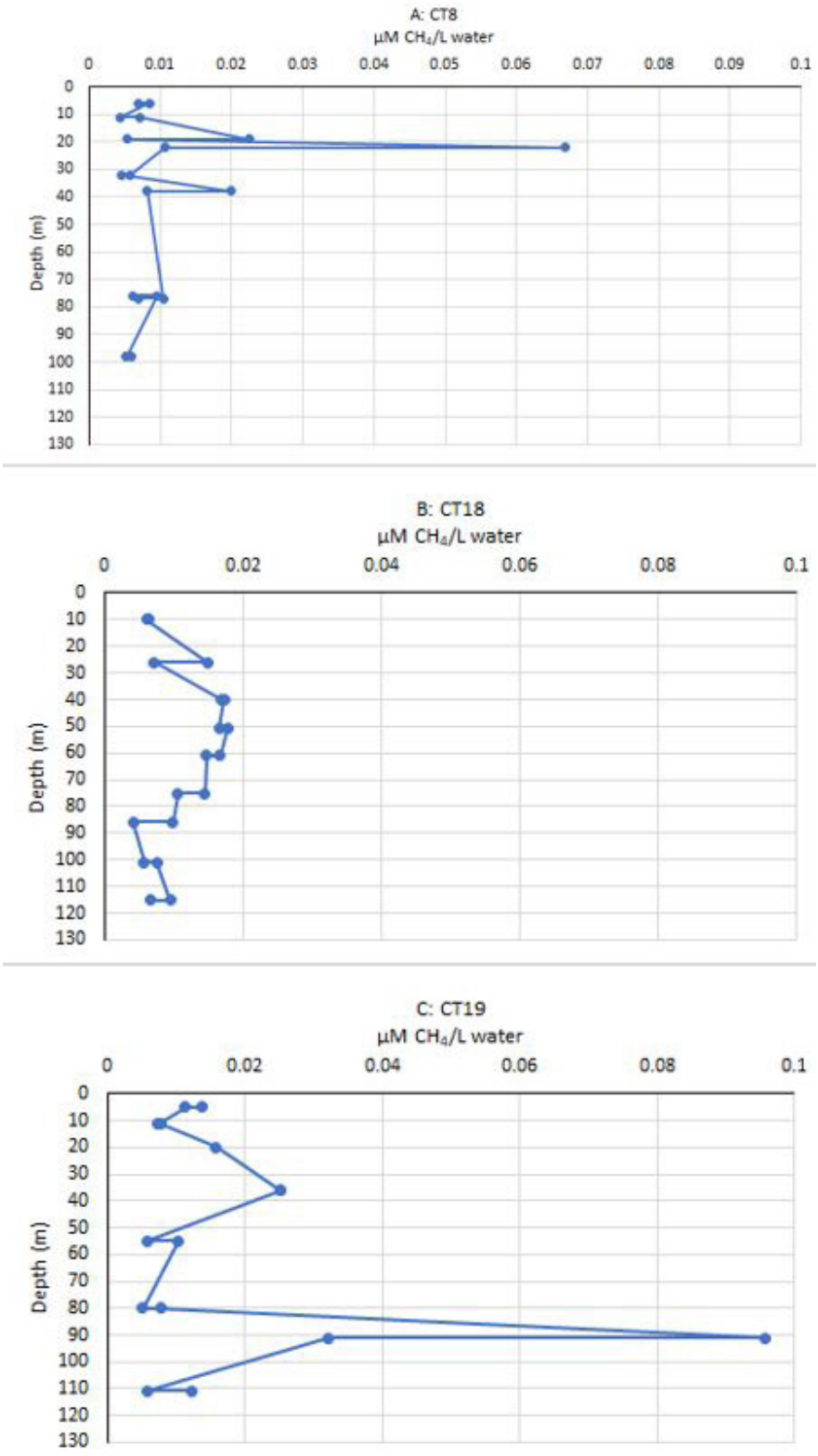

Figure 2.5. CH_4 concentrations measured in water samples collected with the rosette. See text for locations and sample time and date.

Physical Characteristics

2.3.2 CTD Results from ROV Instrument

The SBE 19plus CTD mounted on the ROV recorded temperatures and salinities wherever the vehicle was operating. Because considerable time was devoted to collecting and observing oil and gas from the base of the plume above the erosional pit, the CTD results can be examined to determine whether the discharging plume produced anomalies of salinity or temperature.

Temperature values did not show significant excursions from ambient values recorded by the lowered instrument operating at a distance from the crater. However, salinity values immediately above the crater did display anomalous values (Figure 2.6), with minimum readings close to 28.9 PSU at the deepest part the crater. These low salinity values were only encountered in proximity to the bottom of the northwest corner of the jacket and the erosional pit representing a low salinity plume that extended to at least 100 m depth (i.e., above the height of the well jacket above the seafloor). A similar condition is observed in the salinity surface maps, where low salinity values were observed under 120 m depths in the proximity of the top of the northwest corner of the jacket. In turn, negative salinity anomalies <-1 PSU were found in the surface of the water column, and below 120 m depth in the proximity of the northwest corner of the jacket. The lower salinity anomaly values were found below 130 m over the erosional pit with values close to -4 PSU below the average. These results indicate an ongoing discharge of lower salinity water emanating from the ocean floor and localized to the region above the conductor bundle.

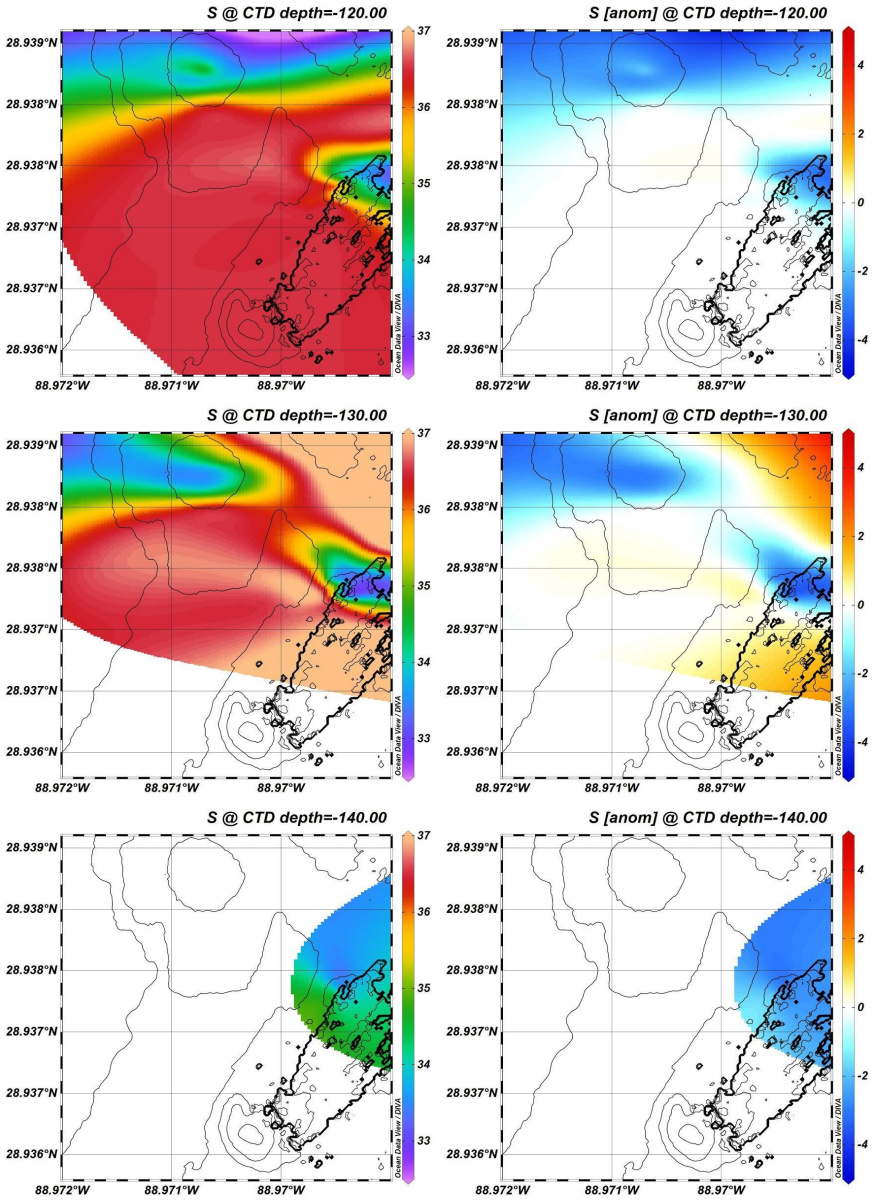

Figure 2.6. Salinity values recorded by the ROV mounted CTD plotted versus depth. Highlighted profiles show salinity recorded when the ROV was operating in and above the crater. Record includes low salinity (<30 PSU) measured in the bottom of the craters.

2.3.3 ADCP Results

The up-looking ADCP deployed next to the erosional pit recorded current velocity from 3-6 September. Values were strongly affected by the upward advection of the oil and gas plume when it passed over the up-looking ADCP beams on 6 September; however, the intensity and sign of the signal depended upon the orientation of the plume with respect to instrument location (Figure 2.7). Maximum values of positive (up-going) advection was observed when the plume was extended directly over the instrument where the plume was at a depth of about 60 m. Results indicate upward velocities of between 20 and 25 cm s^{-1} were characteristic of the plume. Negative values indicate downwelling of water displaced by the plume.

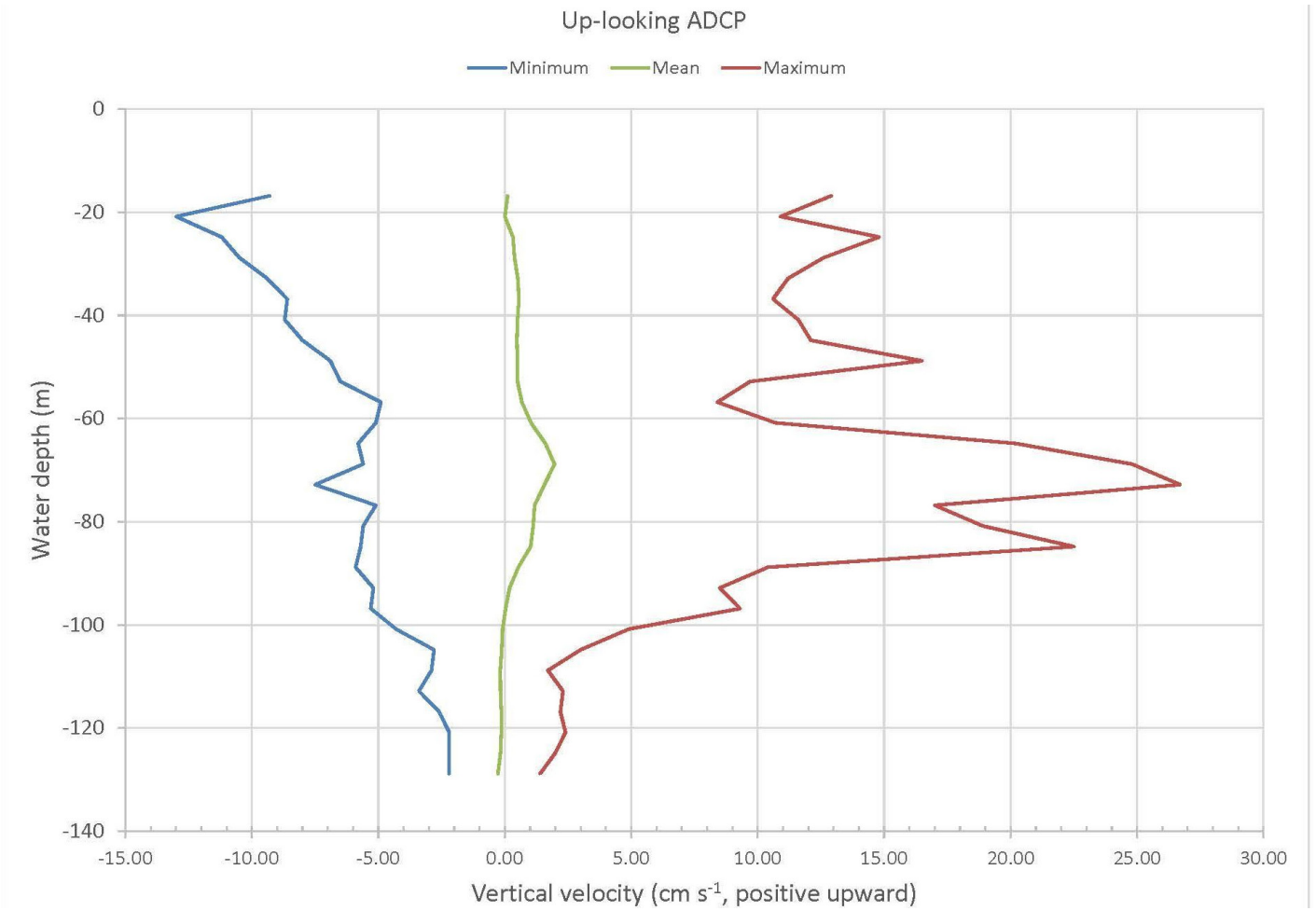

Figure 2.7. Summary values for vertical velocity of water observed from up-looking ADCP deployed at 135 m depth approximately 3 m north of the erosional crater at the NW corner of the well jacket.

Horizontal velocities are provided as contour plots for direction and magnitude (Figure 2.8). Direction and magnitude changed during and following the passage of Tropical Storm Gordon. Prior to the storm, currents were in a predominantly southwestward direction.

Historic records of horizontal velocities extracted from HYCOM model archives (https://www.hycom.org/dataserver) indicate that the site frequently experiences current velocities of approaching 2 knots (0.8 m/s). Strongest currents tended to occur in the upper 25 m of the water column (Figure 2.8).

2.3.4 Cavity Ring-Down Spectrometer Atmospheric Methane Results

Atmospheric methane concentrations were monitored continuously during BMCC operations at the MC20 site. The data rate for measurements of methane, water vapor, and carbon dioxide was 4 Hz and the intake port for the instrument remained positioned 3 m above the water line. Figure 2.9A shows the portion of the ship track that was proximal to the well jacket location on the seafloor.

Background levels of CH_4 were found to be approximately 1.8 ppm (parts per million), which is consistent with global atmospheric levels (https://www.esrl.noaa.gov/gmd/ccgg/trends_ch4/). However, the CRDS also recorded anomalously high CH_4 concentrations (>2.8 ppm) immediately above the northwest corner of the well jacket and in a discernible linear trend that mirrors the jacket legs. A second "hotspot" was detected directly above the former well bay, where acoustic data show a persistent, but faint gas plume. The highest concentrations (>11 ppm) correspond to the locality where gas bubbles and oil drops emanating from the erosional pit were observed reaching the surface of the water.

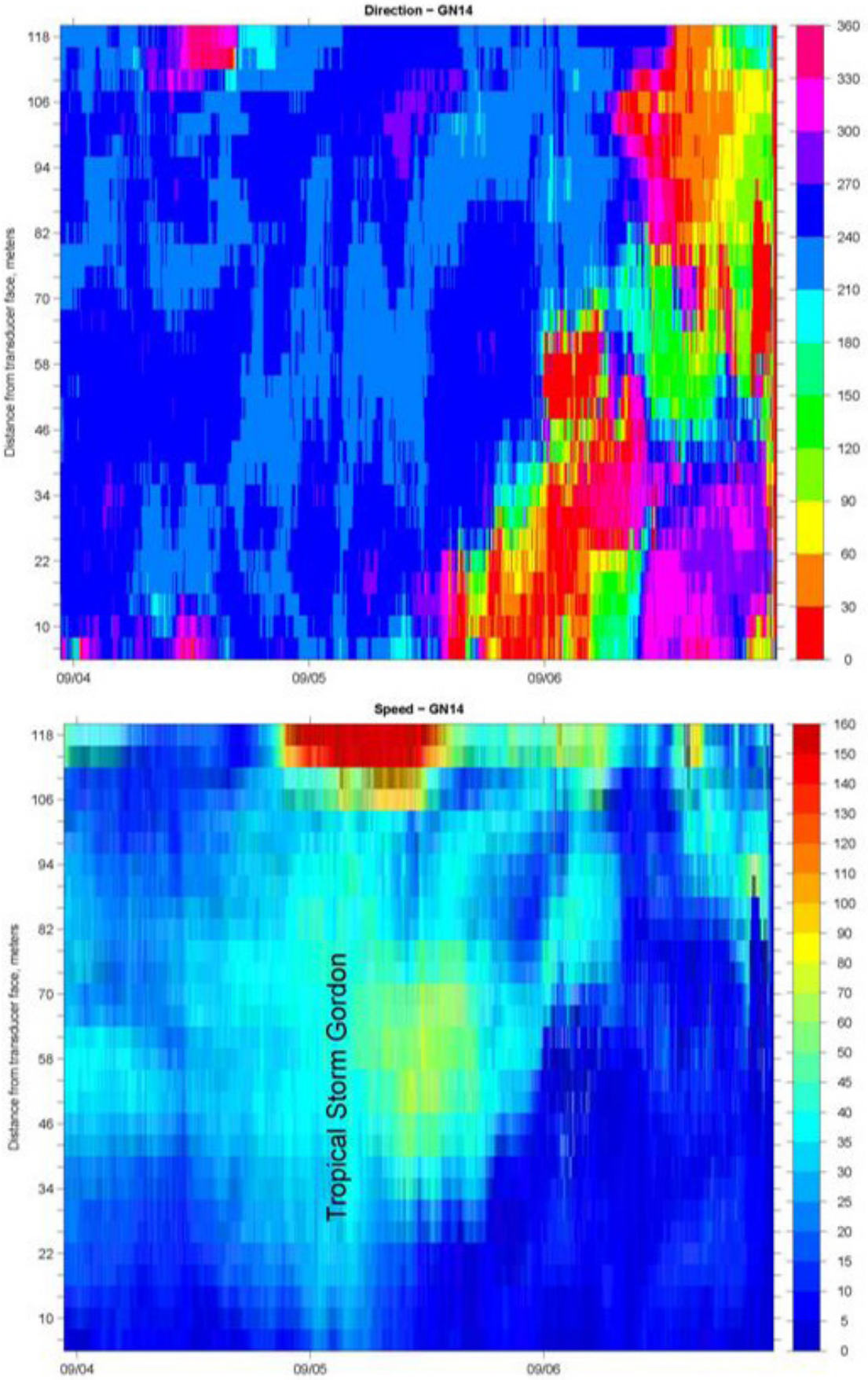

Figure 2.8. Horizontal current direction (top, degrees) and speed (bottom, cm s^{-1}) from up-looking ADCP. Prior to 6 September, currents were generally southwestward. Following passage of Tropical Storm Gordon on 4-5 September, current direction was northward and diminishing in speed.

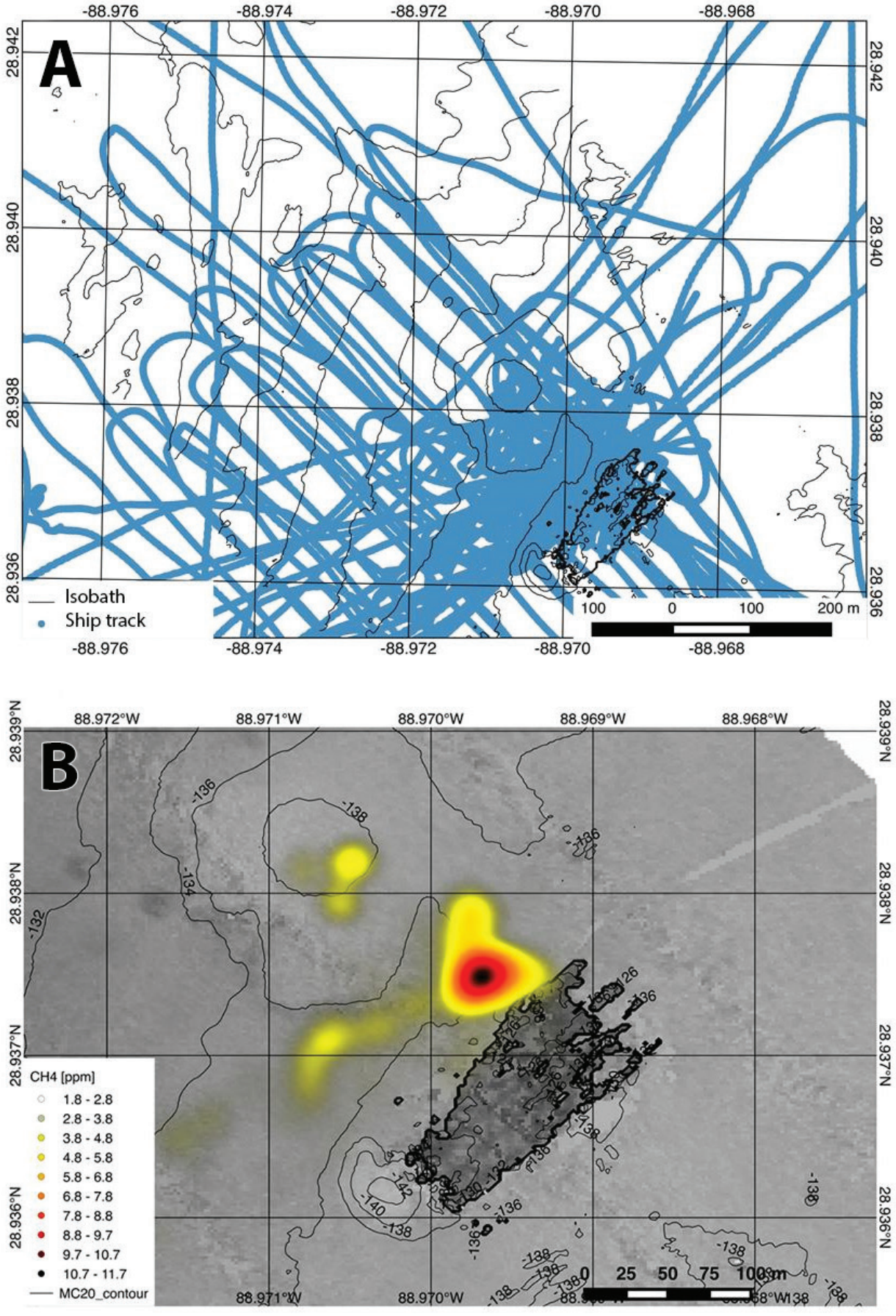

Figure 2.9. Cavity ring-down spectrometer observations of atmospheric methane concentrations: (A) ship track near well jacket; (B) heat map of anomalously high (>2.8 ppm) readings.

2.4 CONCLUSIONS

Water column characteristics document the effects of persistent discharges of gas and fluids at MC20, which are focused in and above the erosional pit at the northwest corner of the well jacket. Negative salinity anomalies of about 3 PSU below ambient water column values were documented in the erosional pit. An upwelling plume was measured episodically with an up-looking ADCP, but these observations were limited to occasions when the plume was deflected into the path of the ADCP beams. Evidence of the biological effect of the hydrocarbon plume may be indicated by the low-oxygen anomaly (Hazen *et al*., 2010) observed between 50 and 70 m depths on 5 September (Figure 2.4). The vertical velocities of 20-25 cm s^{-1} are consistent with rise speed for bubbles that have been reported in the literature (Leifer and MacDonald, 2003). The ADCP data do not distinguish between rising gas bubbles and slower oil drops. Atmospheric methane anomalies indicate a significant flux from the seafloor to the atmosphere through the 135 m water column. Methane "hotspots" over the ocean surface conform to the locations of seafloor discharge points.

2.5 REFERENCES

Androulidakis, Y., V. Kourafalou, T. Özgökmen, O. Garcia-Pineda, B. Lund, M. Le Hénaff, C. Hu, B.K. Haus, G. Novelli, C. Guigand, H. Kang, L. Hole, and J. Horstmann. 2018. Influence of River-Induced Fronts on Hydrocarbon Transport: A Multiplatform Observational Study. Journal of Geophysical Research: Oceans 123(5): 3259-3285. doi: https://doi.org/10.1029/2017JC013514

Baldwin, W.E., S.D. Ackerman, C.R. Worley, W.W. Danforth, and J.D. Chaytor. 2018. High-resolution geophysical data collected along the Mississippi River Delta front offshore of southeastern Louisiana, U.S. Geological Survey Field Activity 2017-003-FA: U.S. Geological Survey data release, https://doi.org/10.5066/F7X929K6

Hazen, T.C., E.A. Dubinsky, T.Z. Desantis, G.L. Andersen, Y.M. Picento, N. Singh, J.K, Jannson, A. Probst, S.E. Borglin, J.L. Fortney, W.T. Stringfellow, M. Bill, M.E. Conrad, L.M. Tom, K.L. Charvarria, T.R. Alusi, R. Lamendella, D.C. Joyner, C. Spier, J. Baelum, M. Auer, M.L. Zemla, R. Chakraborty, E.L. Sonnenthal, P. D'Haeseleer, H.N. Holman, S. Osman, Z. Lu, J.D. Van Nostrand, Y. Deng, J. Zhou, and O.U. Mason. Deep-Sea Oil Plume Enriches indigenous Oil-Degrading Bacteria. Science. 08 OCT 210 : 204-208.

Lamontagne, R.A., J.W. Swinnerton, V.J. Linnenbom, and W.D. Smith. 1973. Methane concentrations in various marine environments. Journal of Geophysical Research: Oceans and Atmospheres 78(24): 5317-5324. doi: https://doi.org/10.1029/JC078i024p05317

Leifer, I., and I. MacDonald. 2003. Dynamics of the gas flux from shallow gas hydrate deposits: interaction between oily hydrate bubbles and the oceanic environment, Earth Planetary Science Letters 210(3-4): 411-424. doi: https://doi.org/10.1016/S0012-821X(03)00173-0

Nodine, M.C., J.Y. Cheon, S.G. Wright, and R.B. Gilbert. 2007. Mudslides during Hurricane Ivan and an Assessment of the Potential for Future Mudslides in the Gulf of Mexico. Phase II Project Report, Prepared for the Minerals Management Service, Under the MMS/OTRC Cooperative Research Agreement 1435-01-04-CA-35515, Task Order 39239, MMS Project Number 552. 192 pp. Online: https://www.bsee.gov/research-record/tap-552-mudslides-during-hurricane-ivan-and-assessment-potential-future-mudslides (Accessed 24 May 2019)

Chapter 3
Surface and ROV Acoustic Mapping of the MC20 Oil and Gas Leak in the Northern Gulf of Mexico

J. Christopher Taylor[1] and Kevin Boswell[2]

Mounted acoustic sensors. Credit: NOAA NOS/NCCOS

ABSTRACT

In 2004, as Hurricane Ivan swept through the northern Gulf of Mexico, the MC20 Taylor Energy Company oil and gas platform collapsed and moved approximately 210 m downslope. Following several surveys to locate the downed platform jacket and associate a subsurface plume and surface sheen with seabed origins, in 2018, NOAA and its partners conducted a comprehensive assessment of the MC20 site. This chapter summarizes ship-based surface echosounder surveys characterizing the spatial structure of the plumes. Inspection of the acoustic backscatter indicates multiple plume components emitting from separate origins on the seafloor within an erosional pit at the northwest corner of the downed jacket. Broad-band acoustic frequency backscatter intensity suggests indicators of oil and gas plumes within the water column. Closer inspection using ROV-integrated echosounders and multibeam sonars confirm the presence of at least four plume sources emitting from the seafloor with acoustic signatures indicating oil separating from gas as well as oil and gas mixtures. In subsequent chapters, the separation of oil from gas from each of the seep sources was verified using in situ optical and direct capture methods. The assessment provides further evidence of an oil and gas leak that has likely occurred since the original toppling of the MC20 platform.

Citation for chapter
Taylor, J.C., and K. Boswell. 2019. Chapter 3. Surface and ROV Acoustic Mapping of the MC20 Oil and Gas Leak in the Northern Gulf of Mexico. pp. 19-42. In: A.L. Mason, J.C. Taylor, and I.R. MacDonald (eds.), An Integrated Assessment of Oil and Gas Release into the Marine Environment at the Former Taylor Energy MC20 Site. NOAA National Ocean Service, National Centers for Coastal Ocean Science. NOAA Technical Memorandum 260. Silver Spring, MD. 147 pp. doi: 10.25923/kykm-sn39

[1] *NOAA National Ocean Service, National Centers for Coastal Ocean Science, Marine Spatial Ecology Division, Biogeography Branch. Silver Spring, MD*
[2] *Florida International University, Department of Marine Biology. North Miami, FL*

Acoustic Mapping

3.1 INTRODUCTION

Gas and oil plumes emanating from the seabed are found world wide from natural hydrocarbon seeps, or caused by catastrophic events and human intervention or failures of oil and gas infrastructure such as the Deep Water Horizon (DWH) spill in 2010 (Crooke *et al*., 2015). In the water column, oil and gas plumes present strong reflectors of transmitted sound from scientific echosounders due to the high contrast in density of the bubbles compared to surrounding liquid seawater medium (Pedersen, 2016). More recently, oil seeps and droplets have also been detected using ship-based echosounders (Weber *et al*., 2012). Ship-based single beam echosounders (SBES) and multibeam echosounders (MBES) can detect the plume throughout the water column and provide shape and intensity characteristics as well as positioning of the plume and defining the source at the seabed without disturbing the seabed or the rising plume (Jerram *et al*., 2012). Calibrated SBES coupled with MBES also allow for quantitative measures of the volume of the plume and acoustic backscatter intensity, which can be used to infer content relative to the absolute flux of oil and gas to the surface (Weber *et al*., 2012).

3.1.1 Past Acoustic Surveys and Observations of Water Column Acoustic Anomalies at MC20

A persistent sheen in the Mississippi Canyon Block 20 (MC20) has been visible over the site of a toppled Taylor Energy Company (TEC) oil and gas platform since it collapsed during Hurricane Ivan in 2004. The composition and source of the sheen have been debated since the events that resulted in the damage to the platform. Several surface and undersea surveys have been conducted at the MC20 site since the platform was displaced. Here, we summarize observations of water column acoustic anomalies indicative of an oil and gas plume from:

1. A survey of opportunity conducted by the National Oceanic and Atmospheric Administration (NOAA) Ship *Okeanos Explorer*;
2. Excerpted images from a report provided to the Sheen Source Location Working Group (SSLWG) from surveys conducted in 2017 (SSLWG; Camilli, 2017);
3. A survey of opportunity conducted by the U.S. Geological Survey (USGS) in 2017; and
4. A site assessment contracted by the Bureau of Safety and Environmental Enforcement (BSEE).

All surveys show consistent presence of a water column plume that originates from an erosional pit at the northwest base of the toppled jacket as well as other acoustic anomalies suggestive of other plumes in the vicinity of the original MC20 wellhead or other sources.

The NOAA Ship *Okeanos Explorer* conducted an opportunistic multibeam survey of the MC20 site in 2012 (NOAA, 2012). The ship has a hull mounted Kongsberg EM302 multibeam sonar to log simultaneous seabed bathymetry and water column backscatter. Features on the seabed show mud and sand waves around the site. Seabed anomalies include the toppled MC20 jacket, an excavation site at the original MC20 platform location, an excavation site from the removal of the platform, and a pit at the northwest corner of the jacket (Figure 3.1). The plume appears to originate from the northwest corner of the jacket in a small bathymetric depression (Figure 3.1).

From 8 March to 8 April 2017, the Federal Government Unified Command SSLWG called for acoustic surveys of the of the MC20 site. Thirteen surveys were conducted in the vicinity of the MC20 site, of which 10 passed over the jacket and detected the water column acoustic anomaly consistent with the plume (Figure 3.2). These surveys also observed a smaller plume at the location of the original platform and wellhead. Other water column anomalies were also detected distant from the jacket. The plume detections were used to predict source origin at the seabed which were generally located in the vicinity of an erosional pit at the northwest corner of the downed jacket (Camili, 2017). Locating the exact seabed origin from the multibeam can be influenced by uncertainty in vessel motion, beam pattern, and noise, as well as possible occlusion of the plume below the surface of the jacket or bathymetric features.

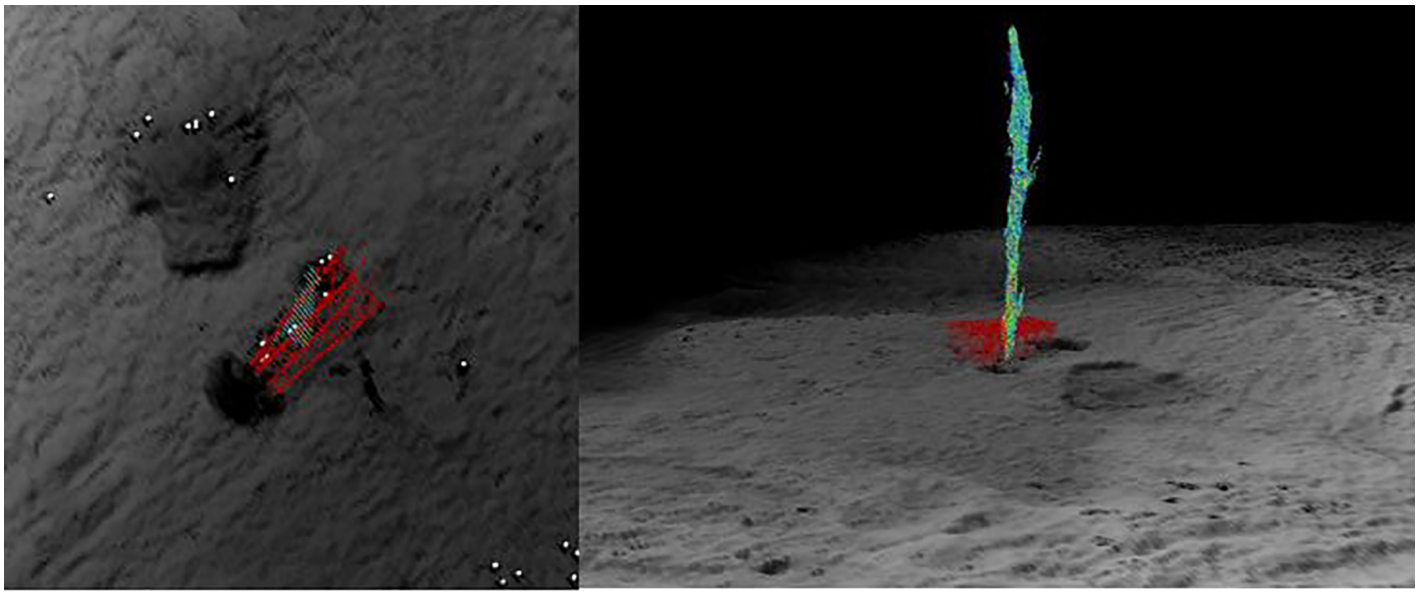

Figure 3.1. Left panel shows a map view of the MC20 site depicting the toppled jacket (red), original location showing sediment excavation, pit at location of former removed platform, and an erosional pit at the northwest corner of jacket. The right panel shows an oblique view facing south with the plume originating at the seabed in the erosional pit to the northwest of the jacket and rising through the water column.

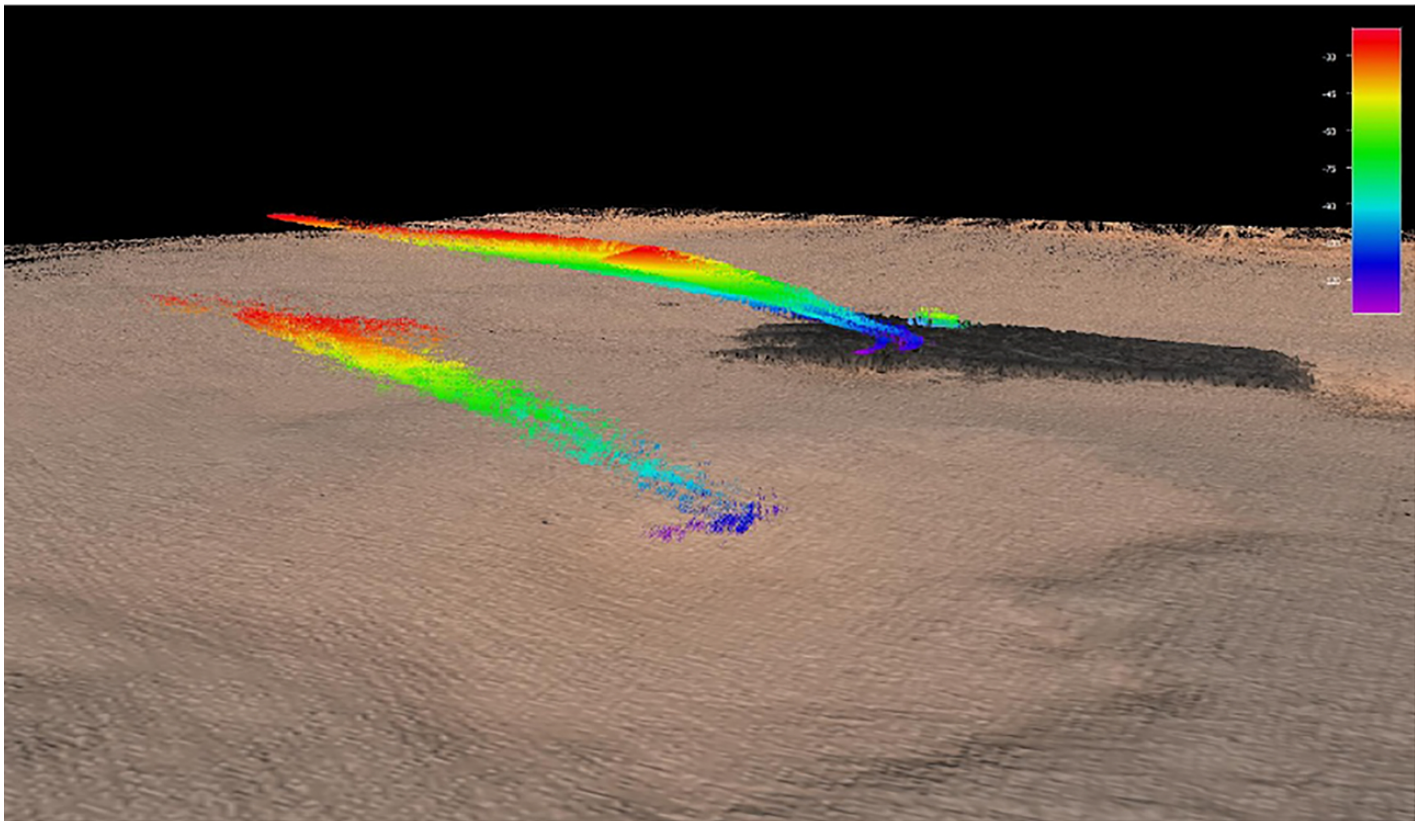

Figure 3.2. Excerpted figure from Camili (2017) showing perspective view of the water column plume anomaly near the jacket (shown in dark gray farfield) and original MC20 Taylor Energy Company (TEC) platform location (foreground). This image appears as Figure 8.4.7 in Camili (2017) report to the SSLWG.

Acoustic Mapping

The USGS conducted a broad geotechnical and geophysical survey of the MC20 block in May 2017. They used a Reson T20P dual-head multibeam sonar to survey the bathymetry (Baldwin *et al.*, 2018; Figure 3.3). Surveys over the downed jacket during a system calibration detected similar bathymetric depressions as in the NOAA 2012 and SSLWG 2017 surveys. The surveys also detected a water column plume that appeared to originate in the vicinity of the original wellhead.

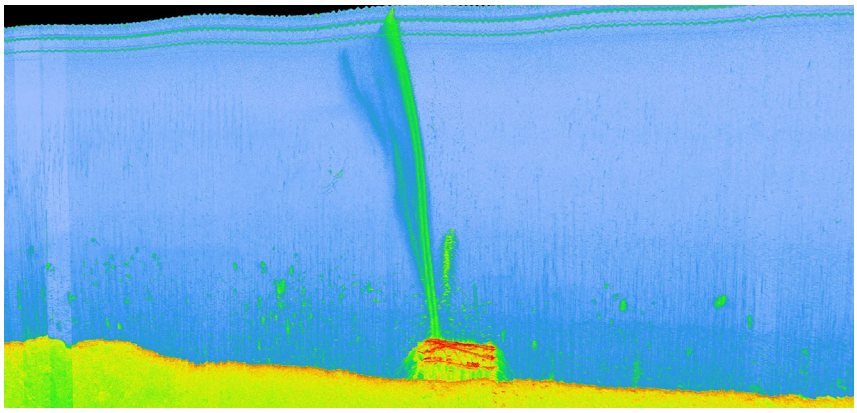

Figure 3.3. Stacked multibeam echogram of the MC20 downed jacket and plume from USGS (2018) multibeam survey.

BSEE contracted a survey of the MC20 site with Norbit, Inc in September 2017. The primary objective of this survey was to collect acoustic, video, and laser images of the plume from a Remotely Operated Vehicle (ROV). The project was also supplemented with a surface echosounder survey. This ROV was outfitted with a orthogonal imaging sonar system providing three-dimensional profiling of the jacket and acoustic anomalies and plumes. The survey detected several features, including the jacket, a hazard anomaly (later attributed to a dormant collector system), and a plume that appeared as more than one component in the water column and more than one source at the seabed. The origins of the plume were located in the center of the bathymetric depression at the northwest corner of the downed jacket (Figure 3.4).

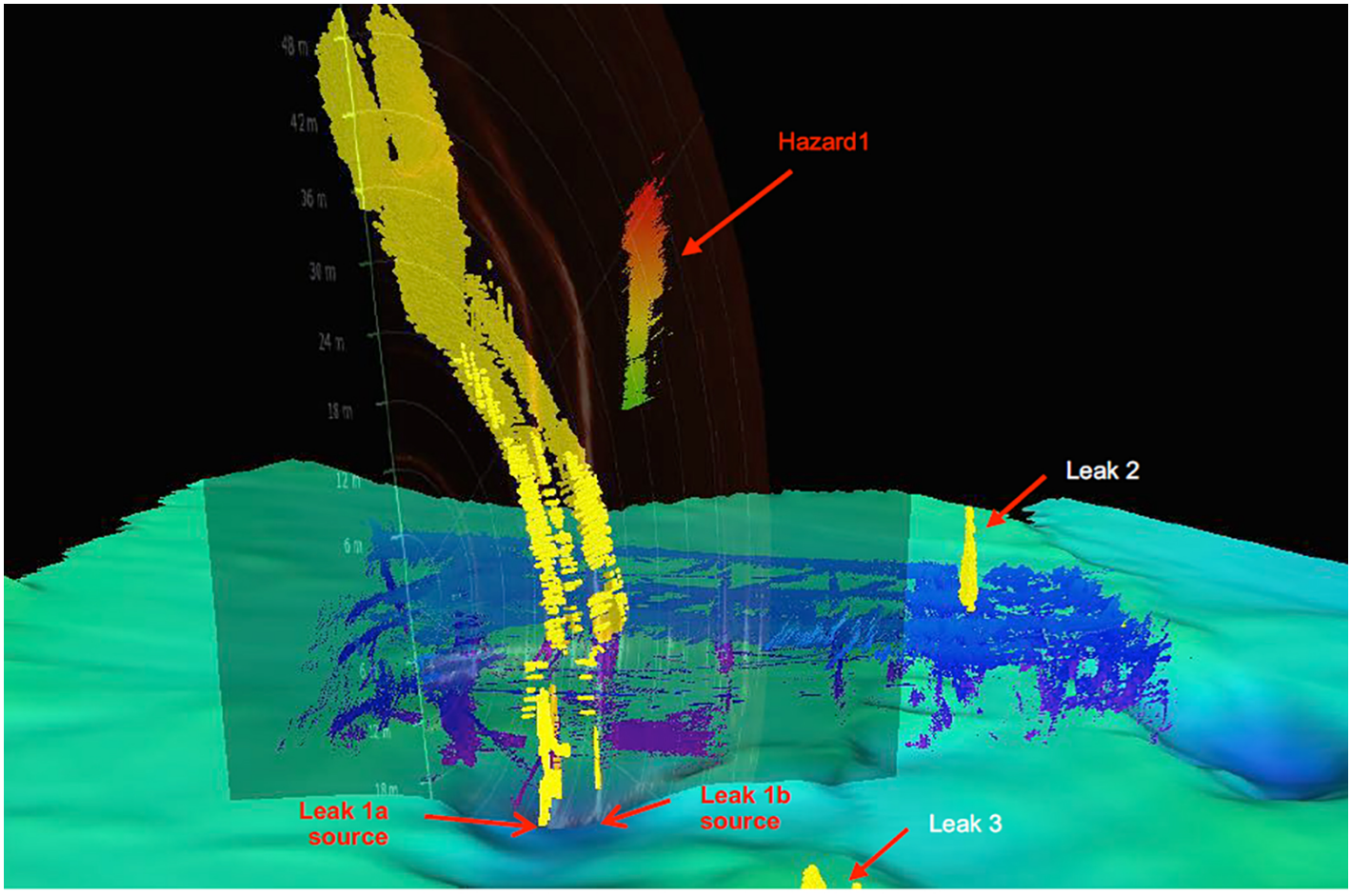

Figure 3.4. Image excerpted from the Norbit (2017) report to BSEE from the September 2017 surveys at MC20. Image shows multiple plume components in the water column and predicts more than one source at the seabed. Other water column anomalies are also noted.

This chapter describes echosounder-based observations and characterizations of the oil and gas plume in the water column over the former Taylor Energy Corporation (TEC) MC20 site as part of an interagency agreement between BSEE and NOAA and in partnership with Florida State University (FSU), Florida International University (FIU), and TDI Brooks, International. The surveys were conducted from 1-7 September 2018. The acoustic component of the mission used two types of echosounder surveys to characterize the MC20 site. The surface based echosounder surveys were used to guide subsurface surveys using an ROV outfitted with additional multibeam imaging sonars and SBES as well as video cameras and water, oil, and gas sampling systems. The subsurface ROV survey provided the precise location of the plume in the water column as well as seabed origins of multiple components and sources of the oil and gas plume. In a subsequent chapter (Chapter 8), we use the calibrated backscatter intensity from surface echosounder surveys coupled with bubble and droplet sizes and models of rise rates to derive estimates of flux for the oil and gas components in the plume.

3.2 METHODS

3.2.1 Echosounder System Installation on R/V *Brooks McCall*

Ship-based echosounders were installed on an overboard pole on the R/V *Brooks McCall* (48.5 m length, 12.4 m width, 2.89 m draft). The overboard pole was attached to the deck of the ship and oriented vertically during survey operations and could be rotated forward supporting transducers above deck during transit. A custom plate at the end of the pole received the acoustic sensors 3.5 m below the surface. The sensors included a HiPAP Model 350 Ultra-Short Baseline transducer (USBL) for tracking the ROV and beacons, a 300 kHz Teledyne RDI Workhorse Acoustic Doppler Current Profiler (ADCP), a 500 kHz Kongsberg Mesotech M3 MBES, and three frequencies of Simrad EK80 SBES transducers operating at 70, 120, and 200 kHz (Figure 3.5). The positions of the echosounder transducers were measured relative to a common reference point on the plate centered on the USBL and translated to the ship's reference frame to provide offset positions relative to the GPS antennas and water surface. To account for ship motion, a Teledyne DMS-25 was installed and positioned midline and measured to the same ship reference frame.

Figure 3.5. Acoustic sensors mounted on overboard pole of R/V Brooks McCall. Sensors are labeled as Simrad EK80 splitbeam transducers operated at 70 kHz (a), 120 kHz (b), 200 kHz (c), the HIPAP USBL (d), Kongberg M3 multibeam echosounder (e) and RDI ADCP (f).

The Kongsberg M3 and Simrad EK80 echosounders were controlled using native software on a single topside workstation to synchronize time across systems. GPS position and heading data were provided as serial communication by the navigation system from the ship. Attitude and heave data were also sent by serial communication from the DMS-25 attitude sensor to the topside workstation. Both serial feeds were split using a virtual serial port emulator so position and attitude data could be written directly into the separate file acquisition systems for each echosounder system.

Acoustic Mapping

The Kongsberg M3 was controlled using KML M3 software (version 2.20). The MBES operates at a frequency of 500 kHz with customizable sonar applications allowing for flexible beam configurations. For ship-based water column and seafloor surveys, we adopted the "Profiling" mode with a 120° across track swath using 256 beams at 1.6° across track by 3° along track beam resolution. Ping transmission rate fluctuates based on range and detection to bottom. Maximum logging range was set to 150 m for the entire mission. Raw data are stored in *.MMB format (but see below on pre-processing data to beamformed sonar data in *.IMB format for analysis).

The three frequency Simrad EK80 echosounders are controlled by EK80 Scientific Echosounder Software (version 1.12.2). Each transducer is a three or four channel split beam allowing for phase correction of target strength within the beam. The software controls the power and ping transmission characteristics for each frequency (Table 3.1). Two types of ping transmission characteristics were used: 1) Continuous wave or narrow band pulse length, and 2) a frequency modulated chirp using a fast ramp across a continuous bandwidth for each transducer. The FM mode allows for frequency response characteristics to be recorded for backscatter intensity, though only narrow band frequency was used in the analysis reported here. EK80 data are recorded in standard Simrad *.RAW format containing ping timing, position information, and digitally sampled power and phase in each ping record. Both M3 and EK80 raw data were stored in day and time labeled directories and duplicated to an external drive at the conclusion of each survey day. Survey logs included start and stop points of lines and turns and event marks when acoustic features were observed.

Table 3.1. Simrad EK80 echosounder transmission characteristics for each operating center and frequency band. Numbers in parentheses indicates nominal frequency bands around each center frequency.

Frequency (kHz)	70 (45-95)	120 (90-150)	200 (150-250)
Beam dimensions (degrees)	18	7	7
Transmit power (W)	500	250	125
Pulse length CW (ms)	0.256	0.256	0.256
Pulse length FM (ms)	2.048	2.048	2.048
Ping interval (s)	0.3	0.3	0.3
Data range (m)	200	200	200
Background noise (dB ref 1m)	-133	-145	-143
Sound velocity (m/s, nominal)	1542	1542	1542
Absorption (dB/m, nominal)	--	0.054	0.102

3.2.2 Simrad EK80 Splitbeam Echosounder Calibration

The EK80 system was calibrated using standard sphere techniques detailed in Demer *et al*. (2015). Summarized here, a 38.1 mm tungsten carbide sphere contained in a monofilament mesh cradle was lowered below the transducers to a depth of at least 10 m. A built-in calibration routine in EK80 software detects and tracks the sphere as it is manually moved through the transducer footprint. At least 1000 targets are recorded with position relative to the main axis of each transducer. On axis system gain are automatically adjusted to match theoretical target strength values for the sphere. The calibration was repeated for each frequency (70, 120 and 200 kHz) and pulse length and type (0.256 ms CW or 2.048 ms FM).

3.2.3 Ship-Based Survey Design

Initial survey design over the MC20 site used north-south orientated lines spaced approximately 50 m apart to detect and map the direction and origin of the plume and jacket structure. Ship navigation software with a base bathymetry layer provided by a previous 2017 USGS survey, projected in NAD83 UTM Zone 16N, was used for sample collection design and planning. When the plume became visible in the acoustic echograms, waypoints were manually translated to the ship navigation system to establish the general trajectory and extent of the plume, which was noted during each survey. Subsequent surveys used parallel lines oriented perpendicular to the trajectory of the plume. During most surveys, additional survey lines were oriented along the axis of the plume in an attempt to characterize the continuous shape of the plume.

3.2.4 Ship Echosounder Data Processing

EK80 and M3 data processing and interpretation was conducted in Echoview software (Echoview, Pty Ltd, version 9.0). Echoview reads native EK80 broadband and narrowband data formats. The raw sonar data from the M3 was first pre-processed using the KML Converter program to rewrite raw beamformed sonar data prior to reading into Echoview. Offset measurements for the positions of GPS antennas and the three EK80 and M3 transducers were specified in the platform and transducer properties. Echoview decomposes the raw data from each EK80 echosounder into a suite of raw variables corresponding to magnitude and phase measurements. Water column averaged sound velocity and absorption was calculated from the CTD cast closest in time to the acoustic survey. System calibration parameters were similarly read into each survey's Echoview processing file.

Initial evaluation noted acoustic noise from attenuated signal due to surface bubbles and time-varied gain noise as well as periodic impulse noise from other acoustic instruments or cross-talk between the echosounders. A background noise removal routine was applied to each frequency as described in deRobertis and Higginbottom (2007). Noise was most prominent on the 200 kHz echosounder, occluding other acoustic signals (aside from the highly reflective seafloor) about 80 m below the surface. Bottom detection used a backstep from peak amplitude and resulted in a continuous line along the seabed. On rare occasions, the algorithm erroneously positioned the seabed due to water column noise and the bottom line was manually edited to correct the position.

Acoustic features were evident in the echogram including the seafloor, the presence of the downed jacket, mid-water scattering layers, traces in the mid-water likely representing individual and schools of fish, and shapes of high backscatter intensity attributed to the oil and gas plumes emanating from the seafloor (Figure 3.6). The water column plumes were observed in all three EK80 frequencies as well as the M3 multibeam swath. Only the data from the 120 kHz and 200 kHz EK80 and M3 multibeam are considered further.

Survey echograms were examined for the presence of water column anomalies indicating plumes. Each instance of the plume in the water column was delineated using an image texture and thresholding algorithm to separate

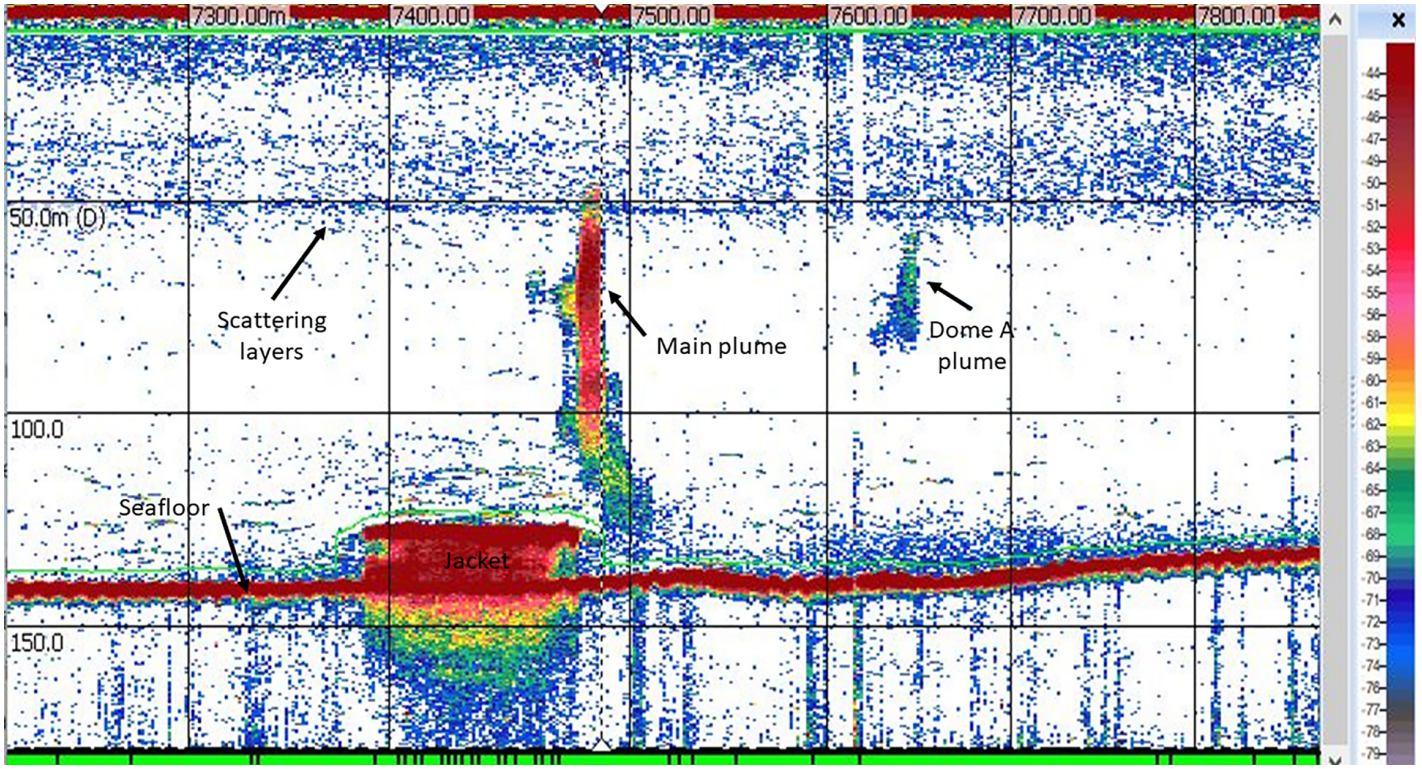

Figure 3.6. Example EK80 echogram from the 120 kHz channel showing acoustic backscatter features in the water column as labeled.

the backscatter associated with the plume from the surrounding water and other midwater features. The isolated plume features were prepared for export in three formats. First, georeferenced samples were exported for visualization of the plume in Fledermaus. Second, mean integrated water column backscatter was separated out by 25 m distance bins to display the aerial footprint of the entire plume. Third, the plume was discretized into cells 1 m deep by the horizontal length of the plume for use in analysis of backscatter and estimation of flux (see Chapter 8). M3 data viewing was synchronized with the EK80 data and examined for each survey for ping sequences that contained a water column plume. A subset of pings was highlighted and extracted when the plume was observed to interact with the seabed. This ping subset was exported as georeferenced backscatter samples for viewing and geopicking in Fledermaus. Manual geopicking selected the geographic position and estimated diameter of the plume at the seabed, which was stored in a data table for each survey and displayed in ArcGIS to guide the ROV survey. Uncertainty in tracing the plume to a precise seabed contact can arise from several sources, including but not limited to, latency in ship motion and plume backscatter interference or shadowing from the downed jacket. These locations should not be taken to represent precision nor variation in the plume origins. Instead, we used an ROV to make observations in closer proximity to the seabed and pinpoint the seabed source of the plumes. Lastly, the full ping sequence from a selection of surveys and lines containing the plume in the M3 multibeam swath was selected from the survey and exported as georeferenced samples for visualizing the three-dimensional shape, backscatter characteristics, and trajectory of the plume in Fledermaus.

3.2.5 ROV-based Echosounder Integration

Simard EK80 and Kongberg M3 sonars were integrated onto SeaTrepid, International's Comanche ROV. A custom engineered multiplexing interface on the ROV allowed for various sensors to be installed with power, network, and serial data communications control provided to the ROV via a fiber optic tether from the surface. The Simrad EK80 WBT Tube is a depth rated version of the Simrad EK80 wideband transceiver contained in a depth rated canister. External cable ports are provided for up to four transducers, as well as power and network communication provided to the multiplex interface. The M3 was similarly installed drawing power and network communication from the multiplex interface. The EK80 WBT Tube operated at three frequencies: 120 kHz, 200 kHz, and 333 kHz. The three transducers were mounted on a rigid plate attached to the upper cross brace near the top of the ROV and above the Kongsberg M3 sonar transducer, which was mounted on the pan and tilt adjacent to the navigation camera (Figure 3.7). Topside, the EK80 WBT Tube was controlled using EK80 scientific echosounder software (version 1.12.2) and the Kongsberg M3 was controlled using KML M3 software (version 2.20). Transducer ping transmission properties were specified in the EK80 software. The 120 kHz

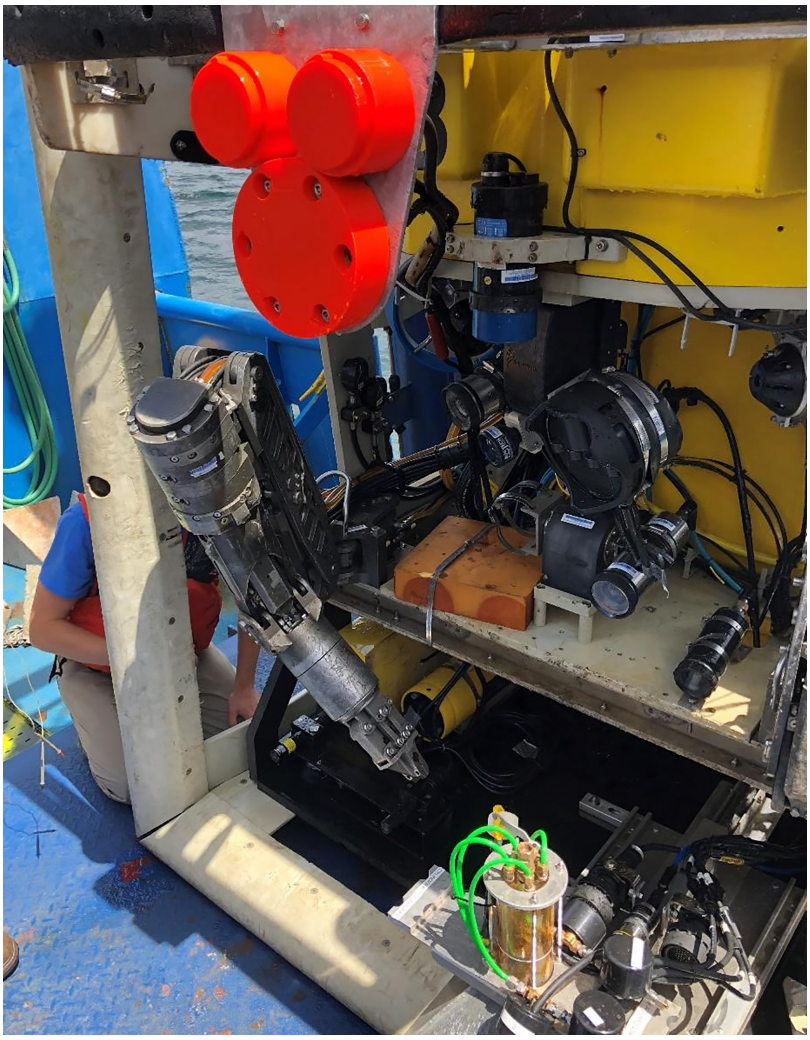

Figure 3.7. Transducers installed on the Comanche ROV. Orange cylinders at top are EK80 transducers, 120 kHz (lower), 200 kHz (upper left), 333 kHz (upper right) and the M3 sonar below on pan and tilt with camera

transducer only operated in narrowband CW mode whereas the 200 kHz was operated in both CW and wideband FM mode (Table 3.2). Initial system checks on the first ROV deployment found the 333 kHz channel to be inoperable and therefore was not used for the remainder of the survey mission. The orientation of the M3 transducer was provided through an internal compass. Position, depth, and heading of the ROV were recorded externally to the EK80 and M3 software (see section 3.2.6). Position offsets were measured relative to the ROV reference point at the USBL transponder.

Table 3.2. Transducer parameters for EK80 WBT Tube system installed on the ROV. The 333 kHz transducer is omitted from the table as it was inoperable during the mission. Nominal values are present with actual values varying on each survey day based on environmental conditions.

Frequency (kHz)	120 (90-150)	200 (150-250)
Beam dimensions (degrees)	7	7
Transmit power (W)	250	125
Pulse length CW (ms)	0.256	0.256
Pulse length FM (ms)	2.048	2.048
Ping interval (s)	0.3	0.3
Data range (m)	<30	<30
Background noise (dB ref 1m)	-140	-138
Sound velocity (m/s, nominal)	1542	1542
Absorption (dB/m, nominal)	0.054	0.102

3.2.6 ROV USBL Position and Echosounder Calibration

The *R/V Brooks McCall* provided a HiPAP 350 USBL transponder to the ROV for vehicle tracking. The HiPAP system was calibrated 5 September 2018 following standard procedures. Error in ROV positioning was found to be 0.08 m in northing and easting and 0.07 m in depth. Calibrating the EK80 wideband echosounders on the ROV adopted a similar procedure to the calibration of the ship pole mounted transducers using a standard 38.1 mm tungsten carbide calibration sphere. In this application, the sphere was lowered over the port side of the ship to a depth of about 25 m, opposite the ROV launch and recovery system. The ROV in the garage was lowered to a depth of about 25 m below the surface and oriented to face the direction of the sphere, bringing the sphere roughly 16 m from the transducers. The ROV or the sphere was maneuvered to position the sphere throughout the footprint of transducer beams. The calibration was repeated for each narrowband CW and wideband FM pulse length used during the surveys. Echosounder system gains and beam patterns were adjusted to match theoretical target strength of the sphere (Demer *et al*., 2015).

3.2.7 ROV Echosounder Survey Design

Following surface echosounder surveys to determine the position and orientation of the plume in the water column, an ROV mission plan was developed among the project investigators. While each ROV mission was unique, the general scope was to make acoustic observations of the main plume at various depths in the water column, locate the seabed origins of the plume relative to the position of downed jacket, and locate the seabed origins of other plumes observed in previous surveys, specifically a reported gas plume at the former location of the MC20 platform.

3.2.8 ROV Echosounder Data Processing and Visualization

All EK80 and M3 data collected on the ROV was read and interpreted in Echoview software (version 9.0, Echoview, Pty Ltd) and visualized in Echoview and Fledermaus (verson 7.8, QPS, Inc). Navigation and depth data were recorded external to the EK80 and M3 echosounders. Echoview was used to synchronize the M3 and EK80 data as well as the GPS positions and depth provided from the USBL. Orientation of the transducers were specified to project backscatter samples in real-world coordinates. Features in the M3 imagery were georeferenced and measured to the nearest 0.01 m.

3.3 RESULTS

3.3.1 Surface Echosounder Surveys

The goal of the surface echosounder surveys was to detect and locate the plume to guide further subsurface observations and sampling, and to characterize the acoustic backscatter properties related to oil and gas constituents of the plume. A total of eight surface echosounder surveys were conducted between 1 and 7 September 2018. At least one survey was conducted each day, except for 4 September, due to evacuation of the MC20 site during severe weather associated with Tropical Storm Gordon. Survey tracklines varied in number and orientation, depending upon the orientation and extent of the water column plume and the daily operating plan coordinated among research investigators. Along-track and cross-track observations of the plume in the SBES and MBES revealed two or more sub-plumes emanating from a seabed position within an erosional pit at the northwest corner of the downed jacket. Visually differentiating the components of the plume in the acoustic echograms depended upon the trajectory of the plume in the water column and the orientation of the survey trackelines. The components of the plume showed differential rise rates consistent with faster rising gas bubbles separated from slower rising oil droplets. On some occasions, relatively low noise on the 200 kHz channel permitted detection of components of the plume with backscatter intensity relatively higher than backscatter intensity in the 120 kHz for portions of the plume, consistent with expected backscatter intensity patterns of liquid filled spheres of oil. Similarly, the high-frequency 500 kHz M3 multibeam surveys provided further evidence of separate components of the plume consistent with separate oil and gas components in the plume.

Individual survey observations are summarized below including survey efforts and visual representations of the plume in the water column. Where plume trajectory and survey trackline orientation permitted, three-dimensional conceptual models of the plume components are presented. Lastly, seabed origins of the plume components are characterized and estimated (where the plume was directly in contact with the seabed) and collectively summarized for all surveys.

1 September 2018

The survey on 1 September was the first survey of the area and was used to conduct a broad overview of the area (Figure 3.8). Ocean currents were not available during this day, but trajectory of the plume indicated a strong southwestward current with the plume extending over 300 m down current from the jacket.

2 September 2018

Two surveys were conducted on this day (Figures 3.9 and 3.10). In the morning, a full survey was conducted to confirm the orientation and trajectory of the plume. A trackline passed over the jacket, detecting the main plume in cross-section, and then continued over the original location of the MC20 platform and detected a smaller plume over the original well head location (Figure 3.9). Plume trajectory again showed a southwestward direction through the water column.

3 September 2018

A single survey was conducted on this day to define the plume trajectory prior to subsurface ROV observations. Similar to the previous two days, currents were southwestward. Three lines were used to detect the plume near the seabed and to map the extent and trajectory of the plume. Cross-section of the plume in the multibeam showed at least two plume components. The along-plume trackline extended over 250 m (Figure 3.11).

5 September 2018

The mission was suspended during 4 September due to the passing of Tropical Storm Gordon and resumed on 5 September. Two surveys were conducted on this day (Figures 3.12 and 3.13). Similar patterns were present, showing the plume extending over 300 m from the jacket under relatively high south west currents (Figure 3.12).

6 September 2018

The current regime changed on 6 September 2018 with the plume trajectory rotating clockwise to the north. In the multibeam cross-section there were at least three identifiable plume components rising through the water column (Figure 3.14).

7 September 2018

The final survey of this mission was conducted on this day. The current velocity dropped significantly resulting in a plume that rose nearly vertically with some deflection at about 30 m below the surface. Oil droplets and gas bubbles were directly observed at the surface (Figure 3.15).

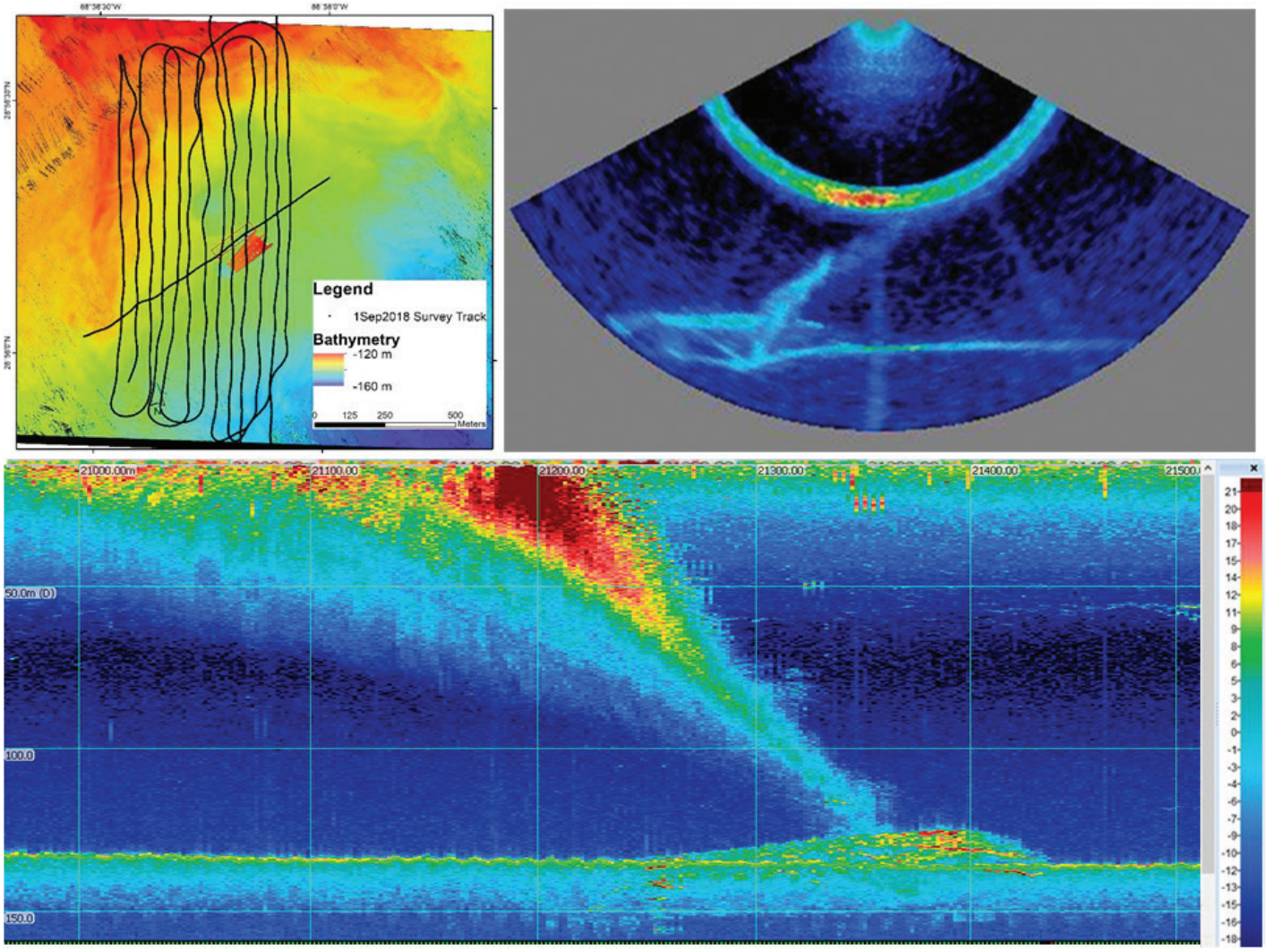

Figure 3.8. Map of the 1 September echosounder survey (Upper left). Bathymetry represented by color ramp and a red box represents the approximate area shown in the maximum intensity echogram. (Upper right) A single ping from the multibeam swath showing the plume emerging from the erosional pit at the northwest base of the jacket. A transmitted pulse from another sonar is evident in this ping as an arc midwater. (Lower) Multibeam echogram shown as maximum intensity across the beam swath and compressed along track to show the trajectory and extent relative to the jacket.

Acoustic Mapping

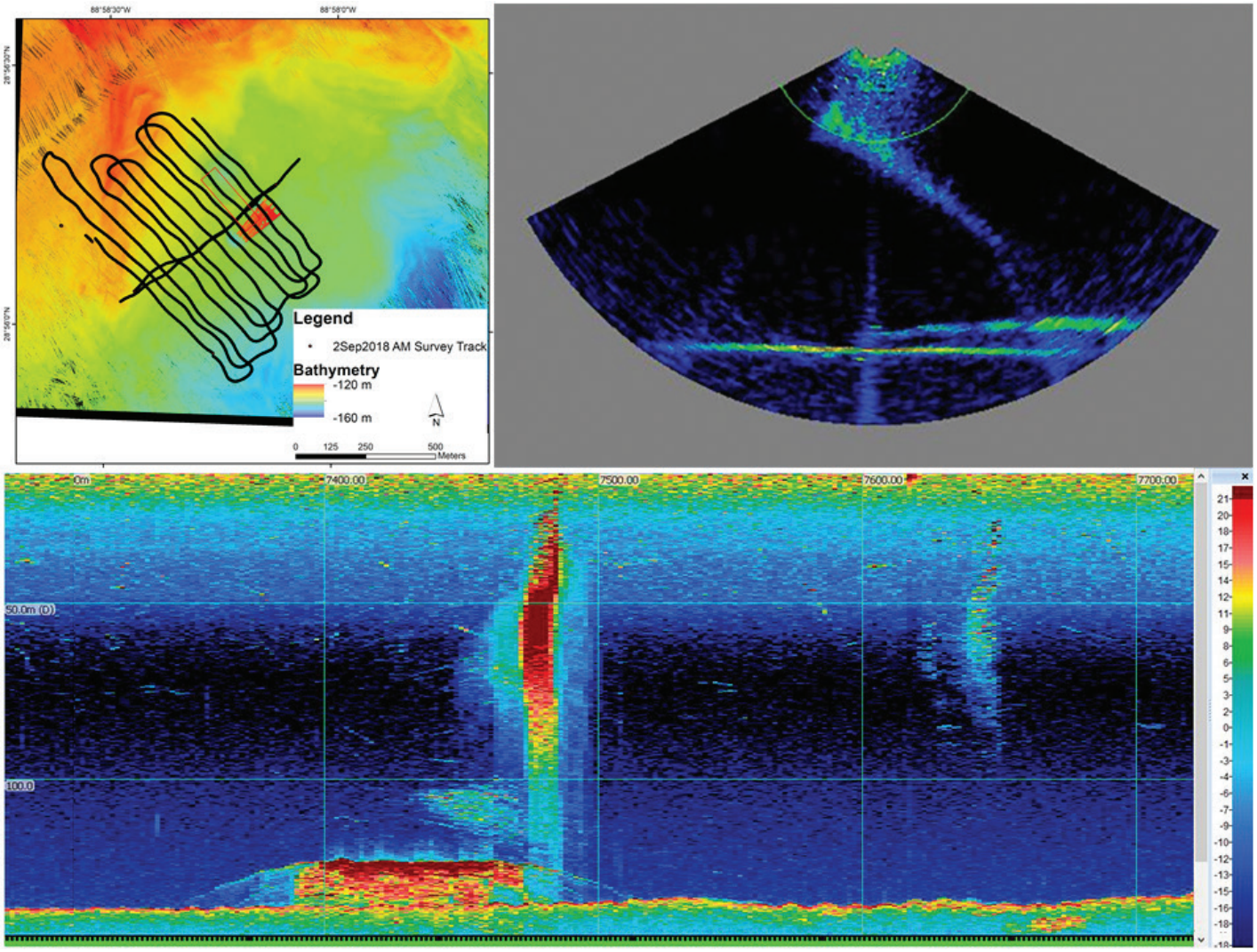

Figure 3.9. Map and sample echogram from 2 September morning survey. (Upper left) Map of the echosounder survey; bathymetry represented by color ramp and a red box represents the approximate area shown in the maximum intensity echogram. (Upper right) A single ping from the multibeam swath. (Lower) Multibeam echogram shown as maximum intensity across the beam swath and compressed along track to show the trajectory and extent relative to the jacket. Note the orientation of the area of interest in the red box on the map showing a cross-section of the plume. The lower echogram shows the main plume over the jacket, but also a lesser plume over the original wellhead location.

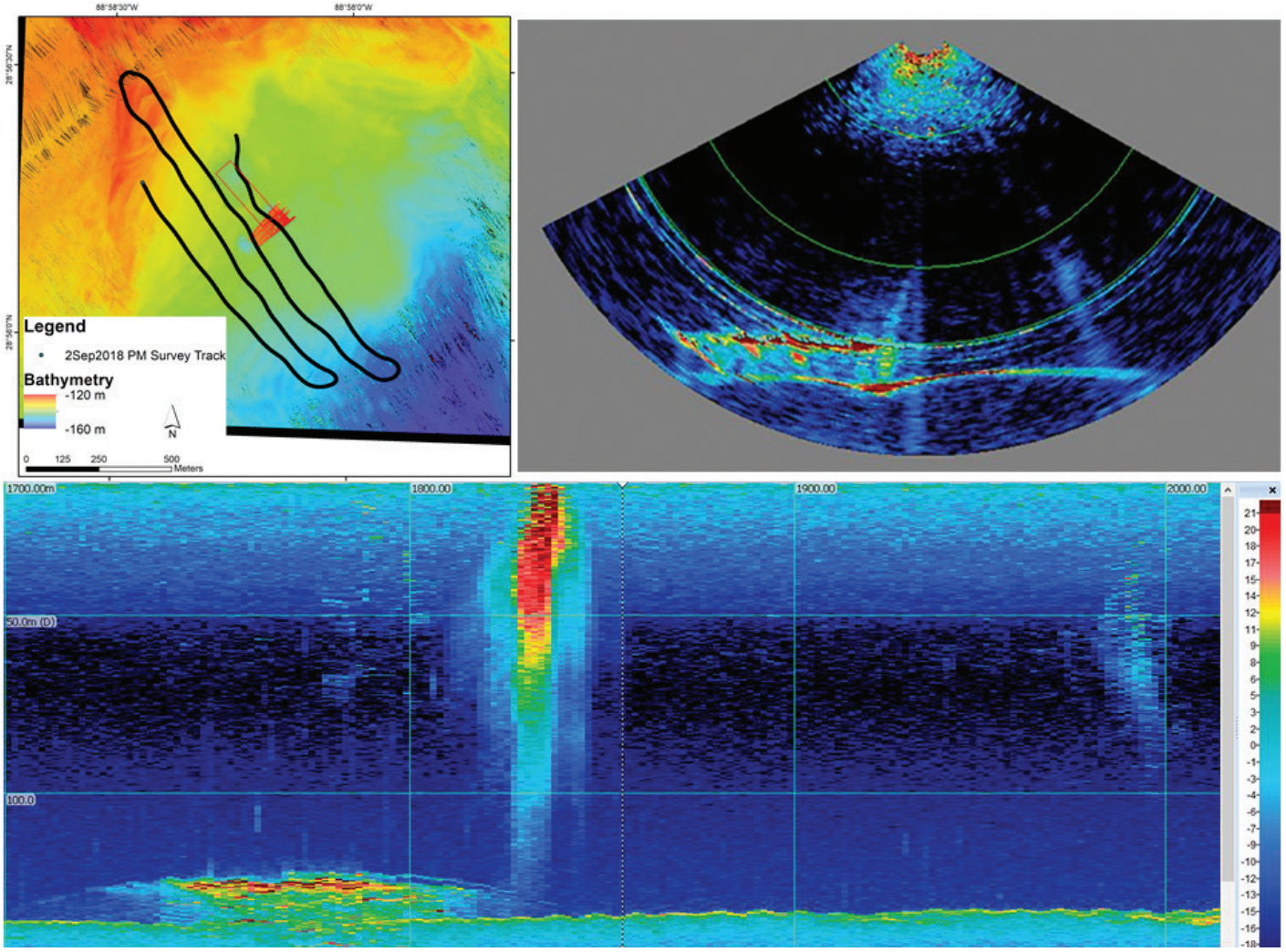

Figure 3.10. Survey during evening of 2 September. (Upper left) Map of the echosounder survey; bathymetry represented by color ramp and a red box represents the approximate area shown in the maximum intensity echogram. (Upper right) A single ping from the multibeam swath. (Lower) Multibeam echogram shown as maximum intensity across the beam swath and compressed along track to show the trajectory and extent relative to the jacket. The main plume over the jacket is the most prominent water column feature. Orientation is across the plume trajectory in this view. Plume distance was not measures during this survey. A smaller plume over the site of the original wellhead is shown in the right of the bottom echogram.

Acoustic Mapping

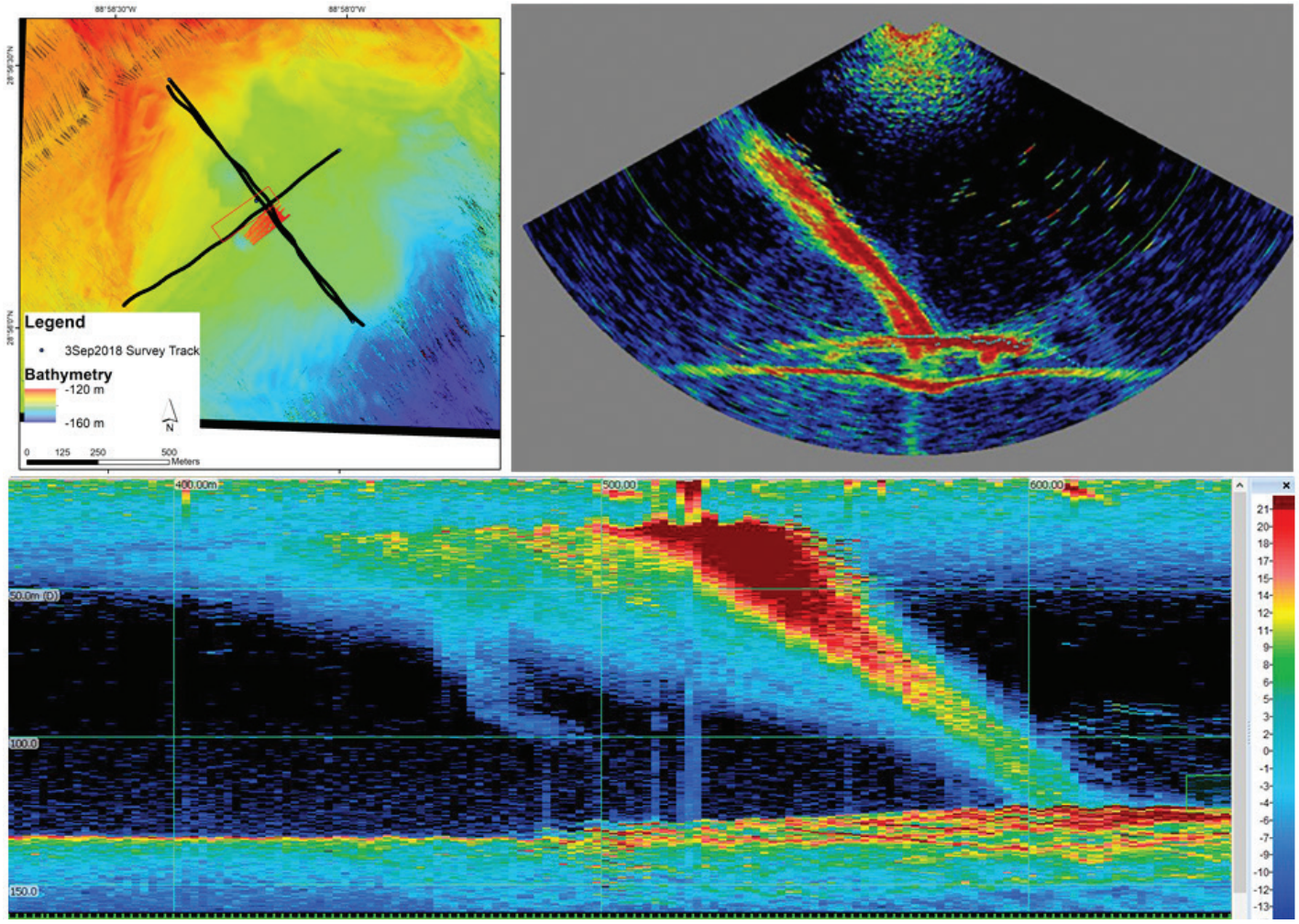

Figure 3.11. Map and sample echograms from survey conducted on 3 September. (Upper left) Map of the echosounder survey; bathymetry represented by color ramp and a red box represents the approximate area shown in the maximum intensity echogram. (Upper right) A single ping from the multibeam swath. (Lower) Multibeam echogram shown as maximum intensity across the beam swath and compressed along track to show the trajectory and extent relative to the jacket. Two plume components are visible in the multibeam swath view.

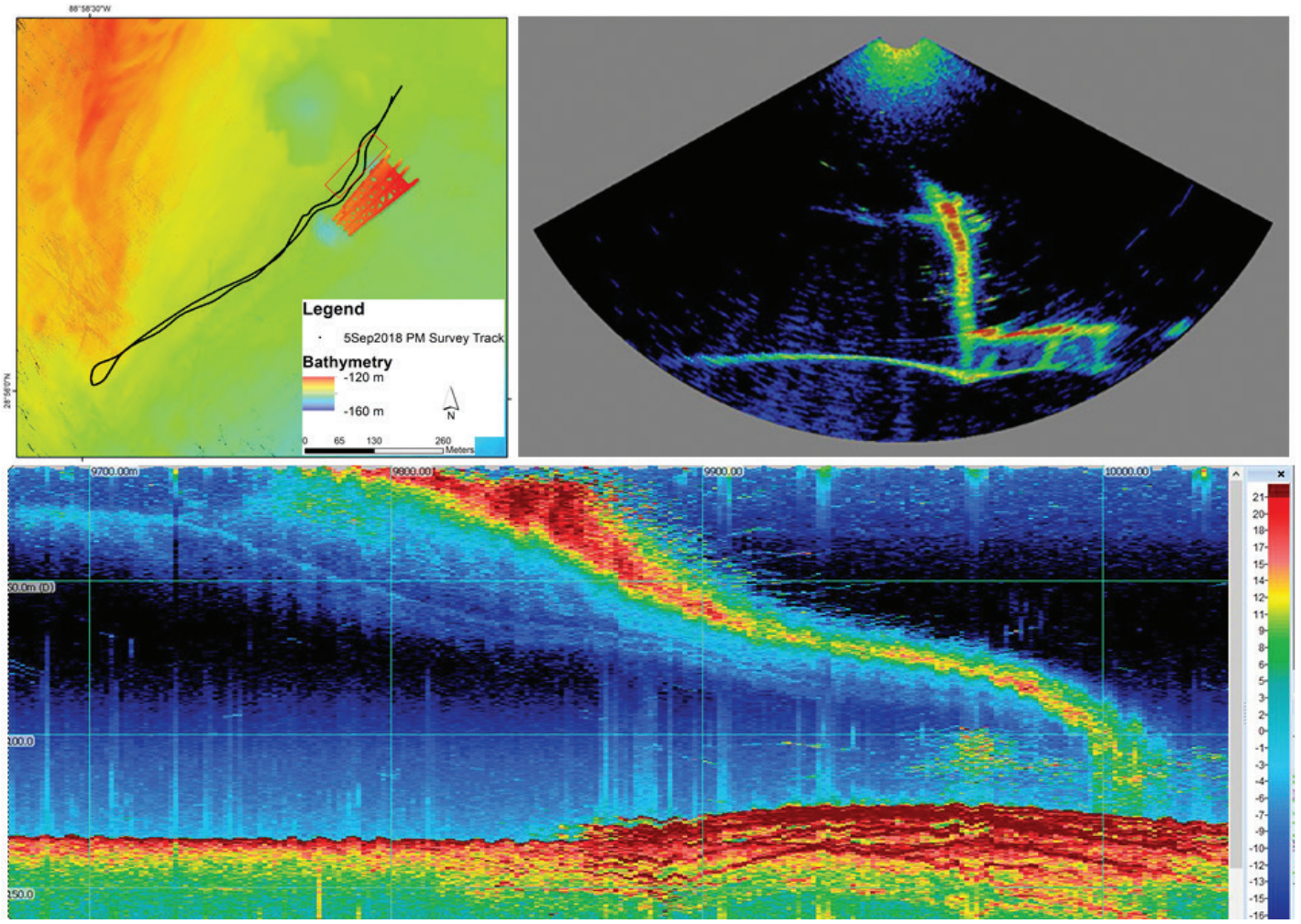

Figure 3.12. Sample map and echograms from surveys conducted morning of 5 September. (Upper left) Map of the echosounder survey; bathymetry represented by color ramp and a red box represents the approximate area shown in the maximum intensity echogram. (Upper right) A single ping from the multibeam swath. (Lower) Multibeam echogram shown as maximum intensity across the beam swath and compressed along track to show the trajectory and extent relative to the jacket. The plume extends at least 300 m from the seabed source under relatively high ocean currents.

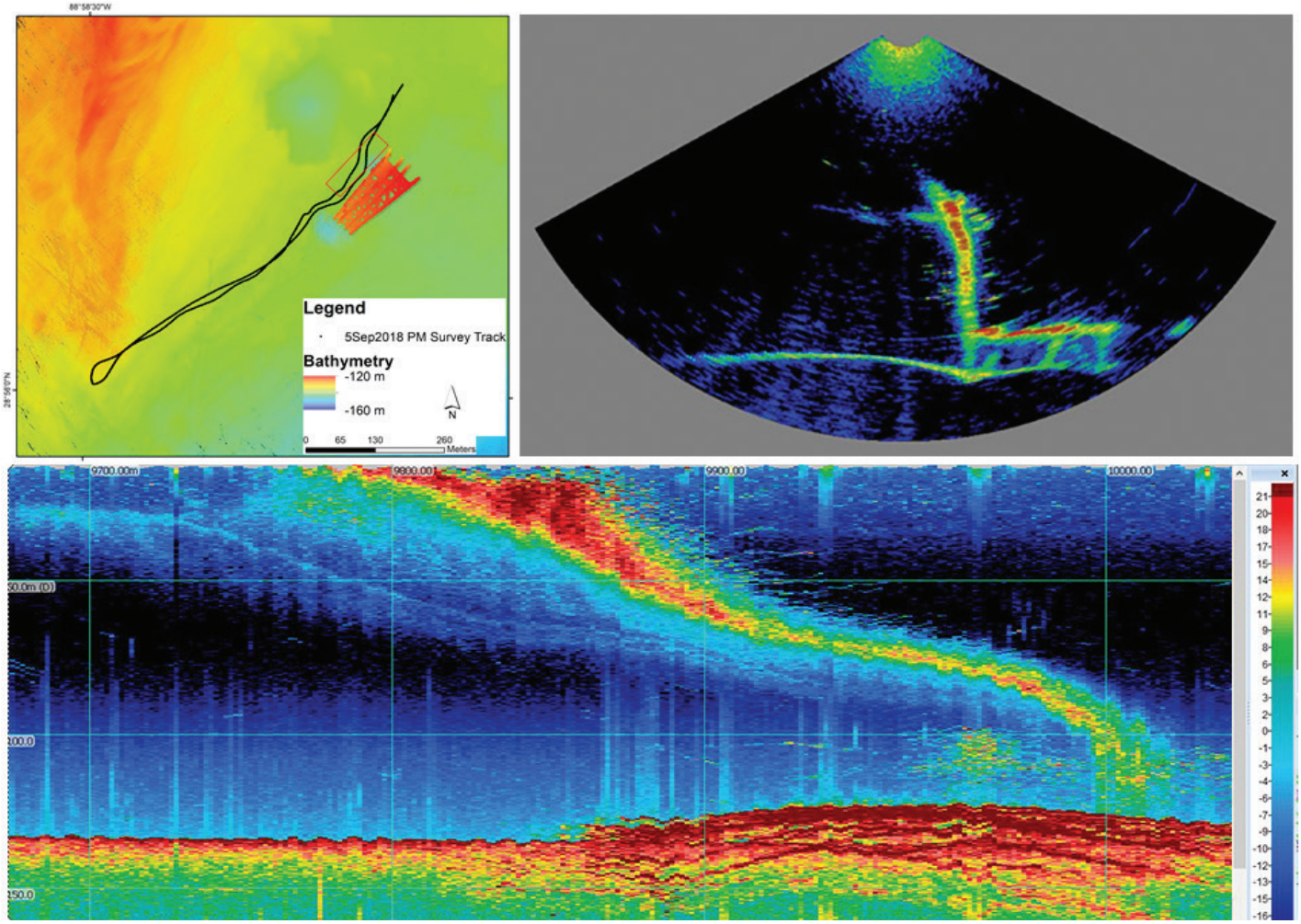

Figure 3.13. Map and sample echograms from survey conducted evening on 5 September. (Upper left) Map of the echosounder survey; bathymetry represented by color ramp and a red box represents the approximate area shown in the maximum intensity echogram. (Upper right) A single ping from the multibeam swath. (Lower) Multibeam echogram shown as maximum intensity across the beam swath and compressed along track to show the trajectory and extent relative to the jacket. Two plume components are visible in the lower echogram.

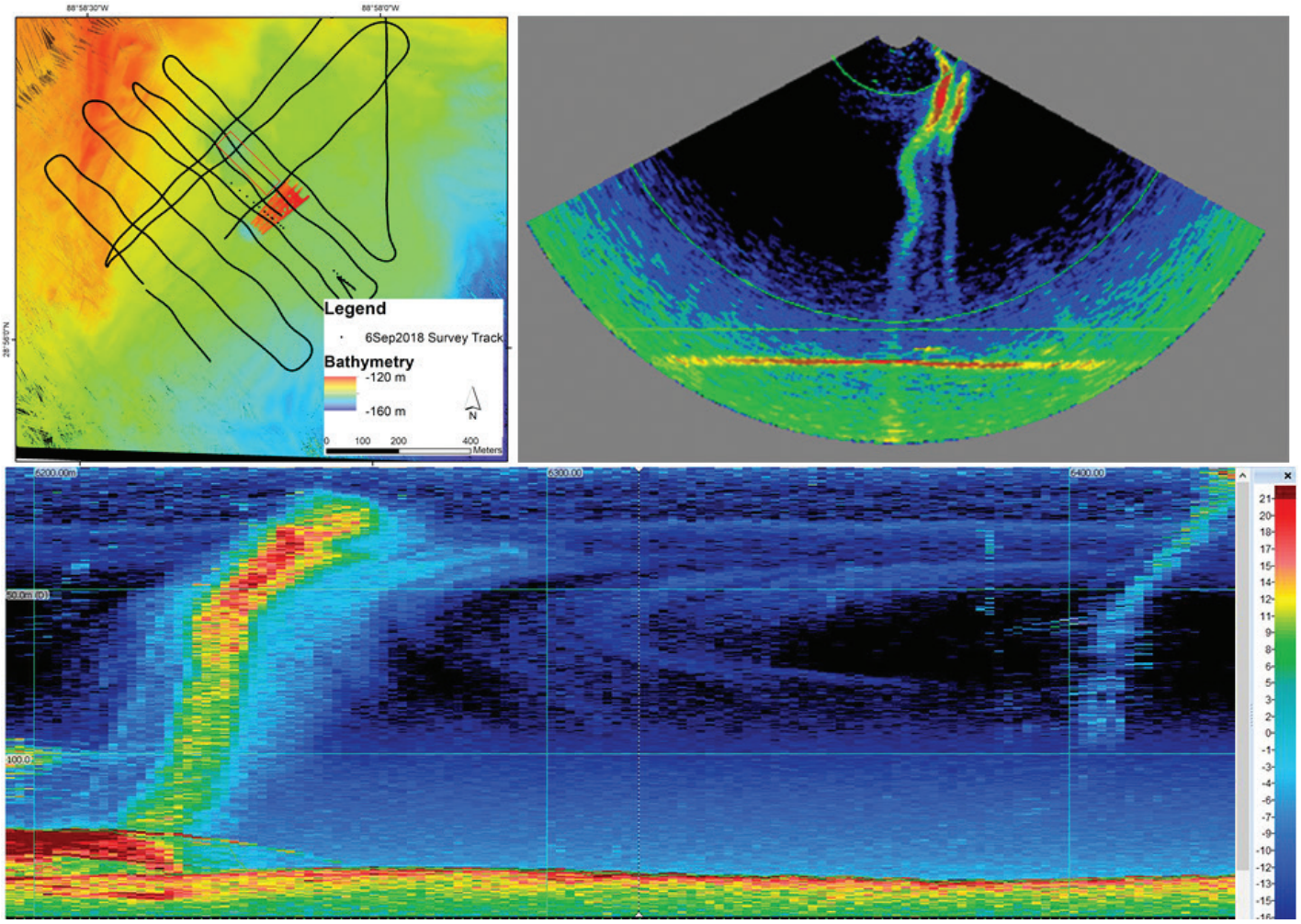

Figure 3.14. Map and sample echograms from survey conducted morning of 6 September. (Upper left) Map of the echosounder survey; bathymetry represented by color ramp and a red box represents the approximate area shown in the maximum intensity echogram. (Upper right) A single ping from the multibeam swath. (Lower) Multibeam echogram shown as maximum intensity across the beam swath and compressed along track to show the trajectory and extent relative to the jacket. Note the three plume components visible in the multibeam swath view above. The main plume is visible over the jacket on the bottom echogram as well as continued evidence of a lower scattering layer. A smaller plume is also visible to the right

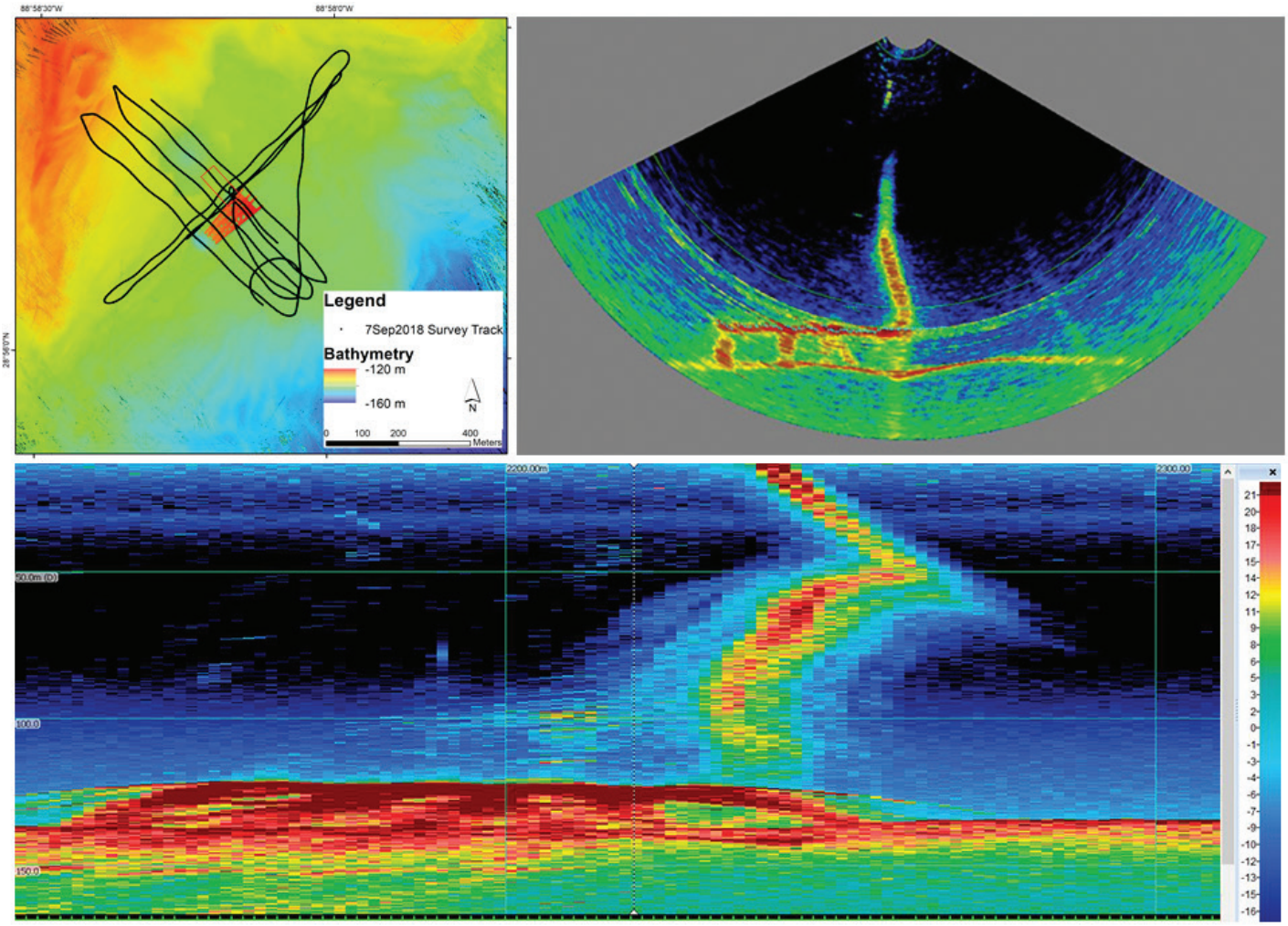

Figure 3.15. Map of survey and example echograms from the survey on the morning of 7 September. Note the nearly vertical rising plume from the jacket. (Upper left) Map of the echosounder survey; bathymetry represented by color ramp and a red box represents the approximate area shown in the maximum intensity echogram. (Upper right) A single ping from the multibeam swath. (Lower) Multibeam echogram shown as maximum intensity across the beam swath and compressed along track to show the trajectory and extent relative to the jacket. Note the vertical shape of the plume in the multibeam swath and echogram below as a result of diminishing and shifting ocean currents.

3.3.2 Interpretation of Plume Components

On 2 September, the heading of the survey trackline permitted closer examination of the components of the plume taking advantage of the wide swath of the MBES to develop a three-dimensional model. The southwestward currents advected the plume to the southwest. Not only were there two apparent high backscatter components as observed on many of the surveys (Figure 3.16), the multibeam model of the plume shows a relatively lower backscatter intensity component consistent with oil rising more slowly. The slower rising components remained

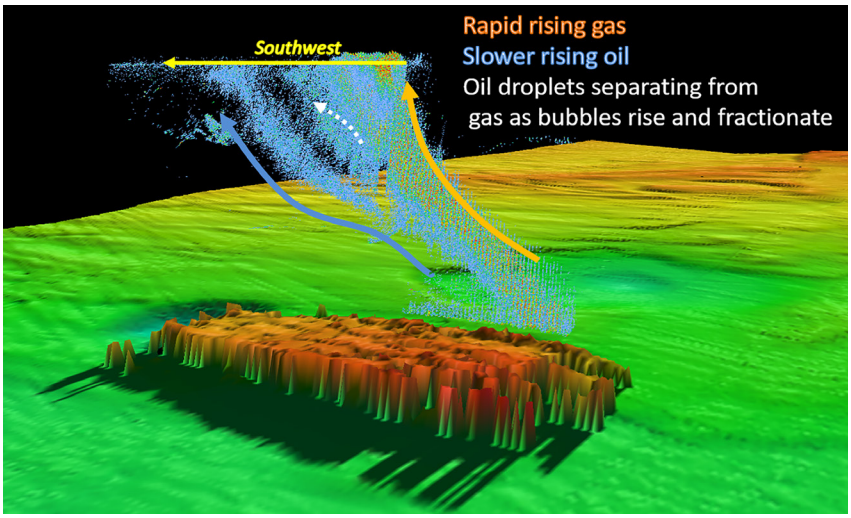

Figure 3.16. Three-dimensional model of the oil and gas plume on 2 September 2018. Relative backscatter intensity from the M3 multibeam is scaled as blue-orange: low-high. Arrows define components of the plume. See text for explanation.

separate and rose through the water column. The plume backscatter model revealed another lower backscatter intensity component higher in the water column separating from the faster rising higher backscatter plume that is consistent with evolution of oil that may have been trapped in gas bubbles that are fractionating and releasing oil near the surface (Figure 3.16).

Examination of backscatter of a cross-section of the plume detected using the 120 kHz and 200 kHz systems revealed differential backscatter consistent with theoretical observations of relative backscatter of oil and gas across acoustic frequencies. Backscatter from oil should be relatively higher at the higher frequency when compared to the lower frequency. In Figure 3.17, the plume cross section includes a lower tail in the 200 kHz and may represent the oil component of the plume. Theoretical models predict a relatively higher backscatter intensity at higher frequency (Anderson, 1950; Loranger, 2019).

By contrast, on 7 September, the current regime changed in direction and magnitude (see Chapter 2) from southwestward to northward direction and decreased in magnitude following the passage of Tropical Storm Gordon. In this new ocean current regime, the plume rose nearly vertically from the seabed source, with some deflection at about 30 m depth, and the oil and gas were more mixed as the plume rose to the surface (Figure 3.18). Direct observations from the ship and from a drone showed two separate gas plumes erupting at the surface. Similarly, oil droplets were also observed rising to form a slick at the surface (Figure 3.19).

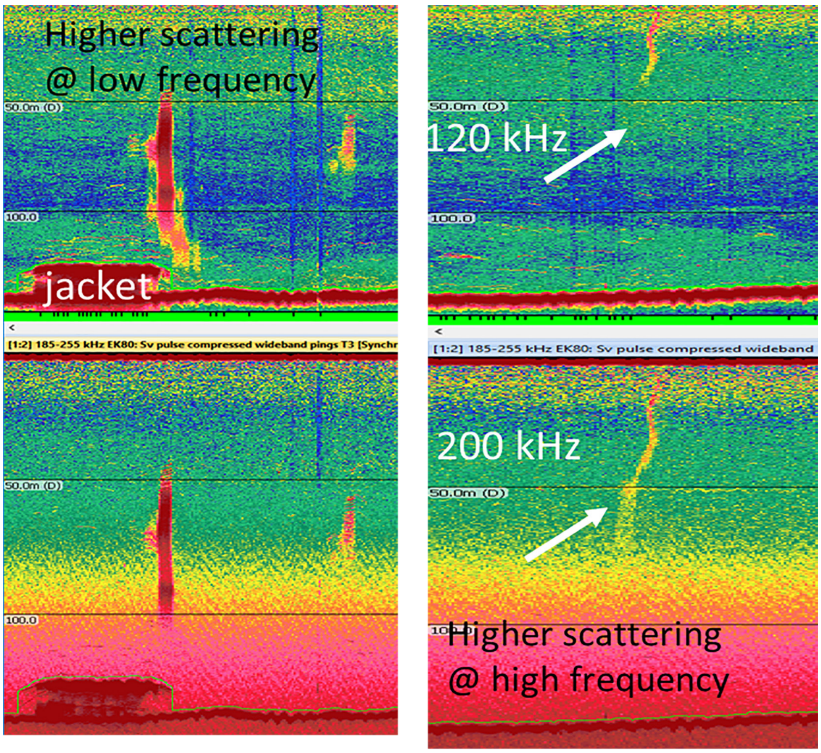

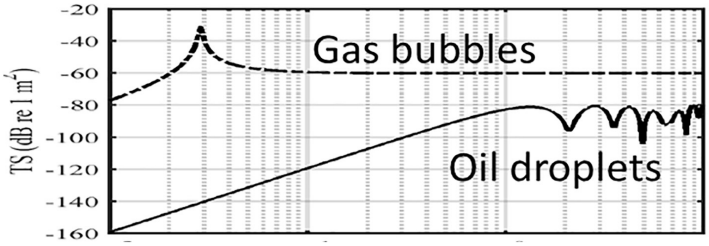

Figure 3.17. Example synchronous echograms for 120 and 200 kHz for two cross sections of the plume composed of primarily bubbles (left, red plume over jacket) and oil droplets (right). White arrows indicate area of plume that was poorly detected in the 120 kHz, detected in the 200 kHz channel.

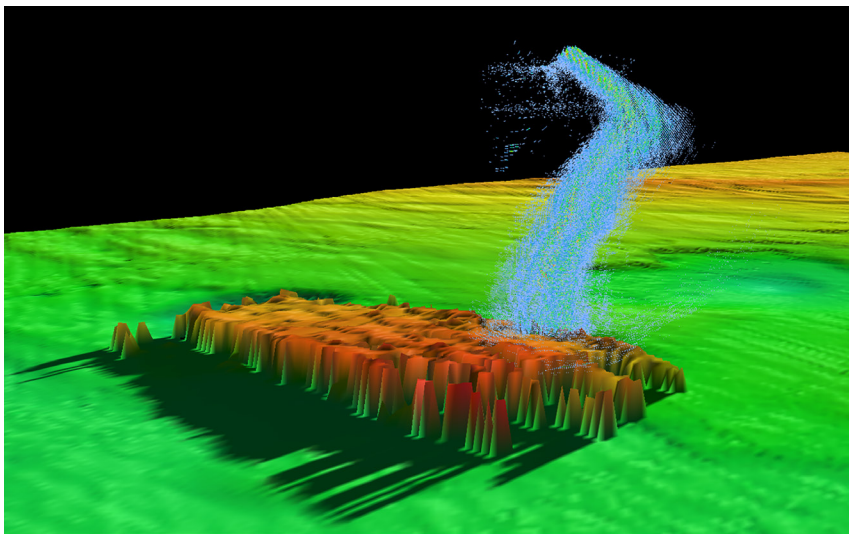

Figure 3.18. Three-dimensional model of the oil and gas plume. M3 multibeam backscatter intensity scale is arbitrarily blue-orange:low-high. Note deflection of vertical rise. See text for explanation.

Figure 3.19. Drone image of R/V Brooks McCall with rising gas plume and oil at the surface. Surfacing gas bubbles identified by white arrows, surfacing oil slick identified by blue arrow.

3.3.3 ROV Subsurface Observations

Six ROV dives were conducted to closely examine the plume through the water column and at the seabed, collect video images of the bubbles and oil droplets, characterize the seabed origins of the plume, and describe and measure the plume components. In this section, we report on imaging sonar and echosounder observations of the plume and origins at the seabed. The ROV provided numerous observations placing the plume in the context of the downed jacket. Each observation located the plume within the area of the erosional pit near the northwest corner of the jacket (Figure 3.20).

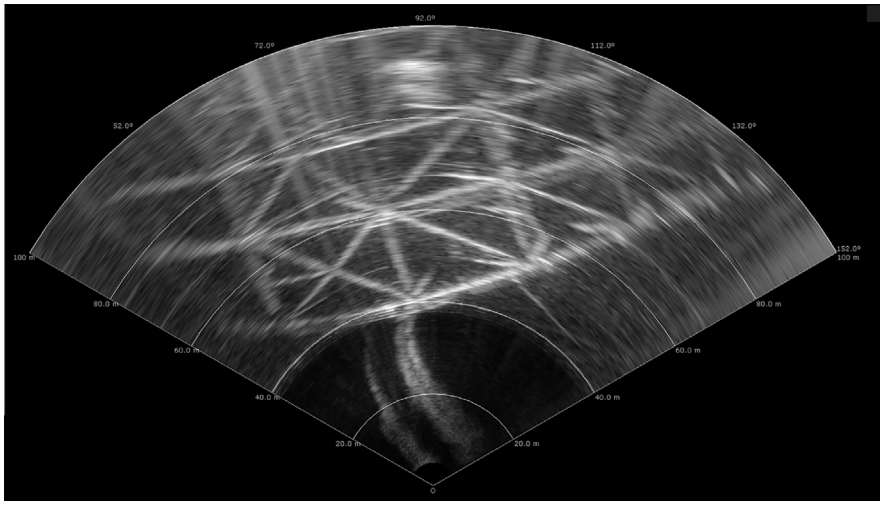

Figure 3.20. M3 imaging sonar perspective from the ROV. MC20 jacket in the background and multiple plumes observed in the foreground.

During 5 September, an ROV dive collected clear images of the plume components and positioned them in the erosional pit and in the spatial context of the downed jacket. Clear sonar imaging revealed the plume originating from the erosional pit. Closer examination with the M3 sonar revealed several features within the erosional pit interpreted as four or five subcomponents of the plume: a pair of smaller plumes to the southwest of the erosional pit, and two separate larger plumes to the north (Figure 3.21). A fifth feature was less defined between the pair of smaller plumes and the southern-most of the two larger plumes. The characteristics of the backscatter intensity suggested the smaller pair were composed of oil, whereas the higher backscatter intensity were composed of gas.

On 6 September, the 200 kHz transducer on the ROV was reoriented downward to scan the plume in close proximity to the seabed. Using the forward facing M3 imaging sonar for navigation, the ROV transited from southwest to northeast. As the ROV passed through the small pair of plumes, oil droplets were visible on the ROV video (Figure 3.22). As the ROV progressed to the north, the plume constituents changed to predominantly gas bubbles and the backscatter intensity increased (Figure 3.22). Unfortunately, the 120kHz echosounder was still oriented horizontally and direct comparison between the frequencies was not possible. Further analysis of the 200 kHz and the broadband acoustic signatures may provide insights into the properties of the oil and gas that could lead to improved estimates of flux of oil versus gas.

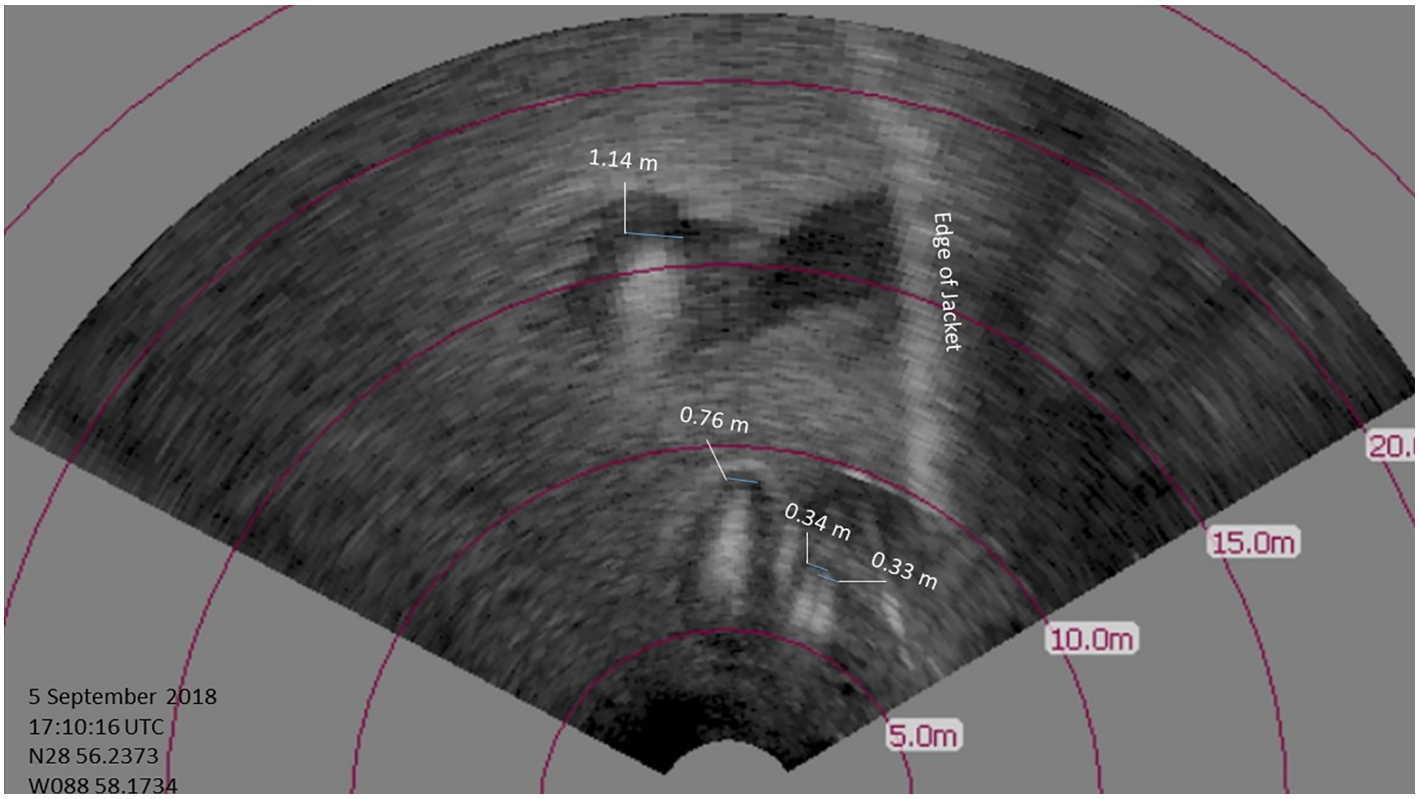

Figure 3.21. M3 imaging sonar perspective from the ROV. MC20 jacket in the background and multiple plumes observed in the foreground.

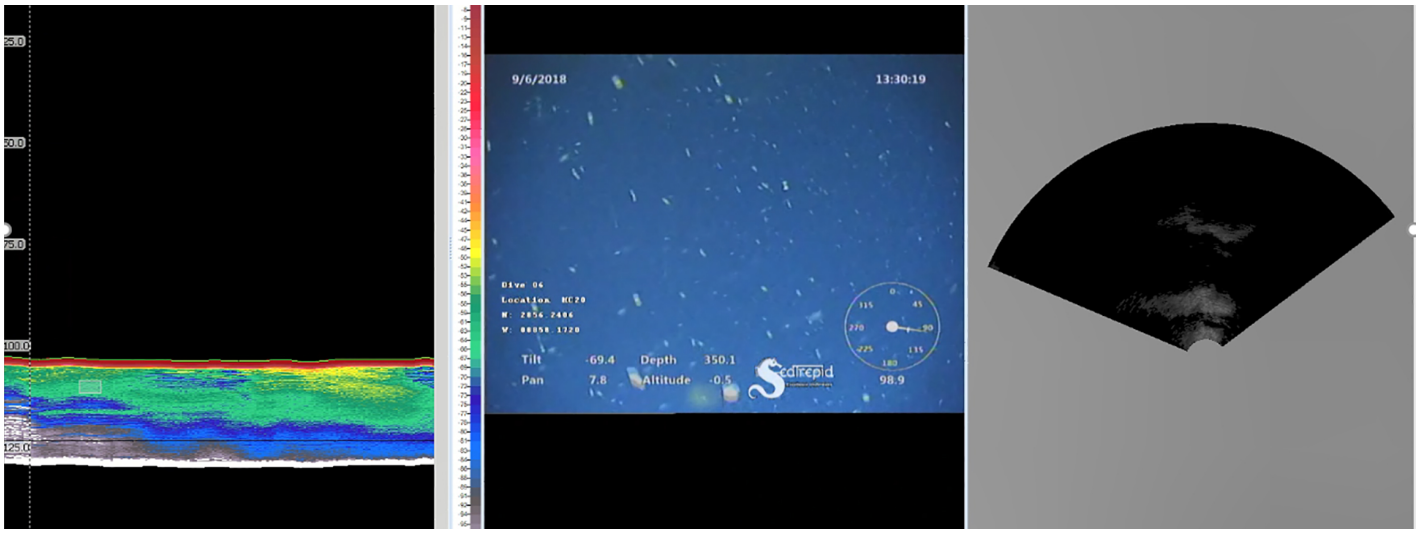

Figure 3.22. Example echogram, video, and imaging sonar observation of the plume from the ROV. In the left panel, the echogram range is corrected for the depth of the ROV. A vertical hash line marks the moment of backscatter intensity of the 200 kHz echosounder synchronized to the video and M3 panels. The synchronized video frame (middle) shows exclusively oil drops and no gas bubbles in the view. Right panel is a ping beam fan of the M3 imaging sonar for navigation and spatial context. With the ROV over the oil component of the plume, the M3 image shows the two gas plumes in the forward, with higher intensity backscatter later in the echogram.

3.4 CONCLUSIONS

Multiple surface surveys were conducted over the MC20 site providing further evidence of a consistent plume originating from an erosional pit that was formed prior to 2012 at the northwest corner of the downed jacket. Origins traced to the seabed are predictions, with error and uncertainty associated with ship motion including the beam pattern of multibeams as reported in Greenaway (2018). The accuracy of identifing the seabed, origin could also be influenced by the strength of currents and advection of the plume close to the seabed as well as the direction and orientation of the multibeam beam fan, and ability to detect the source within the depression in the erosional pit. Therefore, we contend that variation in the seabed origin predictions may not represent movement of the origin of the plume, but instead multiple sources of uncertainty. Closer examination using subsurface vehicles with sonars are likely the only way to provide accurate locations of seabed origins for the plume.

Fortuitous current regime to the southwest in the early days of the mission aided in separating out the components of the plume. Specifically, seabed originating plume components in the southwest area of the erosional pit were advected down current and rose slowly. Observations at the seabed revealed two smaller plume origins, each approximately 0.3 m in diameter. These plumes rose with relatively little mixing with the gas. The largest component of the plume with higher backscatter intensity was composed of faster rising gas that was verified in the closer examinations of the plume near the seabed. Plume components were further investigated by the ROV sonars and revealed multiple components and origins at the seabed within the area of the erosional pit. Two smaller plumes to the southwest were attributed to primarily oil and two to the north were attributed to gas. The acoustic backscatter taken in aggregate by the surface surveys can be used to estimate concentration of oil and gas, but requires validation of size and proportions of oil droplets versus gas bubbles and their depth-specific rise rates.

3.5 REFERENCES

Anderson, V.C. 1950. Sound scattering from a fluid sphere. Journal of the Acoustical Society of America 22(4): 426-431. doi: https://doi.org/10.1121/1.1906621

Baldwin, W.E., S.D. Ackerman, C.R. Worley, W.W. Danforth, and J.D. Chaytor. 2018. High-resolution geophysical data collected along the Mississippi River Delta front offshore of southeastern Louisiana. U.S. Geological Survey Field Activity 2017-003-FA: U.S. Geological Survey data release. Online: https://www.sciencebase.gov/catalog/item/5a9464c1e4b069906068fb10. doi: https://doi.org/10.5066/F7X929K6

Camilli, R. 2017. Final report Describing Spring 2017 Acoustic Survey Operations, Results and Interpretations. Report to the Sheen Source Location Working Group.

Camilli, R., D. Di Iorio, A. Bowen, C.M. Reddy, A.H. Techet, D.R. Yoerger, L.L. Whitcomb, J.S. Seewald, S.P. Sylva, and J. Fenwick. 2012. Acoustic measurement of the *Deepwater Horizon* Macondo well flow rate. Proceedings of the National Academy of Sciences 109(50): 20235-20239. doi: https://doi.org/10.1073/pnas.1100385108

Crooke, E, A. Talukder, A. Ross, C. Trefry, M. Caruso, P. Carragher, C. Stalvies, and S. Armand. 2015. Determination of sea-floor seepage locations in the Mississippi Canyon. Marine and Petroleum Geology (59): 129-135. doi: https://doi.org/10.1016/j.marpetgeo.2014.08.004

De Robertis, A., and I. Higginbottom. 2007. A post-processing technique to estimate the signal-to-noise ratio and remove echosounder background noise. ICES Journal of Marine Science 64(6): 1282-1291. doi: https://doi.org/10.1093/icesjms/fsm112

Demer, D.A., Berger, L., Bernasconi, M., Bethke, E., Boswell, K., Chu, D., Domokos, R. A. Dunford, S. Fässler, S. Gauthier, L.T. Hufnagle, J.M. Jech, N. Bouffant, A. Lebourges-Dhaussy, X. Lurton, G.J. Macaulay, Y. Perrot, T. Ryan, S. Parker-Stetter, S. Stienessen, T. Weber, and N. Williamson. 2015. Calibration of acoustic instruments. ICES Cooperative Research Report No. 326. 133 pp.

Greenaway, S. 2018. Acoustic Water Column Detection of Hydrocarbon Plumes. Unpublished report to the Unified Command Sheen Source Location Working Group Acoustic Sub-team.

Jerram, K., T.C. Weber, and J. Beaudoin (2015), Split-beam echo sounder observations of natural methane seep variability in the northern Gulf of Mexico, Geochemistry, Geophysics, Geosystems 16(3): 736-750. doi: https://doi.org/10.1002/2014GC005429

Loranger, S. 2019. Acoustic detection and quantification of crude oil. Dissertation to the Oceanography Department, University of New Hampshire. 140 pp.

NOAA. 2012. EX1202L3: Gulf of Mexico Exploration on NOAA Ship *Okeanos Explorer* between 20120411 and 20120429. NOAA Dataset. Online data access: https://catalog.data.gov/dataset/ex1202l3-gulf-of-mexico-exploration-on-noaa-ship-okeanos-explorer-between-20120411-and-20120429 (Accessed 20 May 2019)

Pedersen, G. 2016. Simulation of acoustic backscattering from bubbles and droplets under different shape regimes with implications for underwater detection of leakages using active acoustic sensors. The Journal of the Acoustical Society of America 140(4): 3364. doi: https://doi.org/10.1121/1.4970739

Weber, T.C., A. De Robertis, S. F. Greenaway, S. Smith, L. Mayer, and G. Rice. 2012. Estimating oil concentration and flow rate with calibrated vessel-mounted acoustic echo sounders. Proceedings of the National Academy of Sciences 109(50): 20245-20250. doi: https://doi.org/10.1073/pnas.1108771108

Acoustic Mapping

Chapter 4
Quantitative Imaging of Oil and Gas Bubbles Discharged at MC20

Ian R. MacDonald[1], Carrie O'Reilly[1] , Camilo Roa[2], and Mauricio Silva[1]

Bubblometer. Credit: NOAA NOS/NCCOS

ABSTRACT

A custom sampling device was designed and fabricated by the Florida State University project participants. Called the "bubblometer," use of this device allowed the project team to collect physical samples of oil and gas from the hydrocarbon plumes at MC20 and to use a calibrated digital camera and light system to sample the concentration of oil and gas bubbles in the plumes. Image sample collection was carried out wherever there were bubbles visible in the ROV and bubblometer video feeds; image sampling did not target any geographic features or the well jacket. Acoustic imaging of the plume verified that the samples corresponded to the acoustic target generated by the plume (Chapter 3). Samples were geolocated based on the USBL position of the ROV and the depth of the ROV as recorded by an on-board CTD. Analytical results of the oil and gas samples are presented in Chapters 6 and 7 of this report. This chapter describes calibration, field methods for collections, and image processing techniques used to measure and count bubbles in the image samples. A total of 665 image samples were analyzed, which comprised 5,881 gas bubbles and 6,258 oil bubbles. Samples were collected in a depth range of 140-110 m. Mapped in three-dimensional space, oil and/or gas bubbles were observed in two clusters, which correspond to discrete hydrocarbon vent locations visible in the ROV side-scan data (Chapter 3). Vertically, the depths at which bubbles were observed indicate three distinct domains within the first 30 m of the plume's trajectory: Below 135 m, bubbles were within the confines of the erosional crater; between 135 and 125 m, bubbles entered the water column, but were interacting with the well jacket structure; above 125 m, the plume deflected as bubbles were subject to midwater and surface currents. Bubble volumes were estimated by modeling each bubble as an ellipsoid based on measured major and minor bubble axes. Mean volume (standard deviation) of oil bubbles was 234 mm^3 (± 628.3 mm^3). Gas bubble volumes were normalized to conform to a depth of 140 m. Results found that the mean volume of gas bubbles was 246 mm^3 (± 417.5 mm^3). Gas bubbles were found to include a fractional amount of oil that was transported as a layer in the bottom of each bubble. Mean oil content, by volume percent, of the gas bubbles was 35.6% (± 11.98%). The imaging chamber measured 30 x 30 x 20 cm (18 L); these measurements indicate that the mean volume of oil in the plume was 0.19 L/m^3 (± 0.357 L/m^3) near its base; however, different values were found among the depth domains.

Citation for chapter

MacDonald, I.R., C. O'Reilly, C. Roa, and M. Silva. 2019. Chapter 4: Quantitative Imaging of Oil and Gas Bubbles Discharged at MC20. pp. 43-58. In: A.L. Mason, J.C. Taylor, and I.R. MacDonald (eds.), An Integrated Assessment of Oil and Gas Release into the Marine Environment at the Former Taylor Energy MC20 Site. NOAA National Ocean Service, National Centers for Coastal Ocean Science. NOAA Technical Memorandum 260. Silver Spring, MD. 147 pp. doi: 10.25923/kykm-sn39

[1] *Florida State University, Earth , Ocean, and Atmospheric Science, College of Arts and Sciences. Tallahassee, FL.*
[2] *Florida International University, Marine Sciences Program, School of Environment, Arts and Society. Miami, FL.*

Bubblometer

4.1 INTRODUCTION

A primary goal of this integrated MC20 (Mississippi Canyon 20 lease block) project was collection of quantitative data on the hydrocarbon plumes that had been reported by previous investigations of the site. To collect these data, project team members from Florida State University (FSU) designed and fabricated a unique sampling device called the "bubblometer" to measure gaseous and liquid fluids immiscible with sea water that was emanating from the sea floor (Figure 4.1). The principal components of the bubblometer are as follows: 1) A movable frame with hydraulic actuator that allowed the device to be extended from the front of a remotely operated vehicle (ROV) to sample any hydrocarbon plume detected and retracted to stop sampling and, 2) a square, inverted funnel mounted atop a known 30 x 30 cm wide by 20 cm high visualization chamber that is open at the bottom and on one side. The funnel feeds into a 300 mL acrylic tube that can collect oil and gas while being monitored by investigators. Four pressure cylinders, evacuated and sealed at the surface, are plumbed into the collection cylinder and can be filled individually by hydrostatic pressure when their respective valves are opened. The visualization chamber includes a white background; bubbles passing through the chamber are monitored with a high-definition digital video camera and a pair of high-intensity lamps mounted at a fixed distance from the chamber. Calibration exercises prior to deployment found that still frames from the camera can resolve objects within the chamber with a precision of 4 pixels per mm; there is no detectable parallax distortion between the front and back of the chamber. Quantitative image samples were collected by capturing still images from the video recorded when the chamber was in the MC20 plume with bubbles flowing through the chamber. In this chapter, procedures for image collection at sea, method of image processing, and results for bubble quantifications are presented. These results will be further analyzed in detail for estimation of oil fluxes in the plume in Chapter 8 of this report.

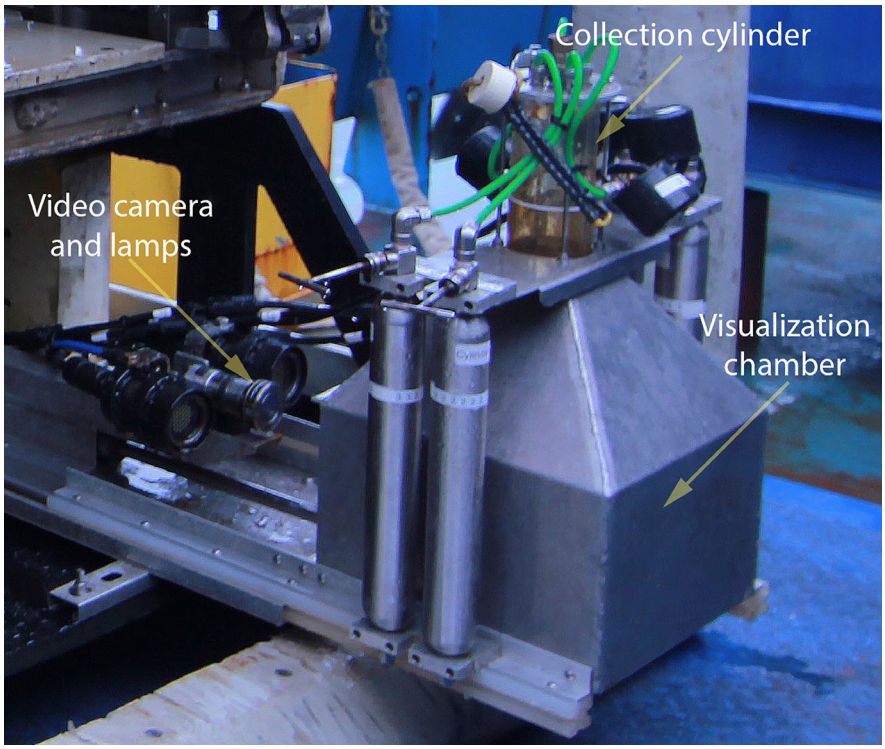

Figure 4.1. Bubblometer extended from front of ROV: Camera and lamps can record inside of chamber when device is extended; bubbles accumulate inside collection cylinder until valves are opened.

4.2 PHYSICAL COLLECTIONS

The bubblometer collected samples of oil and gas in the plume at MC20 by means of four evacuated pressure cylinders. At depth, water pressure forces water, oil, and gas from the collection cylinder into an individual pressure flask when a manual or solenoid valve was opened. Closing the same valve preserved the sample until it could be processed at the surface onboard the ship. Prior to collection, the oil and gas flowed through a 30 x 30 cm wide by 20 cm high visualization chamber and accumulated in the collection cylinder. When sufficient material had accumulated, it was collected into one of the four pressure cylinders by opening the respective valve. Analytical results for these collections are reported in Chapters 6 and 7 of this report.

4.3 OIL AND GAS BUBBLE IMAGE COLLECTION

As released hydrocarbons passed through the visualization chamber, a digital video camera (Deepsea Power & Light model HD Multi Seacam™) with illumination from two high-intensity lamps (Deepsea Power & Light Sealite™ 2300 lumen) recorded the flow. Output from the camera was monitored from the ship while the ROV was positioned within the MC20 hydrocarbon plumes. The bubblometer was then extended into the MC20 plumes while the video record was stored topside on memory cards. Unaltered versions of all video files are maintained by the National Oceanic and Atmospheric Administration (NOAA). Over the course of this field effort, image collections were completed on 2, 3, 5, and 6 of September, 2018. Unfortunately difficulties with video timestamps that matched the images with location data were not properly resolved until the collection efforts on 5 and 6 September, 2018. The results presented here are restricted to those dates (i.e., Dives 4 and 5). Image samples were taken whenever bubbles were observed passing through the chamber. For a typical collection, the ROV was steered toward the acoustic image of the plume until bubbles were observed, then often would slowly rise in the water column along with the bubbles. In total, 665 individual image samples were collected from the video records and were processed so as to standardize their format and prepare them for automated computer vision analysis (described further below).

Ancillary data were also collected so as to constrain interpretation of the bubble images and any issues with these data that might impact some of the collections at the beginning of the cruise. The position of the bubblometer with respect to the map location of the well jacket and plume was determined via the ultra-short baseline (USBL) navigation of the ROV. The depth at which the images were captured was recorded because pressure affects the size of gas bubbles and because depth was a means of tracking the samples with respect to the acoustic images of the plume location that were being separately monitored. Sample depth was also a variable that was used to identify separate domains within the overall hydrocarbon plume. A conductivity, temperature, and depth (CTD) instrument on the ROV provided a real-time read-out of ROV depth (as well as temperature, salinity, and dissolved oxygen) and a record for subsequent analysis.

4.4 IMAGE PREPARATION

Although the bubbles rose through the visualization chamber, their apparent rise speed was affected by the movement of the ROV vertically through the water column. Therefore, rise speed of bubbles and their accumulation rate in the cylinder can not be calculated directly from the raw video records from this survey. Instead, still frames of video were taken at approximately 5 second intervals from each recording, when an entirely new set of bubbles is assumed to have entered the visualization chamber. These images are assumed to be independent samples of the bubble volume concentration and characteristics in each plume, and represent varying depths and locations within the plume (Figure 4.2A). The raw images were processed to remove all portions of the image except for the visualization chamber (Figure 4.2B). The result was a set of images with uniform dimensions in which oil and gas bubbles are shown brightly illuminated against a white background. While oil did stain the chamber walls for some of the images, processing techniques described below were able to isolate the bubbles and categorize them as oil or gas, enumerate, and measure them.

4.5 IMAGE PROCESSING

The objective for processing the still images was to count, measure, and classify bubbles with respect to oil, gas, or mixtures of both. This was accomplished with use of image processing and machine learning techniques adapted for the image samples obtained.

Bubblometer

4.5.1 Description of Data

Images from the bubblometer digital video camera, at depths from 140 to 110 m, were taken and standardized as .jpg files of 1971 x 1173 pixels. The images presented various stages of the plume and the water column with clearly visible oil and gas bubbles (Figure 4.2). In order to get a better estimate of the oil flux, an accurate counting of the number of gas bubbles and oil bubbles is required. The area of the targets, their approximate shape, and their proportions with respect to the total area are also needed.

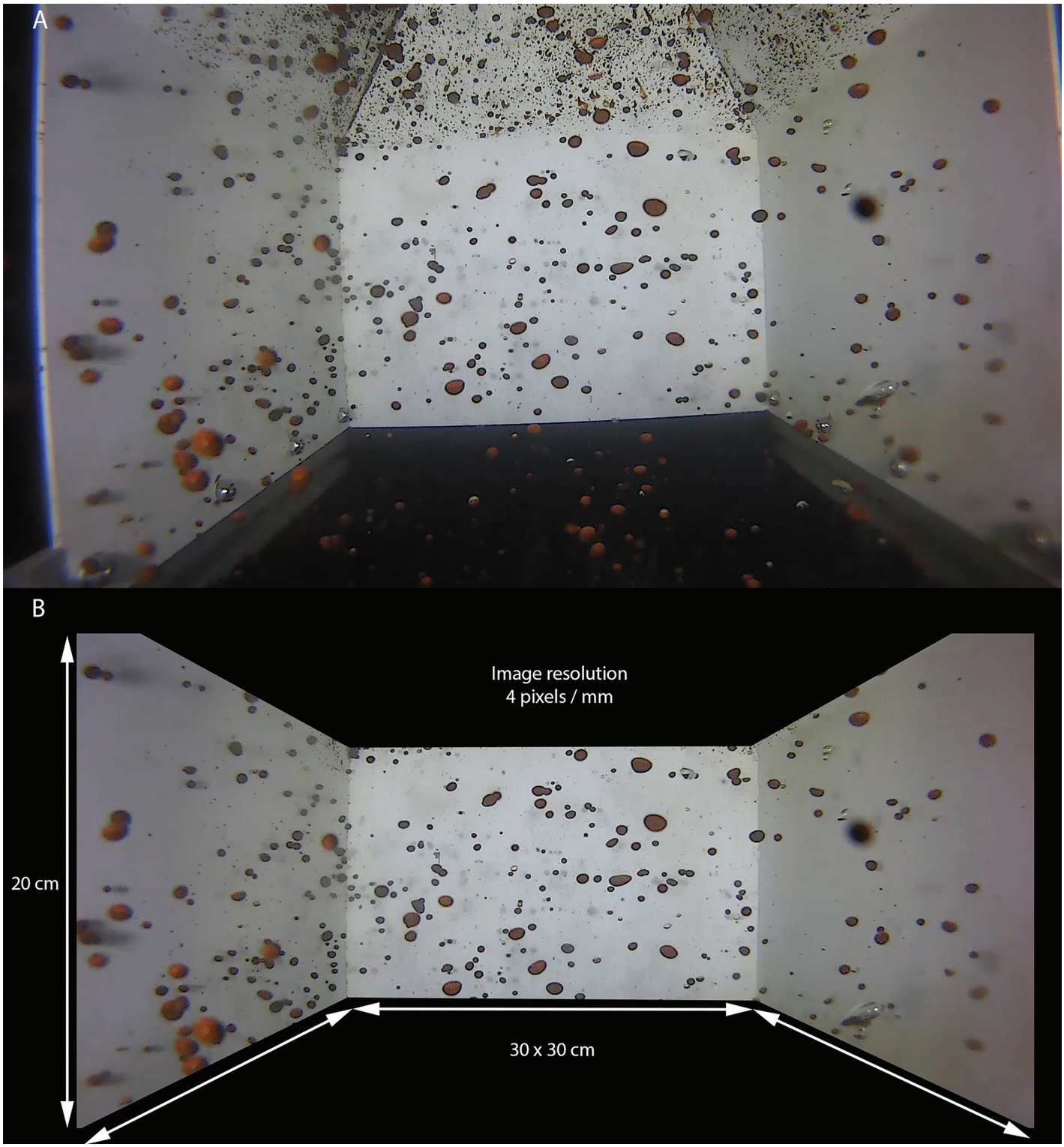

Figure 4.2. Example of the still images recorded with bubblometer digital video camera, Dive 5-3: (A) unprocessed frame grab; (B) same image after cropping to remove non-quantified portions of image and rotating to correct camera placement.

The targets have two main shapes: spherical or ellipsoidal. They could have several colors: completely transparent (rare and small) attributed to bubbles of gas alone (Figure 4.3B, red 1); transparent with a dark band on their lower sides (Figure 4.3A, red 2), attributed to gas with a layer of oil at the bottom of the bubble; yellow tinge, attributed to gas bubbles with oil coating the bubble wall uniformly (Figure 4.3B, red 3); grey-brown shadows, attributed to oil bubbles (Figure 4.3B, yellow 4); or brown, attributed to fully formed oil bubbles (Figure 4.3B, yellow 5). Due to the large number of images, manual detection and classification was not realistic. A computational solution was implemented by treating the issue as a computer vision problem.

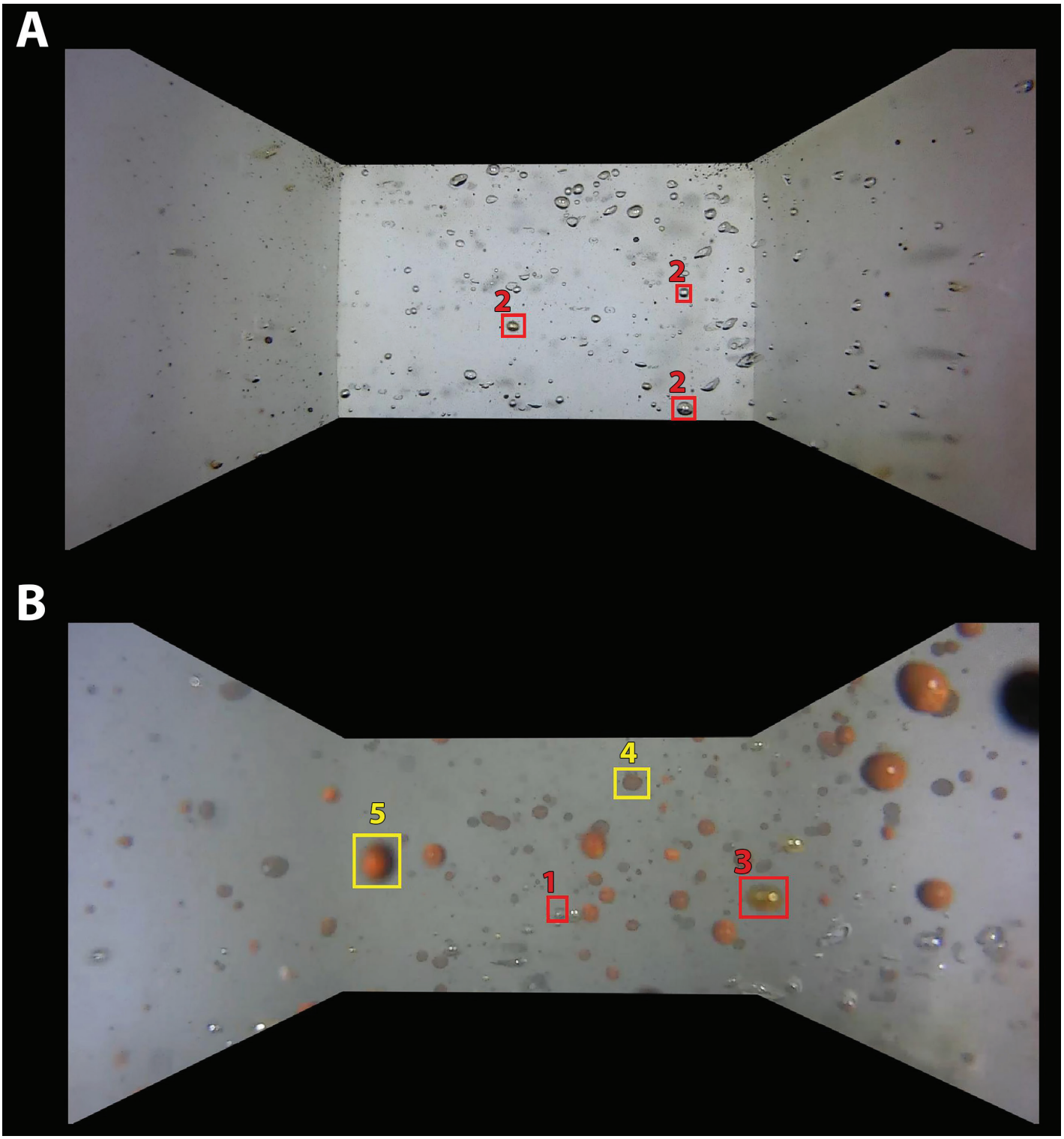

Figure 4.3. Images prepared for computer vision processing: (A) Dive 5-3 Image 175 outlining three gas bubbles in red; (B) Dive 5-3 Image 143 outlining two gas bubbles in red and two oil bubbles in yellow.

4.5.2 Methodology: Classification Using Faster R-CNN

A neural network was chosen for the detection and classification of the bubbles in the image samples. Neural networks are widely used in computer vision to identify objects in pictures and group them; this process is called Object Detection. For the present application, a Faster Region Convolutional Neural Network (Faster R-CNN) was implemented. Faster R-CNNs are a specialized type of neural network that focuses on reading groups of pixels (called regions) from an image and classifying them into predetermined classes. They are different from regular CNNs in the sense that a regular CNN classifies the entire image while an R-CNN classifies sections of the image. The Faster connotation simply denotes that it uses an improved algorithm that is "faster" than the algorithms used by other R-CNNs (Ren *et al*., 2015).

Two classes were selected for the targets: gas bubbles with a minor fraction of oil, and oil bubbles assumed to be predominantly oil. The Faster R-CNN was implemented in Matlab using its Computer Vision toolbox.

4.5.3 Implementation

Several steps are required in order to implement a neural network: it has to be designed, by choosing its layers; it has to be trained, by choosing an appropriate set of training images; and it has to be tested, by applying the detection to an independent set of test images. These steps are detailed below.

4.5.4 Design: Modification of a Pre-trained Network

The process of training a new Faster R-CNN is lengthy, usually taking more than five days. Instead, a pre-trained network, Resnet50, was modified and customized for this purpose (He, 2016). Resnet50 is a CNN widely used in computer vision and image classification and is available online. After adding some layers to it, in this case oil droplets and gas bubbles (Figure 4.4A and B), Resnet50 was then converted into a Faster R-CNN from its default form which resulted in a reduction in training time from over 5 days down to 40 hours.

4.5.5 Training: Ground Truth and Training Set

In order to generate a training set, a Ground Truth must be created. Ground Truth in computer vision is a set of images for which each image has the associated classes to which they belong predetermined. For a Faster R-CNN, this is a group of images with the targets already identified and classified (Figure 4.4). This detection and classification is done manually and the targets are stored in a separate file called Ground Truth.

A set of 68 images was chosen and the targets were manually classified and stored. Both the training set and test sets are taken from the Ground Truth. The training set uses 70% randomly assigned images while the remaining 30% goes to the test set. Targets smaller than 2 mm of radius were intentionally left out since they added noise to the process. The targets were too small for the network to discriminate, resulting in the network detecting small targets more frequently than it should have and in erroneous locations, reducing the accuracy. Half targets, partially occluded targets, or targets too close to the black boundary were also left out of the Ground Truth for similar reasons.

The training process was completed automatically by Matlab. At the end, it provided a detector that can be used on any image, or set of images, and it identifies and classifies their targets (Figure 4.5).

4.5.6 Testing: Preliminary Results and Neural Network Error

The trained detector was tested on the remaining 30% of the images. An example of the detection and classification can be seen in Figure 4.5. It shows an overall accuracy of 60%, which increases to 62% for oil bubbles (Table 4.1). Most of the error is attributable to false positives due to either overlapping detections (Figure 4.6A) or detections that were not considered in the Ground Truth (Figure 4.6B). To prevent overlapping detection, further processing could be applied; however, that implementation was left for future studies. The latter case does not need correction; most of those detections were true detections that were left out of the Ground Truth since they contributed to the overall noise in the network.

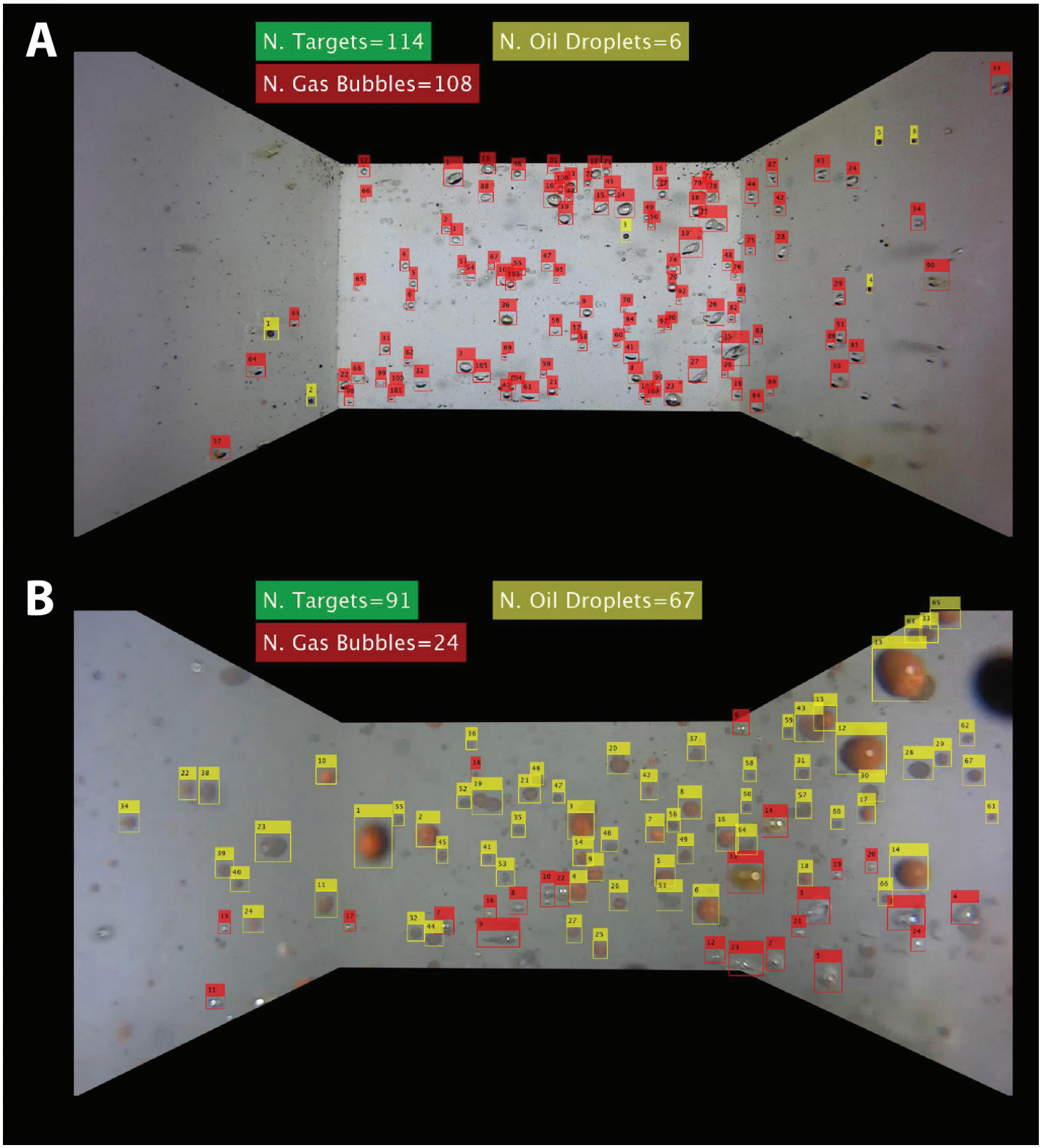

Figure 4.4. Layers added to Resnet50 for predominantly gas (A) and predominantly oil (B) image samples modified into a Faster R-CNN.

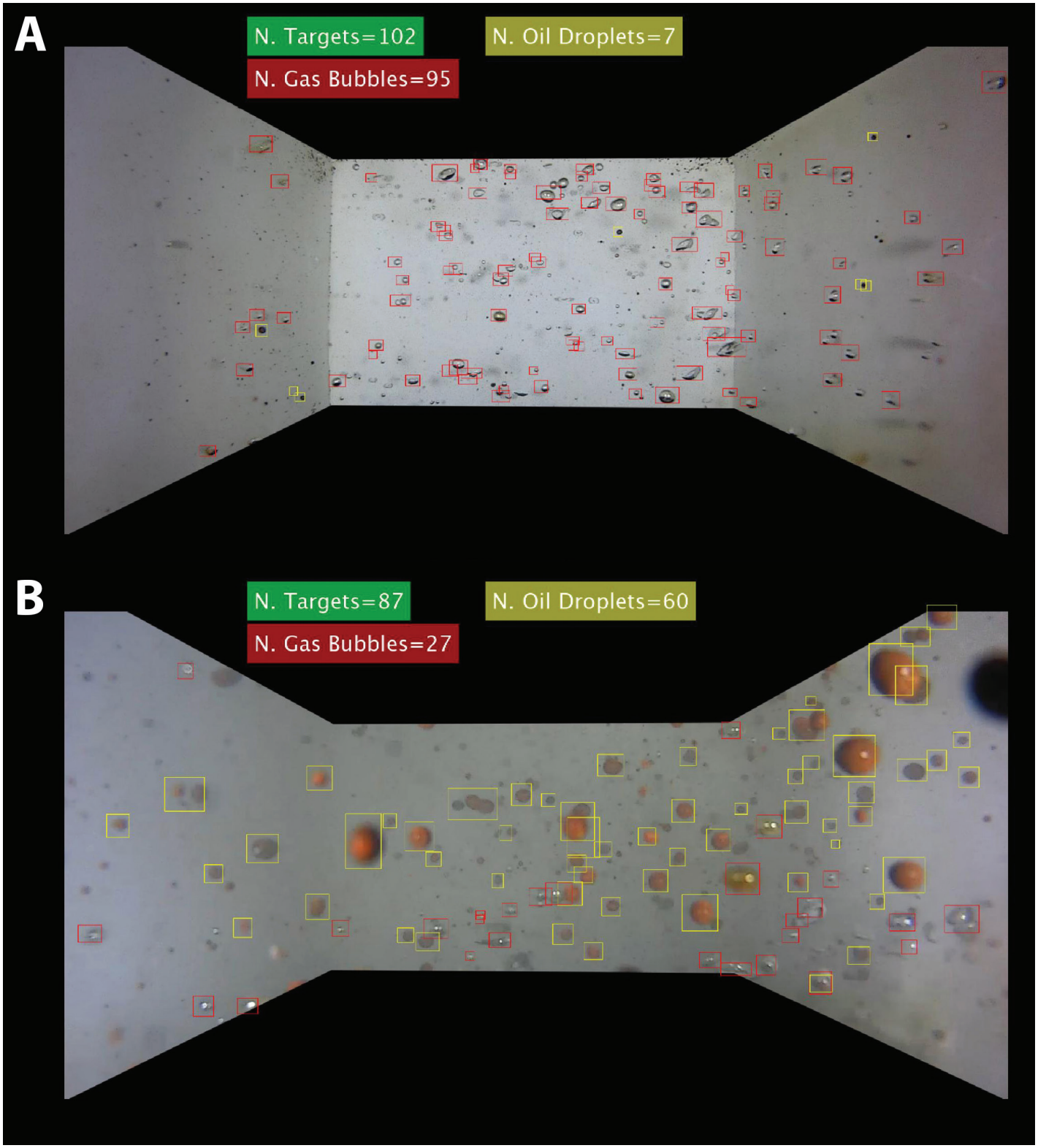

Figure 4.5. Samples of detector results with predominantly gas targets (A) and predominantly oil targets (B).

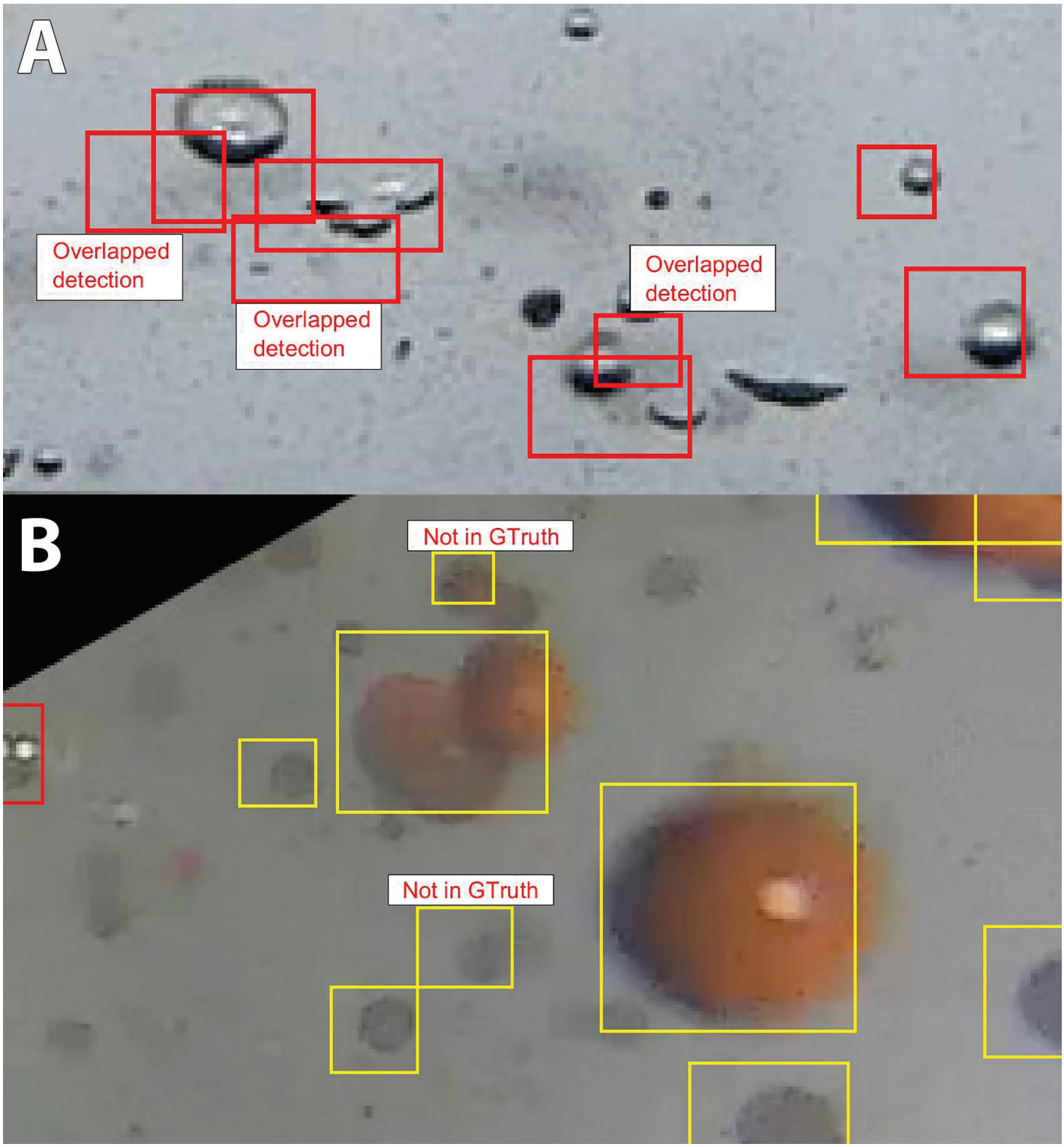

Figure 4.6. Details of bubble detection: (A) overlapping bubbles - note oil layer in bottom of gas bubbles; and (B) targets detected by initial processing, but deleted from ground truth due to not having clearly defined edges.

A different metric to measure the error based on the total area of the targets was also implemented. The sum of the total area of detected bubbles was compared with their equivalents in the Ground Truth. In terms of total area, the error for gas bubbles was 15% and for oil bubbles 28%. This means that the detected total area for oil bubbles, for example, has a difference of 28% with respect to the Ground Truth.

Table 4.1. Average recognition accuracy and area accuracy achieved by the R-CNN algorithm.

		Average Accuracy (%)	Area Error (%)
Gas bubbles	Training Set	66	22
	Test Set	53	11
	All Images	62	18
Oil droplets	Training Set	67	63
	Test Set	74	47
	All Images	64	58
All targets	Training Set	67	24
	Test Set	58	24
	All Images	64	24

4.5.7 Data Export

Properties such as position, area, lengths of axes, number of gas bubbles, and number of oil bubbles were extracted for each image and exported to excel files. This information is further processed in order to get the required statistics.

4.5.8 Scaling the Image Data

Laboratory chemical analysis found that the oil seen in bubble images and recovered by the bubblometer samples had an API gravity of 25.74° (see Chapter 7, Table 7.4). The conversion to specific gravity (SG) is as follows:

$$API = (141.5 / SG) - 131.5$$

Rearranging for specific gravity (g/cm^3), the conversion from API gravity yields the following:

$$0.9 = 141.5 / (131.5 + 25.74)$$

4.6 RESULTS AND DISCUSSION

4.6.1 Oil Bubbles and Mixed Gas-Oil Bubbles

Review of gas bubbles detected by the computer vision algorithm found that they overwhelmingly contained a notable volume of oil entrained in the lower portion of the bubble walls (Figure 4.7). The gas bubbles effectively dragged small pools of oil as they rose through the water column. These oil pools could be observed to oscillate and distort within the larger bubble volumes as they rose through the chamber, ruling out the likelihood of shadows, reflections, or image anomalies. Therefore, estimations of oil flux necessarily include oil transported to the surface in this manner.

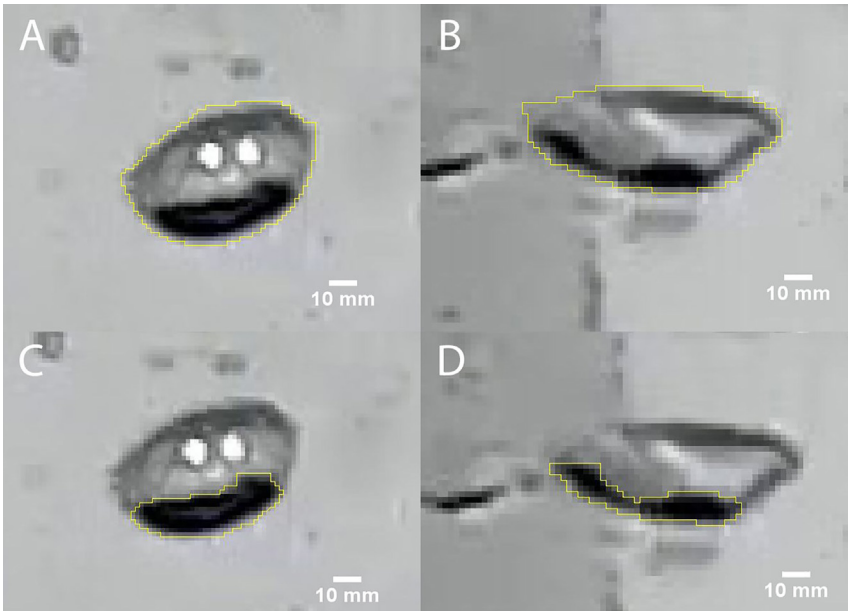

Figure 4.7. Mixed oil and gas bubbles. A-B: Total bubble areas were outlined and measured in ImageJ2 software version 1.52a; C-D: areas of small pools of oil in the lower portion of the bubbles were outlined and measured in ImageJ2 software.

To determine the average volume of oil found in the mixed bubbles, 100 bubbles

were selected at random; their major and minor axes and areas were measured with the use of ImageJ2 software version 1.52a (Figure 4.7). Gas volumes were normalized to a depth of 140 m and proportions of gas and oil volumes were estimated from their respective areas in the images. Oil volume was found on average to be 35.6% (SD ± 11.98%) of total mixed bubble volume. There is a linear relationship between total bubble volume and proportion of oil (Figure 4.8). All gas bubbles were therefore calculated as including 35.6% oil by volume for gas volumes adjusted to a constant 140 m pressure.

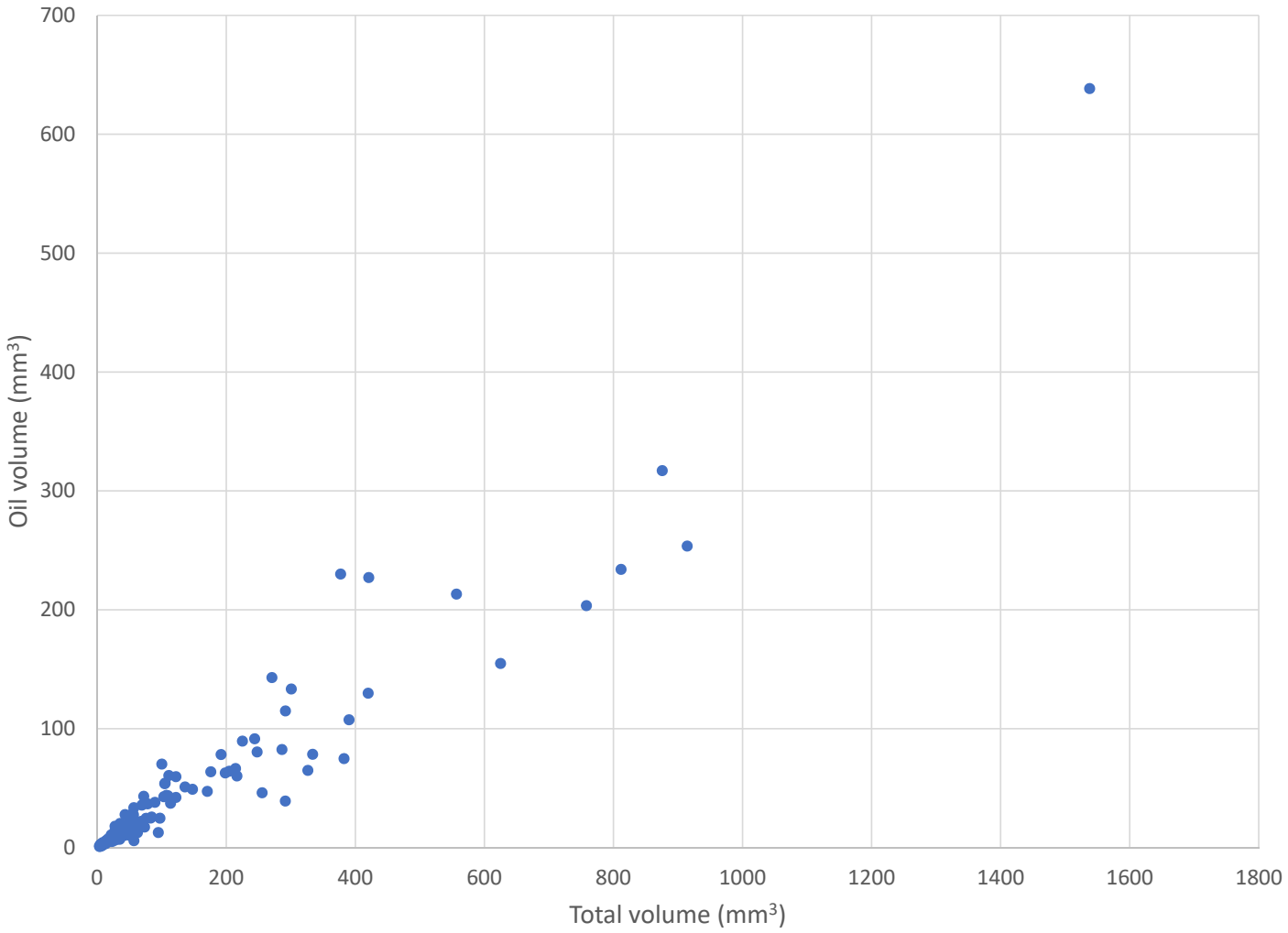

Figure 4.8 Comparison of oil volumes in gas bubbles show linear trend with bubble size.

4.6.2 Frequency Distributions of Oil and Gas Bubbles

A total of 12,139 bubbles (5,881 gas-oil mixture and 6,258 oil) were detected and measured using the computer vision algorithm (Faster R-CNN) described above. The frequency distribution of all oil concentration values (Figure 4.9) is strongly skewed to the right. For skewed data, standard deviation does not provide an accurate picture of the variation with respect to the mean; a more accurate representation of the variation is given by the interquartile range (Q1-Q3). Details of the bubble measurement results are given in Table 4.2. Calculation of the rise speed of bubbles and the associated diameters of these bubbles were calculated from their equivalent spherical volumes for Stokes' Law application (Figure 4.9). These results indicate that small diameter bubbles (approximately 5 mm) are the numerically dominant mode for oil and gas-oil bubbles. However, because the distribution is strongly skewed to the right, and volume increases as a spherical function, approximately 80% of the volume transport was comprised of bubbles larger than the modal diameters (Figure 4.9).

Bubblometer

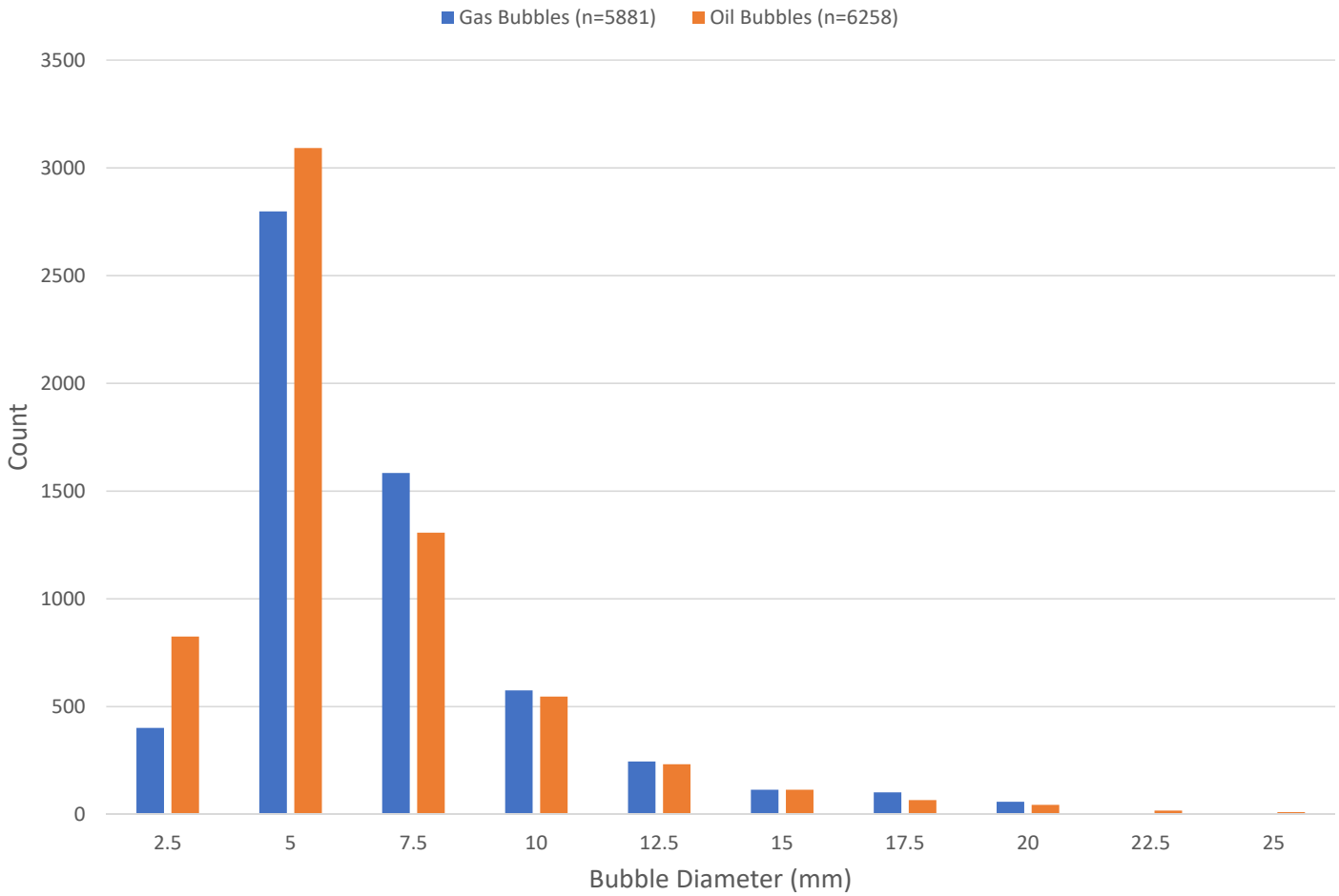

Figure 4.9. Bubble size frequency: Distribution of bubble diameters for oil and gas-oil bubbles detected with computer vision algorithms in digital images from the visualization chamber.

Estimated spherical diameters for the ellipsoid bubbles were used to calculate the rise speed or upward motion of a subset of the bubbles. The oil specific gravity (ρ_p), measured as part of the chemistry detailed in Chapter 7, is converted to 900 kg/m^3 and is taken as the liquid density of oil bubbles. At these depths, ≤145 m, any effect of depth/pressure on oil density is negligible and therefore does not affect oil bubble liquid density between the ocean floor and the surface. The specific gravity of the imaged and collected gas bubbles is taken as the specific gravity of methane at 20°C normalized to a depth of 140 m (14 bar); this yields 9.2 kg/m^3. For bubbles comprising 64.4% gas and 35.6% oil, the composite bubble concentration is assumed to be 321 kg/m^3. The density of seawater (ρ_m) is taken as 1,027 kg/m^3. Seawater dynamic viscosity, at 20°C (μ), was taken as 1.08 x 10^3. For estimates of rise speed (-V), the spherical diameter equivalent of bubble volumes was calculated and applied with use of Stokes' Law (see below).

$$V_t = gd^2(\rho_\rho - \rho_m) / 18\ \mu$$

4.6.3 Concentration of Oil and Gas in Plume

Estimates of oil concentration were calculated from the 665 image samples after preparation and processing with the computer vision algorithm. Oil and gas volumes were calculated as ellipsoids for everything except Stokes' which requires spherical bubbles to allow for Stokes' Law application. Gas volume was normalized to 140 m depth and oil volume in the gas-oil bubbles was taken as 35.6% of the normalized volumes. Given that the visualization chamber of the bubblometer had a total volume of 18 L, the oil concentration in each image sample was scaled to 1 m^3 based on this constant:

$$1000 / 18 = 55.6$$

This is an unbiased estimate of the oil concentration, or mass per volume, in the plumes. Values for the mean and standard deviation of the concentration measurements could likewise be scaled, with the caveat that these values apply to the variability of bubble capture within the chamber. A device that sampled 1 m^3 of the plume might have different error characteristics. A summary plot of individual image estimates partitioned by water depths is shown in Figure 4.10.

An example of the ROV track and the depths of the images is shown in Figure 4.11A. These results show that the data were distinctly partitioned by depth. This corresponds to specific features of the crater and the well jacket. Observations from within the crater (Figure 4.11B) were taken in the depth range 141 to 137 m. Observations from the benthic layer (Figure 4.11C), partially shadowed by the structure of the well jacket were taken in the depth range 137 to 125 m. And finally, observations from the midwater (Figure 4.11D) were taken at depths less than 125 m. These domains are indicated versus the corresponding depth ranges shown in Figure 4.10.

The characteristics of the oil and gas bubbles are summarized by depth range in Table 4.2. Vertical rise velocities are calculated from Stokes' Law, as described above.

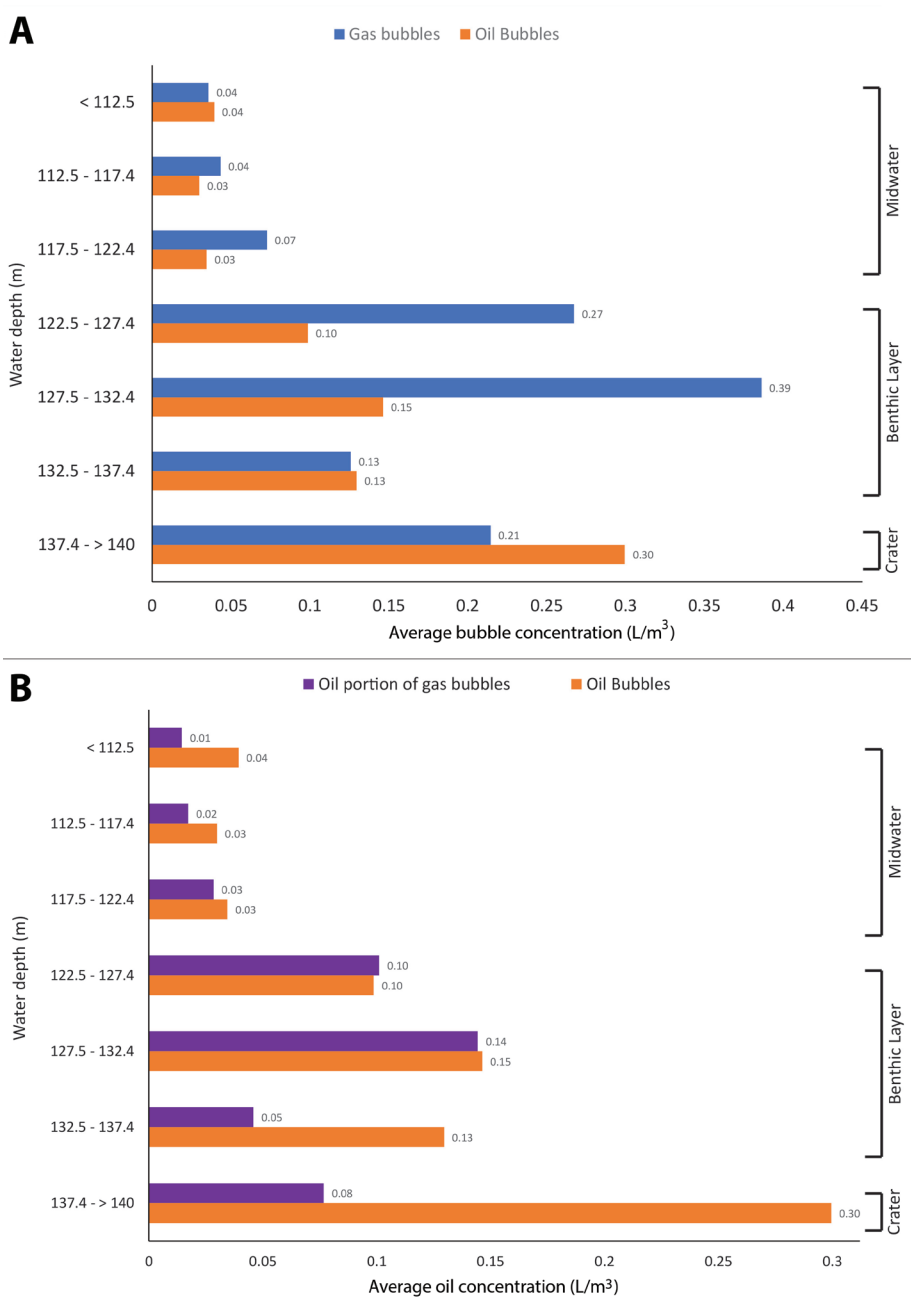

Figure 4.10. Oil concentration estimates from counts and measurements of oil and gas bubbles in the bubblometer chamber for 5 m depth intervals: (A) Concentration of bubbles including entire gas bubbles (L/m^3); (B) Concentration of oil bubbles plus oil fraction of gas bubbles.

4.6.4 Spatial Distribution of Bubble Samples

The image samples of the plume showed distinct patterns of bubbles within the crater, with two clusters of bubbles that correspond to the clusters of individual bubble vents detected acoustically (see Chapter 3, Figures 3.4 and 3.21). To combine the spatial distribution results with the different depth intervals, the samples were split into three depth classes: from 111 to 125 m for samples above the jacket top; from 125.1 to 135 m for samples over the erosional pit until the top of the toppled jacket, and 135.1 to 145 m for samples taken inside of the erosional crater.

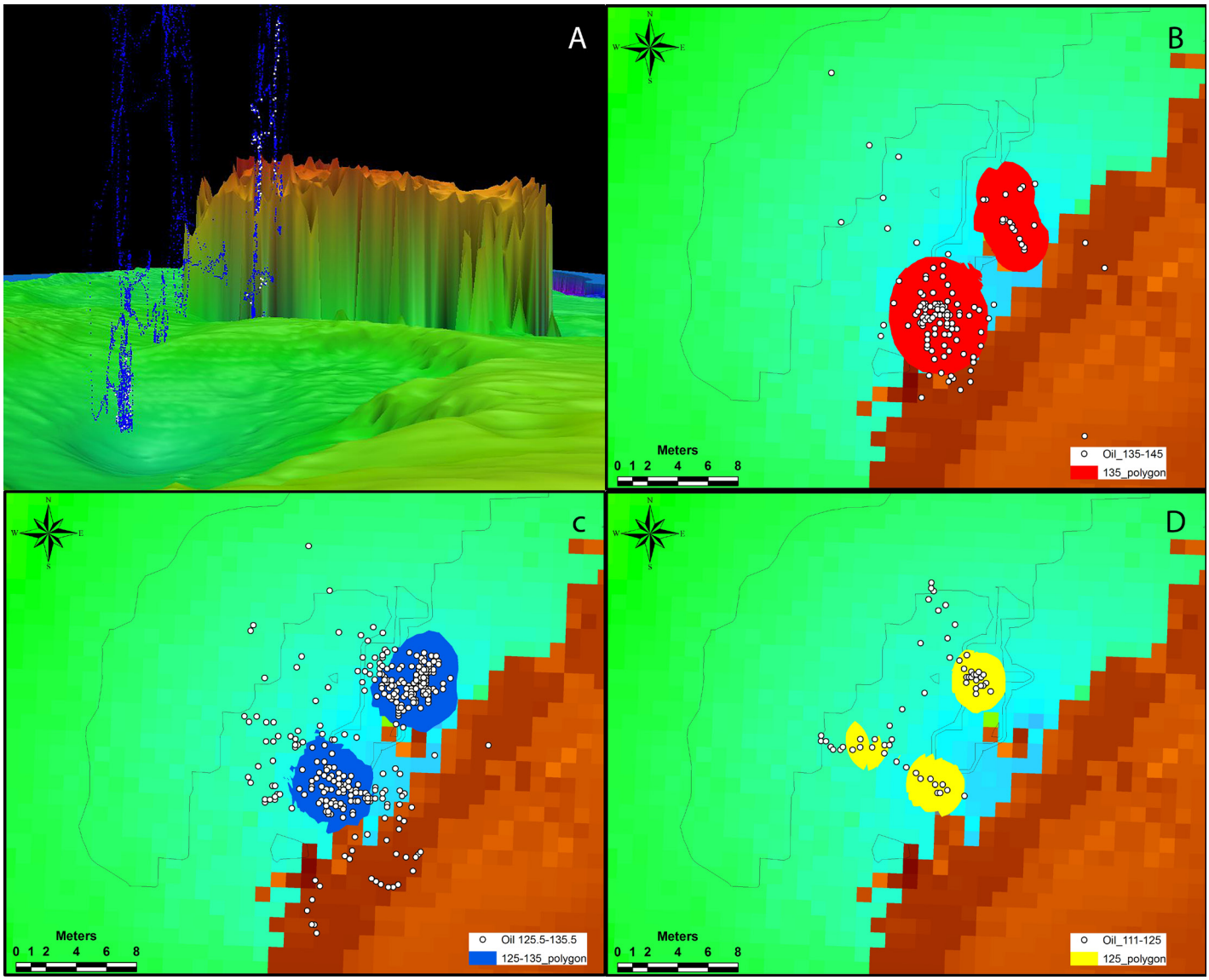

Figure 4.11. Locations of image samples from plume: (A) Vertical plot, blue points show the ROV locations during sampling and white points show where video images were taken on 5 September - outline of well jacket is approximately 10 m above the seabed (green); (B) Samples from plume in crater with outline of kernel polygon for this interval; (C) Samples from plume in benthic layer with outline of kernel polygon for this interval; (D) Samples from plume in midwater with outline of kernel polygon. Brown color represents location of the collapsed well jacket.

Each sample class was the subject of a kernel density point analysis (oil volumes as weighted fields) in order to identify the dominant cross-sectional area for the hydrocarbon plume in each depth interval and to avoid outliers resulting from navigation scatter or turbulent mixing. Once the cross sectional area of the plume for that depth class was identified, the kernel density raster was transformed into a georeferenced polygon (ArcGIS processes: raster reclassification, raster to polygon, merge and dissolved). Image data that fell outside of the transversal area of the plume was discarded from further analysis using the mask clip tool.

Finally, the average of all the samples inside the plume were used to calculate the average volume of the plume (L/m^3), and the rise rate of bubbles in the hydrocarbon plume, using different rise constants by depth and nature of the bubbles (gassy or oily). A summary of results is shown in Table 4.2.

Table 4.2 Summary statistics for bubbles in the depth domains of the plume. Bubble concentration is calculated from volume of bubbles in the imaging chamber. Assumed concentration and spherical diameter are used to calculate rise velocity (negative sinking) from Stokes' Law. Shading indicates midwater (light), benthic layer (medium), and crater (dark) domains.

	Depth range (m)	Mean bubble density (L/m³)	SD	Min	Q1	Median	Q3	Max	Assumed density (kg/m³)	Mean spherical diameter (m)	Stokes' velocity (m/s)
Gas bubbles	<127.5	0.219	0.288	0.002	0.041	0.104	0.315	1.812	320.9	0.0052	-0.0900
	127.5-132.4	0.386	0.407	0.003	0.058	0.233	0.625	1.888	320.9	0.0053	-0.0922
	132.5-137.4	0.126	0.282	0.002	0.009	0.032	0.107	1.393	320.9	0.0060	-0.1186
	137.5->140	0.214	0.384	0.002	0.020	0.039	0.175	1.544	320.9	0.0062	-0.1270
Oil bubbles	<127.5	0.076	0.119	0.002	0.019	0.043	0.091	1.120	900.0	0.0051	-0.0157
	127.5-132.4	0.146	0.346	0.002	0.018	0.050	0.113	3.561	900.0	0.0052	-0.0163
	132.5-137.4	0.130	0.176	0.002	0.030	0.071	0.157	1.299	900.0	0.0055	-0.0182
	137.5->140	0.299	0.811	0.002	0.017	0.065	0.257	5.608	900.0	0.0072	-0.0308

4.7 CONCLUSIONS

The visual samples from the bubblometer consistently showed dense assemblages of oil and gas bubbles in the hydrocarbon plume that originated from the erosional pit at the northwest corner of the collapsed well jacket. Using computer vision algorithms we are able to classify bubbles as either gas or oil and are also able to measure the major and minor axes of classified bubbles so that estimates of volume can be calculated. Gas bubbles were found to contain a measurable fraction of entrained oil by volume (35.6%), which means that the flux of gas bubbles must be included in estimates of total oil flux. The three-dimensional distribution of bubbles in the image samples is consistent with the acoustic images of the plume obtained from the ROV and ship-mounted instruments presented in Chapter 3.

Vertical distribution of bubbles within the measured plume indicates three domains with different characteristics. These include a crater, benthic layer, and mid-water domain. Differences in size distribution and oil content indicate that fluxes should be calculated separately for oil, gas and oil, and for each depth domain.

4.8 REFERENCES

He, K., X. Zhang, S. Ren, and J. Sun. 2016. Identity Mappings in Deep Residual Networks (Resnet). pp. 630-645. In: B. Leibe., J. Matas, N. Sebe, and M. Welling. (eds), Computer Vision – ECCV 2016. 4th European Conference Proceedings, Part VI. Lecture Notes in Computer Science 9908. Springer, Cham. doi: https://doi.org/10.1007/978-3-319-46493-0_38

Ren, S., K. He, G. Ross, and J. Sun. 2015. Faster R-CNN: Towards Real-Time Object Detection with Region Proposal Networks. In: C. Cortes, N.D. Lawrence, D.D. Lee, M. Sugiyama, and R. Garnett (eds.), Advances in Neural Information Processing Systems 28. Proceedings of the 28th International Conference on Neural Information Processing Systems. Online: https://papers.nips.cc/paper/5638-faster-r-cnn-towards-real-time-object-detection-with-region-proposal-networks (Accessed 24 May 2019)

Bubblometer

Chapter 5
Atmospheric Methane (CH_4) Concentrations at the MC20 Site in the Northern Gulf of Mexico

Mauricio Silva[1], Nizar Bel Hadj Ali[2], Tarek Abichou[1], and Ian R. MacDonald[1]

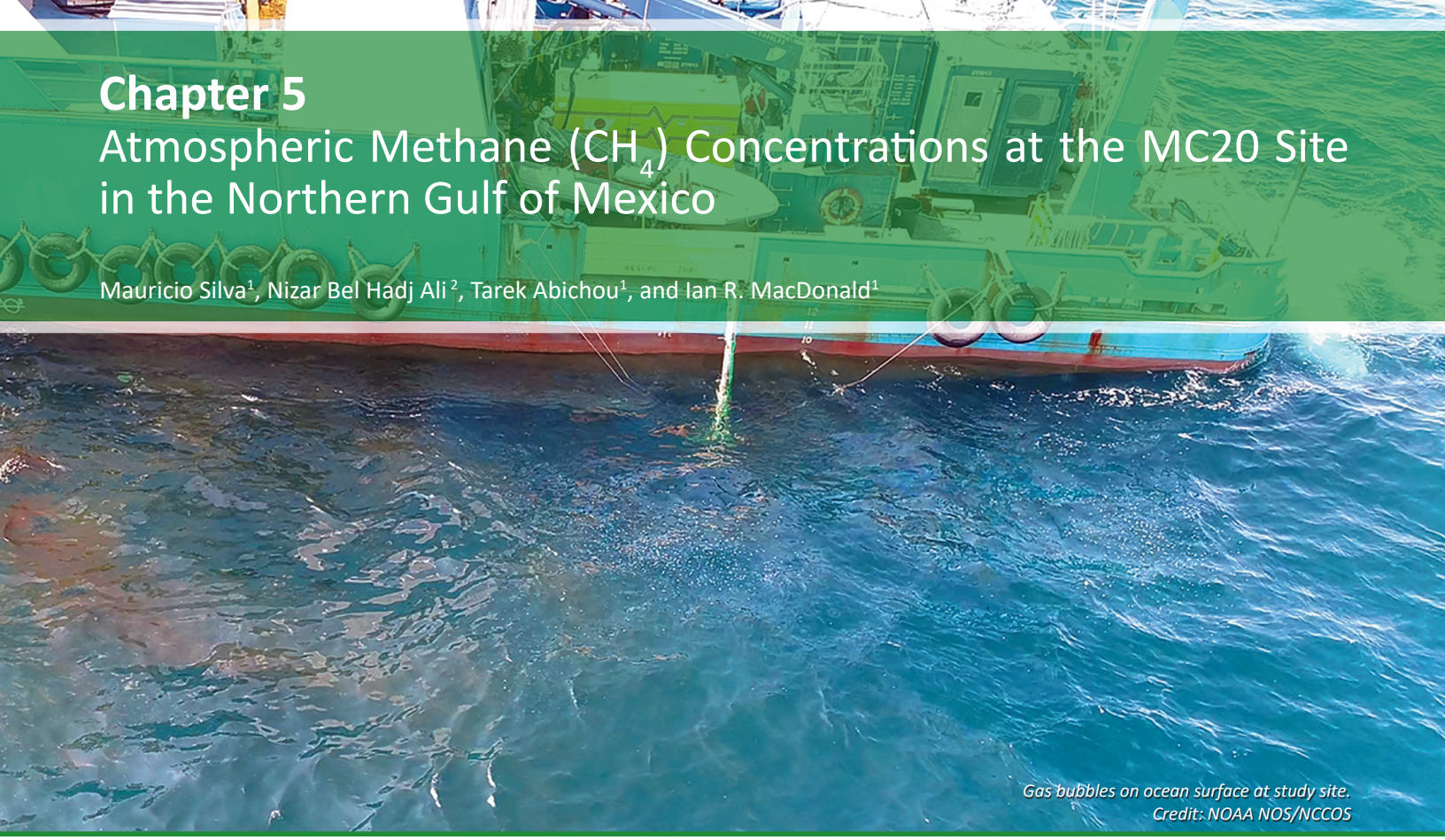

Gas bubbles on ocean surface at study site. Credit: NOAA NOS/NCCOS

ABSTRACT

Atmospheric methane (CH_4) concentrations at 3 m above the ocean surface were characterized for the first time for the Mississippi Canyon 20 (MC20) site. Fifteen years ago, Taylor Energy's production Saratoga Platform-A was destroyed when Hurricane Ivan triggered a mudslide off the Mississippi Delta, toppling and sinking the platform and moving it approximately 210 m downslope. Several inspections of the jacket, conductors, and wells have confirmed the release of hydrocarbons in the form of gas and crude oil to the water column and reaching the surface. Methane concentration in the air, in addition to acetylene (C_2H_2), was measured using a gas tracer analyzer Cavity Ring Down Spectrometer (CRDS) Picarro 2200 connected to a Global Navigation Satellite System (GNSS) Trimble Pro Series using NMEA sentences. Methane concentration in the air fluctuated between 1.8 to 1.9 ppm. However, measurements of CH_4 in the proximity of where gas and oil plumes were detected in the water column spiked from 2.5 up to 9 ppm, with a peak of 11.74 ppm where gas bubbles were observed reaching the water surface. The areal extent of high CH_4 concentration over the ocean surface at the MC20 site was mostly focused around the area where bubbles reached the surface, which denotes a fast rise of CH_4 towards the atmosphere. However, in periods where wind gusts reach as much as 5 to 6 knots, the CH_4 plume was detected as far away as 786 m NNE of the source. A fugitive methane estimation method based on Inverse Plume Modeling was used to estimate methane flux rate from the hydrocarbon plume to the atmosphere. Preliminary results provide an estimated flux of 9 g/s of CH_4.

Citation for chapter
Silva, M., N. Bel Hadj Ali, T. Abichou, and I.R. MacDonald. 2019. Chapter 5. Atmospheric methane (CH_4) concentrations at the MC20 site in the Northern Gulf of Mexico. pp. 59-70. In: A.L. Mason, J.C. Taylor, and I.R. MacDonald (eds.), An Integrated Assessment of Oil and Gas Release into the Marine Environment at the Former Taylor Energy MC20 Site. NOAA National Ocean Service, National Centers for Coastal Ocean Science. NOAA Technical Memorandum 260. Silver Spring, MD. 147 pp. doi: 10.25923/kykm-sn39

[1] *Florida State University, Earth , Oceans, and Atmospheric Sciences, School of Arts and Sciences. Tallahassee, FL.*
[2] *University of Gabes, National Engineering School. Gabes, Tunisia.*

Surface Methane Flux

5.1 INTRODUCTION

Methane (CH_4) emissions in the oceans have been extensively studied and characterized for shallow and deep seep fields, where biogenic and thermogenic hydrocarbons flow freely from deep reservoirs through subterranean fractures upward towards the ocean floor. In these natural environments (e.g., cold seeps) part of the methane that reaches the surface of the seafloor is either directly consumed by chemosynthetic organisms (methanotrophic organisms) or indirectly consumed by sub-products of Anaerobic Oxidation of Methane (AOM).

Methane that reaches the water column is altered by multiple processes including, but not limited to, being dissolved into the ocean by microbial activity through aerobic oxidization into CO_2. In natural seeps, these processes can keep up to 90% of the methane from small bubbles (<2 mm) from reaching the ocean surface and escaping into the atmosphere (Chen, 2018), even from relatively shallow cold seeps (<150 m depth) such as those present in U.S. coastal waters.

During catastrophic events, such as oil and gas spills at offshore production sites, methane can be released in sufficiently high quantities such that the system is not capable of dissolving the total volume of hydrocarbons present. If a spill event occurs at a shallow enough depth, a large portion of the gas discharged can potentially reach the ocean surface and escape into the atmosphere. It is important to note that during the Deepwater Horizon (DWH) incident, where up to 500,000 tons of methane was released into the water column (Joye *et al*., 2011), only a small fraction (0.01%) reached Earth's atmosphere (Yvon-Lewis, 2011) while most of the methane became dissolved and entrained in the ocean (Socolofsky and Adams, 2005).

Methane concentrations in marine environments are most commonly subscribed to natural seeps. Only under ideal conditions, where methane concentrations are observed in the water column, are empirical measurements of gas flux from the water into the atmosphere measured. Persistent hydrocarbon discharge into the water column and ocean surface by the toppled Taylor Energy Company (TEC) platform at the Mississippi Canyon 20 (MC20) lease block site provides an unparalleled opportunity to characterize and quantify the amount of methane released from the water column into the atmosphere from an oil and gas release event. This chapter details a novel approach for measuring, in real-time, methane concentrations near the ocean surface and calculates a flux rate estimate of methane from the MC20 erosional pit, through the water column, to the atmosphere.

5.2 METHODS

5.2.1 Data Acquisition

Atmospheric methane concentrations just above the ocean surface were measured using a Cavity Ring-Down Spectrometer (CRDS) Picarro G2203 Analyzer for CH_4/C_2H_2 and water vapor. The CRDS works under the premise that individual gas molecules have distinct infrared spectrums (scatter/absorption). When a gas sample is enclosed at sub-atmospheric pressure, the infrared spectrum of a gas can be plotted in a series of sharp and unique lines at distinctive wavelengths. When these lines are well-spaced and their wavelengths well-known, it is possible to determine the concentration of any gas specie by measuring the strength of their absorption and the amount of light that is scattered.

In the absence of a gas sample, in the CRDS-Picarro, a beam from a single-frequency laser diode enters a cavity composed of three highly reflective mirrors. When the laser is on, the cavity quickly fills with laser light that bounces from one mirror to the next. A photodetector recognizes the amount of light lost through one of the mirrors to produce a signal that is proportional to the intensity in the cavity. The laser light inside the cavity continues to bounce between the mirrors (about 100,000 times), but since the mirrors have 99.999%

reflectivity, the light intensity inside the cavity starts to decline, eventually to zero in an exponential mode. The decay, or "ring down", is measured in real-time by the photodetector, and the time it takes for the light to completely decay in an empty cavity is determined by the given unit's mirror reflectivity.

Conversely, when the unit's cavity is filled with a gas sample, in this case methane, the gas will absorb part of the laser light in addition to the known loss of light intensity by the mirrors. This addition accelerates the "ring down" time, which allows the instrument to calculate and quantify, with high precision, the gas concentration in a given sample. This whole process takes less than 0.250 seconds.

The CRDS-Picarro was installed in the dry lab of the R/V *Brooks McCall* and plugged in to an Uninterruptible Power Supply (UPS) unit in order to keep electrical current stable. Air samples were drawn from intake tubing (Tygon ¼ inch Outside Diameter) which ran from the inside of the dry lab, where the CRDS-Picarro was located, towards the bow-starboard side of the second level deck of the vessel, away from any potential influence from the exhaust gases of the vessel engines. Tygon tubing has an extremely low adsorption rate reducing any potential sample bias due to the relatively long flow path between the air intake and the instrument.

Air sample readings were automatically georeferenced in real-time using a Trimble® GPS antenna connected to the computer of the CRDS. The GPS antenna was placed on the upper deck of the vessel to avoid any loss in the reception of data from GPS satellites. The antenna was also located in the same position line of the sample intake tubing (bow-starboard) in order to increase the precision of the georeferencing process (Figure 5.1).

Figure 5.1. CRDS-Picarro placement inside of the dry-lab of the R/V Brooks McCall *(left); and sample intake tube location on the forward lower deck, starboard side of the vessel (right).*

The CRDS-Picarro survey was conducted independently of any other scientific operations running at any given time. The CRDS-Picarro was powered on and collecting/analyzing air samples 24 hours a day during the entire research expedition. The larger MC20 site and immediately adjacent areas were intentionally covered by the survey, with specific emphasis on the areas where the oil slick had been visibly observed, in order to allow a thorough understanding and spatial coverage of the methane concentrations in the collapsed jacket area (Figure 5.2).

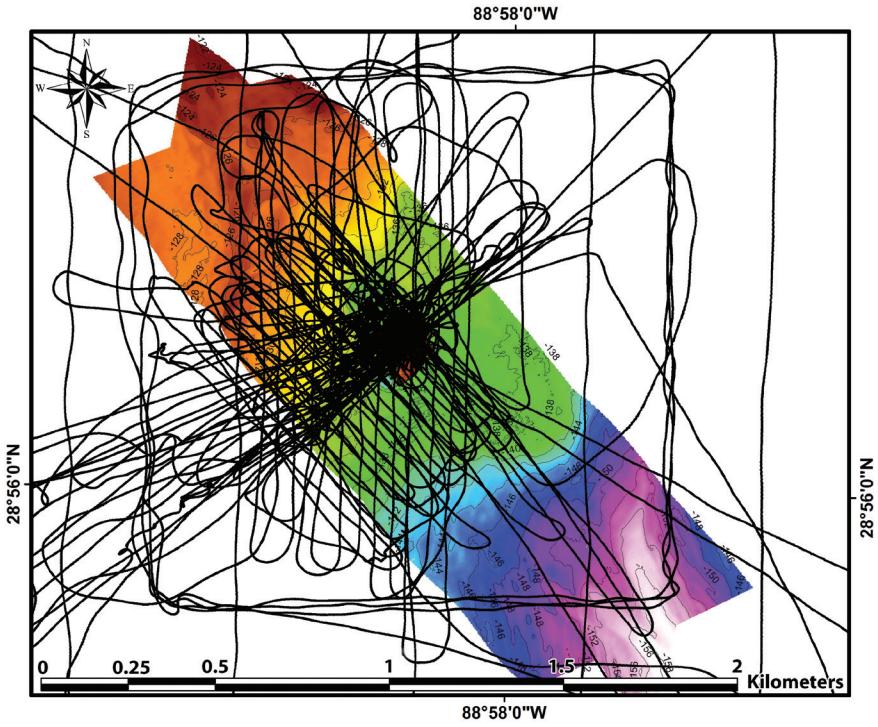

Figure 5.2. Localization of the CRDS-Picarro readings within the MC20 study area. Black lines denote ship track overlayed on bathymetric imagry of the MC20 site.

Tera-Term software was used to merge all collected data into one *.ascii file including the sample measurements

from the CRDS-Picarro along with georeferenced locations provided by the GPS antenna. These files however had two different issues that were later addressed during the post processing stage of the data (Figure 5.3). First, the GPS antenna provided a georeferenced location in National Marine Electronic Association (NMEA) sentences at a rate of one data point per second while the Picarro CRDS stream provided four readings of each gas chemistry parameter per second over the same time period. The second problem was a latency related time gap between when each sample was taken (and georeferenced) and when the sample was actually processed by the instrument. The sample intake tube was required to be at minimum 10.5 m long in order to achieve optimal location on the vessel to collect samples and also to avoid vessel exhaust gases. The result was a 55.25 second delay between when an air sample was collected by the intake tube and when it was actually processed and measured by the CRDS-Picarro.

```
$GPGGA,183149.00,3201.178648,N,08115.821210,W,2,09,0.9,6.08,M,-31.88,M,6.0,0135*74
$GPGLL,3201.178648,N,08115.821210,W,183149.00,A,D*79
$GPVTG,152.8,T,152.8,M,005.6,N,010.3,K,D*27
$GPGSV,4,1,13,27,57,057,48,11,17,176,39,08,69,171,49,30,10,305,*72
$GPGSV,4,2,13,26,05,065,,09,55,270,46,18,10,156,38,07,34,316,47*77
$GPGSV,4,3,13,16,28,049,41,23,50,200,48,,,,,,,*73
$GPGSV,4,4,13,46,00,000,,48,24,247,42,51,43,223,44,,,,*44
$GPGSA,A,3,08,07,23,27,16,09,18,11,30,,,,1.5,0.9,1.2*33
$GPZDA,183149.00,11,04,2018,07,00*68
$GPRMC,183149.00,A,3201.178648,N,08115.821210,W,005.6,152.8,110418,0.0,E,D*25
  1523457082.77     0.2406     2.1221     1.1614 20180411.0000 143122.7660
  1523457083.07     0.2081     2.1221     1.1614 20180411.0000 143123.0660
  1523457083.34     0.2081     2.1221     1.1650 20180411.0000 143123.3430
  1523457083.59     0.2951     2.1221     1.1650 20180411.0000 143123.5910
$GPGGA,183150.00,3201.177328,N,08115.820333,W,2,09,0.9,6.17,M,-31.88,M,7.0,0135*7E
$GPGLL,3201.177328,N,08115.820333,W,183150.00,A,D*7C
$GPVTG,147.6,T,147.6,M,005.3,N,009.9,K,D*20
$GPGSV,4,1,13,27,57,057,48,11,17,176,43,08,69,171,49,30,10,305,38*74
$GPGSV,4,2,13,26,05,065,,09,55,270,48,18,10,156,38,07,34,316,47*79
$GPGSV,4,3,13,16,28,049,38,23,50,200,48,,,,,,,*7D
$GPGSV,4,4,13,46,00,000,,48,24,247,41,51,43,223,44,,,,*47
$GPGSA,A,3,08,07,23,27,16,09,18,11,30,,,,1.5,0.9,1.2*33
$GPZDA,183150.00,11,04,2018,07,00*60
$GPRMC,183150.00,A,3201.177328,N,08115.820333,W,005.3,147.6,110418,0.0,E,D*2F
  1523457083.93     0.2951     2.1267     1.1650 20180411.0000 143123.9270
$GPGGA,183151.00,3201.175963,N,08115.819447,W,2,09,0.9,6.18,M,-31.88,M,7.0,0135*79
$GPGLL,3201.175963,N,08115.819447,W,183151.00,A,D*74
$GPVTG,147.7,T,147.7,M,005.6,N,010.4,K,D*20
$GPGSV,4,1,13,27,57,057,48,11,17,176,43,08,69,171,48,30,10,305,37*7A
$GPGSV,4,2,13,26,05,065,,09,55,270,47,18,10,156,37,07,34,316,47*79
$GPGSV,4,3,13,16,28,049,39,23,50,200,48,,,,,,,*7C
$GPGSV,4,4,13,46,00,000,,48,24,247,41,51,43,223,44,,,,*47
$GPGSA,A,3,08,07,23,27,16,09,18,11,30,,,,1.5,0.9,1.2*33
$GPZDA,183151.00,11,04,2018,07,00*61
$GPRMC,183151.00,A,3201.175963,N,08115.819447,W,005.6,147.7,110418,0.0,E,D*23
```

Figure 5.3. Example of the file created by the Tera-Term software merging CRDS readings and GPS. String data sentences that starts with "$" correspond to the GPS NMEA sentences. Integer data correspond to the CRDS-Picarro measurements

5.2.2 Tracer Experiment

During the final day of operations a tracer experiment was conducted in order to establish if methane concentrations in the air in the study area could be linked to the persistent hydrocarbon plume that reached the ocean surface near the toppled MC20 oil platform, and also to establish the path and dispersion of methane gas in the area. Because the CRDS-Picarro 2203 has the capability of detecting acetylene gas with a precision in the parts per million range, the tracer experiment also utilized this gas as a reference compound. Acetylene has been widely used in the quantification of fugitive methane in landfills (Mønster *et al*., 2014; Mønster *et al*., 2015). In order to adapt this technique for the open ocean, a floating raft was constructed which held an acetylene tank (Figure 5.4). The acetylene tank was also connected to a mass flow meter to allow for the controlled release of a quantity of tracer gas into the atmosphere (15 L/min). In addition, a meteorological station installed on the raft collected records of the ambient wind speed and direction, temperature, and humidity in the area during the controlled acetylene

Figure 5.4. Mounting and deployment process of the tracer gas experiment raft.

release event. The raft was deployed, as close as was possible, to the area where the MC20 hydrocarbon plume reached the ocean surface. To avoid drifting, the raft was anchored using floating polypropylene line and a mushroom anchor. Once the raft was successfully deployed, the R/V *Brooks McCall* vessel drifted downwind in order to increase the chances of detecting both atmospheric methane concentrations and the known volume of tracer gas.

5.2.3 Data Analysis

Once the collected CRDS-GPS files were created, the resulting *.ascii files were uploaded into Matlab for analysis. Each file was run through a script code specially created to:

1. Delete unnecessary NMEA sentences from the file;
2. Match the CRDS time with corrected GPS time including the 55.25 second delay;
3. Interpolate coordinates for CRDS measurements in between data that already had been georeferenced by the GPS;
4. Create a new file which included CRDS date-time, coordinates, methane, acetylene, and water vapor; and finally;
5. Create plots for each parameter.

New georeferenced CRDS reading files were exported into ArcGis 10.6.1 and QGis for visualization and spatial analysis routines. Once all CRDS measurements were plotted into ArcMap, the "Optimized Hot-Spot Analysis" routine (Getis-Ord Gi statistical analysis) was applied in order to create a statistically significant map that illustrated areas where it was more likely to find elevated concentrations of methane (hotspots) over background levels (1.85 ppm, parts per million).

5.2.4 Inverse Plume Modeling

Kormi *et al*. (2018) proposed a novel approach that relies on ambient air and methane concentration measurements, coupled with an optimization-based identification method, to estimate fugitive methane emissions. This method was originally developed for landfill methane emission estimations. In this method, concentration measurements are used to infer emissions though dispersion modeling and optimization. This is achieved through tracing dispersed methane back to potential emission sources. In the subsequent paragraphs, we briefly summarize this optimization-based approach, and refer the reader to Kormi *et al*. (2018) for a more thoroughly detailed presentation of the method.

Model input parameters of this methane emission estimation method include methane concentration measurements and locations along with meteorological conditions (the most important are wind speed and direction, insolation, and temperature). An implemented code is used to generate multiple configurations of source positions and emission rates. Each sample configuration is evaluated through calculating the corresponding methane concentrations at each measurement point. This is done through the backward application of an atmospheric dispersion model. As such, source identification can be treated as an inverse optimization task where the objective is to obtain the configuration of sources (locations and emission rates) that best fits the measured concentrations. The performance of a source configuration is further evaluated through the difference between measured and predicted methane concentrations. To predict methane concentrations at locations where effective measurements are performed, a detailed dispersion model is needed. In this proposed method, modeling of methane dispersion is done using a Gaussian dispersion equation (1). This equation models the dispersion of a non-reactive gaseous pollutant (here methane) from an elevated point source. Equation (1) predicts the steady state concentration (C) in $\mu g/m^3$ at a point (x, y, z) located downwind from the source.

Surface Methane Flux

$$(1) \qquad C(x,y,z) = \frac{Q}{2\pi u \sigma_y \sigma_z} e^{-\frac{y^2}{2\sigma_y^2}} \left(e^{-\frac{(z+H)^2}{2\sigma_z^2}} + e^{-\frac{(z-H)^2}{2\sigma_z^2}} \right)$$

In Equation (1) "Q" is the emission rate (µg/s), "σ_y"and "σ_z" (m) are the horizontal and vertical spread parameters that are functions of wind distance "x", and atmospheric stability is a measure of the resistance of the atmosphere to vertical air motion. Continuing, "u" is the average wind speed at stack height (m/s), "y" is the crosswind distance from the source to the receptor (m), "z" is the vertical distance above the ground (m), and "H" is the effective stack height (physical stack height plus plume rise) expressed in m.

The Gaussian dispersion equation uses a relatively simple calculation requiring only two dispersion parameters (σ_y and σ_z) to identify the variation of gas concentrations away from the diffusion source. These dispersion coefficients, σ_y and σ_z, are functions of wind speed, cloud cover, and surface heating by the sun. Generally, the evaluation of the diffusion coefficients is based on atmospheric stability class. In the employed method, Pasquill-Gifford stability classes are used, and dispersion coefficients are calculated using the Briggs model (Briggs, 1965; Table 5.1).

Table 5.1. Briggs model for dispersion coefficients

Pasquill stability class	σ_y (m)	σ_z (m)
A	$0.22x(1 + 0.0001x)^{-0.5}$	$0.20x$
B	$0.16x(1 + 0.0001x)^{-0.5}$	$0.12x$
C	$0.11x(1 + 0.0001x)^{-0.5}$	$0.11x(1 + 0.0001x)^{-0.5}$
D	$0.08x(1 + 0.0001x)^{-0.5}$	$0.08x(1 + 0.0001x)^{-0.5}$

The optimization task is tackled using Genetic Algorithms. As a stochastic search method, including Genetic Algorithm optimization can efficiently explore complex and large solution space using special strategies. Although there is no guarantee of reaching a global optimum, near optimal solutions are usually obtained.

5.3 RESULTS AND DISCUSSION

In total, 1,562,347 air samples (total CRDS readings) were collected at the MC20 site and adjacent areas over six days. Statistics of the air sample readings are summarized in Table 5.2. Background levels of methane concentrations in the air were estimated to be 1.85-1.86 ppm and are depicted as blue in the layer above the ocean surface in Figure 5.5. These values compare favorably with background methane concentrations reported for land and coastal polar areas (Webster *et al*., 2015; Aref'ev *et al*., 2016; EPA, 2016). As such, any concentration of methane measured above 1.85 ppm was treated as an addition of methane to the atmosphere by an external factor, specifically measurable levels of seep gases at the ocean surface. The minimum concentration of methane measured during this survey was 1.77 ppm (recorded outside of the MC20 site area) while the maximum concentration of methane measured for this survey was 11.74 ppm (recorded directly over the collapsed jacket in an area we refer to as the "bubbling zone"). The maximum concentration was specifically recorded where gas and oil bubbles from the hydrocarbon plume were visibly reaching the ocean surface (Figure 5.6 and Figure 5.7). To identify the exact coordinates where the hydrocarbon plume was reaching the ocean surface each day (due to variability in ocean dynamics) the plumes were tracked, mapped, and video recorded from their source until the they reached the ocean surface using multibeam echosounders placed on the ship and remotely operated vehicle (ROV; see Chapter 3) and also using a high definition digital video camera mounted on the Bubblelometer chamber (see Chapter 4).

Table 5.2. Summary statistics for air samples analyzed by the CRDS-Picarro at the MC20 site during the survey in September 2018.

Statistics/sample	C_2H_2 (ppb)	CH_4 (ppm)	H_2O vapor (%)
Minimum	-1.3388	1.77	1.5695
Maximum	1,014.1512	11.74	7.8904
Mean	0.2539	1.93	3.5569
Median	-0.0104	1.86	3.3205
Standard Deviation	4.6284	0.27	0.7137

For visualization and practical purposes, methane concentration values below 1.90 ppm (background methane) were not included.

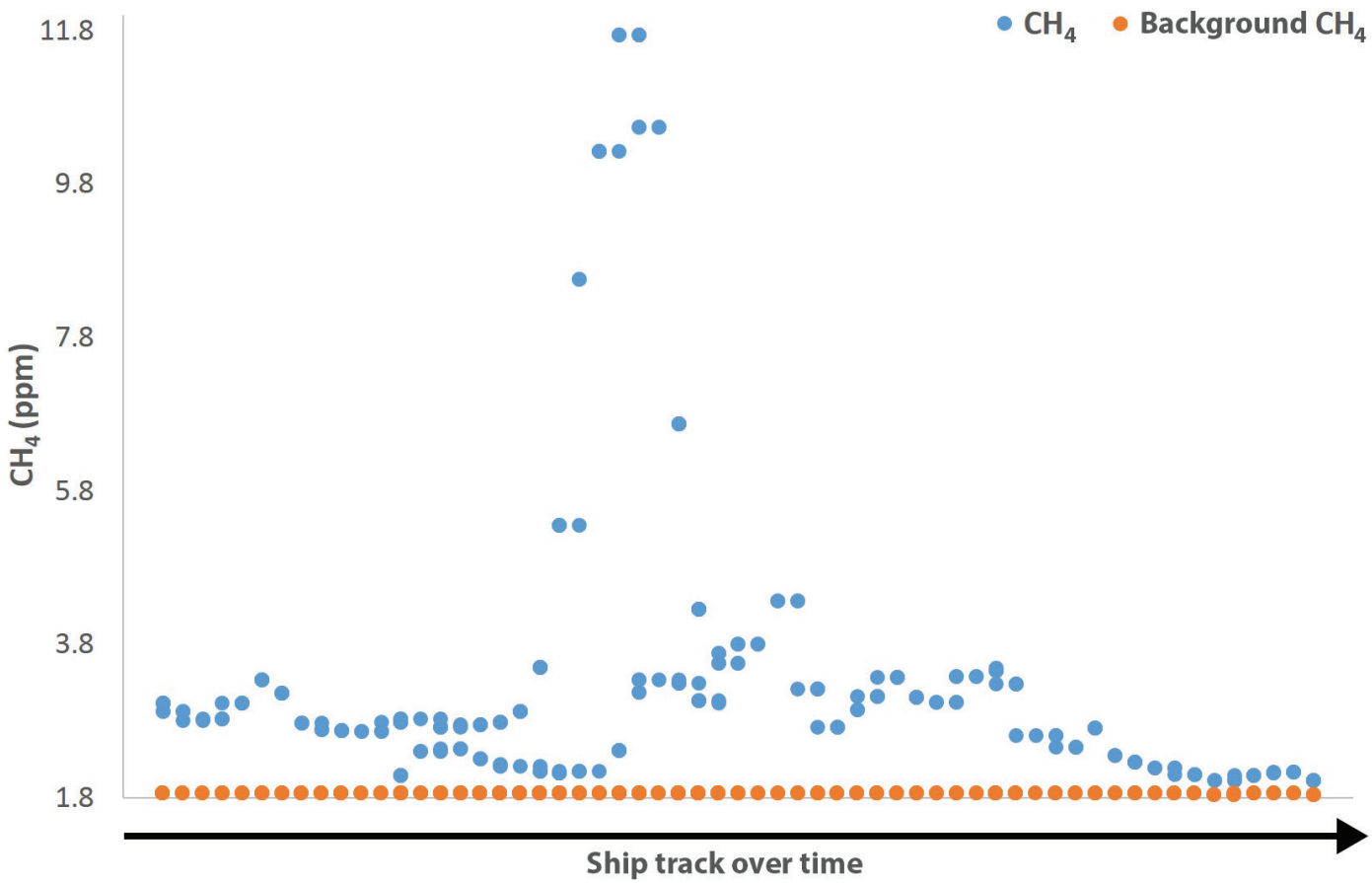

Figure 5.5. Graph example of air methane concentration (ppm) from one of the survey tracks in the study area.

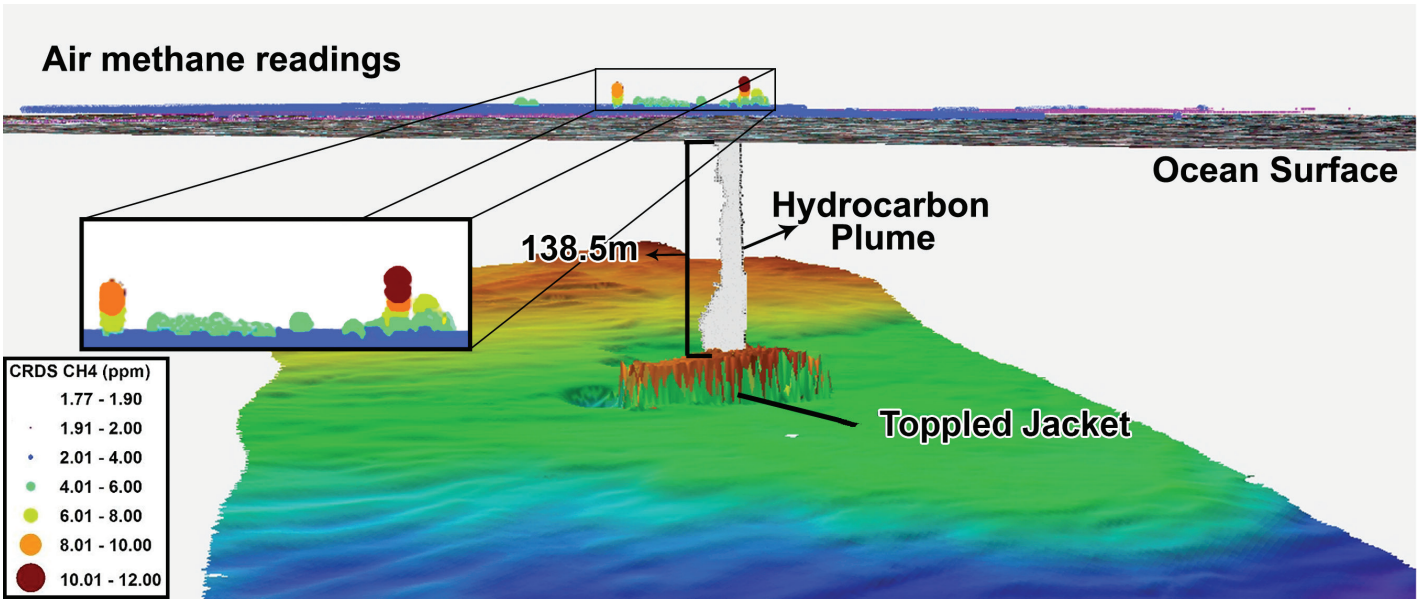

Figure 5.6. Diagram of the setting of the MC20 study area and where the CRDS operated air sampling for methane concentrations. Lower frame background colors denote bathymetry.

Surface Methane Flux

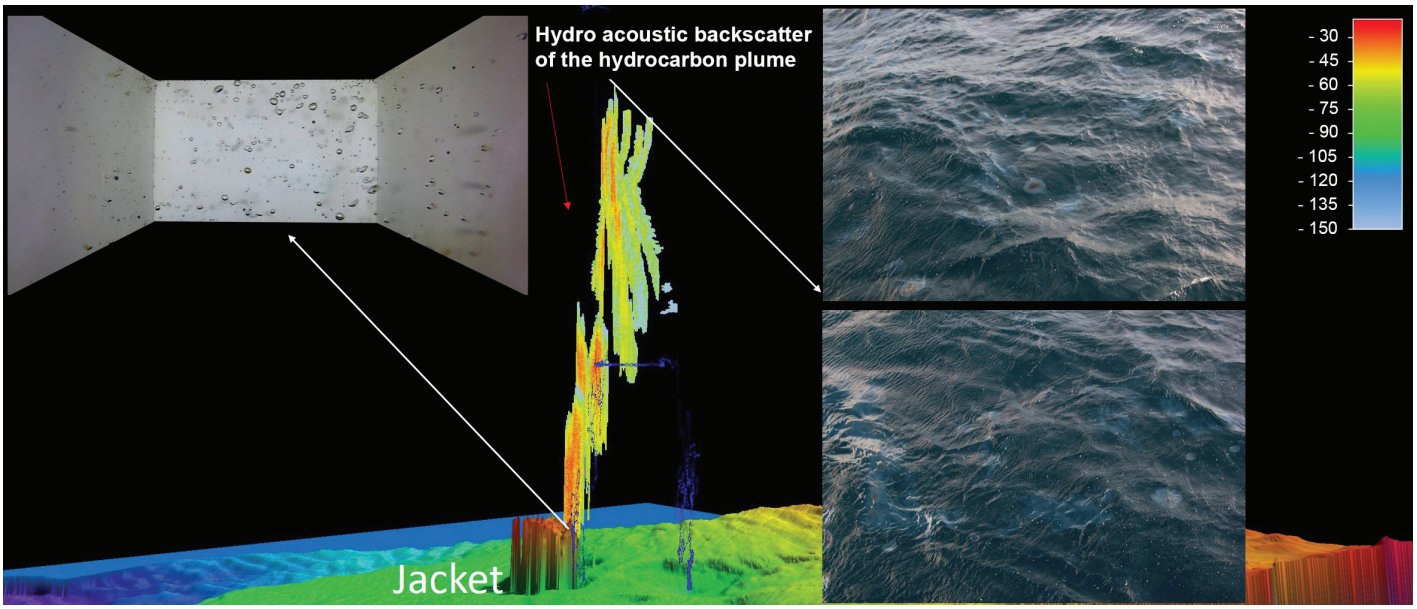

Figure 5.7. Diagram of the hydrocarbon plume and its composition in the water column and when it reaches the surface forming the "bubbling zone".

In terms of variability and location of elevated air methane concentrations over atmospheric background values, the highest concentrations (10-11.74 ppm) were found directly over the top of the northwest corner of the collapsed jacket (Figure 5.8), where the hydrocarbon plume visibly reached the ocean surface ("bubbling zone") during low wind periods (<5 knots). Methane concentrations between 4.0 to 10.0 ppm were frequently found in these low wind periods (<10 knots) but no farther than 200 m away of the visible "bubbling zone". In periods where the wind speed was greater than 15 knots, methane concentrations over the background threshold (>2.0 ppm) were detected as far as 1.2 km NNW from the jacket (Figure 5.9). In general, the highest methane concentrations detectable in the air (6.00 to 11.74 ppm) were observed in the morning during relatively calm wind conditions. When this occurred, low methane concentrations in the air (1.9-2 ppm) were measured not far from the bubbling zone (<100 m), which indicates a relatively rapid rise of methane towards the upper atmosphere (Chimney Effect). Conversely, in periods of relatively strong winds (>15 knots) methane that did reach the ocean surface was found to rapidly disperse, in this case towards the NNW, with average methane concentration values in the range of 2.0 to 4.0 ppm. Similar behavior in methane dispersion, under Gaussian Plume Dispersion modelled conditions for surface winds, have been described for methane emissions from landfills (Czepiel *et al*., 2003; Taylor, 2017).

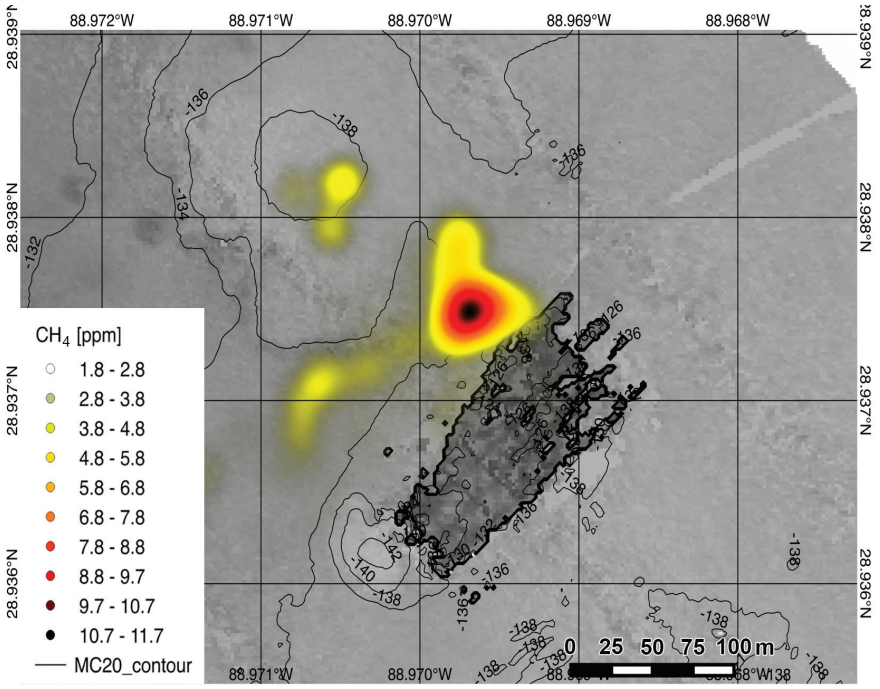

Figure 5.8. Heat map of the likelihood of encountering air methane concentration higher than the background threshold.

Hotspot analysis and resulting heat maps shows that there is a high probability of encountering relatively high methane concentrations in the air (>6 ppm) near the northwest corner of the toppled jacket, close to where the "bubbling zone" was most frequently located. Although there was some variability in the exact location where the hydrocarbon plume reached the ocean surface, the highest concentrations of methane were likely to be found in a 5 m diameter area near the water surface above the northwest corner of the collapsed jacket, independent of the observed ambient wind conditions. Two other areas, 100 m northwest and 100 m west of the jacket, also had a high likelihood for accumulation of elevated levels of air methane during moderate wind conditions (10-15 knots; Figure 5.10).

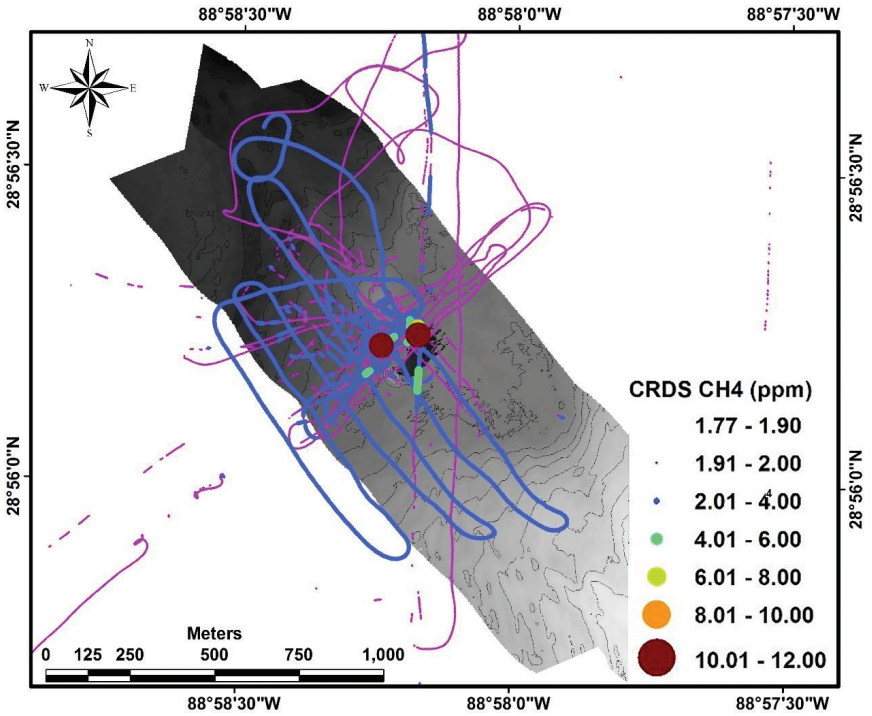

Figure 5.9. Detected air methane concentrations over the background threshold in the study area. Colored lines denote ship track during measurement collection where air methane concentrations exceeded 1.90 ppm. Greyscale denotes bathymetry with dark grey being shallower and light grey being deeper.

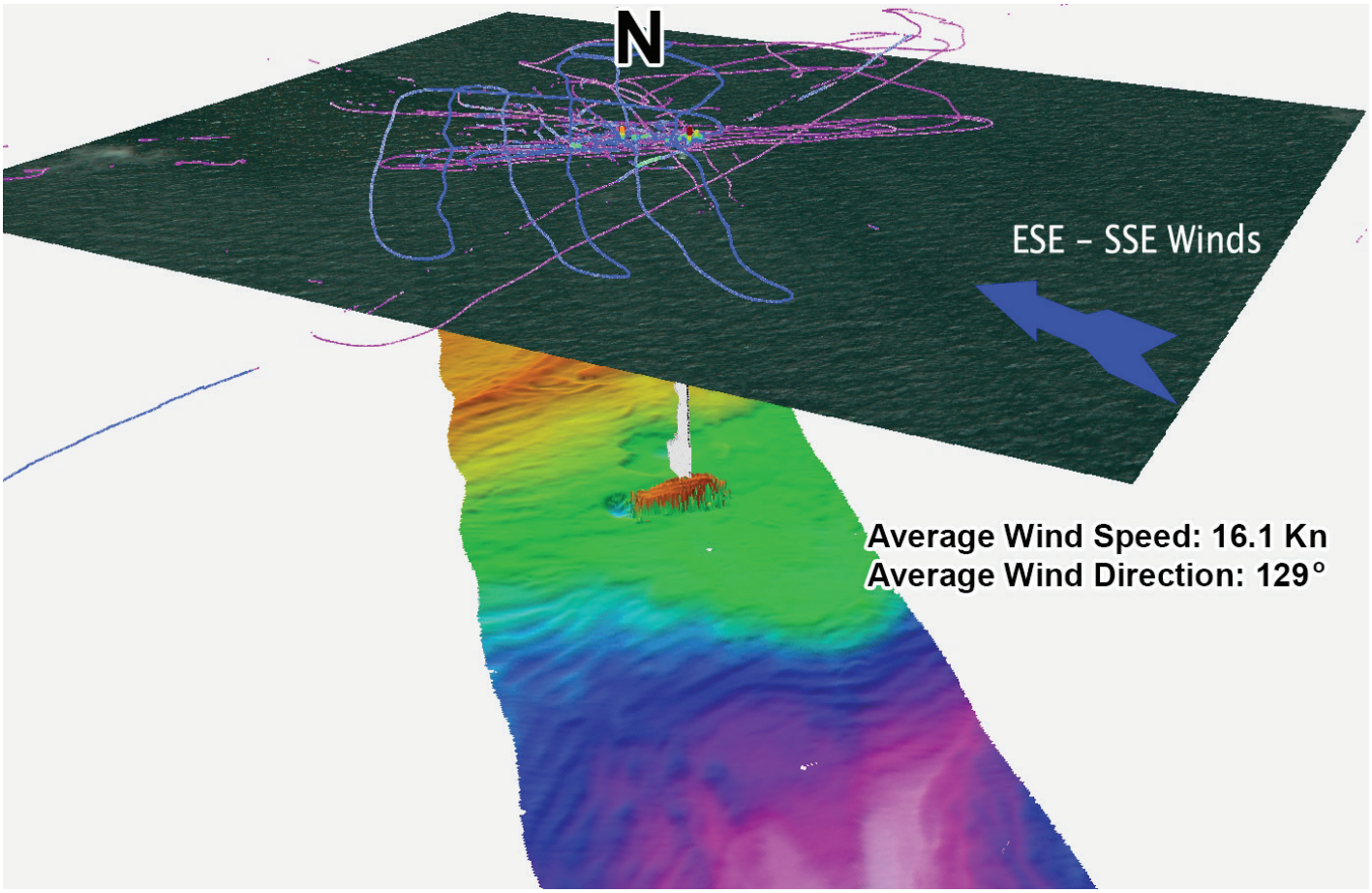

Figure 5.10. 3D view of the methane concentrations detected in the study area. Winds from the ESE and SSE dispersed the methane in the air towards land. Upper layer represents data from Figure 5.9 projected in 3D onto ocean floor bathymetry (color ramp) including a model of the plume rising through the water column (center, white).

Surface Methane Flux

5.3.1 Tracer Experiment and Plume Modeling

During the acetylene tracer experiment and the normal methane survey, background acetylene concentrations fluctuated between 0 to 0.8953 parts per billion (ppb). During the tracer experiment three major spikes on the CRDS for acetylene were detected with values that exceeded 200 ppb of acetylene in the air. The highest concentration of the acetylene tracer gas was detected only a few meters away from the raft deployment in the "bubbling zone" (1,024.1512 ppb) and after that, two more spikes on the tracer gas were detected downwind (11.16 knots, ESE) at approximately 310 m and 430 m away from the deployment site, respectively (Figure 5.11).

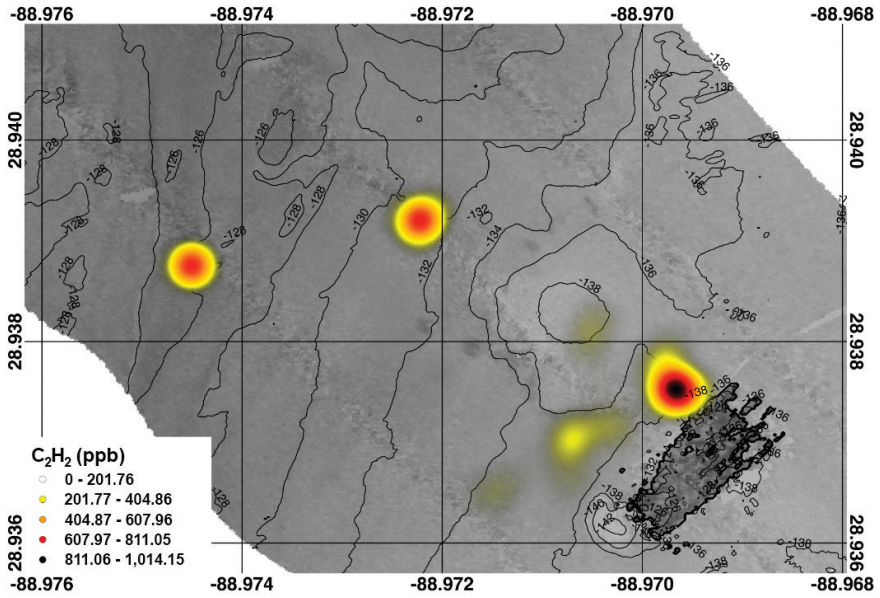

Figure 5.11. Heat map of the detected concentrations in air of acetylene during the tracer experiment.

Because the vessel R/V *Brooks McCall* was drifting downwind during the tracer study raft deployment there were at least three opportunities where the tracer spikes almost perfectly matched the relatively high measurements of methane in the air, further confirming that the source of additional methane in the air was sourced from the "bubbling zone" where the hydrocarbon plume was actively reaching the ocean surface (Figure 5.12).

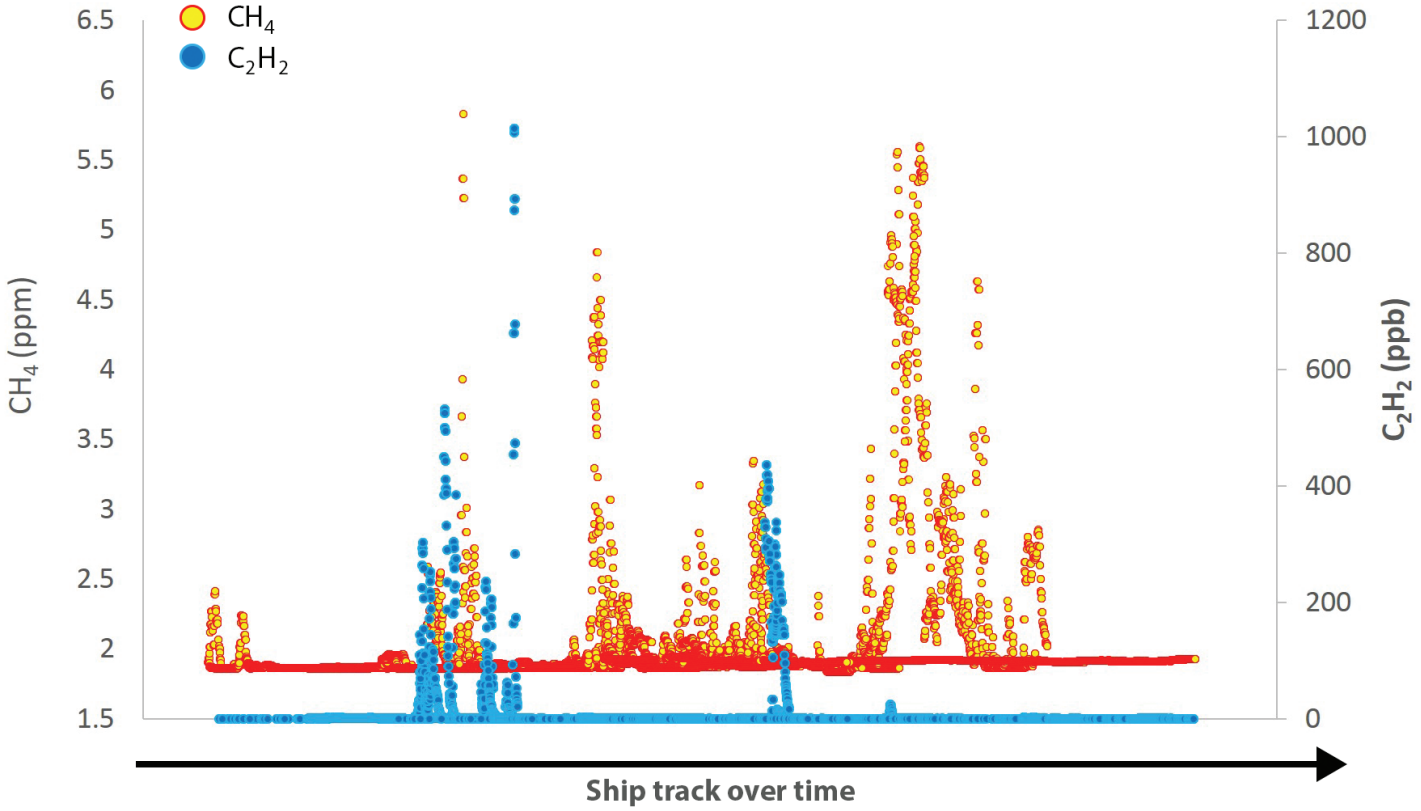

Figure 5.12. Methane and tracer gas (acetylene) air concentrations in the study area. Variations in concentrations are due to movement of the ship in and out of the atmospheric plume of methane and the tracer gas being driven by prevailing winds.

Tracer gas (acetylene) air concentration measurements were also employed to calibrate/validate the Inverse Plume Measurements method that is proposed to estimate methane gas flux estimates. Acetylene measurements are used as an input for the method in order to test its ability to predict the actual emission flux of the tracer gas (15 L/min). Wind direction and speed, along with a set 4,175 data points (acetylene concentrations and measurement locations), were used as input for the identification method. The average acetylene emission rate predicted by the method was equal to 0.26 g/s which approximately correspond to the actual release rate of 15 L/min. The results obtained with the tracer (acetylene) gas release, in a controlled manner, shows that the Inverse Plume Modeling method can be used to estimate methane emission rates.

The Inverse Plume Modeling combined with atmospheric methane concentrations was used to estimate methane flux rate from the hydrocarbon plume into the atmosphere. As for the estimation of the methane flux rate, preliminary estimates provide an average methane flux rate equal to 9 g/s with a standard deviation of 1.1 g/s. This corresponds to an emission flux that is higher than 0.7 tons/per day. However, it is important to note that this estimation method is prone to variability in wind direction and speed.

5.4 CONCLUSIONS

During the six full days of this survey mission at the MC20 study site, 1,562,347 georeferenced air samples (CRDS readings) were collected which allowed for confirmation that background values of atmospheric methane fluctuated between 1.85 and 1.90 ppm. During this survey abnormally high readings, including those significantly higher than background values of atmospheric methane concentrations, often occurred in proximity to surface waters over the toppled jacket. Atmospheric methane concentration in the vicinity of waters above the jacket typically fluctuated between 4 and 6 ppm. Even higher methane concentrations (>7 ppm) were detected in the surrounding areas where the gas hydrocarbon plume tended to reach the ocean surface (bubbling zone). The highest atmospheric methane concentration detected during the whole expedition was 11.74 ppm, which was measured nearly on top of the “bubbling zone” in a period of relatively low wind activity.

In terms of spatial analysis of the abnormal atmospheric methane concentration in the study site, the highest probability of encountering elevated methane concentrations was primarily observed to be directly on top of northwest corner of the collapsed jacket where hydrocarbon plumes tended to reach the ocean surface under relatively low wind conditions. Methane concentrations above background concentrations (>1.85 ppm) were detected up to a maximum of 1.2 km northwest of the “bubbling zone” during this survey.

Results of the tracer experiment for the study area confirm that the source of additional methane in the air was predominantly located near the area where MC20 hydrocarbon plumes reached the ocean surface, as well as where the raft with the tracer was deployed (adjacent to the bubbling zone). The final estimation of methane flux rate (0.7 tons per day) was made through the application of Inverse Plume Modeling coupled with established measurements of atmospheric methane concentrations.

Our modeled flux rate can be put into context by comparing it to the amount of atmospheric methane released by the Deepwater Horizon (DWH) event, where only 0.01%, or 50 tons, of the estimated 500,000 tons of released methane reached the atmosphere (Joye *et al*., 2011; Yvon-Lewis *et al*., 2011). By dividing that estimated 50 tons of atmospheric methane release by the 83 days the spill was active, we calculate an estimated daily surface methane flux of 0.6 tons per day for DWH. It is interesting to note that although the total daily methane flux during DWH was orders of magnitude higher than that occurring at MC20, because of the relatively shallow depth at MC20 the daily atmospheric methane flux is actually greater than the daily atmospheric discharge that occurred during DWH. Following this line of reasoning we calculate that atmospheric discharge of methane at MC20 equals the total atmospheric methane discharge during DWH approximately every 71.4 days.

5.5 REFERENCES

Aref'ev, V.N., R.M. Akimenko, F.V. Kashin, and L.B. Upenek. 2016. Background Component of Methane Concentration in Surface Air (Obninsk Monitoring Station). Izvestiya, Atmospheric and Oceanic Physics 52(1): 42-50. doi: https://doi.org/10.1134/S0001433815060031

Briggs, G.A. 1965. A plume rise model compared with observations. Journal of the Air Pollution Control Association 15(9): 433-438. doi: https://doi.org/10.1080/00022470.1965.10468404

Chen, J. 2018. From the seep to the surface: the ascent and dissolution of methane bubbles in the ocean. Geophysical Research Letters. arXiv:1802.09162

Czepiel, P.M., J.H. Shorter, B. Mosher, E. Allwine, J.B. McManus, R.C. Harriss, C.E. Kolb, and B.K. Lamb. 2003. The influence of atmospheric pressure on landfill methane emissions. Waste Management. Volume 23(7): 593-598. doi: https://doi.org/10.1016/S0956-053X(03)00103-X

EPA. 2016. Climate Change Indicators in the United States: Atmospheric Concentrations of Greenhouse Gases. Climate Change Indicators Website. U.S. Environmental Protection Agency, Climate Change Indicators, Greenhouse Gases. Online: https://www.epa.gov/climate-indicators/climate-change-indicators-atmospheric-concentrations-greenhouse-gases (Accessed 20 May 2019)

Joye, S.B., I.R. MacDonald, I. Leifer, and V. Asper. 2011. Magnitude and oxidation potential of hydrocarbon gases released from the BP oil well blowout. Nature Geoscience 4: 160-164. doi: https://doi.org/10.1038/ngeo1067

Kormi, T., S. Mhadhebi, N. Bel Hadj Ali, T. Abichou, and R. Green. 2018. Estimation of fugitive landfill methane emissions using surface emission monitoring and Genetic Algorithms optimization. Waste Management 72: 313-328. doi: https://doi.org/10.1016/j.wasman.2016.11.024

Mønster, J.G., J. Samuelsson, P. Kjeldsen, C.W. Rella, C. Scheutz. 2014. Quantifying methane emission from fugitive sources by combining tracer release and downwind measurements - A sensitivity analysis based on multiple field surveys. Waste Management 34(8): 1416-1428. doi: https://doi.org/10.1016/j.wasman.2014.03.025

Mønster, J., J. Samuelsson, P. Kjeldsen, and C. Scheutz. 2015. Quantification of methane emissions from 15 Danish landfills using the mobile tracer dispersion method. Waste Management 35: 177-186. doi: https://doi.org/10.1016/j.wasman.2014.09.006

Socolofsky, S.A., and E.E. Adams. 2005. Role of slip velocity in the behavior of stratified multiphase plumes. Journal of Hydraulic Engineering 131(4): 273-282. doi: https://doi.org/10.1061/(ASCE)0733-9429(2005)131:4(273)

Taylor, D. 2007 Atmospheric Dispersion Modeling to Inform A Landfill Methane Emissions Measurement Method. Thesis Dissertation. UC Berkley.

Webster K.D., J.R. White, and L.M. Pratt. 2015. Ground-Level Concentrations of Atmospheric Methane in Southwest Greenland Evaluated Using Open-Path Laser Spectroscopy and Cavity-Enhanced Absorption Spectroscopy. Arctic, Antarctic, and Alpine Research 47(4):599-609. doi: https://doi.org/10.1657/AAAR0014-051

Yvon-Lewis, S.A., L. Hu, and J. Kessler. 2011. Methane flux to the atmosphere from the Deepwater Horizon oil disaster. Geophysical Research Letters. Volume 38: L01602. doi: https://doi.org/10.1029/2010GL045928

Chapter 6
Chemical Analysis of Gas Samples Collected from the MC20 Leak in the Northern Gulf of Mexico

Michael A. Gaskins[1], Bernie B. Bernard[1], and Jim Brooks[1]

Bubblometer. Credit: NOAA NOS/NCCOS

ABSTRACT

An oil sheen and gas bubbles have been observed to be continuously released from the seabed in MC20 several kilometers offshore of Louisiana. Gas, oil, sediment, and water samples were collected by scientists and technical staff through a collaborative effort by NOAA, BSEE, and TDI-Brooks International aboard the R/V Brooks McCall *in early September 2018. The hydrocarbons were extracted and then analyzed via gas chromatography and isotope ratio mass spectrometry at B&B Laboratories in College Station, Texas. The concentrations and carbon isotopic ratios of the light hydrocarbon gases were determined to discern that the gas originates from a thermogenic release.*

Citation for chapter
Gaskins, M., B. Bernard, and J. Brooks. 2019. Chapter 6: Chemical Analysis of Gas Samples Collected from the MC20 Leak in the Northern Gulf of Mexico. pp. 71-78. In: A.L. Mason, J.C. Taylor, and I.R. MacDonald (eds.), An Integrated Assessment of Oil and Gas Release into the Marine Environment at the Former Taylor Energy MC20 Site. NOAA National Ocean Service, National Centers for Coastal Ocean Science. NOAA Technical Memorandum 260. Silver Spring, MD. 147 pp. doi: 10.25923/kykm-sn39

[1] *TDI-Brooks International. College Station, TX.*

Gas Chemistry

6.1 INTRODUCTION

The molecular and isotopic compositions of the hydrocarbons in the gas bubbles collected by a Remotely Operated Vehicle (ROV) in the plumes at the MC20 site are the main focus of this chapter; these data are used in concert with the hydrocarbon constituents of the oil to characterize and identify the source of the release observed at the MC20 site. The methodology and equipment used to collect these gas samples are outlined in Chapter 7.

6.1.1 Overview

Offshore oil and gas exploration began late in the 19th century and has increased substantially as the challenges of exploring, drilling, and producing subsea hydrocarbon sources are overcome by innovative technologies and methodologies (Austin *et al*., 2008). Since then, countless scientists have devoted their careers to collecting and characterizing hydrocarbons in sediment, water, and gas samples collected to understand the intricate details and patterns of nature to identify and characterize what reservoirs exist beneath the ocean floor.

The light hydrocarbon gases that are of most interest to geochemists range in size and molecular weight from methane (C_1) to *n*-pentane (C_5). These gases are the products of the thermocatalytic cracking of kerogen from source rocks and larger hydrocarbons in petroleum reservoirs over time (Lerche, 1991). Interestingly, marine microbial communities also produce light hydrocarbons through anaerobic metabolic pathways that have evolved over millions of years to adapt to the availability of resources in the environments in which they live beneath the sea floor (Ermler *et al*., 1997; Ferry, 2011). Gases from thermogenic and biogenic sources often mix as the gases migrate, which can alter the light hydrocarbon molecular composition measured in a marine gas sample. Therefore, deriving the main source of a marine light hydrocarbon gas between migrating thermogenic gases or those produced by biogenic gases produced by local microbiota can be quite challenging. Numerous proxies have been developed by geochemists and accepted as industry standards to differentiate between these two potential light hydrocarbon sources. The same methodologies and proxies can also be used to characterize and provide a molecular "fingerprint" for thermogenic gas produced by a well and can even be used to link it to an associated petroleum reservoir.

Since 1996, TDI-Brooks International has conducted offshore Surface Geochemical Exploration (SGE) studies all over the world and employs two main proxies to determine the origin of marine gases collected - quantities and proportionality of the C_1-C_5 alkane gases, and their carbon isotopic ratios. The quantities of the C_1-C_5 alkane gases are plotted in the Gas Wetness and Triangular Plots and are compared against a worldwide database of gas samples of known origin. The C_1-C_5 carbon isotopic ratios are compared to gas samples of known origin in standard Bernard and Faber Plots. The sum of information learned by these two proxies and their mathematical similarities with other gas samples from around the world are used to interpret the source of a marine gas sample.

6.1.2 Concentrations of Light Hydrocarbon Gases

One of the earliest diagnostic tools or proxies used to characterize marine gas samples was to determine the concentrations and relative ratios of the C_1-C_5 constituents via headspace gas chromatography (HS-GC) configured with a flame ionization detector (FID).

The gases of particular interest in marine samples are: methane, ethene, ethane, propene, propane, isobutane, butenes, *n*-butane, neopentane, isopentane, and *n*-pentane. Methane is typically the predominant hydrocarbon constituent in gas samples and is often several orders of magnitude greater than the C_{2+} gases regardless if the gas is of biogenic and/or thermogenic origin. Trace amounts of C_{2+} alkane gases may be present in marine sediments due to microbial metabolism, but typically do not exceed a few parts per million by volume (ppmV) unless the adjacent migration of thermogenic gas is locally observed. The presence of

alkene, otherwise known as olefin, and C_1-C_3 alkane gases indicates biogenic contribution to a marine sediment gas sample - especially when accompanied by an absence of C_4-C_5 alkane gases. The presence of thermogenic gas is often indicated by a continuous C_2-C_5 alkane pattern that increases in thermogenicity with increasing concentrations of C_4-C_5 alkanes.

However, it is common for thermogenic or biogenic gases to be diluted as they encounter other gases (primarily nitrogen) in the environment which proportionally dilutes all of the C_1-C_5 gases; thus, determining the source of a diluted gas becomes increasingly more difficult if the C_{2+} components of significantly less abundances relative to methane are diluted until they are no longer detectable. A mature thermogenic deep well gas may be diluted during migration such that some or all of the C_{2+} components are miniscule or even absent and may potentially be misinterpreted as a biogenic gas.

6.1.3 Carbon Isotopic Ratios of Light Hydrocarbon Gases

Quantifying C_1-C_5 gases and their relative proportionality may not provide sufficient insight to distinguish the source(s) of the hydrocarbon constituents of a marine gas sample. Geochemists have employed the use of carbon isotope ratio mass spectrometry (IRMS) since the 1950s to determine the $^{13}C/^{12}C$ ratios of rocks and gases to provide clues about their origin. In order to normalize carbon isotopic ratios, geochemists have accepted the carbon dioxide $^{13}C/^{12}C$ ratio from an isotopically heavy Cretaceous belemnite from South Carolina as the reference point with which to compare and report other carbon isotopic ratio measurements. Carbon isotope ratio data are typically represented in “parts per mil” (denoted by ‰) on the PeeDee Belemnite (PDB) scale and are typically negative indicating that they are isotopically lighter than that standard material.

Microbiological enzymatic processes show a slight preference of ^{12}C to ^{13}C during carbon consumption and are typically isotopically “lighter” as a result. Gases that are produced from the thermocatalytic cracking of hydrocarbons in a reservoir are also isotopically lighter than are their carbon parents due to cracking kinetics of bond cleavages, but are slightly enriched in ^{13}C as compared to biogenically produced gases and are thus found to be isotopically “heavier.” In addition, the $^{13}C/^{12}C$ ratio decreases or becomes lighter as the number of carbons decrease in light hydrocarbon gases of thermogenic origin. However, fractionation may occur which alters the isotopic ratios of the hydrocarbons as the gas migrates and mixes with other sources and is exposed to new physical and chemical conditions in nature. The sum of these phenomena provides a distinct carbon isotopic “fingerprint” that facilitates source identification of a marine gas sample.

6.2 METHODS

Three gas samples were taken by an ROV that collected gas bubbles from the plumes observed at the MC20 site as described in Chapter 7 of this report. The gas samples were transferred to foil gas bags with a valve containing a septum to allow subsampling with a gas-tight syringe. In addition, 15 sediment and 4 water column samples were collected and immediately transferred to pint sized aluminum cans for headspace gas analysis. The cans were gently agitated to break up the sediment and release any interstitial gases into the headspace of the container. A septum was attached to the top of the container to allow the gas to be subsampled and analyzed using a gas-tight syringe.

6.2.1 Headspace Gas (HS) Analysis by GC/FID

Triplicate 10 µL aliquots of each gas bag sample were injected via a gas-tight syringe onto a HS-GC/FID configured with a porous layer open tubular (PLOT) column to separate and quantitate the C_1-C_5 light hydrocarbon gases. Single 1 mL injections of each of the 19 sample cans containing water or sediment were analyzed. External standards containing all of the analytes of interest were used to calibrate the HS-GC prior to sample analysis and to verify the calibration throughout the analysis.

6.2.2 Carbon Isotopic Ratio Analysis by GC/IRMS

Multiple injections of each gas bag sample of various injection volumes were introduced into the GC/IRMS configured with a PLOT column to separate the C_1-C_5 hydrocarbon gases and determine their carbon isotopic ratios. A reference carbon dioxide standard (-37.5 ‰ versus PDB) was used linearize the detector to ensure that the carbon isotopic ratio is consistent throughout the optimum detection range and as an internal reference standard for each injection. An external standard containing all of the C_1-C_5 analytes of interest of known carbon isotopic ratios was used to verify the PDB accuracy of the GC/IRMS.

6.3 RESULTS AND DISCUSSION

The data for the two proxies were collected by the previously described methodologies and were imported into multiple models or plots typically utilized for gas source determination by TDI-Brooks International. The averages of light hydrocarbon compositions of the three samples collected from the plume at the MC20 site are shown in Table 6.1 based on HS-GC/FID analysis.

Headspace analysis of the sample cans containing water from the rosette sampler and boxcore samples contained trace amounts of methane, but minimal levels of C_{2+} hydrocarbons.

Table 6.1. Hydrocarbon composition of MC20 gases.

	Plume Sample 1 (9/3/18)	Plume Sample 2 (9/5/18)	Plume Sample 3 (9/3/18)	MW-1 from Macondo MC252*
Methane (C_1)	92.7%	94.9%	94.8%	82.5%
Ethene	0.00%	0.00%	0.00%	NA
Ethane (C_2)	3.45%	2.48%	2.51%	8.3%
Propene	0.00%	0.00%	0.00%	NA
Propane (C_3)	2.40%	1.69%	1.75%	5.3%
i-butane (C_4)	0.51%	0.36%	0.38%	0.97%
Butenes	0.00%	0.00%	0.00%	NA
n-Butane (C_4)	0.58%	0.39%	0.40%	1.9%
neo-Pentane (C_5)	0.01%	0.00%	0.01%	NA
i-Pentane (C_5)	0.20%	0.12%	0.12%	0.52%
n-Pentane (C_5)	0.12%	0.06%	0.07%	0.52%

* Reported by Reddy *et al.*, 2011

6.3.1 Gas Wetness Plot

The most primitive model used to determine the origin of a marine gas sample is the "Gas Wetness Plot" which compares the total alkane gases to the sum of C_{2+} alkane gases in ppmV. The data for three gas samples and 19 canned samples are plotted in the Gas Wetness Plot in Figure 6.1.

The percentage lines of the Gas Wetness Plot denote the percent by volume proportions of the constituents of a gas sample. The volume of a gas is proportional to the quantity in moles and can be used to determine mole fractions of each light hydrocarbon in a gas sample. Based on the mathematical relationships depicted in this plot, a gas sample is likely to be thermogenic if the C_{2+} component is greater than 1 % of the molecular composition of a gas sample provided that the sum of the alkane gases in the sample is greater than those observed in the background. The color-coded dots represent well gas samples from TDI-Brooks International that have been diluted by factors of 100, 1,000, and 10,000 for comparison.

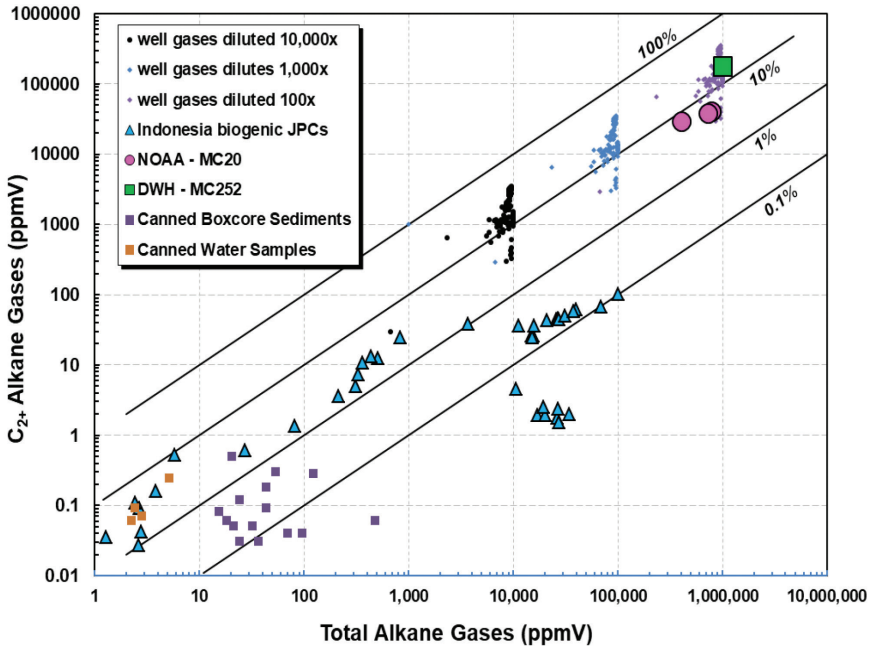

Figure 6.1. Gas Wetness Plot.

Note that only the sums of the C_1-C_5 and C_{2+} components are affected by dilution of the gas sample as the proportionality of the C_1-C_5 is conserved. The light blue triangles represent Jumbo Piston Cores (JPCs) that were acquired by TDI-Brooks in Indonesia that only contain biogenic gas most likely derived from anaerobic microbiological activity and the reduction of olefin (alkene) gases to alkanes; these data may potentially be misinterpreted as thermogenic due to their slightly elevated C_{2+} expression, but are significantly different than the proportionality expressed by thermogenic well gases. Gas data from samples collected from the water column during the MC252 Deepwater Horizon release (Reddy *et al*., 2011) have also been included for comparison and are represented by a green square in this and subsequent plots.

According to this model, the three MC20 gas samples are >5 % C_{2+} alkanes which suggests that they are very wet and almost exclusively comprised of thermogenic gas. In addition, the absence of olefin gases suggests that little to no microbial contribution was made to these samples. The canned water and sediment samples contained traces of dry biogenic gases due to the miniscule concentrations or absence of C_{2+} hydrocarbons.

6.3.2 Triangle Plot

The Triangle Plot was developed by TDI-Brooks International to further scrutinize and characterize the wetness of a marine gas sample by comparing the C_2+C_3 alkanes to the C_4+C_5 alkanes. Local microbes do not produce significant quantities of C_4 and C_5 alkanes in marine sediment environments. Therefore, this model clearly differentiates biogenic and thermogenic gas sources and determines if any mixing has occurred by highlighting the abundance of C_2 and C_3 alkanes to their absence of C_4 and C_5 alkanes. The data for three gas samples are plotted in the Triangle Plot in Figure 6.2.

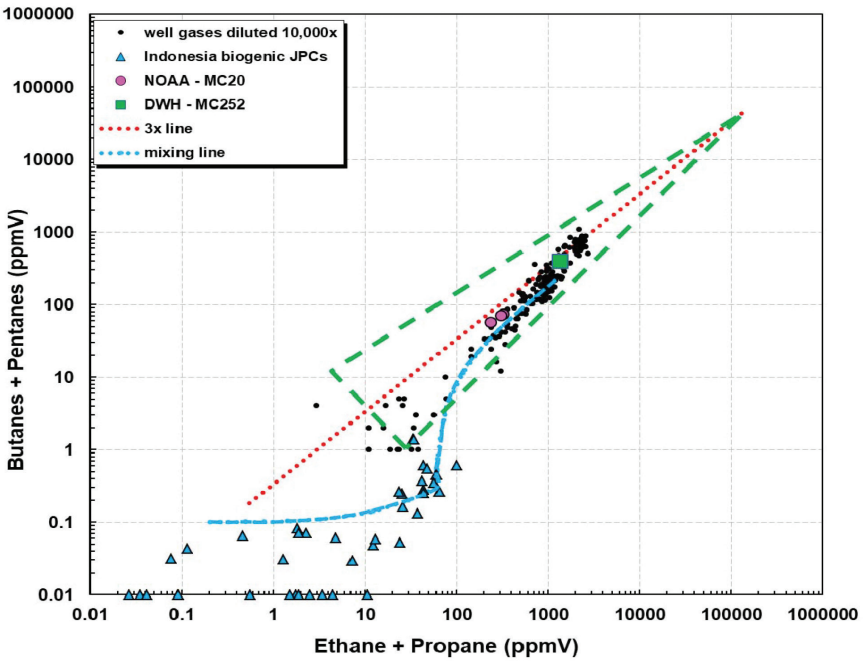

Figure 6.2. Triangle Plot developed by TDI-Brooks International.

In nature, wet well gases exhibit approximately three times as much C_2+C_3 alkanes as the C_4+C_5 alkanes; this trend is represented by the dotted red line in the Triangle Plot. The green dashed triangle represents the region where unfractionated thermogenic gases would plot. The blue dashed line, known as the "mixing line", represents the mathematical relationship on a logarithmic scale if a 100% thermogenic gas was increasingly diluted by a biogenic gas until it approaches 100% biogenic gas (i.e., 99% thermogenic/1% biogenic, etc.). Note that the blue mixing line intersects with the green triangle when the sample is comprised of approximately 98% biogenic and 2% thermogenic gases. The same known thermogenic well gases (including MC252 Deepwater Horizon) and biogenic JPCs from the Gas Wetness Plot have also been included in this Triangle Plot for comparison.

This model shows that the three MC20 gas samples are 100% thermogenic and are void of biogenic input and are consistent with data from produced well gases from around the world.

6.3.3 Bernard Plot

The Bernard Plot (Bernard, 1978) carries the same ideologies of the Triangle Plot even further and includes another valuable parameter to characterize and determine the source(s) of a marine gas sample, the $^{13}C/^{12}C$ ratio of methane ($\delta^{13}C$). Because the C_1-C_3 alkane gases can be produced biogenically and/or thermogenically, the relationship of interest in this model is between the methane carbon isotopic ratio and the quotient of $C_1/(C_2+C_3)$ alkanes. As a result, the Bernard Plot can be used to determine the proportionality of the predominant source(s) of a marine gas sample. The three gase samples collected at the MC20 site were analyzed by GC/IRMS and their methane carbon isotopic ratio was used to generate the Bernard Plot in Figure 6.3.

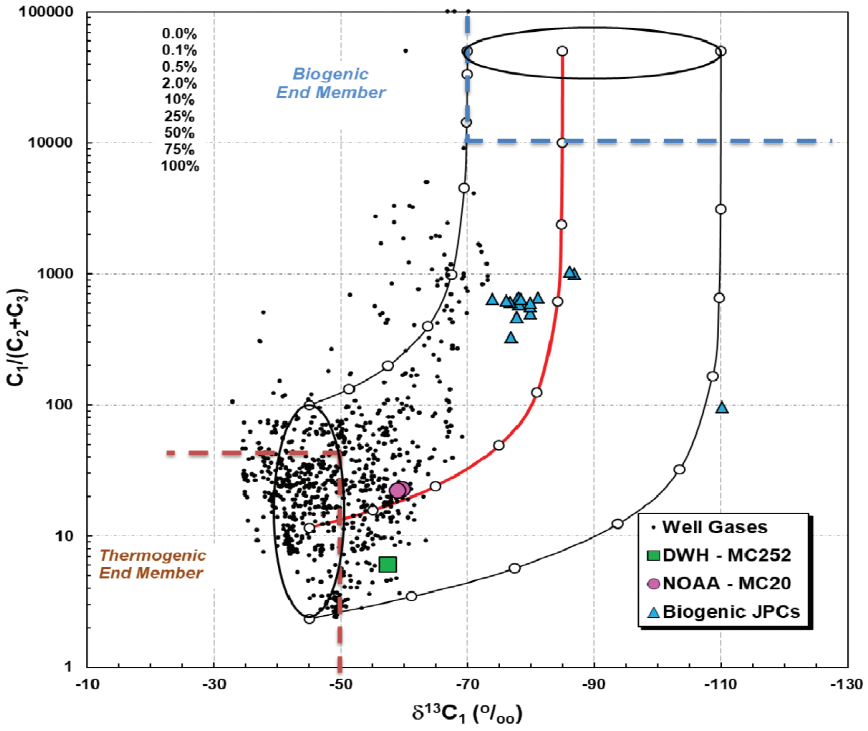

Figure 6.3. Bernard Plot developed by Dr. Bernie Bernard of TDI-Brooks International.

Biogenic gases are predominantly comprised of methane which equates to $C_1/(C_2+C_3)$ ratios of >1,000 and exhibit a carbon isotopic ratio more negative than -60 ‰ for methane. Gases of purely thermogenic origin have $C_1/(C_2+C_3)$ ratios <50 and carbon isotopic ratios more positive than -60‰ for methane. Thermogenic well gases from the TDI-Brooks International database were included in Figure 6.3 for reference. Note that as thermogenic gases are diluted with biogenic or other gases that the $C_1/(C_2+C_3)$ ratio increases by several orders of magnitude and the carbon isotopic ratio becomes slightly more negative.

The $C_1/(C_2+C_3)$ ratios for the three MC20 gas samples are 15.9, 22.8, and 22.2, respectively. The carbon isotopic ratios for methane for these three samples are -59.1‰, -59.7‰, and -59.0‰, respectively. The $C_1/(C_2+C_3)$ ratio and methane carbon isotopic ratio for the gas produced my MC252 Deepwater Horizon are 6.1 and -57.5‰, respectively. Therefore, these three gas samples are exclusively thermogenic based on these data and compared with data from produced well gases from around the world including that of MC252.

6.3.4 Faber Plots

Eckhard Faber introduced a model to study the empirical relationships of the carbon isotopic ratios of the C_1-C_3 alkane gases to determine source and maturity of a thermogenic gas (Faber, 1987). In nature, the carbon isotopic ratios of methane, ethane, and propane are related and typically become isotopically heavier (more positive) with increasing maturity of the hydrocarbon source from which they are derived. In addition, these plots can be used to determine if a well gas originated from one or more sources and the overall maturity of the gas. This mathematical relationship is termed as vitrinite reflectance and is denoted by "R_o". The $\delta^{13}C$ data for the C_1 and C_3 alkanes are plotted in two Faber Plots in Figure 6.4 and Figure 6.5, respectively.

The red trend line represents the mathematical relationship described by Faber in the debut publication of this model. It was originally believed that single-sourced gases would plot on this empirical trend line, but well gas data from around the world proves that this is not always the case; this phenomenon has yet to be understood,

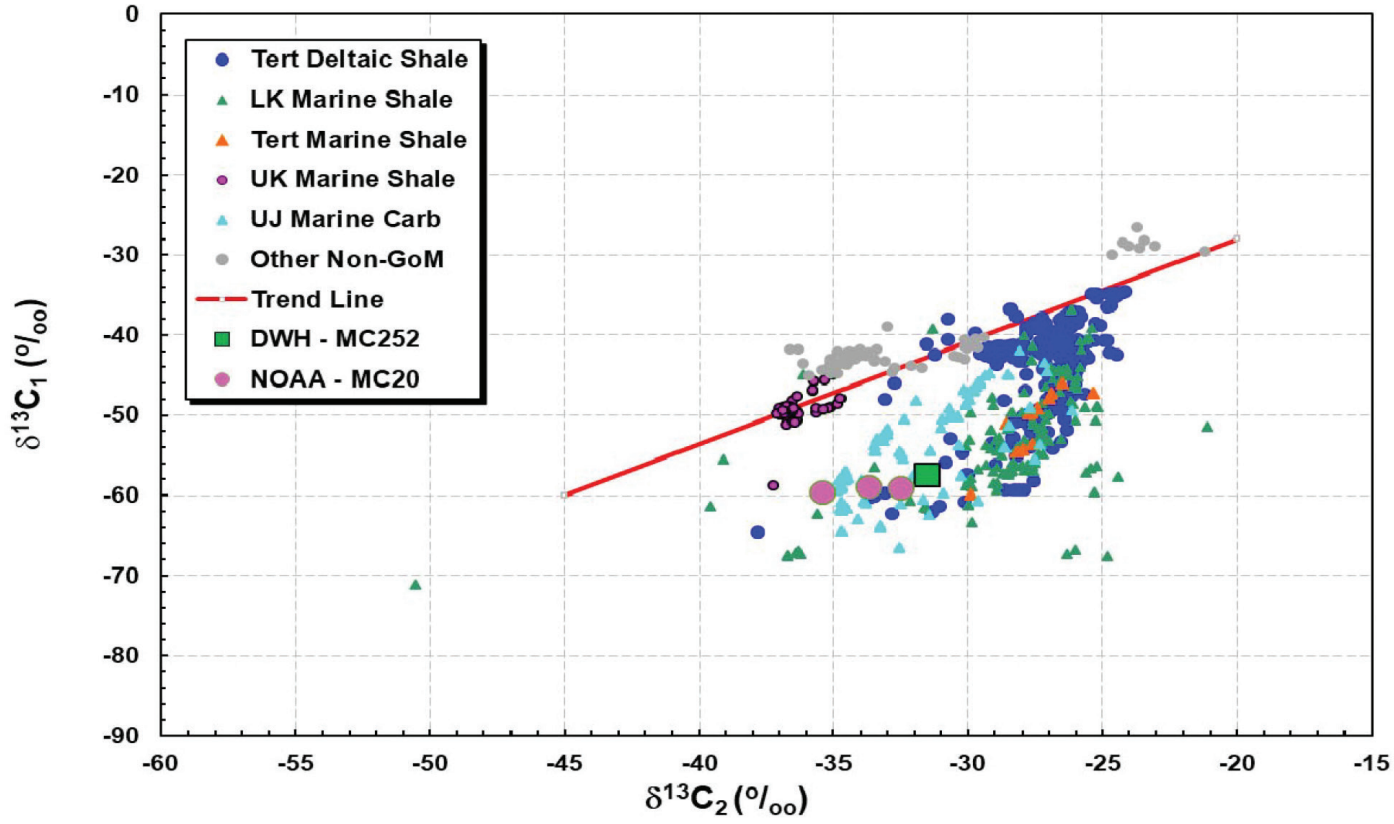

Figure 6.4. Faber Plots depicting $\delta^{13}C$ relationship of methane (C_1) and ethane (C_2).

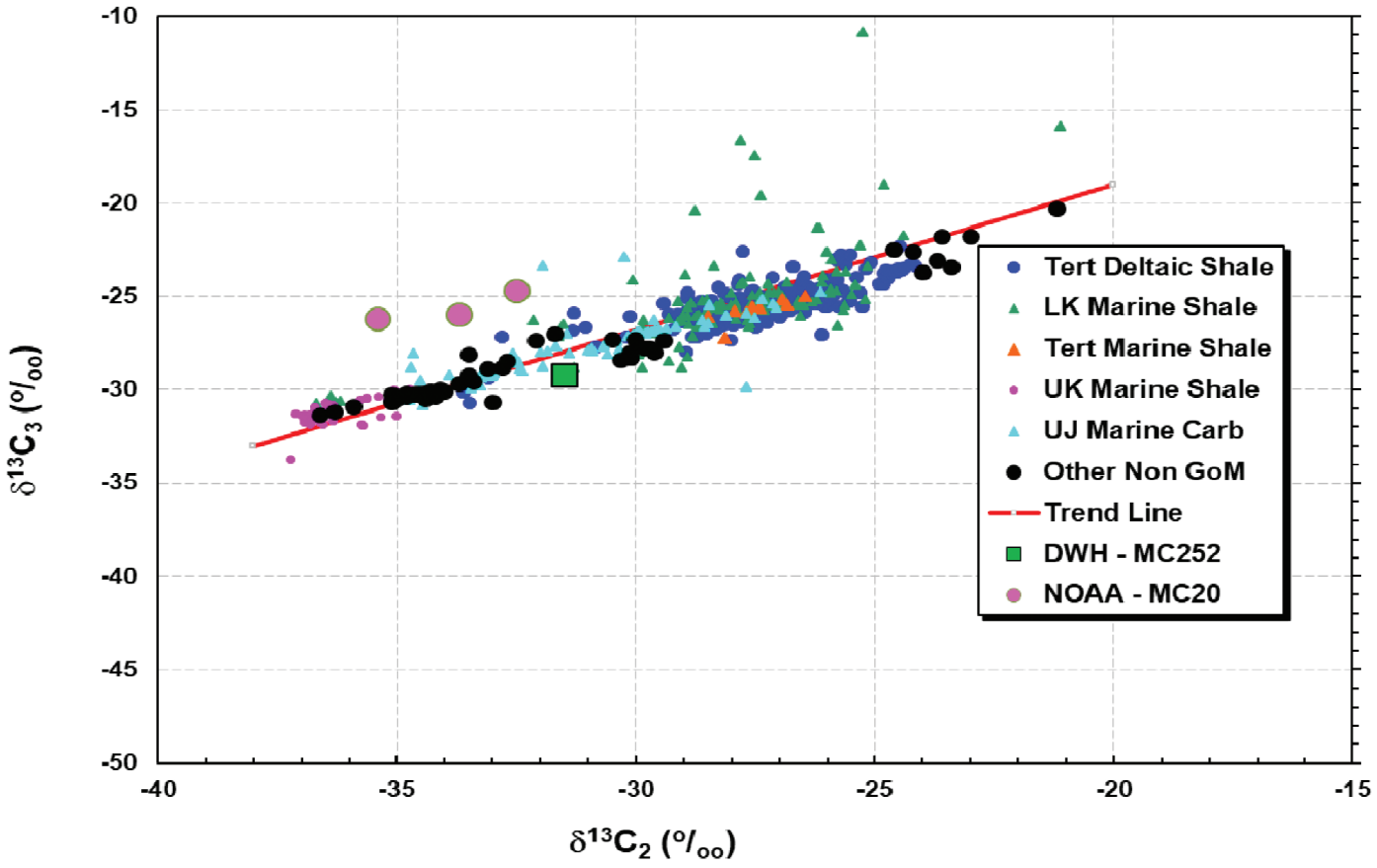

Figure 6.5. Faber Plots depicting $\delta^{13}C$ relationship of methane (C_1) and propane (C_3).

but proves to be a reliable method to describe the diversity within and between gas families and is extremely useful in identifying the source(s) of a gas sample. Gas sources are commonly associated with a specific petroleum reservoir and can provide valuable information to identify the source and nature of a hydrocarbon release. For this reason, well gases from a TDI-Brooks International database were included in these plots to provide a visual representation of gases originating from various thermogenic sources from around the world including MC252.

The Faber model clearly shows that not only is the MC20 gas thermogenic, but also that it originated from a similar Upper Jurassic Marine Carbonate gas source (UJ Marine Carbonate on the Faber Plots) that has been previously described to be associated with the same petroleum reservoir as MC252 Deepwater Horizon. Interestingly, the biomarker fingerprint of the oil collected at MC20 suggests that it originated from a similar mid-Cretaceous Shale source as the oil from MC252 Deepwater Horizon (see Chapter 7 of this report).

The chemical and isotopic composition of the gas samples collected at MC20 suggests the gas is solely thermogenic and is likely a continuous release as it has not been significantly mixed or fractionated as it exits from a mature petroleum reservoir, migrates through the sediment, and bubbles through the water column.

6.4 REFERENCES

Austin, D.E., T. Priest, L. Penney, J. Pratt, A.G. Pulsipher, J. Abel and J. Taylor. 2008. History of the offshore oil and gas industry in southern Louisiana. Volume I: Papers on the evolving offshore industry. U.S. Dept. of the Interior, Minerals Management Service, Gulf of Mexico OCS Region. New Orleans, LA. OCS Study MMS 2008-042. 264 pp.

Bernard, B. 1978. Light Hydrocarbons in Marine Sediments. Technical Report 78-5-T. PhD Thesis, Texas A&M Press, College Station, TX. 144 pp.

Ermler U., W. Grabarse, S. Shima, M. Goubeaud, and R.K. Thauer. 1997. Crystal Structure of Methyl-Coenzyme M Reductase: The Key Enzyme of Biological Methane Formation. Science 278(5342): 1457-1462. doi: https://doi.org/10.1126/science.278.5342.1457

Faber, E. 1987. Zur Isotopengeochemie gasförmiger Kohlenwasserstoffe. Erdöl Erdgas und Kohle 103: 210-218.

Ferry, J.G. 2011. Fundamentals of methanogenic pathways that are key to the biomethanation of complex biomass. Current Opinion in Biotechnology 22(3): 351-357. doi: https://doi.org/10.1016/j.copbio.2011.04.011

Lerche, I. 1991. Inverse Methods and Kinetic Models of hydrocarbon Generation: I. Theoretical Considerations. Mathematical Geology 23(1): 137-155. doi: https://doi.org/10.1007/BF02065972

Reddy, C.M., J.S. Arey, J.S., Seewald, S. Sylva, K. Lemkau, R.K. Nelson, C.A. Carmichael, C.P. McIntyre, J. Fenwick, G.T. Ventura, B. Van Mooy, and R. Camilli. 2011. Composition and fate of gas and oil released to the water column during *Deepwater Horizon* oil spill. Proceedings of the National Academy of Sciences 109(50): 20229-20234. doi: https://doi.org/10.1073/pnas.1101242108

Chapter 7
An Assessment of Oil-related Chemical Contaminants in Sediment, Water, and Oil from the MC20 Site in the Northern Gulf of Mexico

Andrew L. Mason[1], Annie P. Jacob[1,2], Mary M. Rider[1,2], Michael A. Gaskins[3], S. Ian Hartwell[1], and Ian R. MacDonald[4]

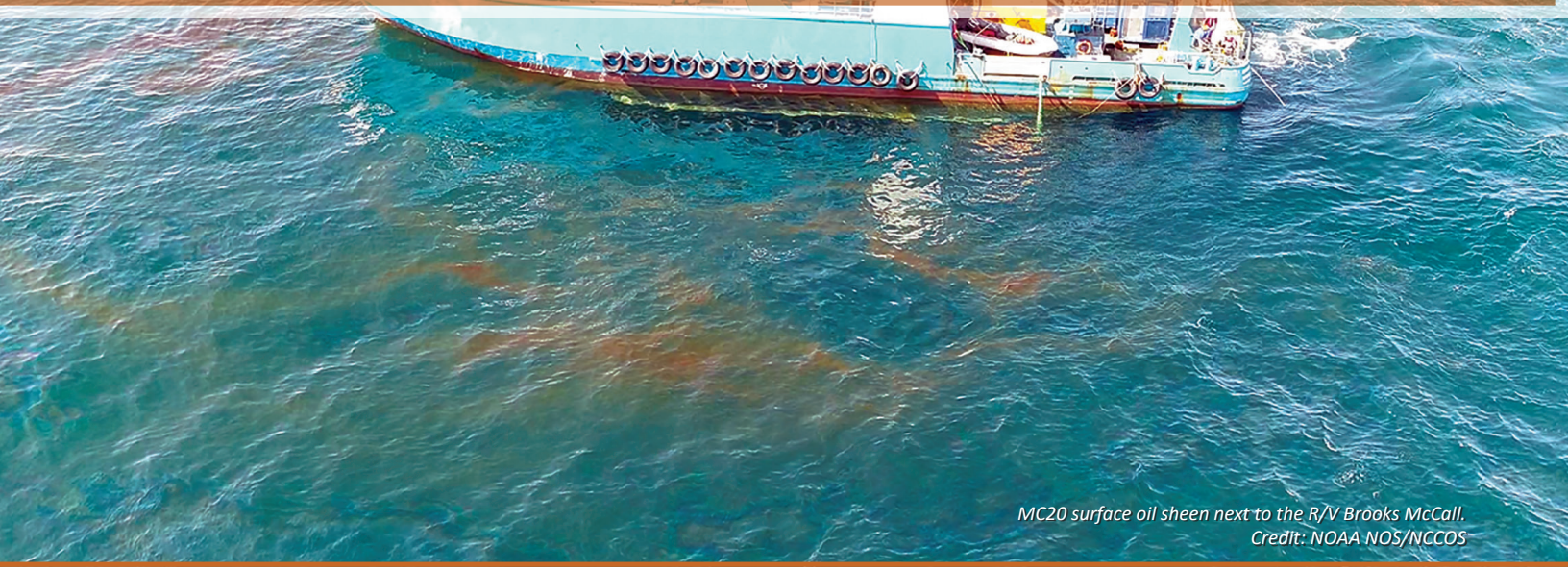

MC20 surface oil sheen next to the R/V Brooks McCall. Credit: NOAA NOS/NCCOS

ABSTRACT

Oil, water, and sediment samples collected as part of a joint NOAA/BSEE survey conducted from 1 September 2018 to 7 September 2018 were analyzed for oil-related chemical contaminants. These include saturated hydrocarbons, Polycyclic Aromatic Hydrocarbons (PAHs), and petroleum biomarkers. Concentrations of oil-related contamination in sediments decline as distance from the northwest corner of the toppled Taylor Energy MC20 well jacket increases. No measurable evidence for MC20 oils were found in sediments >500 m from the erosional pit. Sediment concentrations at the perimeter of the erosional pit at the northwest corner of the jacket are an order of magnitude higher than those found in the rest of the study area. Oil-related compounds measured in the sediments at the perimeter of the erosional pit are severely degraded as compared to mildly degraded oil collected mid-water column and at the surface indicating that oils in the water column and at the surface are not primarily sourced from sediment at MC20. Mid-water column collected oil is mildly degraded and closely resembles historic reservoir degraded oil from MC20 Well #9 in both its API oil gravity and its n-C17 and n-C18 relative ratio to their pristane and phytane counterparts. Subtle heterogeneities observed between mid-water column captured bulk oil, mid-water column captured water, and surface water sheen samples, along with the variations observed from three historic MC20 oils point toward current ongoing release from multiple wells at the MC20 site.

Citation for chapter
Mason, A.L., A.P. Jacob, M.M. Rider, M.A. Gaskins, S.I. Hartwell, and I.R. MacDonald. 2019. Chapter 7: An Assessment of Oil-related Chemical Contaminants in Sediment, Water, and Oil from the MC20 Site in the Northern Gulf of Mexico. pp. 9-106. In: A.L. Mason, J.C. Taylor, and I.R. MacDonald (eds.), An Integrated Assessment of Oil and Gas Release into the Marine Environment at the Former Taylor Energy MC20 Site. NOAA National Ocean Service, National Centers for Coastal Ocean Science. NOAA Technical Memorandum 260. Silver Spring, MD. 147 pp. doi: 10.25923/kykm-sn39

[1] *NOAA National Ocean Service, National Centers for Coastal Ocean Science, Stressor Detection and Impacts Division, Monitoring and Assessment Branch. Silver Spring, MD*
[2] *CSS Inc., Fairfax, VA.*
[3] *TDI-Brooks International. College Station, TX*
[4] *Florida State University, Earth, Ocean, and Atmospheric Sciences, College of Arts and Sciences. Tallahassee, FL*

Sediment, Water, and Oil Chemistry

7.1 INTRODUCTION

This chapter focuses on the results from chemical analysis of (non-gaseous) oil-related chemical contaminants within oil, water, and sediments collected during the joint National Oceanic and Atmospheric Administration (NOAA)/Bureau of Safety and Environmental Enforcement (BSEE) survey at the former Taylor Energy (TEC) Mississippi Canyon Block 20 (MC20) site. The concentrations of over 132 individual oil-related compounds or compound groups, including Polycyclic Aromatic Hydrocarbons (PAHs), saturated hydrocarbons, and petroleum biomarkers were measured across all matrices.

The characterization of oil and gas being released at the MC20 site was identified as a priority outcome of this overall survey effort along with the characterization of flow rate estimates that are documented in Chapter 8 of this Report. Because of the priority nature of this topic and the complex relationship between science, policy, and management at this site, particular care was taken in the sampling design to avoid any potential impact or biasing of the results due to related field data collection efforts.

Among the identified chemistry sub-priorities, of particular interest was the chemical characterization of gas being released at MC20, specifically addressing whether the gas source is biogenic or thermogenic, and thereby pointing to either degradation of remnant oil or an ongoing release of well-related oil and gas. The full analysis and characterization of the suite of gas samples collected for this study are presented in Chapter 6 of this document.

7.1.1 Overview of the Chemical Contaminants

Quantifying the concentrations of oil-related chemical contaminants in multiple matrices allows us to describe the nature of the oil present (e.g., degraded versus fresh), make conclusions about its source and fate in the environment, and begin to document potential stresses the observed concentrations can cause in the marine environment by comparing them to accepted guidelines. Each class of contaminant analyzed for this project is discussed below.

Polycyclic Aromatic Hydrocarbons. This class of oil-related compounds, also referred to as PAHs, are usually less abundant in crude oil than saturated hydrocarbons and include one or more aromatic benzene rings in their structure (NRC, 1985). PAHs can be associated with the use and combustion of fossil fuels and other organic materials. Additional natural sources of PAHs can include decay of organic material (vegetation) and forest fires. The complete list of PAHs analyzed in this study can be found in Table 7.1 and were measured in samples from water, oil, and sediments. The PAHs analyzed here are two to six ring aromatic compounds. PAHs can bioaccumulate in both aquatic and terrestrial organisms and many individual compounds are toxic. Some compounds such as benzo[a]pyrene, benzo[a]anthracene, chrysene, benzo[b]fluoranthene, benzo[k]fluoranthene, dibenzo[a,h]anthracene, and indeno[1,2,3-c,d]pyrene, are likely carcinogenic (ATSDR, 1995).

Saturated Hydrocarbons. Comprised of non-aromatic saturated normal and branched *n*-alkanes, this class of oil-related compounds typically range from 1-40 carbon atoms, though up to 60 carbon atoms have been reported (NRC, 1985). The water, oil, and sediment samples from this survey included the measurement of *n*-alkanes ranging from C9 to C40 along with isoprenoid *n*-alkanes C15, C16, C18, Pristane, and Phytane (Table 7.1). Saturated hydrocarbons are commonly associated with non-combusted fuels such as crude oil, diesel, or gasoline.

7.1.2 Petroleum Biomarkers

Petroleum biomarkers represent a sub-class of source-specific petroleum hydrocarbon compounds whose relative ratios within a sample can be used to describe various characteristics including source rock, depositional environment, and degradation and maturity levels. For this study, we analyzed chemical fossil biomarkers including terpanes, steranes, and aromatic dinosteroids along with stable carbon isotope compositions of C15+ aliphatic and aromatic fractions to characterize source-specific features of the crude oil present in oil and sediment samples. This analysis allowed for the prediction of corresponding source rock type, age, and thermal maturity of both oil in sediments and from oil captured mid-water column.

Table 7.1. List of additional target compounds, Polycyclic Aromatic Hydrocarbons (PAHs), and saturated hydrocarbons analyzed by TDI-Brooks International as part of this study.

Additional Target Compounds	PAHs - Low Molecular Weight (LMW)	PAHs - High Molecular Weight (HMW)	Saturated hydrocarbons
cis/trans Decalin	**Naphthalene**	**Fluoranthene**	*n*-C9 *n*-C36
C1-Decalins	**C1-Naphthalenes**	**Pyrene**	*n*-C10 *n*-C37
C2-Decalins	**C2-Naphthalenes**	**C1-Fluoranthenes/Pyrenes**	*n*-C11 *n*-C38
C3-Decalins	**C3-Naphthalenes**	**C2-Fluoranthenes/Pyrenes**	*n*-C12 *n*-C39
C4-Decalins	**C4-Naphthalenes**	**C3-Fluoranthenes/Pyrenes**	*n*-C13 *n*-C40
2-Methylnaphthalene	Benzothiophene	C4-Fluoranthenes/Pyrenes	*i*-C15
1-Methylnaphthalene	C1-Benzothiophenes	**Naphthobenzothiophene**	*n*-C14
2,6-Dimethylnaphthalene	C2-Benzothiophenes	**C1-Naphthobenzothiophenes**	*i*-C16
1,6,7-Trimethylnaphthalene	C3-Benzothiophenes	**C2-Naphthobenzothiophenes**	*n*-C15
1-Methylfluorene	C4-Benzothiophenes	**C3-Naphthobenzothiophenes**	*n*-C16
4-Methyldibenzothiophene	**Biphenyl**	C4-Naphthobenzothiophenes	*i*-C18
2/3-Methyldibenzothiophene	**Acenaphthylene**	**Benz(a)anthracene**	*n*-C17
1-Methyldibenzothiophene	**Acenaphthene**	**Chrysene/Triphenylene**	Pristane
3-Methylphenanthrene	Dibenzofuran	**C1-Chrysenes**	*n*-C18
2-Methylphenanthrene	**Fluorene**	**C2-Chrysenes**	Phytane
2-Methylanthracene	**C1-Fluorenes**	**C3-Chrysenes**	*n*-C19
4/9-Methylphenanthrene	**C2-Fluorenes**	**C4-Chrysenes**	*n*-C20
1-Methylphenanthrene	**C3-Fluorenes**	**Benzo(b)fluoranthene**	*n*-C21
3,6-Dimethylphenanthrene	Carbazole	**Benzo(k,j)fluoranthene**	*n*-C22
Retene	**Anthracene**	Benzo(a)fluoranthene	*n*-C23
2-Methylfluoranthene	**Phenanthrene**	**Benzo(e)pyrene**	*n*-C24
Benzo(b)fluorene	**C1-Phenanthrenes/Anthracenes**	**Benzo(a)pyrene**	*n*-C25
C29-Hopane	**C2-Phenanthrenes/Anthracenes**	**Perylene**	*n*-C26
18a-Oleanane	**C3-Phenanthrenes/Anthracenes**	**Indeno(1,2,3-c,d)pyrene**	*n*-C27
C30-Hopane	**C4-Phenanthrenes/Anthracenes**	**Dibenzo(a,h)anthracene**	*n*-C28
C20-TAS	**Dibenzothiophene**	**C1-Dibenzo(a,h)anthracenes**	*n*-C29
C21-TAS	**C1-Dibenzothiophenes**	**C2-Dibenzo(a,h)anthracenes**	*n*-C30
C26(20S)-TAS	**C2-Dibenzothiophenes**	**C3-Dibenzo(a,h)anthracenes**	*n*-C31
C26(20R)/C27(20S)-TAS	**C3-Dibenzothiophenes**	**Benzo(g,h,i)perylene**	*n*-C32
C28(20S)-TAS	C4-Dibenzothiophenes		*n*-C33
C27(20R)-TAS			*n*-C34
C28(20R)-TAS			*n*-C35

Note: Bold compounds represent Minerals Management Service (MMS) PAHs (n=48), *n* = normal, *i* = isoprenoid.

7.2 METHODS

Separate sampling strategies were developed for each individual matrix (water and sediment) in accordance with established NOAA National Status and Trends (NS&T) Program protocols. For sediment collection efforts, a targeted transect design was selected to allow for the characterization of oil-related chemical contamination in relation to the distance from the northwest corner of the downed jacket. A total of 15 sediment samples were collected but only 10 were selected for chemical analysis due to budgetary constraints. Selection was based on including all reference sites followed by the 7 closest sites to the collapsed jacket. Samples were collected starting at a reference site 2,990.2 m (BC13) from the northwest corner of the jacket and the identified release point(s) (described in Chapter 3 of this document) along a heading of approximately 60°. Distance between sampling locations was targeted at 1 km intervals until approximately 1 km distance from the northwest corner of the jacket was reached. Within 1 km of the northwest corner of the jacket, samples were targeted at planned intervals of approximately 100 m and ended with a sample at the perimeter of the erosional pit (27.9 m north-northwest from identified release point(s) detailed in Chapter 3; Figure 7.1). Table 7.2 presents the distance in meters that each sediment sample site falls from the identified release point(s). Two additional targeted reference sites were sampled on the opposite side of the collapsed jacket on a heading of 60° at 1 and 2 km. Sediment sample collection was designed to have as minimal an impact on the other concurrent study areas of the overall survey. To achieve this, sediment sampling activities did not commence until 5 September 2018 and only then began with the collection of the first reference site Box Core 13 (BC13) located approximately 3 km south-southwest of the identified release point(s). The remainder of all sediment sampling activity occurred overnight between 6 and 7 September 2018 and ended with the collection of sediment at the perimeter of the erosional pit located at the northwest corner of the downed jacket in the early morning of 7 September.

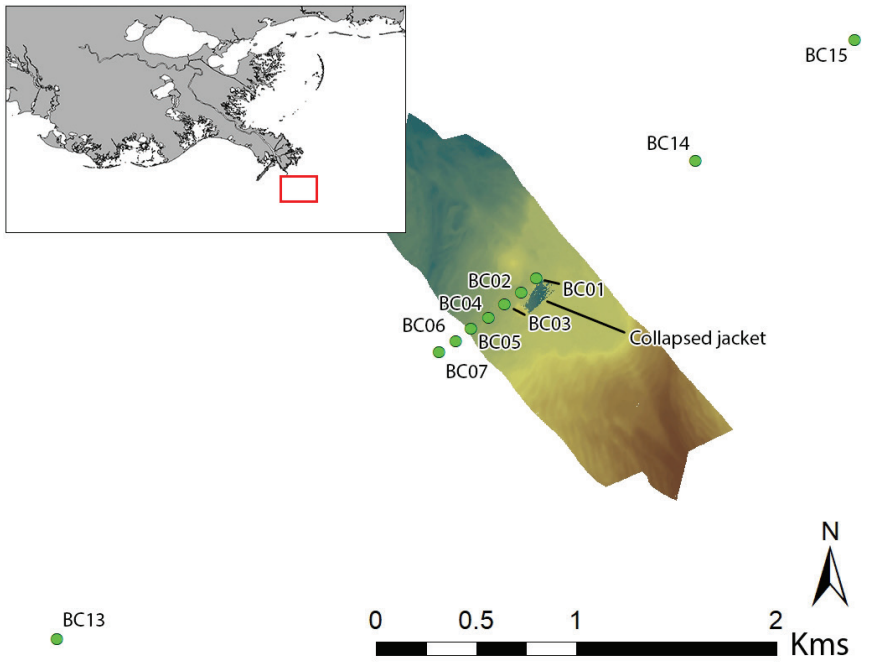

Figure 7.1. Map of sediment locations collected and analyzed for this survey.

Table 7.2. Information for sediment samples collected as part of this MC20 study. Date and time is recorded in UTC (24 hour) while location data is in WGS1984.

Site	Date	Latitude	Longitude	Depth (m)	Distance from release (m)
BC01	9/7/18 5:29	N28 56.2560	W088 58.1714	135.42	27.9
BC02	9/7/18 4:58	N28 56.2176	W088 58.2181	134.55	99.8
BC03	9/7/18 4:27	N28 56.1842	W088 58.2685	134.13	203.2
BC04	9/7/18 4:04	N28 56.1477	W088 58.3158	133.92	304.4
BC05	9/7/18 3:44	N28 56.1174	W088 58.3690	132.34	406.9
BC06	9/7/18 3:15	N28 56.0843	W088 58.4159	131.86	505.7
BC07	9/7/18 2:54	N28 56.0524	W088 58.4664	128.66	604.8
BC13	9/6/18 4:02	N28 55.2625	W088 59.6240	133.69	2,990.2
BC14	9/7/18 6:08	N28 56.5811	W088 57.6889	129.57	995.9
BC15	9/7/18 6:47	N28 56.9134	W088 57.2063	133.73	2,006.8

Physical characteristics of the water column including temperature, salinity, and dissolved oxygen were all measured as part of each remotely operated vehichle (ROV) dive. A Seabird SBE 19 Plus conductivity, temperature, and depth (CTD) probe was mounted on the ROV sled and recorded data every 0.25 seconds.

Complete results of the physical characteristics of the water column collected during this survey are described in detail in Chapter 2 of this Report.

Laboratory analytical Method Detection Limits (MDLs) for each analyte and matrix can be found in Appendix B. The complete chemistry dataset for this survey can be found in Appendix C and is available for download from NOAA's DIVER database. Raw data values provided by TDI Brooks flagged with identifier code "U" were below the MDL and are estimated concentrations. These values were converted to zero values in all calculations and for results analysis.

7.2.1 Sampling Protocols

Sediments samples were collected using a 27 L box corer. The location of the box core samples was tracked using an Ultra-short baseline (USBL) beacon locator that was calibrated prior to deployment using the methods described in Chapter 3 of this document. As stated above, samples were targeted at predetermined intervals with the actual location recorded at the time of sample collection. Prior to each sampling effort, the box core sampling device and attached weights and frame were cleaned using soap and water and scrub brushes. Additionally, the interior of the box core was cleaned using alcohol wipes prior to deployment following methods developed by Pisarski *et al*. (2018). Chemistry samples were collected from the top 5 cm of collected sediment using a pre-cleaned stainless steel scoop. Sediment grain size samples were also collected from the top 5 cm of the box core. Though not analyzed for this survey, two 30 cm cores were also collected from the box cores at each sample location. Chemistry samples were placed into certified pre-cleaned 250-mL iChem glass jars, sealed, labelled, and immediately frozen (-40°C). Grain size samples were placed into Whirl-pak™ sample bags, labelled, and immediately refrigerated (approximately 3°C).

Surface water samples were collected from within the visible surface sheen near where oil was observed to be reaching the ocean surface using a stainless steel bucket lowered over the side of the ship. The bucket was thoroughly pre-cleaned using soap and water, then wiped down using alcohol wipes following methods developed by Pisarski *et al*. (2018). Once on deck, certified pre-cleaned 1-L amber jars were filled from the sample bucket surface water until full. Sample jars were sealed, labelled, and immediately refrigerated (approximately 3°C).

Subsurface water, oil, and gas samples were all collected via specialized equipment attached to the bubblometer chamber described in Chapter 4 of this document. To begin a sample collection effort, the master valve at the top of the sample collection graduated cylinder is closed and the bubblometer chamber and attached inverted funnel extended via its hydraulic arm out in front of the SeaTrepid Commanche ROV. The ROV would then travel throughout the water column allowing rising gas and oil to enter the collection graduated cylinder displacing the ambient site water trapped when the master valve was closed. Sample collection ended when the bubblometer chamber was retracted into the ROV sled, closing off the inverted funnel to any additional oil and gas rising through the water column. Once a viable oil, gas, and water sample was present in the sample collection graduated cylinder either a manually operated valve or electronically controlled solenoid valve would open, allowing ambient pressure at depth combined with surface evacuated vacuum sample collection chambers to force the combined sample (oil-gas-water), via its own separate dedicated tubing, into a numbered sample chamber. The process could be repeated up to four times during an ROV dive without having to surface, evacuate, clean, and reset the sample chambers. Once on deck, manual valves were closed at the top of each sample chamber and the chambers were disconnected and removed from the bubblometer frame. The exterior of the sample chambers were cleaned using water and towels and prepped for individual sample collection by cleaning and drying the top threaded valve fitting. Gas samples were collected first using stainless steel tubing, fittings, and a bleeder valve to control the release of pressurized gas. Gas samples were placed into Supelco™ inert foil gas sampling bags with a low bleed Thermogreen LB-2 septa screw cap.

The order of procedure for each gas sample transfer was as follows:

1. Remove foil gas sample bag safety cap;
2. Attach bleeder hose tube onto foil gas sample bag;
3. Slowly open main collection chamber manual valve;
4. Open foil gas sample bag valve one quarter turn;
5. Slowly open bleeder valve while securely holding foil gas sample bag onto bleeder tube;
6. Fill gas sample bag until full and close bleeder valve;
7. Close foil gas sample bag valve, remove bag from bleeder hose tube, and replace safety cap; and
8. Repeat steps 1 through 7 until ambient pressure in collection chamber is reached. All gas samples were labelled and frozen (-40°C) immediately after being collected.

Collection of the oil and water mixture from the sample chambers was completed by closing the manual chamber valve, inverting the chamber, removing the bottom threaded plug, and draining the combined contents into a certified pre-cleaned iChem 250 mL jar. The jars containing sample were immediately sealed, labelled, and refrigerated at approximately 3°C. At the laboratory, the oil fraction was separated from the water fraction to allow for individual analysis. As was the case for sediments, more samples were collected than were analyzed. A total of six individual bulk oil and water mixtures were collected though due to budget constraints only one was analyzed.

Once subsurface oil, gas, and water sample collection from the sample chambers was completed, each individual cylinder and its related fittings and valves were rinsed twice with dichloromethane solvent to remove any residual sample before being mounted back onto the bubblometer frame. All related fittings and the bubblometer chamber, inverted funnel, and sample collection graduated cylinder were also rigorously cleaned with a combination of soap, water, scrub brushes, and alcohol wipes (Pisarski *et al*., 2018) between sample deployment efforts. Despite the rigorous cleaning of the connecting tubes, some contamination was detected in the sample blank collected after cleaning (Appendix C). There is no biasing of the results however as the mid-water column samples (WAT 01, WAT 02) included for this analysis are from the first deployment of the sample chambers and therefore not affected by any previous or subsequent sample efforts.

All samples were cataloged and Chain-of-Custody (CoC) maintained throughout the sample collection and delivery process to the laboratory. Samples were hand carried in signed and sealed coolers on blue ice (non-water) and arrived at the laboratory in good condition.

All laboratory analyses were performed using protocols from the NS&T Program by TDI-Brooks International or its subcontractor GeoMark Research, which provided additional biomarker analysis for sediment and oil samples. GeoMark Research did not report concentrations of individual biomarkers but determined diagnostic ratios among them allowing for comparisons to one another and to a large proprietary database of Gulf of Mexico crude oils. The 64 polycyclic aromatic hydrocarbons (PAHs), sulfur-containing aromatics, and decalins along with 27 individual alkyl-PAH isomers and selected terpanes and triaromatic steroids were analyzed using gas chromatography/mass spectrometry in selected ion monitoring mode while the 37 saturated hydrocarbons and total petroleum hydrocarbons (TPH) were analyzed by gas chromatography/flame ionization detection. Additional detailed descriptions of NS&T protocols, including quality assurance/quality control (QA/QC) used for these analysis can be found in Kimbrough *et al*. (2006).

NOAA numerical sediment quality guidelines (SQG) developed by Long and Morgan (1990) and Long *et al*. (1995), known as Effects Range-Median (ERM), and Effects Range-Low (ERL), each express statistically derived contamination levels above which toxic effects can be expected. These guidelines express statistically derived

levels of chemical contamination in surficial sediments below which effects to benthic organisms were rarely (<10%) expected (ERL) and above which toxic effects would be expected to be observed with at least a 50% frequency (ERM). The ratio of the ERM value to the sediment concentration for each chemical, or sum of chemicals such as total PAHs, is called the ERM quotient or ERMq (Long *et al*., 1998). This quotient expresses how close measured concentrations are to the established ERM level on a zero to one scale. A quotient of one or greater means the concentrations are at or above the ERM. This also normalizes the ERMs for different chemicals to a common scale. By averaging the mean ERMq of contaminants it is possible to express a measure of contamination across the entirety of all analytes. Previous studies by Hyland *et al*. (1999) suggest that mean ERMq values of 0.1 in southeast U.S. coastal waters represent a threshold above which degradation in benthic communities start appearing. The mean quotient of the ERMs and contaminant concentrations have been calculated on a site-by-site basis.

A total of 10 sediment samples, six water samples, and one oil sample analyzed in triplicate were chemically characterized for this survey. The full list of samples for this study are shown in Table 7.3.

Table 7.3. List of MC20 samples analyzed for this study.

Site	Matix	Chemical analysis	Type
BC01	Sediment	Aliphatics, PAHs, and Biomarkers	Primary
BC02	Sediment	Aliphatics, PAHs, and Biomarkers	Primary
BC03	Sediment	Aliphatics, PAHs, and Biomarkers	Primary
BC04	Sediment	Aliphatics, PAHs, and Biomarkers	Primary
BC05	Sediment	Aliphatics, PAHs, and Biomarkers	Primary
BC06	Sediment	Aliphatics, PAHs, and Biomarkers	Primary
BC07	Sediment	Aliphatics, PAHs, and Biomarkers	Primary
BC13	Sediment	Aliphatics, PAHs, and Biomarkers	Reference
BC14	Sediment	Aliphatics, PAHs, and Biomarkers	Reference
BC15	Sediment	Aliphatics, PAHs, and Biomarkers	Reference
MC20 Oil	Oil	Aliphatics, PAHs, and Biomarkers	Primary
SRM MC252 Oil	Oil	Aliphatics, PAHs, and Biomarkers	Reference
WAT08A	Water	Aliphatics and PAHs	Primary
WAT08B	Water	Aliphatics and PAHs	Primary
WAT11A	Water	Aliphatics and PAHs	Primary
WAT11B	Water	Aliphatics and PAHs	Primary
WAT01	Water	Aliphatics and PAHs	Primary
WAT02	Water	Aliphatics and PAHs	Reference

7.3 RESULTS AND DISCUSSION

7.3.1 Physical Variables of the Water Column

For sediment samples, the mean water depth at collection was 132.78 ± 2.19 m (standard deviation, SD) with a minimum depth of 128.66 m at Box Core site 07 (BC07, approximately 600 m south-southwest of release point(s)) and a maximum depth of 135.42 m at Box Core site 01 (BC01, located at the perimeter of the erosional pit at the northwest corner of the downed jacket).

During this survey, the physical characteristics of the water column including dissolved oxygen, temperature, and salinity were measured over five separate ROV dives. Those measurements total over 240,000 individual samples each for the above mentioned water column variables. The mean concentration of dissolved oxygen observed throughout the water column was 5.12 ± 0.19 mg/L with a minimum of 4.37 mg/L and a maximum of 5.47 mg/L. Water temperature during the survey ranged from 18.31°C to 29.98°C with a mean of 20.39 ± 2.11 C°. The final measured physical water column characteristic was salinity. Salinity throughout the water column had a mean value of 35.36 ± 1.51 Practical Salinity Units (PSU). The maximum salinity recorded was 36.95 PSU while the minimum was 28.06 PSU. A complete analysis of temperature, salinity, and dissolved oxygen data collected by the ROV SeaBird 19 Plus CTD is presented in Chapter 2 of this document.

7.3.2 Total Organic Carbon and Grain Size

The mean percent total organic carbon (TOC) in the sediments analyzed was 1.50 ± 0.27% and had a maximum value of 1.78% at site BC07 and a minimum value of 0.94% at reference site BC15. Many contaminants, including oil-related compounds, tend to accumulate in sediments with higher TOC values (Shine and Wallace, 2000; Hassett *et al*. 1980). This is also true for sediments that have a higher proportion of fine grain sediments (i.e., silt and clay fractions). The relationship is due to the higher surface area per unit volume available for contaminant adsorption onto smaller grain size sediments. For this study, the silt and clay percentages are summed and reported as percent fines (% clay + % silt = % fines). Percent fines had a mean of 94.66 ± 1.57% with a maximum of 96.97% at site BC15 and a minimum of 92.95% at site BC04. This is differentiated from the inverse components comprised of percent sand and percent gravel. There were no measured levels of gravel in this study. Percent sand in the analyzed sediment samples had a mean of 5.35 ± 1.57% with a maximum of 7.05% (BC04) and a minimum of 3.03% (reference site BC15).

7.3.3 Chemical Contaminants

Results from the analysis of chemical contaminants in the sediment, surface and subsurface water, and oil are described below. Detailed information on the analysis of gas samples can be found in Chapter 6 of this document.

Saturated Hydrocarbon Compounds and Total Petroleum Hydrocarbons (TPH)

Saturated hydrocarbon compounds refers to the list of normal and isoprenoid alkanes found in Table 7.1, while Total Petroleum Hydrocarbons (TPH) is a term used to describe a broad family of several hundred chemical compounds that originally come from crude oil and can be useful as a general indicator of petroleum contamination (ATSDR, 1999). Because the measure of TPH does not discriminate between the individual components that make up crude oils, TPH cannot be used as an indicator of overall impacts to marine life. Even so, we present here TPH measured values as an overall indication of petroleum related pollution at the MC20 site along with saturated hydrocarbon compounds.

Sediment Samples

The mean concentration for Total Saturated Hydrocarbon (TSH) compounds in sediments for this survey was 7.49 ± 2.14 µg/dry g. The median concentration of TSHs in sediment was 6.80 µg/dry g. The minimum concentration for TSHs was 5.93 µg/dry g (BC03) while the maximum concentration was 13.41 µg/dry g (BC01). TSH concentrations within the study area decreased between our box core site at the perimeter of the erosional pit (BC01, 27.9 m from release point(s)) and our box core site 99.8 m from the release point(s) (BC02). Saturated hydrocarbon histograms as percent of total weight for sediment sites BC01 through BC05 and the reference site BC13 are presented in Figure 7.2. It is important to note that as distance from the release point(s) increases, the percent of total weight of *n*-C31, a biomarker of terrestrial plant matter, also increases, indicating a decreasing influence of MC20 oil and a return to background conditions for this region of the Gulf of Mexico.

The mean concentration of TPH in sediment samples collected for this study was 697.80 ± 1,145.19 µg/dry g. The maximum TPH concentration measured was 3,889 µg/dry g found at site BC01 at the perimeter of the erosional pit at the northwest corner of the collapsed jacket. The minimum TPH concentration of 167 µg/dry g was found at our reference site BC13 (approximately 3 km south-southwest of release point(s)). Concentrations of TPH within the study area decreased as distance from the identified release point(s) increased (Figure 7.3). The Unresolved Complex Mixture (UCM) or "hump" is visible in the chromatogram (Figure 7.2 insets) of the sediment from BC01 and, as with TSH, decreases as distance from the release point(s) increases before disappearing from samples beyond approximately 500 m (not visible in BC06, BC07, or BC13-BC15). In contrast, we found an inverse increase in the percent contribution of *n*-C31 to the total saturated

hydrocarbons. Concentrations of *n*-C31, along with other odd *n*-alkanes such as C29, C33, and C35, comprise highly biodegradation resistant plant waxes signifying normal background conditions. The increased percent of *n*-C31 is an indicator of the shift from MC20 oil contamination to background conditions present in marine sediments for this region of the Gulf of Mexico. The presence of the sizable UCM hump in sediment from BC01, compared with the minimal UCM hump in BC02 through BC05, contains oil that is considerably more biodegraded as compared to the mid-water column oil and water samples detailed in the sections below.

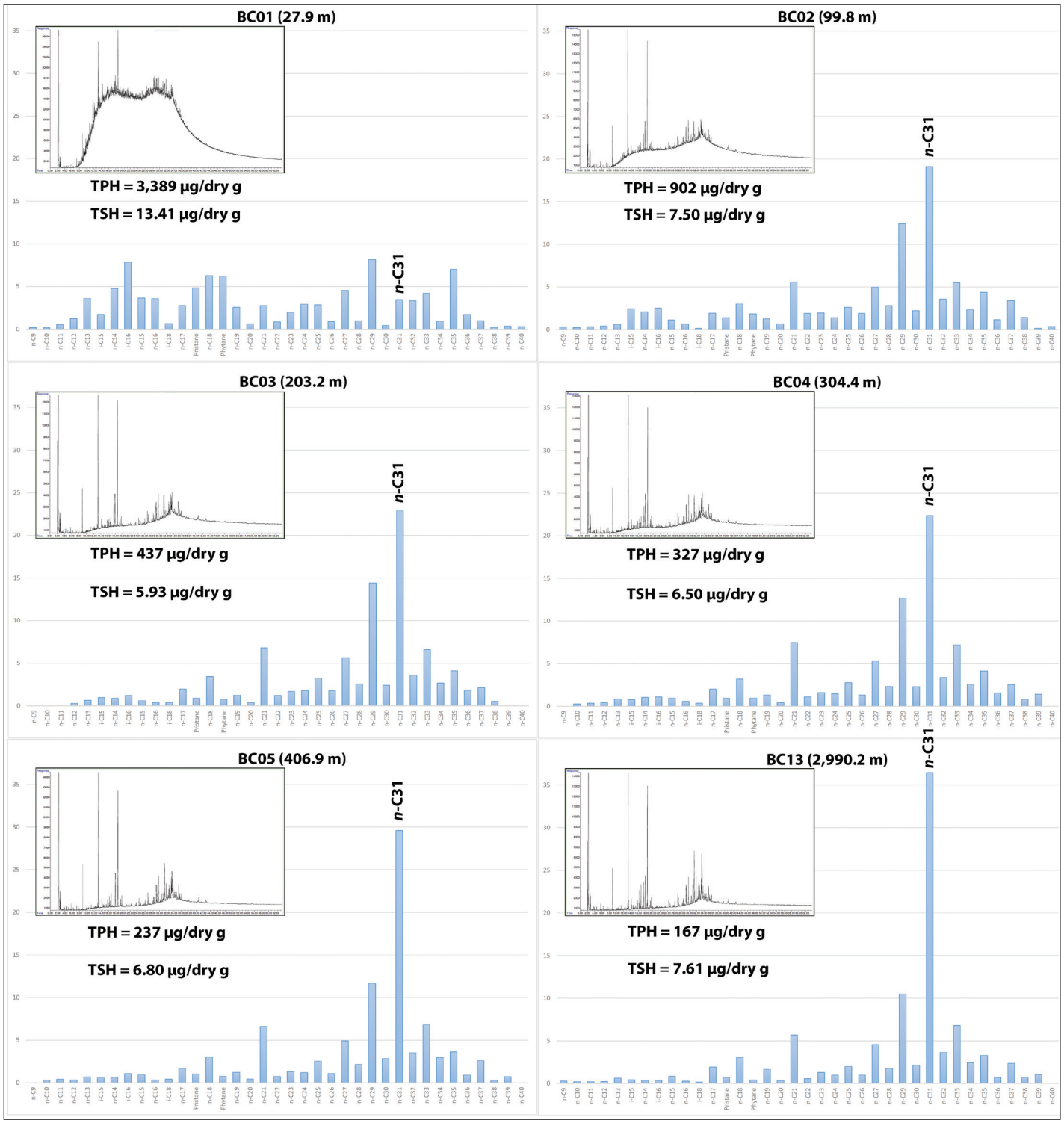

Figure 7.2. Histograms of saturated hydrocarbon compounds expressed as percent of total weight (blue) with gas chromatography (GC)/flame ionization detector (FID) chromatograms (insets) for select sediment sample sites. Consistent large peaks across chromatograms (insets) represent laboratory standards. Distance from plume release point in meters presented in parenthesis. TPH = Total Petroleum Hydrocarbons, TSH = Total Saturated Hydrocarbons.

Sediment, Water, and Oil Chemistry

Water Samples

Total saturated hydrocarbons were analyzed in the six water samples collected for this study. Four of the six samples were collected from the surface slick while two samples were collected mid-water column (Figure 7.4). The surface slick samples represent two physical locations with two samples collected at each of the locations. Of the two water column samples, WAT02 was taken at approximately 10 m depth outside the plume and surface slick (reference site - Cylinder 2, 2 September 2018), and WAT01 (Cylinder 3, 2 September 2018) represents an integrated sample taken during the ROV track presented in Figure 7.5. Total saturated hydrocarbons for all water samples had a mean concentration of 814.75 ± 1,436.39 µg/L with a minimum 0 µg/L (Non-Detection <46.43 µg/L at WAT02 - reference site) and a maximum value of 3,728.73 µg/L (WAT01 – within the plume at the northwest corner of the jacket). Each of the surface water samples and WAT01 contain *n*-alkanes similar to the oil collected mid-water column (see below) except that the four surface water samples have much lower concentrations of the more volatile *n*-alkanes, possibly due to evaporation of the volatile fraction once they reach the ocean surface. The saturated hydrocarbons measured in these samples are consistent with free oil droplets mixed in with the water.

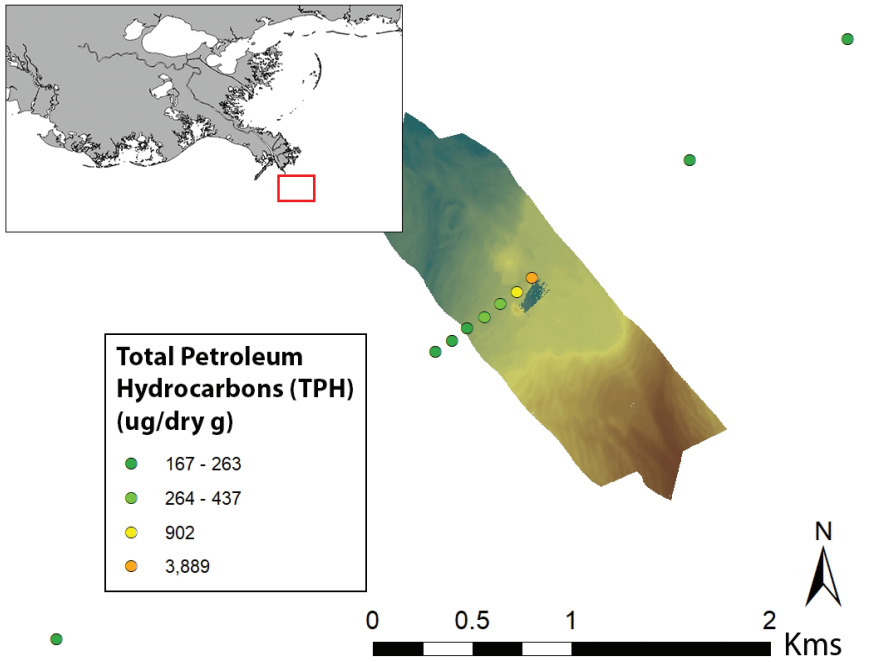

Figure 7.3. Map showing the Total Petroleum Hydrocarbons (TPH) at the MC20 site.

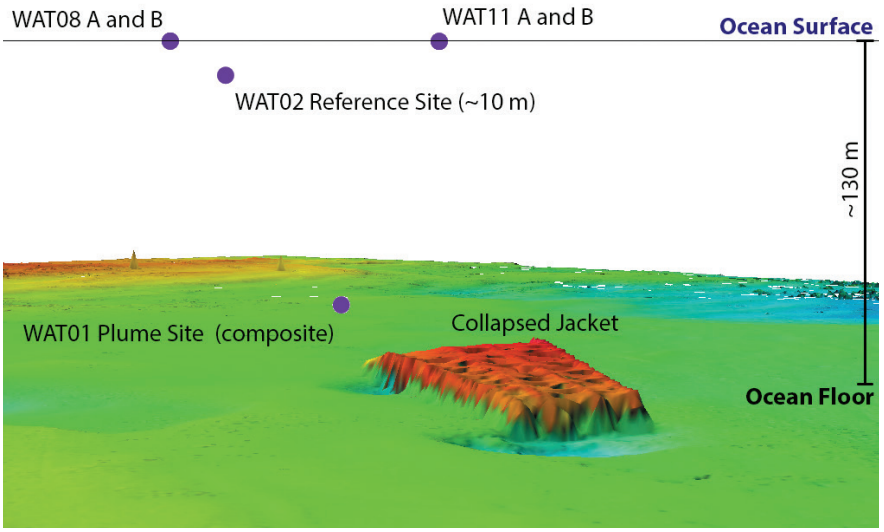

Figure 7.4. Map of water samples collected during this survey. WAT08 and WAT11 both represent two surface samples each, while WAT02 represents a composite reference site sampled outside of the oil and gas plume. WAT01 represents a composite sample inside the oil and gas plume at the northwest corner of the collapsed jacket.

The mean concentration of TPH in the six water samples collected for this study was 33,635 ± 55,772.75 µg/L. The maximum concentration of TPH was 146,498 µg/L in sample WAT01 (within the plume at the northwest corner of the jacket). We did not detect TPH at the reference site WAT02 (Method Detection Limit of 46.43 µg/L) collected outside of the visible plume (ROV video) and at approximately 10 m depth.

The concentrations of TPH observed in the plume were an order of magnitude higher than those observed in surface waters near where the plume was surfacing. The order of magnitude difference in TPH concentrations from this study point toward loss of petroleum hydrocarbons, possibly due to evaporation at the surface. Current, wind, and wave conditions at the time of surface water collections were relatively mild and samples were collected from a fairly dense surface sheen expression. Additionally, we see no obvious presence of

dissolved hydrocarbons in the water as any present dissolved hydrocarbons are being overshadowed by oil droplets present in the water.

Oil Product Sample

Approximately 240 mL of oil product were collected over six individual collection efforts for this study. The mean oil product volume per sample collection effort was 38.33 ± 34.44 mL with a minimum collection volume of approximately 1 mL from bubblometer chamber cylinder 1 on 3 September 2018 and a maximum collection volume of approximately 90 mL from cylinder 2 on the same date. It is important to note that the variability in collection amounts was not due to an observed change in the flux rate of the plume, but the direct result of the ability of the ROV operator to stay within the plume (affected by current, depth, and positioning of the support vessel) as well as the volume of gas also being collected concurrently and what type of sample collection was being targeted (oil versus gas). While gas, oil, and water were collected during each collection effort, each individual matrix was often targeted for separate cylinders. For example, during the 3 September ROV chemistry collections for cylinder 1, gas collection was targeted and as such collected approximately 1 mL of oil, three full foil gas bags, and approximately 155 mL of decanted water. Cylinder 2, during the same ROV dive, targeted oil collections and contained approximately 90 mL of oil, two full and one partially filled foil gas bags, and approximately 140 mL of decanted water. Gas collection volumes were heavily influenced by the depth that the gas was collected from and the resultant expansion when retrieved at ambient surface pressures.

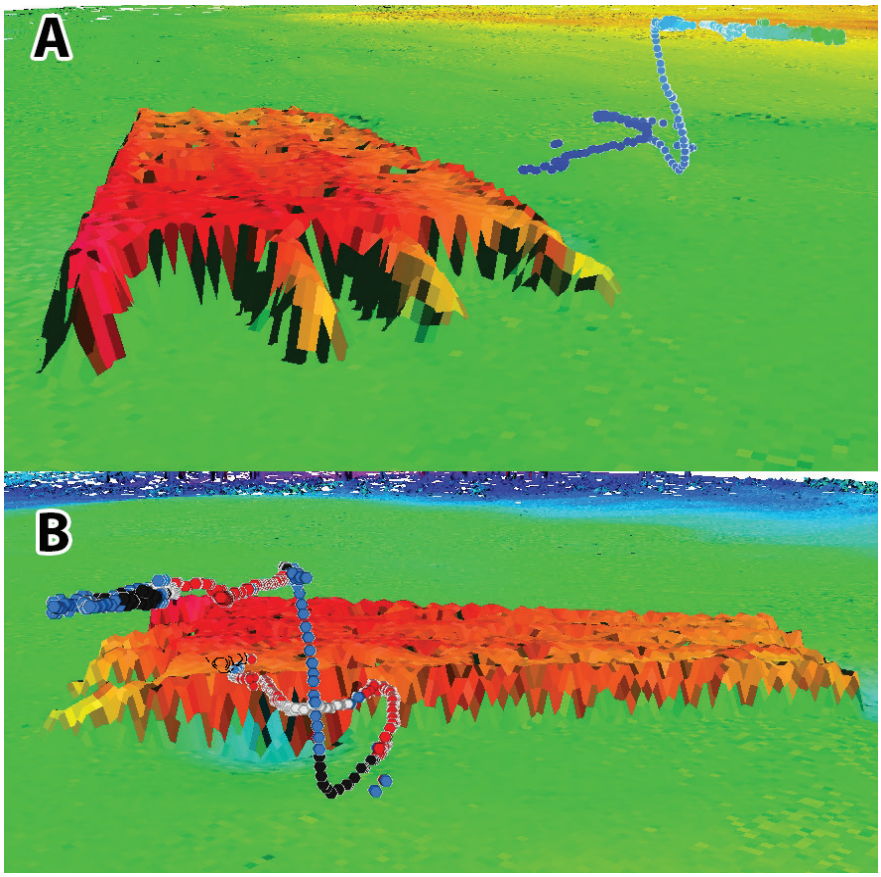

Figure 7.5. Two views of the same ROV track for collection of WAT02 (MC20 mid-water column water) subsurface composite sample. Green to dark blue in Panel A represents starting position to ending position for ROV track. Panel B depicts visually observed collection conditions from ROV video feed where blue = no visually observed oil or gas, black = oil observed, white = gas observed, red = both oil and gas observed together.

Because the sampling process using the bubblometer chamber represents a composite sample of the plume at the time of collection, one sample of collected oil was analyzed for this study (cylinder 2, 3 September 2018). The composite oil sample was taken during the ROV track presented in Figure 7.6.

Total *n*-alkanes in the oil were analyzed in triplicate to confirm results. The mean concentration of total *n*-alkanes in the oil product was 22.2 ± 0.25 µg/dry mg. The minimum concentration of total *n*-alkanes in the oil product was 21.9 µg/dry mg while the maximum concentration was 22.4 µg/dry mg. The oil collected mid-water column contains a greater relative abundance of *n*-alkanes than what was measured in the sediments (see above). This further indicates that oil being released from the seafloor is less biodegraded than the oil remaining in the sediments analyzed as part of this study.

As was done with all oil product analysis, TPH in the oil product sample was analyzed in triplicate to confirm

results. The mean TPH in the oil product collected was 471 ± 3.75 µg/mg. The minimum TPH concentration was 467 µg/mg while the maximum concentration was 475 µg/mg.

Comparison with Other Data

Samples of any original MC20 production/exploration oil(s) have been difficult to locate and were not able to be procured or analyzed for this study. However, some limited data on original MC20 oils do exist as part of a larger proprietary study of northern Gulf of Mexico oils conducted by the Geochemical Environmental Research Group (GERG) in the 1980s. Through personal communication (Wade, pers. comm.), data from three MC20 oil reservoirs representing two separate wells have been obtained for comparison in this report (Wade, unpublished data). While it is not known precisely when these original oil samples were collected, we do know that the data was generated on 22 March 1985. This data is included in Table 7.4 and Appendix C for reference. Saturated hydrocarbon data for these three historic MC20 oils show distinct signatures for each reservoir. Most interestingly, data from Well #9 closely resemble those measured in the water column from 2018, namely in the relationship of pristane and phytane to *n*-C17 and *n*-C18, respectively. MC20 oil collected mid-water column and oil from Well #9 (1985) show the same pattern of biodegradation in the above relationships (pristane and phytane greater than *n*-C17 and *n*-C18, respectively; Figure 7.7). Both *n*-C17 and *n*-C18 are preferentially biodegraded and their relative ratio to their pristane and phytane counterparts, along with its relatively higher asphaltenes percentage, indicate that the oil in MC20 Well #9 is degraded in the reservoir. MC20 Well #2's reservoir oils do not appear to be degraded in the reservoir and their API Gravity (oil density) values and asphaltene percentages also point to this conclusion. The fact that there is so much variation between two of the MC20 site's original 25 producing wells further explains the observed heterogeneities in MC20 oil captured mid-water column and in surface sheens, and can be a confounding factor when trying to pinpoint the source of oil captured mid-water column.

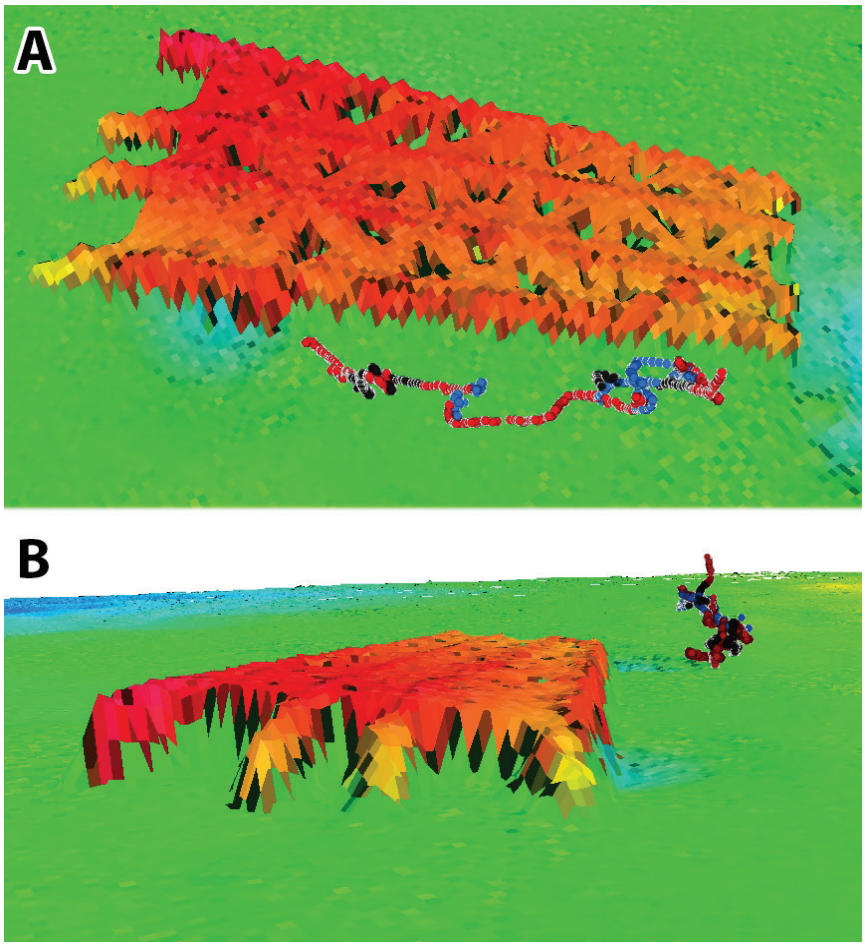

Figure 7.6. Two views of the same ROV track for collection of WAT05 (MC20 mid-water column oil) subsurface composite sample. Collections began at the highest point in the water column. Colors in both panels A and B depict visually observed collection conditions from ROV video feed where blue = no visually observed oil or gas, black = oil observed, red = both oil and gas observed together.

Table 7.4. Comparison of 1985 MC20 oils with 2018 MC20 mid-water column collected oil.

Identification	Latitude	Longitude	Depth (m)	API Gravity	Asphaltenes (%)
MC20 oil (2018)	28.93711	-88.96958	Water Column	25.74	Not measured
MC20 Well #9	28.92666	-88.97475	3,409	26.7	0.67
MC20 Well #2 A	28.93324	-88.98083	2,642	30.2	0.45
MC20 Well #2 B	28.93324	-88.98083	3,053	30.2	0.42

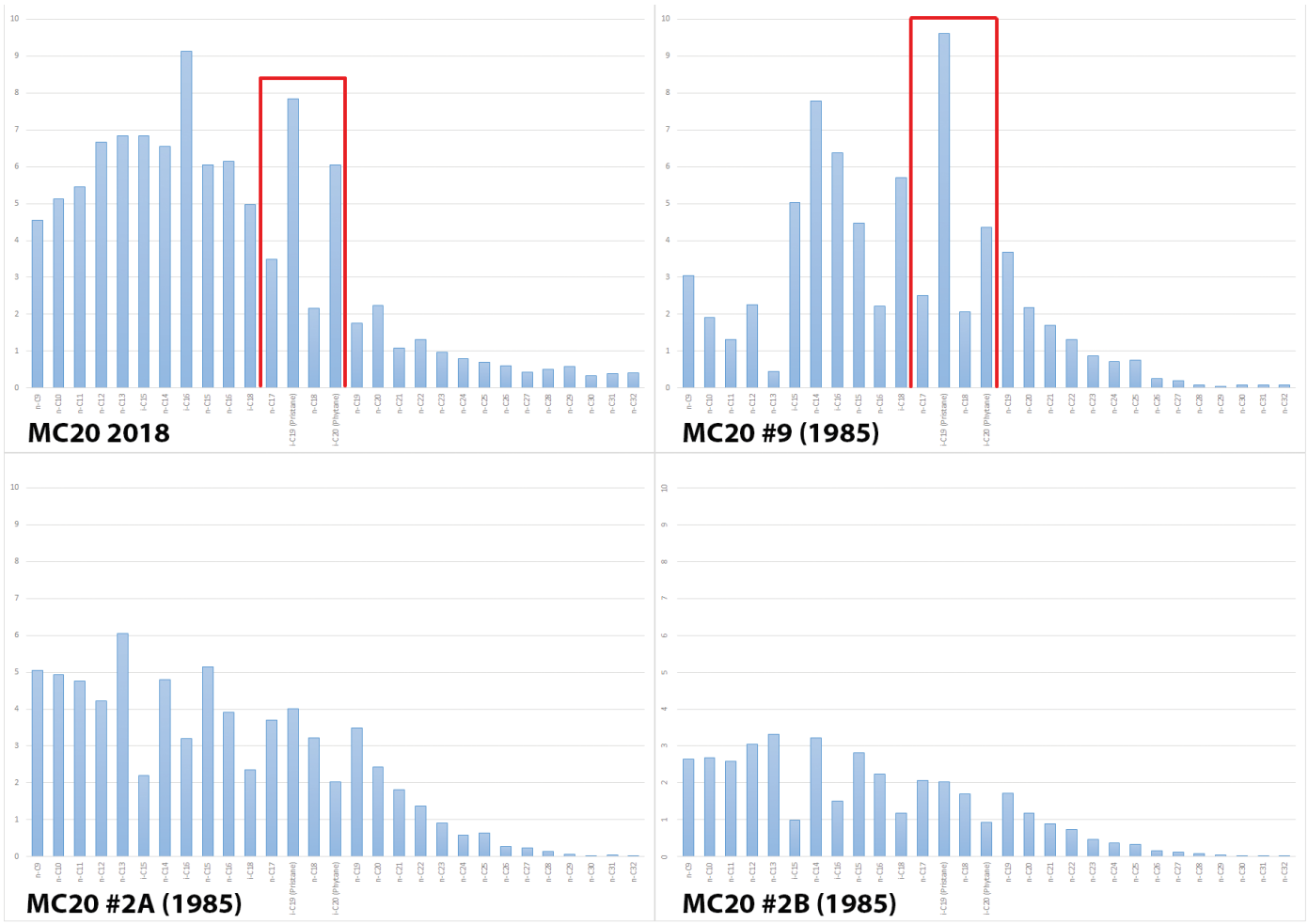

Figure 7.7. Select saturated hydrocarbon compound comparison (as percent of total weight) between MC20 2018 mid-water column oil and MC20 1985 oils. X-axis = n-C9 through n-C32, from left to right. Red bars highlight the degraded nature of the oil through the relationship between n-C17/n-C18 and pristane/phytane.

7.3.4 Polycyclic Aromatic Hydrocarbons

Sediment Samples

Total PAHs in this study refers to the sum total concentrations of all 64 individual PAHs, sulfur-containing aromatics, and decalins listed in Table 7.1. The mean concentration for sum total PAHs for this survey was 3,757.5 ± 7,498.3 ng/dry g. The median concentration of total PAHs in sediments was 1,197 ng/dry g. The minimum concentration for total PAHs was 758 ng/dry g (reference site BC13) while the maximum concentration was 24,972 ng/dry g (BC01 located in the erosional pit at the northwest corner of the collapsed jacket).

Total PAH concentrations within the study area decreased as distance from the identified release point(s) increased (Figure 7.8).

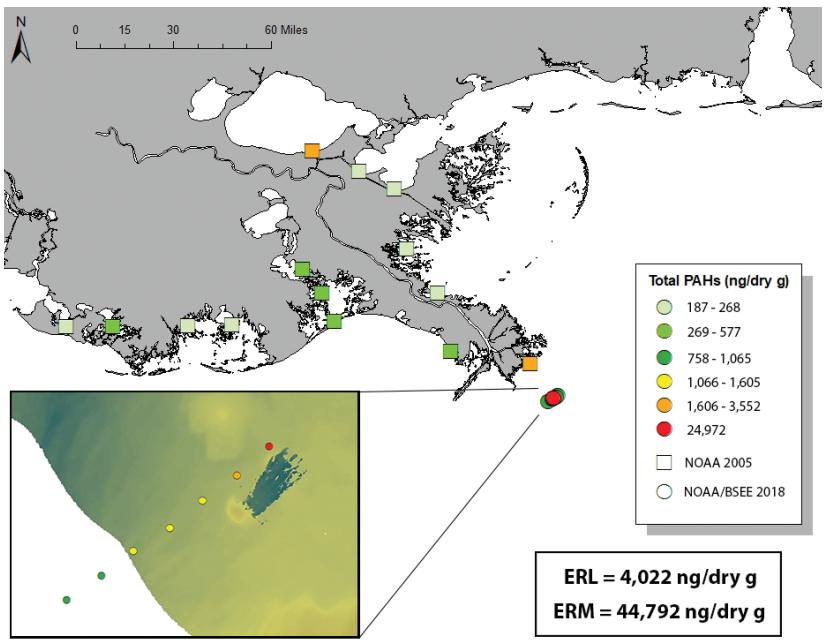

Figure 7.8. Map of MC20 total PAH sediment samples as compared to NOAA Mussel Watch sediment samples collected in 2005.

This pattern was also present in TPH concentrations. For both total PAHs and TPH, beyond 406.9 m (site BC05) sediment concentrations appear to reach background levels. PAH histograms for sediment sites BC01 through BC05 and reference site BC13 are presented in Figure 7.9. These figures show the relative change in PAHs as distance from the release point(s) increases, especially in the relative percentage of perylene (red) as compared to other PAHs. Perylene is a biogenic PAH that dominates Gulf of Mexico sediments. Sediment PAH analysis for this study finds the relative percentage of perylene decreases as we approach the erosional pit at the northwest corner of the downed jacket, showing increased concentrations the closer the sediments are to the identified release point(s). By looking at the percent of perylene we can see that beyond sediment site BC05 PAHs associated with MC20 decreased to background levels.

The ratio of the percent Low Molecular Weight (LMW) PAHs (≤3 rings) and percent High Molecular Weight (HMW) PAHs (≥4 rings) in sediment samples is presented in Figure 7.10. The mean percent of total for LMW PAHs in sediments was 32.9 ± 7.16% while the mean percent of total for HMW PAHs in sediments was 67.10

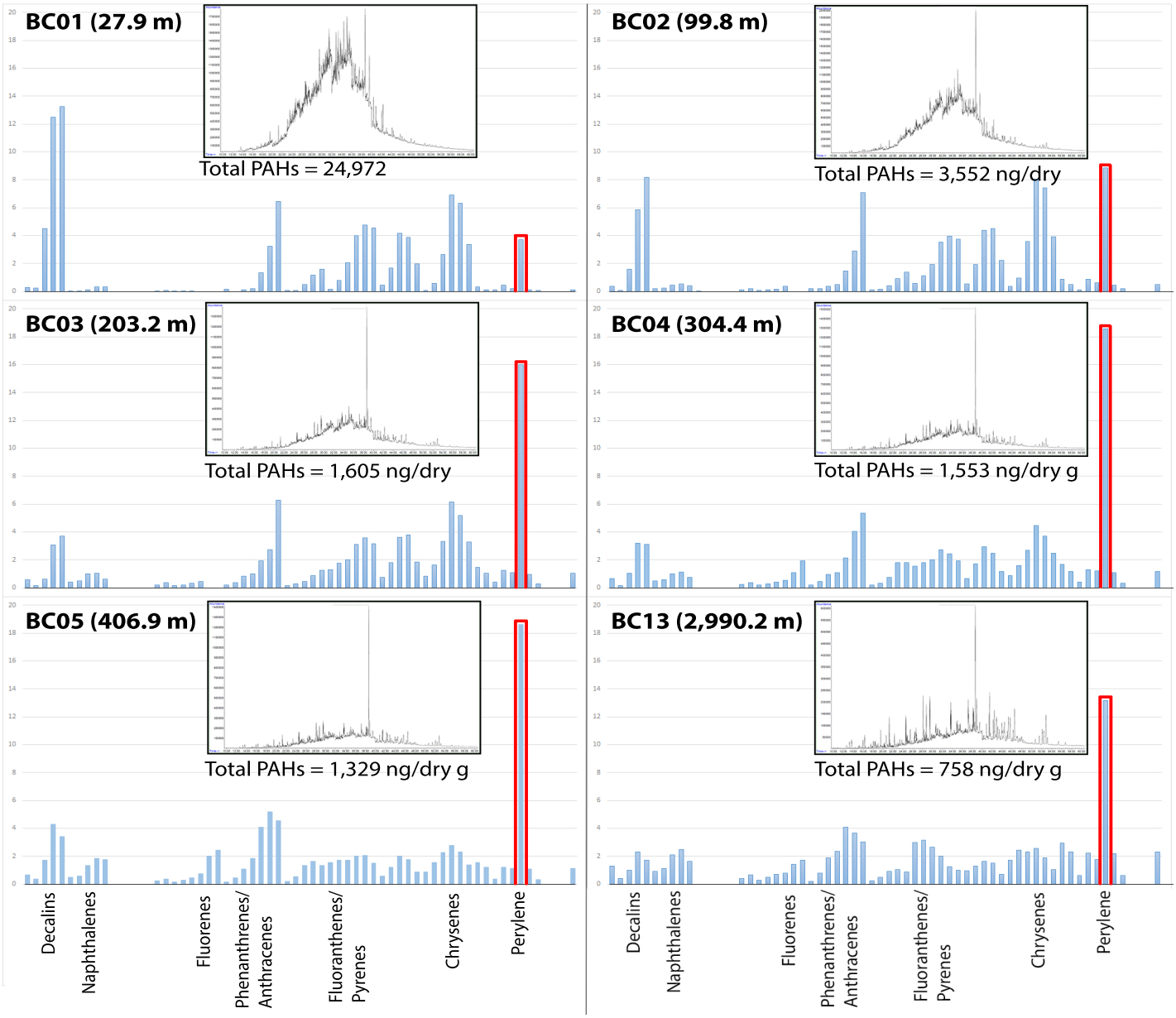

Figure 7.9. PAH as percent of total weight histograms (blue) with GC/FID chromatograms (insets) for select sediment sample sites. Red highlight denotes relative change in percent perylene between sediment sites. Consistent large peak across chromatograms represents laboratory standard. Distance from plume release point in meters presented in parenthesis.

± 7.16%. The minimum percent of total for LMW PAHs was 22.8% at site BC02 (approximately 100 m from the identified release point(s)) while the maximum was 40.9% at site BC05 (approximately 400 m from the identified release point(s)). The minimum and maximum percent of total for HMW PAHs was the inverse of the above at 59.1% and 77.2% at sites BC05 and BC02 respectively. By themselves, the ratio of LMW to HMW PAHs in sediments are not particularly informative, however having these values calculated allows for comparisons between LMW and HMW PAHs in the water which is discussed later in this chapter.

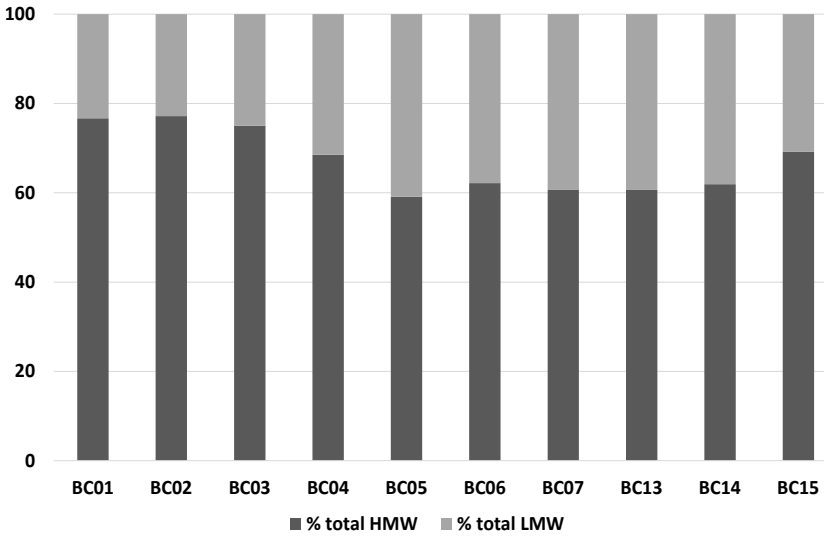

Figure 7.10. Composition of HMW and LMW as a percent of total PAHs in MC20 sediments.

Comparison with Other Data

In an effort to provide regional context to our analytical sediment PAH concentrations, we looked at a few sets of publicly available sediment PAH data from the northern Gulf of Mexico. These comparisons are detailed below.

In 2006, the Minerals Management Service (MMS), now split into the Bureau of Safety and Environmental Enforcement (BSEE) and the Bureau of Ocean and Energy Management (BOEM), conducted a study of oil drilling locations in the Gulf of Mexico (Continental Shelf Associates, Inc., 2006) which included both near-field (<500 m) and far-field (>10 km) PAH analysis in nearby marine sediments. Though the sediments sampled for MMS are located in deeper waters than those at MC20, their proximity to oil and gas drilling sites represent a good indicator of expected oil contamination in marine sediments adjacent to offshore drilling locations. The closest site to MC20 included in the MMS study is at Mississippi Canyon Block 292 (MC292). The list of PAH compounds used to calculate total PAHs for the MMS study included 48 compounds compared to 64 for this study. In order to make a direct comparison, total PAH values for this study were summed using the same 48 compounds as those used for MMS (Table 7.1). Sediment PAH concentrations at the MC292 site ranged from 43 to 748 ng/dry g. With the exception of our reference site BC13 (677 ng/dry g, n=48; 2,990.2 m from release point(s)), nearly all the MMS concentrations fall below those measured in sediments for this study. The highest MMS concentration of 748 ng/dry g found at MC292 also approached the concentration measured from our reference site BC14 (752 ng/dry g, n=48; 995.9 m from release point(s)).

The entire MMS study near-field sites (<500 m; n=83) had a median total PAH concentration of 232 ng/dry g. MC20 sediment total PAHs within this study's "measureable impact area" (<500 m from release point(s)) all have higher concentrations than those measured by MMS at MC292, indicating likely impact from the ongoing release of oil into the marine environment. It is important to note that the nearest MMS study location of MC292 is on the continental slope and farther from land-based sources of PAHs, not higher on the continental shelf and closer to shore like MC20.

To give further regional context to our analytical sediment PAH concentrations, our results are also compared to previously collected sediment data from NOAA's Mussel Watch Program (MWP). The MWP currently has 14 historical sediment collection sites in Louisiana coastal waters (Figure 7.8). The value of comparing MC20 samples to those of MWP is that they provide an idea of what nearby sediment total PAH concentrations in the region were around the time of the original release event. Total PAH concentrations from the most

recent sediment collections completed in 2005 generally show lower concentrations than those measured for this study. Two sites from the MWP dataset, one located in Lake Pontchartrain and one in the Pass-a-Loutre State Wildlife Management Area, fall within the same range of total PAHs measured in this survey. The Lake Pontchartrain MWP site is located adjacent to the Lake Pontchartrain Causeway, a nearby harbor and marina, and the outfall of the 17th Street Canal. This location helps explain the relatively elevated total PAH concentrations for this site. For the MWP site located in the Pass-a-Loutre State Wildlife Management Area, the relatively elevated concentrations are less clear.

The NS&T Program includes a historical national-level contaminant monitoring database containing samples and analysis ranging from 1986 through the present. This contaminant monitoring database, includes a wide range of chemicals including PAHs. Using this continually growing database we can compare the results of this study further by examining how the total PAHs measured at MC20 compare to the median and 85th percentile values for all current comparable NS&T total PAH data. The reason we choose these two values, median and 85th percentile, is that they represent the middle value for the dataset, and a value above which can represent potentially elevated concentrations. The median concentration of all NS&T total PAHs (2006/2007 NS&T data) is 395 ng/dry g while 85th percentile concentration is 2,883 ng/dry g. All sediment sites, including the reference sites, exceeded the NS&T median for total PAHs. Sites BC01 inside the erosional pit at the northwest corner of the jacket, along with BC02 at approximately 100 m distance from the release point(s) both exceeded the NS&T 85th percentile concentration.

NOAA Sediment Quality Guidelines for Total PAHs.

The NS&T Program has developed effects-based, numeric guidelines that allow for the estimation of likely toxic effects of certain sediment contaminants (Long *et al*., 1998). As discussed earlier, these guidelines are comprised of the Effects Range-Low (ERL) and Effects Range-Median (ERM) and represent thresholds below which toxic effects would rarely be observed (<ERL) and above which toxic effects would frequently be seen (>ERM). Values between the ERL and ERM thresholds represent concentrations at which toxic effects occasionally may be observed (NOAA NS&T, 1998). ERL and ERM values for total PAHs (n=64) are shown in Figure 7.8. With the exception of the sediment sample collected from within the erosional pit at the northwest corner of the jacket (BC01), no other sediment samples, including those from MWP historical samples, exceeded the ERL.

ERL and ERM guidelines have also been calculated for a number of individual PAHs. These guidelines are shown in Table 7.5. No sediment samples analyzed for this study exceeded any of the ERL or ERM thresholds for individual PAH compounds. When comparing the same individual PAH compounds to the calculated NS&T median and 85th percentile values, a number of sites had exceedances of the NS&T median. None of the MC20 sites exceeded the NS&T 85th percentiles. Additional results for individual PAHs and their related thresholds are presented in Table 7.5.

Table 7.5. Comparison of MC20 sediment sample concentrations for select PAHs with NOAA NS&T data and guidelines.

	Sites										NS&T Statistics and Guidelines			
Compound	BC01	BC02	BC03	BC04	BC05	BC06	BC07	BC13	BC14	BC15	Median	85th percentile	ERL	ERM
Acenaphthylene	13.1	7.37	5.48	5.89	4.90	4.65	4.89	5.01	4.77	4.68	2.1	15.1	44	640
Anthracene	ND	6.69	6.06	6.77	5.94	5.47	5.53	5.94	5.55	5.73	3.4	38.7	85.3	1,100
Napthalene	7.07	6.68	6.58	7.32	6.40	6.08	6.71	6.99	7.29	7.33	3.7	27.6	160	2,100
Benzo-a-pyrene	48.2	21.1	17.0	18.6	15.0	14.6	14.4	13.2	13.8	14.9	14.7	127	430	1,600
Dibenzo(a,h) anthracene	16.7	6.09	4.61	4.88	4.03	3.93	3.12	4.59	4.14	3.9	5	23.8	63.4	260

All concentrations are in ng/dry g. ND = Non Detect

Water samples

Total PAHs were also measured in the six water samples collected for this study. Total PAHs for all water samples had a mean concentration of 824.13 ± 1,424.38 µg/L with a minimum 0.04 µg/L (WAT02 – reference site) and a maximum value of 3,700.93 µg/L (WAT01 – within the plume at the northwest corner of the jacket). PAH histograms (Figure 7.11) of water samples show that water PAHs are consistent with particulate oil. Sample WAT01 (Figure 7.11, dark blue) also still contains prominent decalins, naphthalene, and methyl-naphthalenes, which are absent from surface water oil possibly due to evaporation upon reaching the surface, and closely resembles the mid-water column oil that was collected and analyzed.

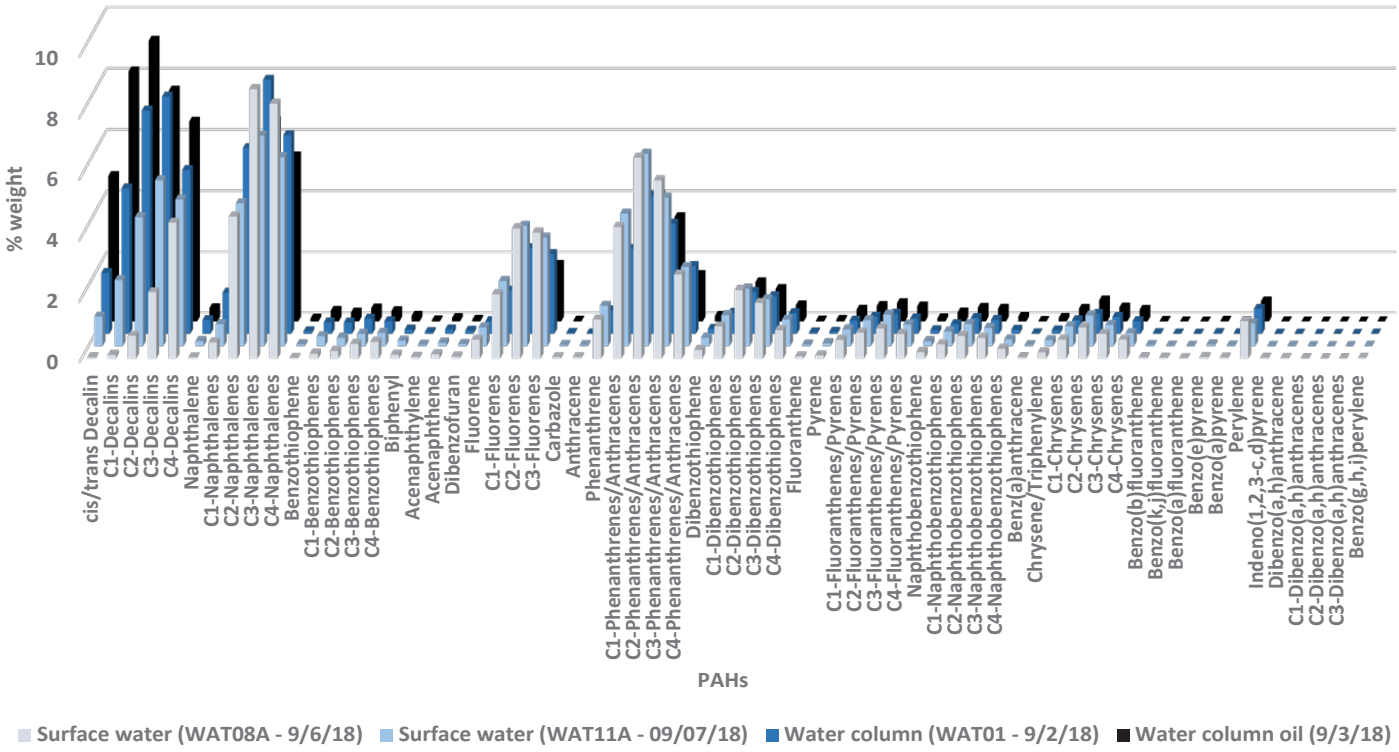

Figure 7.11. Comparison of subsurface collected oil, subsurface collected water, and surface water by percent weight of total Polycyclic Aromatic Hydrocarbons (PAHs) including decalins.

The ratio of the percent Low Molecular Weight (LMW) PAHs (≤3 rings) and percent High Molecular Weight (HMW) PAHs (≥4 rings) in water samples is presented in Figure 7.12. The mean percent of total for LMW PAHs in water was 87.66 ± 1.20% while the mean percent of total for HMW PAHs in water was 12.34 ± 1.20%. The minimum percent of total for LMW PAHs was 86.29% at surface water site WAT08b while the maximum was 89.60 % in water column sample WAT01 (within the plume at the northwest corner of the collapsed jacket). The minimum and maximum percent of total for HMW PAHs was the inverse of the above at 10.40% and 13.71%, respectively.

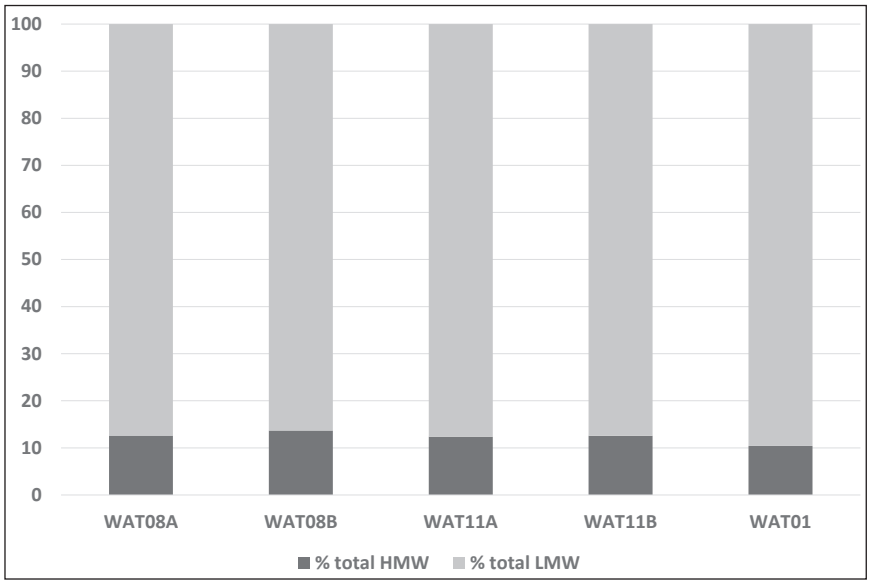

Figure 7.12. Composition of HMW and LMW as a percent of total PAHs in MC20 water samples.

WAT02, which was collected outside of the rising plume, is excluded from the above calculations and in Figure 7.12 as the measured concentrations were below the MDL. For the remaining five water samples, the ratios were very similar, displaying a much larger percentage of LMW PAHs than HMW PAHs. The ratio of HMW PAHs in sample WAT01 are slightly higher than those in the other water samples as the PAHs in WAT01 have not reached the surface and experienced losses of LMW PAHs, such as naphthalenes, to evaporation. When comparing the %LMW versus %HMW in water samples to those observed in sediments (Figure 7.10), we see that the oil collected from the water column and surface sheen is "fresher" than the oil collected in any sediment samples. In other words, oil escaping the ocean floor at the identified release point(s) within the erosional pit is "fresher" than the oil found at the perimeter of the pit and oil in sediments up to approximately 3000 m away.

LMW PAHs dissolved in water tend to be indicative of petrogenic sources (Karlsson and Viklander, 2008) and are often acutely toxic to aquatic organisms (Neff, 1979). It is important to note that the measurement of total PAHs in water samples from this study include both the dissolved fraction and Water Associated Fraction (WAF) LMW PAHs along with the more hydrophobic and less soluble HMW compounds. WAF, sometimes referred to as the Water Soluble Fraction (WSF) or Water Accommodated Fraction (also WAF), represents the fraction of LMW PAHs that rapidly disperse into water (Log K_{OW} <4) and are not persistent in the aquatic environment due to their high volatility (Perrichon *et al*., 2016). While there most likely is WAF present in samples from MC20 water, there appears to be no "excess" of the more soluble PAHs present. The distributions of PAHs in water samples are indicative of particulate oil, and any dissolved PAHs present are most likely being overwhelmed by particulate or surface sheen oil. Water samples WAT08A,B (surface), WAT11A,B (surface), and WAT01 (mid-water) had no recoverable bulk oil fractions, as opposed to mid-water column sample WAT05 which had recoverable bulk oil from the sample collection effort. Oil related chemicals measured in WAT08A,B and WAT11A,B therefore comprise primarily particulate and surface sheen oil. The separated water portions remaining from mid-water column sample WAT05 (oil sample) after the oil fraction was manually removed in the laboratory was not analyzed individually for this study.

Oil sample

Total PAHs in the oil were prepared and analyzed in triplicate to confirm results. The mean concentration of total PAHs in the oil product was 17,389 ± 132 µg/dry g. The minimum concentration of total PAHs in oil product was 17,252 µg/dry g while the maximum concentration was 17,515 µg/dry g.

When comparing the ratio of percent LMW to HMW PAHs found in the oil product, the ratio was very similar to those found in the water samples from this study, displaying a much larger percentage of LMW PAHs than HMW PAHs (11% HMW vs. 89% LMW). As stated previously, there appears to be no "excess" of the more soluble PAHs present and the distributions of PAHs in water samples are indicative of particulate oil. Any dissolved PAHs present are most likely being overwhelmed by particulate or surface sheen oil.

7.3.5 Biomarkers

The ten sediment samples collected for this study along with the oil product sample and the Standard Reference Material (SRM – NIST oil standard 2779) oil from MC252 were analyzed for a suite of 56 individual terpane and sterane biomarkers (chemical fossils) and stable carbon isotope compositions of the C15+ aliphatic and aromatic hydrocarbon fractions (Table 7.6). This analysis allowed for the detailed characterization and comparison of the specific crude oil(s) present and to predict corresponding source rock type, age, and thermal maturity. These samples were statistically compared to GeoMark Research, LTD's greater Gulf of Mexico database of approximately 1,200 oils (Zumberge, 1997; GoMark, 2006). Analytical and statistical methods for the following results can be found in Zumberge *et al*. (2005).

GeoMark compared the biomarkers and stable isotope results using hierarchical cluster analysis and principal component analysis (PCA) to show that the WAT05 oil collected herein was from the same oil family as MC20 oil(s) within their database. This was achieved by using the same 56 biomarkers and carbon isotopes as those shown in Table 7.6. These oils are believed to have been sourced from mid-Cretaceous shales and, at MC20, occur in various Pliocene-aged reservoirs. Other oils from this same hierarchical cluster or "family", which GeoMark refers to as the 5-10 family (Figure 7.13), include other Mississippi Canyon oils, such as the Macondo oil released during the Deepwater Horizon.

Because of interferences from naturally-occurring organic matter in the sediments studied, GeoMark was unable to further confirm that the oil in BC01 and BC02 was specifically from the 5-10 family (Figure 7.13), only from Family 5 in general. Owing to the increasing influences of "background" hydrocarbons in the sediments further from the source, the specific family of oil in the other sediments studied could not be determined.

Table 7.6. List of GeoMark biomarker compounds analyzed for this study.

GeoMark Biomarker Compounds	
C19H34 tricyclic diterpane	17α, 21β-trishomohopane (22S-C33S)
C20H36 tricyclic diterpane	17α, 21β-trishomohopane (22R-C33R)
C21H38 tricyclic diterpane	17α, 21β-extended hopane (22S-C34S)
C22H40 tricyclic terpane	17α, 21β-extended hopane (22R-C34R)
C23H42 tricyclic terpane	17α, 21β-extended hopane (22S-C35S)
C24H44 tricyclic terpane	17α, 21β-extended hopane (22R-C35R)
C25SH46 tricyclic terpane	13β, 17α-diacholestane (20S)
C25RH46 tricyclic terpane	13β, 17α-diacholestane (20R)
C24H42 teteracyclic terpane	5α-cholestane (20S) + 5β-cholestane (20R)
C26SH48 tricyclic terpane	5α, 14β, 17β-cholestane (20R) + 13β, 17α-diastigmastane (20S-S4)
C26RH48 tricyclic terpane	5α, 14β, 17β-cholestane (20R) + 13β, 17α-diastigmastane (20S-S4B)
18α, 21β-22,29,30-trisnorhopane	5α, 14β, 17β-cholestane (20S-S5)
17α, 18α,21β-25,28,30-trisnorhopane	5α, 14β, 17β-cholestane (20S-S5B)
17α, 21β-22,29,30-trisnorhopane	5α-cholestane (20R)
C28 demethylated hopane	diastigmastane
17a, 18a, 21b-28, 30-bisnorhopane	5α-ergostane (20S)
C29 demethylated hopane	5α, 14β, 17β-ergostane (20R) + 5β-ergoastane (20R-S9)
17α, 21β-30-norhopane	5α, 14β, 17β-ergostane (20R) + 5β-ergoastane (20R-S9B)
18α-30-norneohopane	5α, 14β, 17β-ergostane (20S-S10)
17α, 15α-methyl-27-norhopane (diahopane)	5α, 14β, 17β-ergostane (20S-S10B)
oleanane	5α-ergostane (20R)
17α, 21β-hopane	5α-stigmastane (20S)
17β, 21α-moretane	5α, 14β, 17β-stigmastane (20R-S13)
17α, 21β-30-homohopane (22S-C31S)	5α, 14β, 17β-stigmastane (20R-S13B)
17α, 21β-30-homohopane (22S-C31R)	5α, 14β, 17β-stigmastane (20S) + 5β-stigmastane (20R-S14)
gammacerane	5α, 14β, 17β-stigmastane (20S) + 5β-stigmastane (20R-S14B)
17α, 21β-bishomohopane (22S-C32S)	d4-5α-stigmastane (20R)
17α, 21β-bishomohopane (22R-C32R)	5α-stigmastane (20R)

Sediment, Water, and Oil Chemistry

Figure 7.13 shows the resultant dendrogram generated by GeoMark. The correlation coefficient determines the number of clusters/families where a coefficient of 0.75 gives 9 families while a higher correlation of 0.86 yields 22 families of oil.

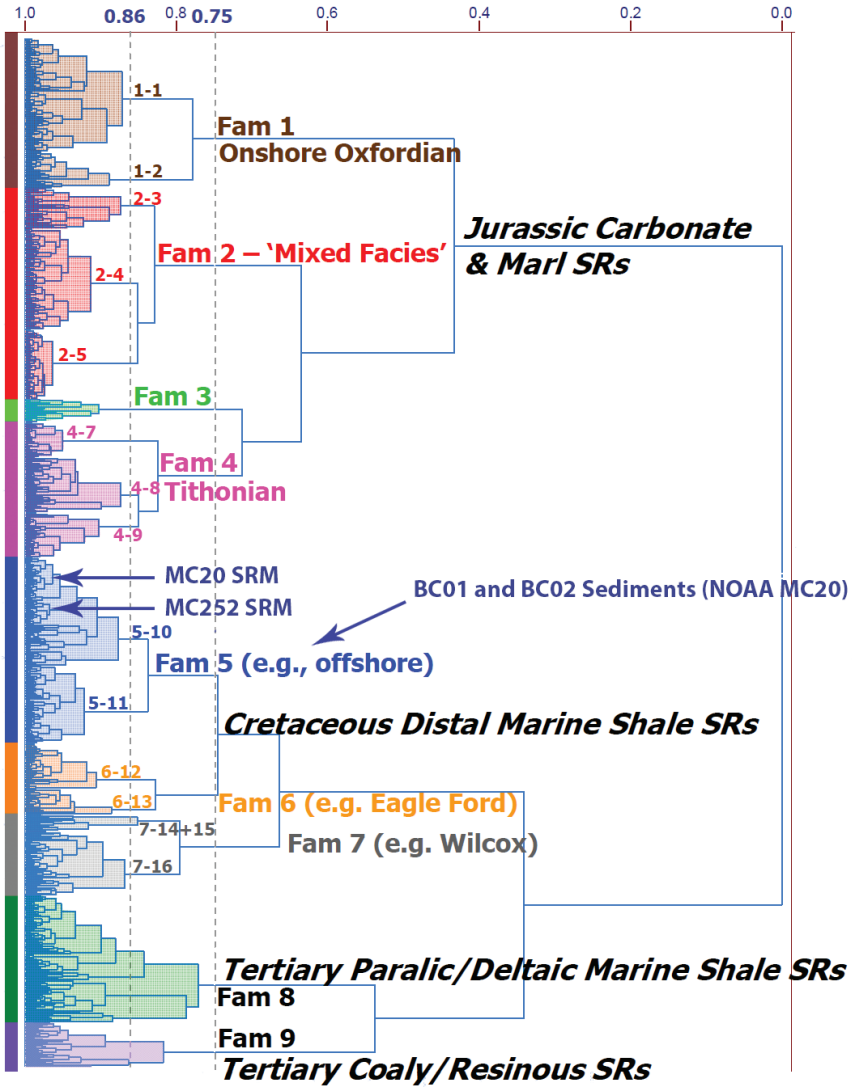

Figure 7.13. Dendrogram of the approximately 1,200 Greater Gulf of Mexico GeoMark biomarker oils. Correlation coefficient values, 0.86 and 0.75, are shown along the top. Fam = Family, SR = Source Rock, SRM = Standard Reference Material.

With the Mississippi Canyon (MC) oils (including MC20 oil(s) from Pliocene reservoirs previously analyzed by GeoMark and within their proprietary database, MC20 oil collected during this study, and MC252 collected during the Deepwater Horizon oil spill) added to the statistical mix of the approximately 1,200 greater Gulf of Mexico oils, they all fall within Family 5-10, oils believed to be sourced from mid-Cretaceous shales (Figure 7.13). Thus, the specific character of the MC20 oil collected from the water column herein exhibits comparable biomarker and stable isotope characteristics as other MC oils, including MC20 oil(s) from GeoMark's database.

Even though MC20 extract samples from the perimeter of the erosional pit (BC01) and at approximately 100 m from the release point(s) (BC02) have the most hydrocarbon (HC) extracts and the least amount of interfering Recent Organic Matter (ROM), their steranes have been compromised by more severe biodegradation (Table 7.7). However, the resistant terpanes and carbon isotopes strongly suggest that the mid water column collected oil sample and extracts from BC01 and BC02 are highly correlative and share a common Cretaceous shale source rock (Family 5). The other sediment samples all show indications of thermogenic oil, but there is too much interfering ROM for reliable statistical correlation to the MC20 and SRM oils.

Although the sterane distributions found at site BC01 is compromised by severe biodegradation, the more resistant terpanes, especially the tricyclics, show a high degree of similarity with the nearby mid water collected oil sample (Figure 7.14). This, together with very similar carbon isotopic compositions, suggest that the nearest sediment samples and the oil also share a common Cretaceous shale source rock. Site BC07 (at approximately 600 m distance from the release point(s)) and the other sediment samples with relatively low HC concentrations contain ROM components (mostly immature ββ-hopanes and hopenes) that preclude relievable statistical correlations with mid-water column MC20 oil.

Table 7.7. Biomarker results from NOAA MC20 sediments and oil. EOM = Extractable Organic Material, HC = Hydrocarbons. All concentrations in parts per million (ppm).

Sample	Matrix	Distance from release (m)	GOM Block	EOM (ppm)	HC (ppm)	Comment	Family
BC01	Sediment	27.9	MC20	5,733	4,446	Heavy biodegradation	~Family 5
BC02	Sediment	99.8	MC20	991	585	Heavy biodegradation	~Family 5
BC03	Sediment	203.2	MC20	611	279	ROM interference	-
BC04	Sediment	304.4	MC20	513	226	ROM interference	-
BC05	Sediment	406.9	MC20	652	173	ROM interference	-
BC06	Sediment	505.7	MC20	378	166	ROM interference	-
BC07	Sediment	604.8	MC20	312	140	ROM interference	-
BC13	Sediment	2,990.20	SP073	126	126	ROM interference	-
BC14	Sediment	995.9	MC20	146	146	ROM interference	-
BC15	Sediment	2,006.80	MC20	120	120	ROM interference	-
MC20 Oil	Oil	-	MC20	-	-	Mild biodegradation	Family 5-10/11
MC252 Oil (SRM)	Oil	-	MC252	-	-	Non-degraded Macondo oil	Family 5-10

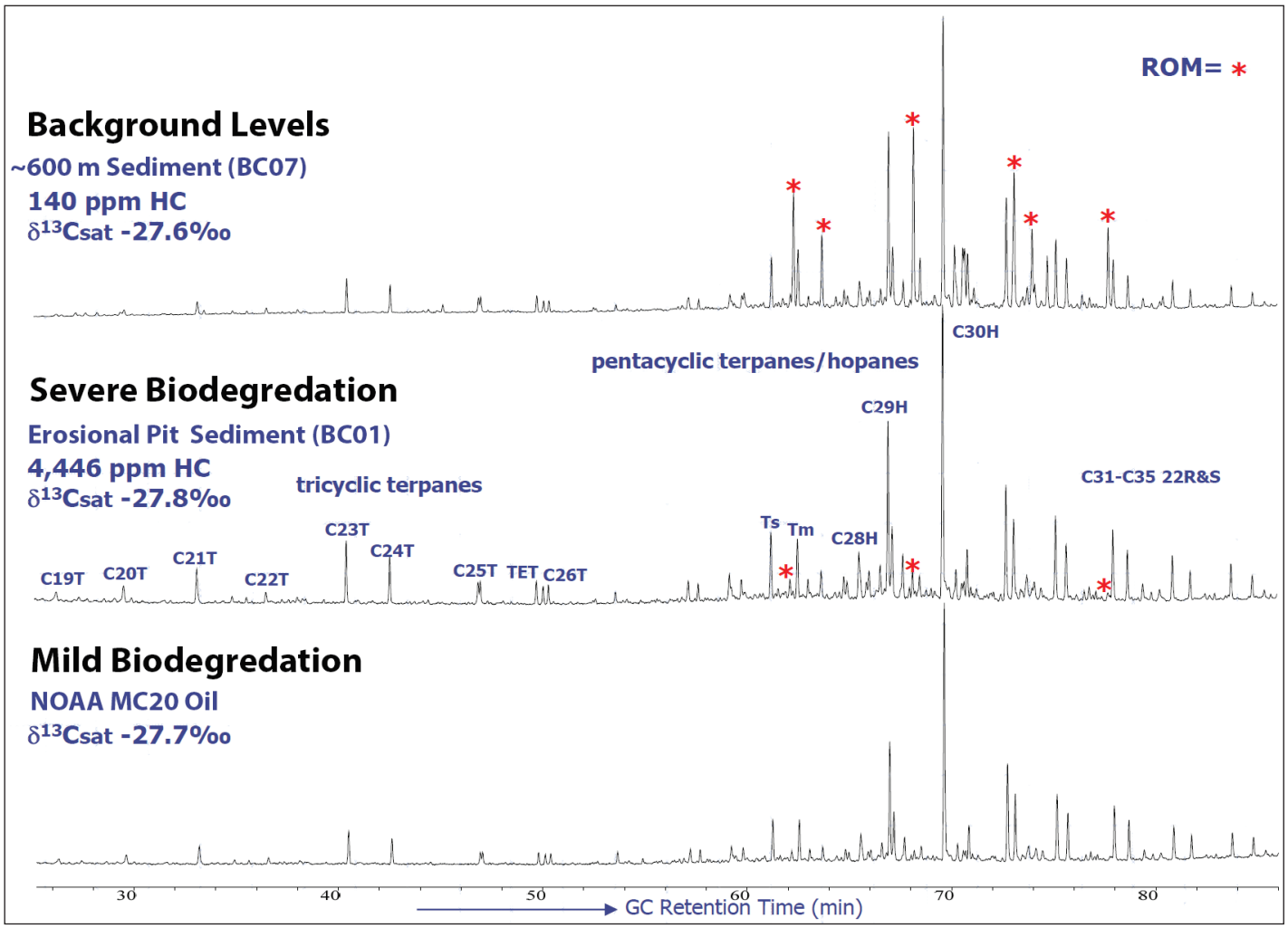

Figure 7.14. Saturated petroleum biomarker comparison between NOAA MC20 sediments (BC01 and BC07) and oil (subsurface collected via ROV). ROM = Recent Organic Material.

Sediment, Water, and Oil Chemistry

As was seen with the distribution of concentrations of total PAHs and TPH, concentrations of HCs for biomarker analysis (C15 + saturates + aromatics) also decreased as distance from the release point(s) increased (Figure 7.15).

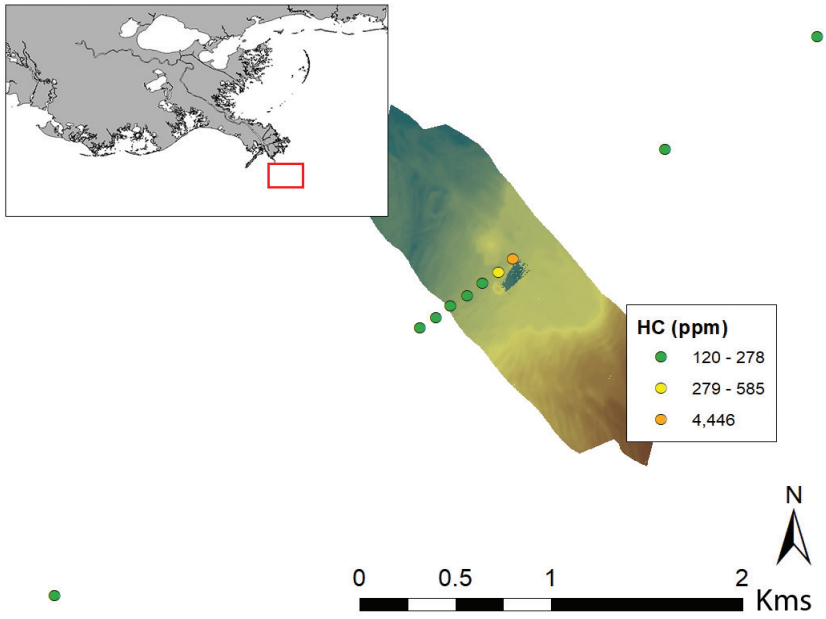

Figure 7.15. Map of biomarker hydrocarbon (HC) concentrations (C15 + saturates + aromatics).

7.4 CONCLUSIONS

While each of the subcategories of chemical contaminant class and analysis type point toward individual results and conclusions, the design of this study allows for broader conclusions based on the combined results. The following section details the individual and combined conclusions from those chemical analysis results.

Total Polycyclic Aromatic Hydrocarbons (PAH), Total Petroleum Hydrocarbons (TPH), biomarker Hydrocarbons (HC), and total *n*-alkanes in sediments all decrease as distance from the northwest corner of the collapsed jacket and the identified release point(s) increases. The highest concentrations of total PAHs, TPHs, HCs, and total *n*-alkanes were also consistently at concentrations at least an order of magnitude higher at the perimeter of the erosional pit than in the rest of the study area. While this pattern appears across all of the above chemical compound classes, there is a significant correlation (at the 95% confidence level) only between distance from the release point(s) and TPH for sites BC01 through BC05 (R^2 = 8411). Beyond 500 m there is no measurable level of MC20 specific oil in the sediments. This does not mean that MC20 related oil is not being deposited beyond 500 m, simply that concentrations in the sediments are no longer dominated by MC20 oil and that natural processes and backround deposition of organic materials interfere with our ability to detect the oil. TPH in sediments has an inverse relationship to distance from the release point(s) (TPH increases as distance decreases; logNormal distribution - F > 0.0283).

Concentrations of oil in sediments at MC20 are higher than those measured by MMS (Continental Shelf Associates, Inc., 2006) adjacent to other Gulf of Mexico drill sites, likely owing to the excess of oil released from both the original accident and the ongoing release, greater proximity to other sources on the shelf (compared to MMS study sites), and greater proximity to Mississippi River effluent's influence on shelf sediments. The concentrations of total PAHs in sediments around the MC20 site are also an order of magnitude higher than all but two of the sediment sites measured by NOAA's Mussel Watch Program along the nearby Louisiana coastline. Full characterization of the distribution of oil related contaminants in sediments at the MC20 site will require future sampling efforts.

Looking at the percent weight of total for saturated hydrocarbons in water column and surface water samples, we observe a progressive loss of *n*-alkanes in the *n*-C9 through *n*-C14 range and a resultant increase (as a percent of the total) in the degradation resistant acyclic isoprenoids pristane and phytane (Figure 7.16). This loss is indicative of weathering from evaporation, and photolysis. The variability among water column oil (WAT05) and water column water (WAT01) indicates that the oil being released from the seafloor is not homogeneously weathered and may potentially vary in the short-term. This heterogeneity in weathering is also accompanied by heterogeneity in the specific biomarkers of the emanating oil. Taken together, this collective heterogeneity is evidence that there is more than one leaking oil well with multiple oils entering the marine environment

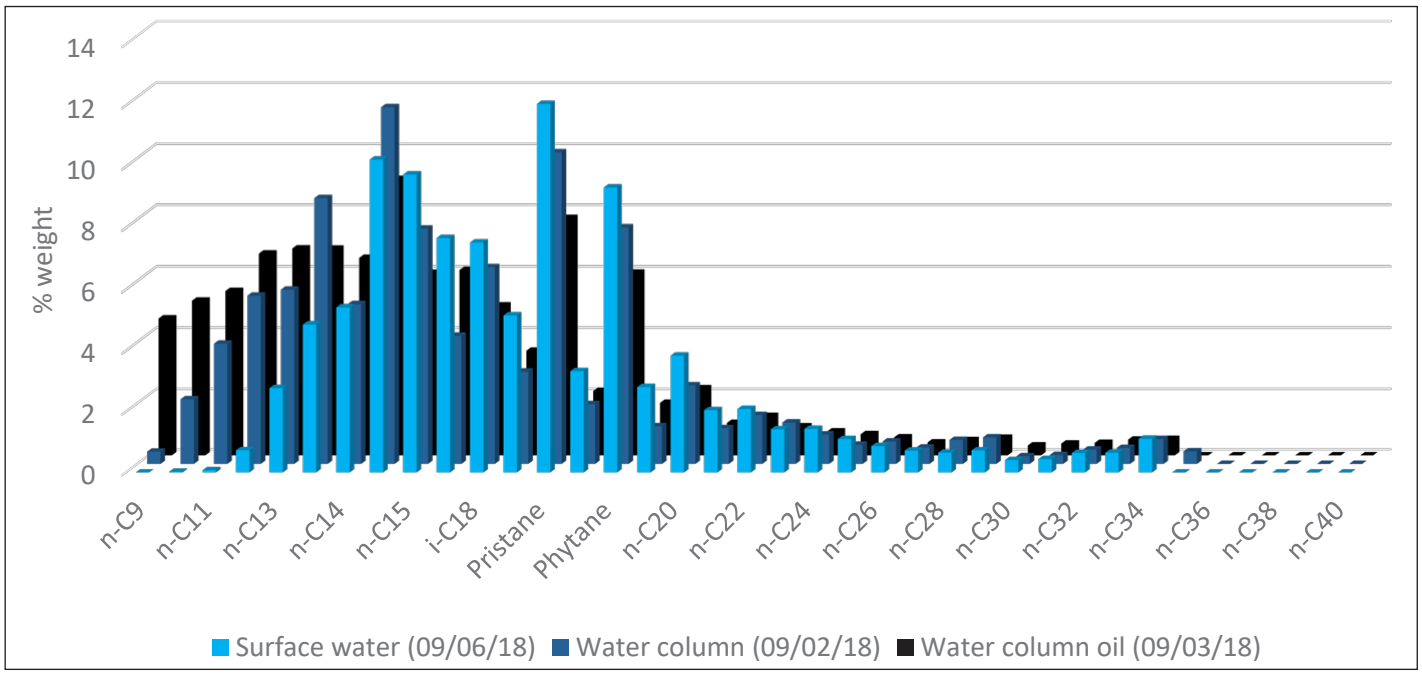

Figure 7.16. Comparison of subsurface collected oil, subsurface collected water, and surface water by percent weight of total n-alkanes.

at depth and commingling to various degrees under different physical ocean current and surface conditions. Adding to the conclusion of ongoing release from multiple leaking wells at the MC20 site is the data from the two original wells (three reservoirs) analyzed by GERG in 1985. The fact that oil from Well #9 is degraded in the reservoir along with the variability between the oils from Wells #9 and #2 all help to explain why we continue to see heterogeneous degraded oil continuing to be released into the marine environment. It is therefore not surprising that subtle heterogeneities are observed in this and other datasets.

Similar results were observed in the lighter Low Molecular Weight (LMW) PAHs, especially in the decalins and naphthalene, where we observe progressive losses and a resultant increase (as a percent of the total) in the relatively heavier LMW PAHs including fluorenes and phenanthrene/anthracenes (Figure 7.11) possibly due to evaporation at the surface. Subtleties between surface water samples and mid-water column collected oil again point toward heterogeneities in the multiple MC20 oils being released from the ocean floor.

By comparing TPH, saturated hydrocarbons, and PAH data for all three matrices (MC20 subsurface oil, erosional pit sediment (BC01), subsurface water (WAT01), and surface water (WAT11A) we can further try to understand the source and fate of the oil entering the environment. The severely degraded nature of the saturated hydrocarbons in sediments proximal to the erosional pit precludes them being the primary source of the mildly degraded MC20 oil collected and measured in the water column. The similarity between the subsurface collected MC20 oil, subsurface collected water, and surface water samples also point towards a primary source other than the sediment. Looking at the results from other chapters in this document also supports this conclusion (see Chapters 3 and 6). The oil escaping the seafloor from the identified release point(s) is less weathered than oil residues in the surrounding sediments.

A low dissolved oxygen anomaly between 50 and 70 m detected by a CTD cast on 5 September (Chapter 2) may indicate catabolizing of hydrocarbons through microbial respiration (Hazen *et al*., 2010). This process could also help explain some of the variability between mid-water column collected water (WAT01) and mid-water column collected oil (WAT05).

Sediment, Water, and Oil Chemistry

With the location of the erosional pit residing above the terminal end of the damaged conductor bundle (Figure 7.17), along with the finding that oil in the water column is only mildly degraded as compared to the heavily degraded sediment oils (Figure 7.14), we conclude that oil continues to be actively released into the marine environment. Because the conductor bundle terminus is buried under approximately 20 m of deposited sediment from the original mud slide, any released oil and gas must travel through that sediment before reaching the ocean floor. That distance would most likely include channelization and varying residence times for oil as different fractions partition into the adjacent sediment, are resuspended by upward motion of both oil and gas, or pass through relatively unimpeded. The fact that we find relatively little long chain *n*-alkanes as a percent of total weight in the subsurface collected oil, subsurface water, and surface water and find those fractions in the sediments (Figure 7.18), points toward rapid partitioning out of the heavier fractions once the water column is reached, if not partially before, and precipitation of these fractions onto the nearby ocean floor sediments. Additionally, biodegradation of oil as it passes through the top 1-2 m of sediment is possible (Wenger and Isaksen, 2002) and could further explain some of the mild degradation of mid-water column collected MC20 oil.

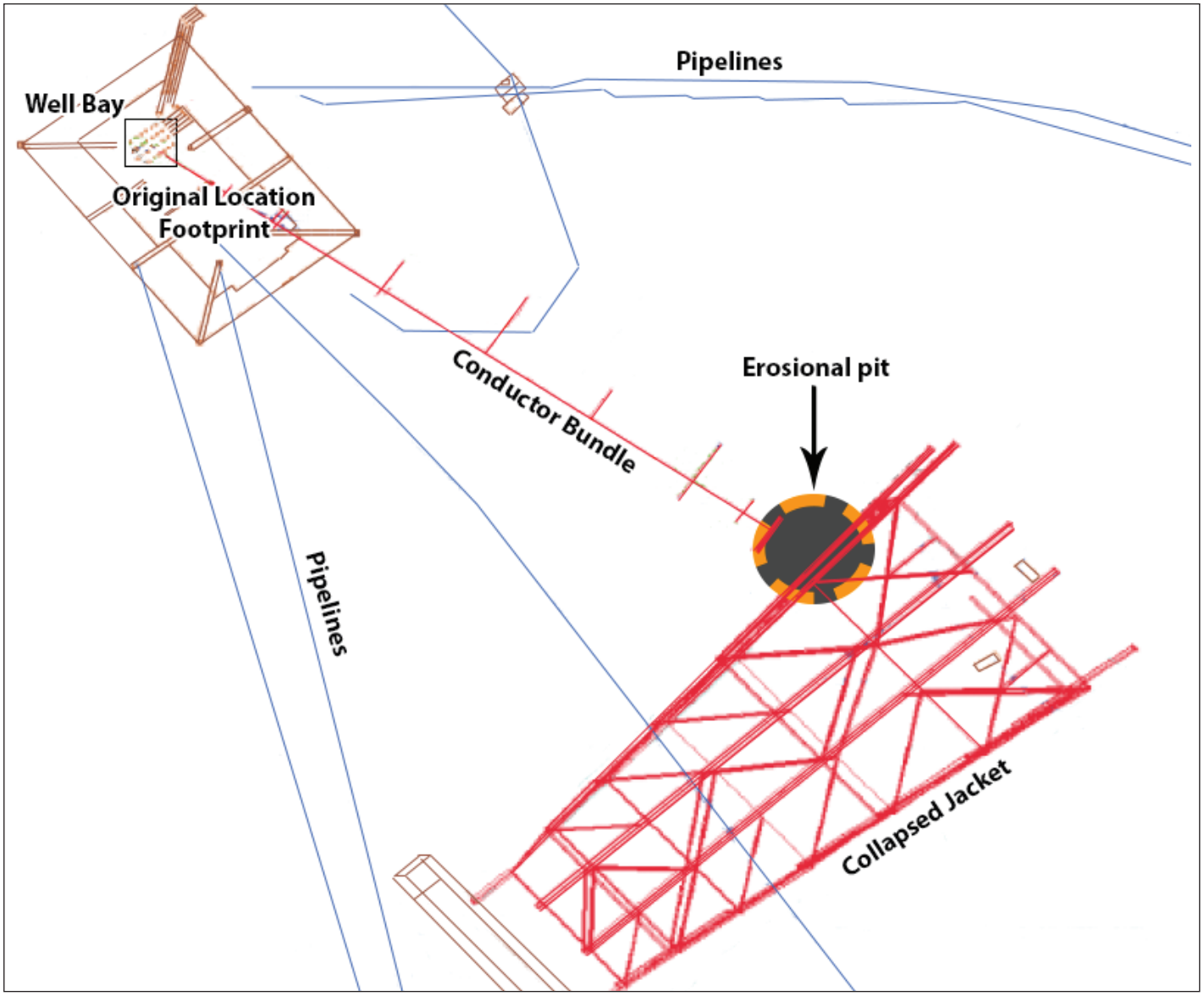

Figure 7.17. Map depicting the location of the collapsed jacket structure in relation to its original position along with the location of the conductor bundle terminating at the northwest corner of the jacket. Erosional pit marker is an approximation. Adapted from Staves et al. (2013).

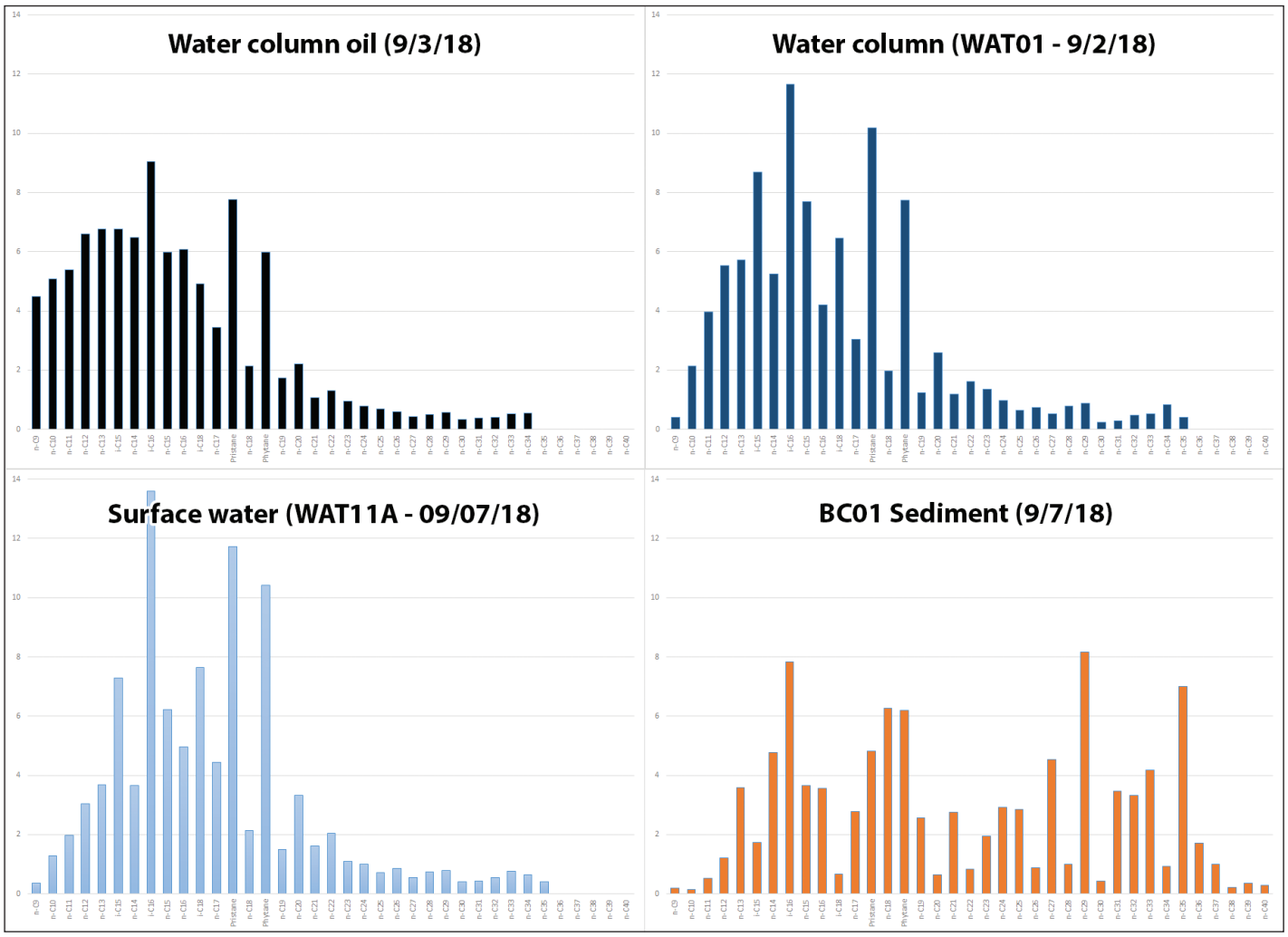

Figure 7.18. Histogram comparison between saturated hydrocarbons as percent of total weight for MC20 subsurface collected oil (black- WAT05), subsurface collected water (dark blue – WAT01), surface water (light blue – WAT11A), and erosional pit perimeter sediment (orange – BC01). X-axis = n-C9 through n-C40 from left to right.

The simplest explanation for the degradation observed in mid-water column oil at the MC20 site comes from the original 1985 oil data analyzed by GERG for Well #9, where the oil in the reservoir is degraded. While we cannot say whether any of the oil collected mid-water column for this study is from Well #9, the fact that at least one of the reservoirs that were tapped as part of the total 25 producing MC20 wells (at the time of the destruction of the platform) was degraded points toward the possibility that other Wells at MC20 may also have exhibited similar properties.

Taken together, results from this analysis of oil related compounds in the water column, sediments, and surface slick all point toward continued release of MC20 oil from multiple Pliocene oil reservoirs.

7.5 REFERENCES

ATSDR. 1995. Toxicological Profile for Polycyclic Aromatic Hydrocarbons (PAHs). U.S. Department of Health and Human Services, Agency for Toxic Substances and Disease Registry. Atlanta, GA. 487 pp. Online: https://www.atsdr.cdc.gov/toxprofiles/tp.asp?id=122&tid=25 (Accessed 24 May 2019)

ATSDR. 1999. Toxicological Profile for Total Petroleum Hydrocarbons (TPH). U.S. Department of Health and Human Services, Agency for Toxic Substances and Disease Registry. Atlanta, GA. 315 pp. Online: https://www.atsdr.cdc.gov/ToxProfiles/tp.asp?id=424&tid=75 (Accessed 24 May 2019)

Continental Shelf Associates, Inc. 2006. Effects of Oil and Gas Exploration and Development at Selected Continental Slope Sites in the Gulf of Mexico. Volume II: Technical Report. U.S. Department of the Interior, Minerals Management Service, Gulf of Mexico OCS Region, New Orleans, LA. OCS Study MMS 2006-045. 636 pp.

Douglas, G.S., S.D. Emsbo-Mattingly, S.A. Stout, A.D. Uhler, and K.J. McCarthy. 2007. Chapter 9 - Chemical Fingerprinting Methods. pp. 311-454. In: B.L. Murphy and R.D. Morrison (eds.), Introduction to Environmental Forensics (Second Edition). Academic Press. 776 pp.

GeoMark. 2006. GeoMark RFDbase, Oil Database. Online database: https://www.rfdbase.com (Accessed 24 May 2019)

Hassett, J.J., J.C. Means, W.L. Banwart, and S.G. Wood. 1980. Sorption Related Properties of Sediments and Energy Related Pollutants. U.S. Environmental Protection Agency, Environmental Research Laboratory. EPA-600/3-8-041. 133 pp.

Hazen, T.C., E.A. Dubinsky, T.Z. Desantis, G.L. Andersen, Y.M. Picento, N. Singh, J.K, Jannson, A. Probst, S.E. Borglin, J.L. Fortney, W.T. Stringfellow, M. Bill, M.E. Conrad, L.M. Tom, K.L. Charvarria, T.R. Alusi, R. Lamendella, D.C. Joyner, C. Spier, J. Baelum, M. Auer, M.L. Zemla, R. Chakraborty, E.L. Sonnenthal, P. D'Haeseleer, H.N. Holman, S. Osman, Z. Lu, J.D. Van Nostrand, Y. Deng, J. Zhou, and O.U. Mason. Deep-Sea Oil Plume Enriches indigenous Oil-Degrading Bacteria. Science. 08 OCT 210 : 204-208.

Hyland, J.L., R.F. Van Dolah, and T.R. Snoots. 1999. Predicting stress in benthic communities of southeastern U.S. estuaries in relation to chemical contamination of sediments. Environmental Toxicology and Chemistry 18(11): 2557-2564. doi: https://doi.org/10.1002/etc.5620181124

Karlsson, K., and M. Viklander. 2008. Polycyclic Aromatic Hydrocarbons (PAH) in Water and Sediment from Gully Pots. Water, Air, and Soil Pollution 188(1-4): 271-282. doi: https://doi.org/10.1007/s11270-007-9543-5

Kimbrough, K.L., G.G. Lauenstein, and W.E. Johnson (eds). 2006. Organic Contaminant Analytical Methods of the National Status and Trends Program: Update 2000-2006. National Oceanic and Atmospheric Administration, National Status and Trends Program. NOAA Technical Memorandum NOS NCCOS 30. Silver Spring, MD. 137 pp.

Long, E.R., L.F. Field, and D.D. MacDonald. 1998. Predicting toxicity in marine sediments with numerical sediment quality guidelines. Environmental Toxicology and Chemistry 17(4): 714-727. doi: https://doi.org/10.1002/etc.5620170428

Long, E.R., D.D. MacDonald, S.L. Smith, and F.D. Calder. 1995. Incidence of adverse biological effects within ranges of chemical concentrations in marine and estuarine sediments. Environment and Management 19(1): 81-97. doi: https://doi.org/10.1007/BF02472006

Long, E.R., and L.G. Morgan. 1990. The Potential for Biological Effects of Sediment-Sorbed Contaminants Tested in the National Status and Trends Program. National Oceanic and Atmospheric Administration, National Ocean Service. NOAA Technical Memorandum NOS OMA 52. Rockville, MD. 175 pp.

NOAA NS&T. 1998. NS&T Program: National Status and Trends Program for Marine Environmental Quality. National Oceanic and Atmospheric Administration, National Ocean Service, National Status and Trends Program. 32 pp.

NRC. 1985. Oil in the sea: Inputs, fates, and effects. National Academy Press, Washington D.C. 601 pp. doi: https://doi.org/10.17226/314

Neff, J.M. 1979. Polycyclic aromatic hydrocarbons in the aquatic environment: Sources, fates and biological effects. Applied Science Publishers. 262 pp.

Perrichon, P., K. Le Menach, F. Akcha, J. Cachot, H. Budzinski, and P. Bustamante. 2016. Toxicity assessment of water-accommodated fractions from two different oils using a zebrafish (*Danio rerio*) embryo-larval bioassay with a multilevel approach. Science of the Total Environment 568: 952-966. doi: https://doi.org/10.1016/j.scitotenv.2016.04.186

Pisarski, E.C., E.F. Wirth, S.I. Hartwell, B.S. Shaddrix, D.R. Whitall, D.A. Apeti, M.H. Fulton, and G. Baker. 2018. Assessment of Hydrocarbon Carryover Potential for Six Field Cleaning Protocols. NOAA Technical Memorandum NOS NCCOS 247. Silver Spring, MD. 36 pp. doi: https://doi.org/10.7289/V5/TM-NOS-NCCOS-247

Shine, J. and G. Wallace. 2000. Chemical aspects of organic carbon and ecosystem stress in benthic ecosystems. pp. 40-44. In: Ad hoc Benthic Indicator Group – Results of Initial Planning Meeting. IOC Technical Series No 57. UNESCO. 65 pp.

Staves, J., L. Robinson, and D. Aurand. 2013. Ecological Risk Assessment: Consensus Workshop. An Examination of the Potential Ecological Impacts of Response Alternatives Being Considered for Sheen Abatement for the Remnants of the Taylor Energy Company, LLC MC-20A Platform – Gulf of Mexico. A report to Taylor Energy Company, LLC. HDR Ecosystem Management. Lusby, MD. 50 pp.

Stout, S.A. 2015. Chemical Evidence for the Presence and Distribution of Macondo Oil in Deep-Sea Sediments following the Deepwater Horizon Oil Spill. NewFields Environmental Forensics Practice, LLC, Rockland, MA

Wade, T. Geochemical Environmental Research Group (GERG), College of Geosciences, Texas A&M University. Personal communication

Wade, T. Unpublished data. MC20 oil data from 1985 for three reservoirs. April 3, 2019. Geochemical Environmental Research Group (GERG), College of Geosciences, Texas A&M University.

Wenger, L.M., and G.H. Isaksen. 2002. Control of hydrocarbon seepage intensity on level of biodegradation in sea bottom sediments. Organic Geochemistry 33(12): 1277-1292. doi: https://doi.org/10.1016/S0146-6380(02)00116-X

Zumberge, J.E., H.A. Illich, J.C. Pratsch, and S.W. Brown. 1997. The petroleum geochemistry of the Gulf of Mexico oils. Non-proprietary study by GeoMark Research.

Zumberge, J.E., J.A. Russell, and S.A. Reid. 2005. Charging of Elk Hills reservoirs as determined by oil geochemistry. American Association of Petroleum Geologists (AAPG) Bulletin 89(1): 1347-1371. doi: https://doi.org/10.1306/05100504003

Sediment, Water, and Oil Chemistry

Chapter 8
Estimates of Oil Flux to the Ocean at MC20 using Optical and Acoustical Methods

Ian R. MacDonald[1], J. Christopher Taylor[2], Camilo Roa[3], and Carrie O'Reilly[1]

Sampling equipment being lowered into water at study site. Credit: NOAA NOS/NCCOS

ABSTRACT

Estimating flux of oil and gas from the seabed to the surface at the MC20 Taylor Energy Corporation (TEC) site presented challenges due to the mixture of gas and oil bubbles in the plume. Flux of oil from the seabed through the water column was estimated using two remote sensing techniques. Using the bubblometer, bubble proportions and densities were derived from 665 images, categorized by depth in the water column (crater at the erosional pit, benthic layer near jacket, and midwater above jacket). Densities were scaled to the cross sectional area of the plume at the three depth positions. Rise velocities also assumed theoretical values, using Stokes' Law, ranging from 2 cm/s (oil bubbles) to 13 cm/s (gas and oil bubbles). Flux of oil in each depth layer was estimated to be: Crater, 61 to 108 barrels per day; Benthic layer, 52 to 89 barrels per day; Midwater, 19 to 33 barrels per day. Acoustic backscatter from cross-sections of the plume were delineated and analyzed to estimate concentration of gas and oil bubbles in the plume. The mixture of oil and gas was assumed to be homogeneous, but proportional to the ratio and sizes of oil and gas bubbles observed in the bubblometer, including considerations for gas bubbles that contained, on average, 35.6% oil by volume. To derive flux from the oil density measurements, bubble rise velocities were derived in two ways: a theoretical model and empirical observations from the advection of the plume caused by currents. Rise velocities were found to be 6-7 cm/s for slower rising oil components of the plume and between 18 and 24 cm/s for faster rising gas bubbles in the plume. Acoustic measures of oil flux ranged from 9 (large bubbles and higher gas proportion) to 47 bbl/d (small bubbles and higher oil proportion). Visual assessment agrees most closely to the acoustic results in the midwater domain. Neither method fully resolves how much oil is retained near the sediment due to heavier oil not rising, or oil that actually reaches the surface of the ocean because lateral advection diminishing the vertical fluxes to a degree that is not well-resolved by the present data.

Citation for chapter
MacDonald, I.R., J.C. Taylor, C. Roa, and C. O'Reilly. 2019. Chapter 8. Estimates of Oil Flux to the Ocean at MC20 using Optical and Acoustical Methods. pp.107-118. In: A.L. Mason, J.C. Taylor, and I.R. MacDonald (eds.), An Integrated Assessment of Oil and Gas Release into the Marine Environment at the Former Taylor Energy MC20 Site. NOAA National Ocean Service, National Centers for Coastal Ocean Science. NOAA Technical Memorandum 260. Silver Spring, MD. 147pp. doi: 10.25923/kykm-sn39

[1] *Florida State University, Earth , Ocean, and Atmospheric Science, College of Arts and Sciences. Tallahassee, FL.*
[2] *NOAA National Ocean Service, National Centers for Coastal Ocean Science, Marine Spatial Ecology Division, Biogeography Branch. Silver Spring, MD*
[3] *Florida International University, Marine Sciences Program, School of Environment, Arts and Society. Miami, FL.*

Flux Rates

8.1 INTRODUCTION

The circumstances at Mississippi Canyon 20 (MC20) Taylor Energy Corporation (TEC) site pose a significant challenge for the estimation of the flux of oil from the seabed to the surface. Evidence presented in the previous chapters of this report indicate that the solitary source of the surface oil slicks observed at the site are individual streams of hydrocarbons escaping within a discrete erosional feature at the northwest base of the collapsed well jacket. These streams merge into a prominent, rising plume of oil and gas that has been detected in numerous previous investigations, as was detailed in Chapter 3. Note that European researchers refer to the acoustic signatures of hydrocarbon bubbles in the water column as "flares" (Romer *et al*., 2012), while this report uses the term "plume" to recognize the lateral dispersion during vertical transport of buoyant hydrocarbons and associated fluids (Fabregat *et al*., 2015). Previous researchers have used acoustic methods to track underwater plumes containing a mixture of oil and gas released from the Deepwater Horizon (DWH) blowout (Camilli *et al*., 2010) and to measure the rate of the flow (Camilli *et al*., 2012; Weber *et al*., 2012). Similar studies have been conducted for elsewhere in the Gulf of Mexico and North Sea seeps where bubbles were formed from methane alone (Weber *et al*., 2014; Romer *et al*., 2017) and large regions of the Cascadia Margin where the abundance of seepage-related targets have been analyzed to infer annual fluxes (Riedel *et al*., 2018).

Quantification of bubble flux based on visual methods have been reviewed by Leifer and Patro (2002) and applied to quantifying natural hydrocarbon seeps where bubbles contained mixtures of oil and gas (Leifer and MacDonald, 2003; Johansen *et al*., 2017). However, until the present effort, no investigations using visual methods had been successfully undertaken at MC20. Data available for constraining the acoustic results, and for developing independent estimates, were uniquely obtained at the site with the use of quantitative image sampling of the plume.

In this chapter, we derive estimates of oil flux to the surface at MC20 using two methods. First, video images were used to determine the size, density, and volume of oil droplets and relied on measurements from acoustics to scale density to absolute concentrations and flux. Second, acoustic backscatter from surface surveys was used to calculate density of particle gas and oil droplets and additionally used to model the concentration and rise rates in order to estimate the flux of oil at MC20 on 5 September 2018 of the survey detailed in the previous chapters of this report. We conclude with comments on remaining uncertainty in these estimates and discuss areas where further research can improve our calculations of flux from the MC20 site, including applications in response to future hydrocarbon leaks.

8.2 MATERIALS AND METHODS

8.2.1 Visual Quantification of Bubble Flux

In Chapter 4 of this report, methods for collecting, processing, and analyzing digital images of oil and gas bubbles were presented in detail. Briefly, a custom device (bubblometer) was used to collect calibrated images of bubbles in a 30 x 30 x 20 cm chamber as the bubbles were encountered near the collapsed MC20 well jacket. A computer vision algorithm was developed that classified bubbles as gas or oil and measured their major and minor axes. Analysis of the gas bubbles found that oil comprised about 35.6% of the total bubble volume. Some 12,139 bubbles were counted and measured among 665 image samples. Statistical analysis of the bubbles found size frequency distributions that were skewed to the right, with small bubbles numerically dominant, and with characteristics that changed with depth. The spread of the data is best indicated by the range between the median and mean values. It was important to geolocate the observations of bubbles by latitude and longitude as well as depth. This analysis showed that bubbles were observed in two clusters that corresponded to locations of distinct groups of release points documented in the remotely operated vehicle (ROV) imaging sonar data (Chapter 3). The physical constraints on the plumes suggested that the bubble image

samples corresponded to three depth domains: the **crater** - i.e., bubbles sampled in the erosional pit below the level of the surrounding seabed; the **benthic layer -** i.e., bubbles sampled above the pit, but within the shadow of the well jacket; and **midwater** - i.e., above the well jacket. Spatial processing in ArcGIS and Fledermaus was used to define plume cross-sections for oil and gas-oil bubbles in each domain.

In this chapter, these results are further analyzed to estimate fluxes of oil. The gas flux component is not considered in this analysis, though Chapter 5 develops a surface methane flux estimate using a separate dataset. Specifically, the plume cross-sections are used to partition the oil and gas-oil bubbles into discrete sample populations for each depth domain. Rise speeds for the bubbles are calculated from the Stokes' equation based on the density of oil in oil bubbles and oil plus gas in the gas-oil bubbles. This yields separate flux estimates for each category.

8.2.2 Acoustic Backscatter Derivations of Oil Flux

Acoustic survey data were collected as described in Chapter 3. Briefly, initial survey design over the MC20 site used north-south orientated lines spaced approximately 50 m apart to detect and map the direction of and origin of the plume and collapsed jacket structure. Subsequent surveys used parallel lines oriented perpendicular to the trajectory of the plume. During most surveys, additional survey lines were oriented along the axis of the plume in an attempt to characterize the continuous shape of the plume. The acoustic surface survey on the morning of 5 September 2018 was selected for analysis of oil flux as it provided several cross sections of the plume. In addition, a bottom moored Acoustic Doppler Current Profiler (ADCP) near the erosional pit was operating concurrently and allowed for synoptic current velocities. The echograms were processed to isolate the plume features from the background and delineated by a polygon with a unique region identifier for each cross section. The entire echogram was then divided into 1 m depth bins and regions were exported which contained average volume backscatter intensity, time of day (UTC), depth below surface, volume of water sampled, and the cross-section area of the plume.

As reported in Chapter 3 and Chapter 4, the plume consisted of multiple components: predominantly oil bubble components and gas bubble components. Video analysis revealed the gas bubbles contained, on average, 35% oil by volume. While concentrations from acoustic backscatter included both oil and gas, for this chapter we only report on the flux of oil including both oil bubbles and the oil contained in the gas bubbles.

The total flux is the summation of concentrations for oil and gas through each 1 m depth bin for each cross section of the plume. Total volume backscatter in the plume is the sum of the backscatter of all individual gas and oil bubbles. Estimating concentration of oil in the volume backscatter considered a mixture of gas and oil bubbles using the proportion of gas and oil bubbles by surface area as recorded in the bubblometer (see Chapter 4 and above). Backscatter of oil and gas bubbles adopted theoretical models based on bubble size and assuming simple spheres of a liquid (for oil) and gas (for gas mixed with oil) as presented in Loranger (2019). Bubble sizes were provided as bubble radii recorded in the bubblometer (see Chapter 4), using the minimum, mean, and maximum radii for both gas and oil bubbles. Once the concentration of bubbles is determined in plume cross sections, the volume of oil is calculated by summing the volume of all oil bubbles and the volume of proportion of oil contained in gas bubbles. Concentrations were estimated for n 1-m thick bins of each plume cross section where the area of the plume is a rectangle of 1 m high by the width of the echogram at that depth (Figure 8.1). The area of the plume for gas and oil bubbles is the same since droplets and bubbles are assumed to be distributed homogeneously over the echogram bin. Even though we suspect oil and gas are separated in the plume due to differential rise rates and position of the plume sources at the seabed (see Chapter 3), we did not discriminate plume components.

Flux Rates

Flux requires a measure of rise velocity for concentrations passing through a unit area. Two estimation methods were used to determine the fastest rise rates in the plume assumed for gas bubbles and the slowest rise rates assumed for oil bubbles. The first method is based on the radii and rise velocity approximations found by Zheng and Yapa (2000; Figure 8.2); the other is based on the empirical calculation from the cross section passes of the plume (see Chapter 3). The rise rate estimates were calculated from the maximum rise rate for the maximum radius and the minimum rise rate due to the minimum radius. The distribution is assumed to be linearly increasing as the targets approach the surface. Using theoretical properties presented in Zheng and Yapa (2000), for gas bubbles, a maximum radius of 2.8 mm, and a minimum radius of 1.2 mm, give a top rise rate of 24 cm/s and a bottom rise rate of 22 cm/s, respectively. Similarly, for oil droplets, a maximum radius of 1.8 mm, and a minimum radius of 1.2 mm, give a top rise rate of 12 cm/s and bottom rise rate of 6 cm/s, respectively.

We also used the echogram cross sections of the plume to empirically measure the rise rates of the plume. Each plume cross section was used to identify the deepest point representing the slowest rising components of the plume, and the shallowest margin of the plume representing the fastest rising components (Figure 8.3).

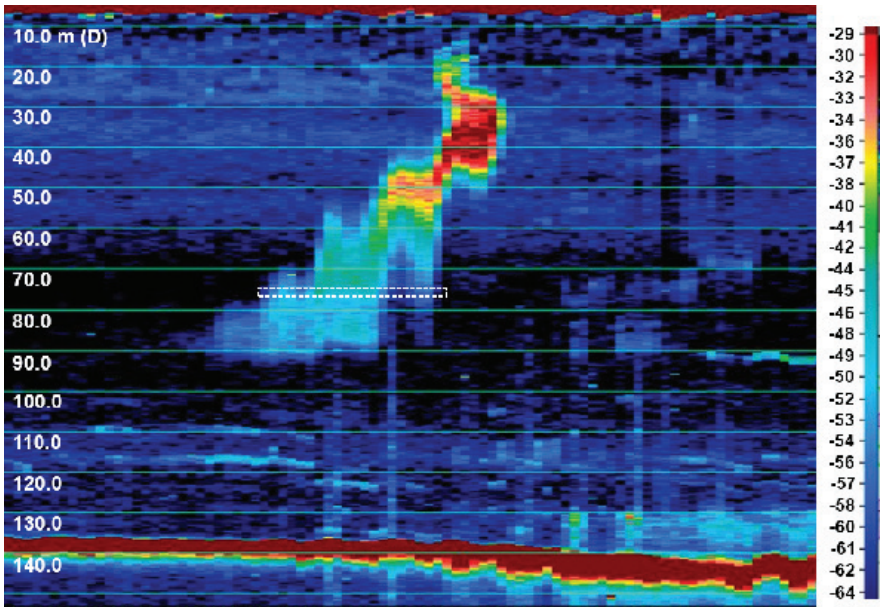

Figure 8.1. Sample echogram showing cross section of plume used in analysis of flux. Dark red at bottom is seabed. Plume is represented by blue color as lower backscatter (slower rising oil) and red color as higher backscatter (faster rising gas). Dashed rectangle shows approximate 1 m depth segment used to integrate backscatter intensity and measure area cross section for flux calculations.

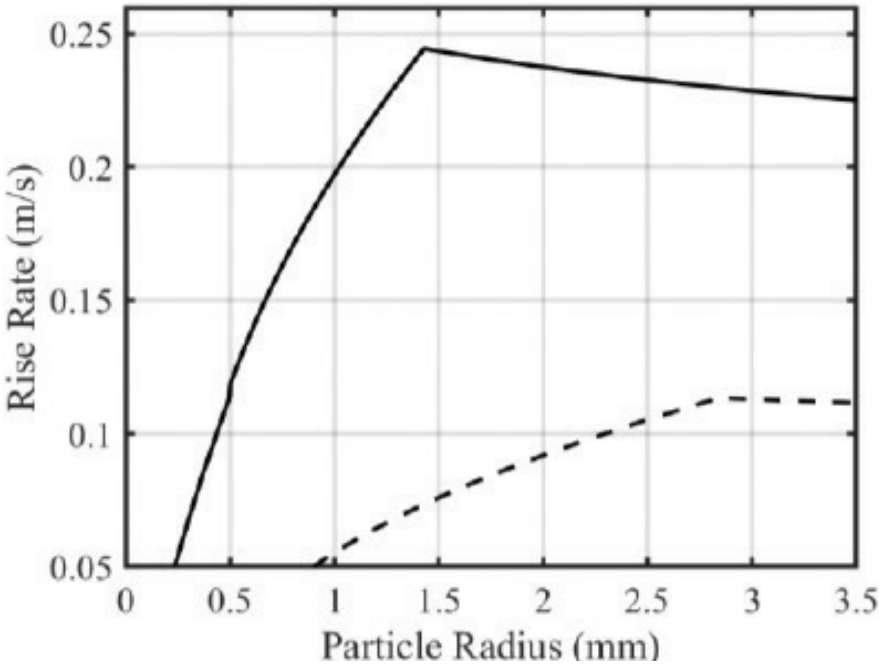

Figure 8.2. Rise rate versus target radius predicted by Zheng and Yapa (2000) for oil (dashed line) and methane bubbles (solid line) in seawater at a depth of 40 meters.

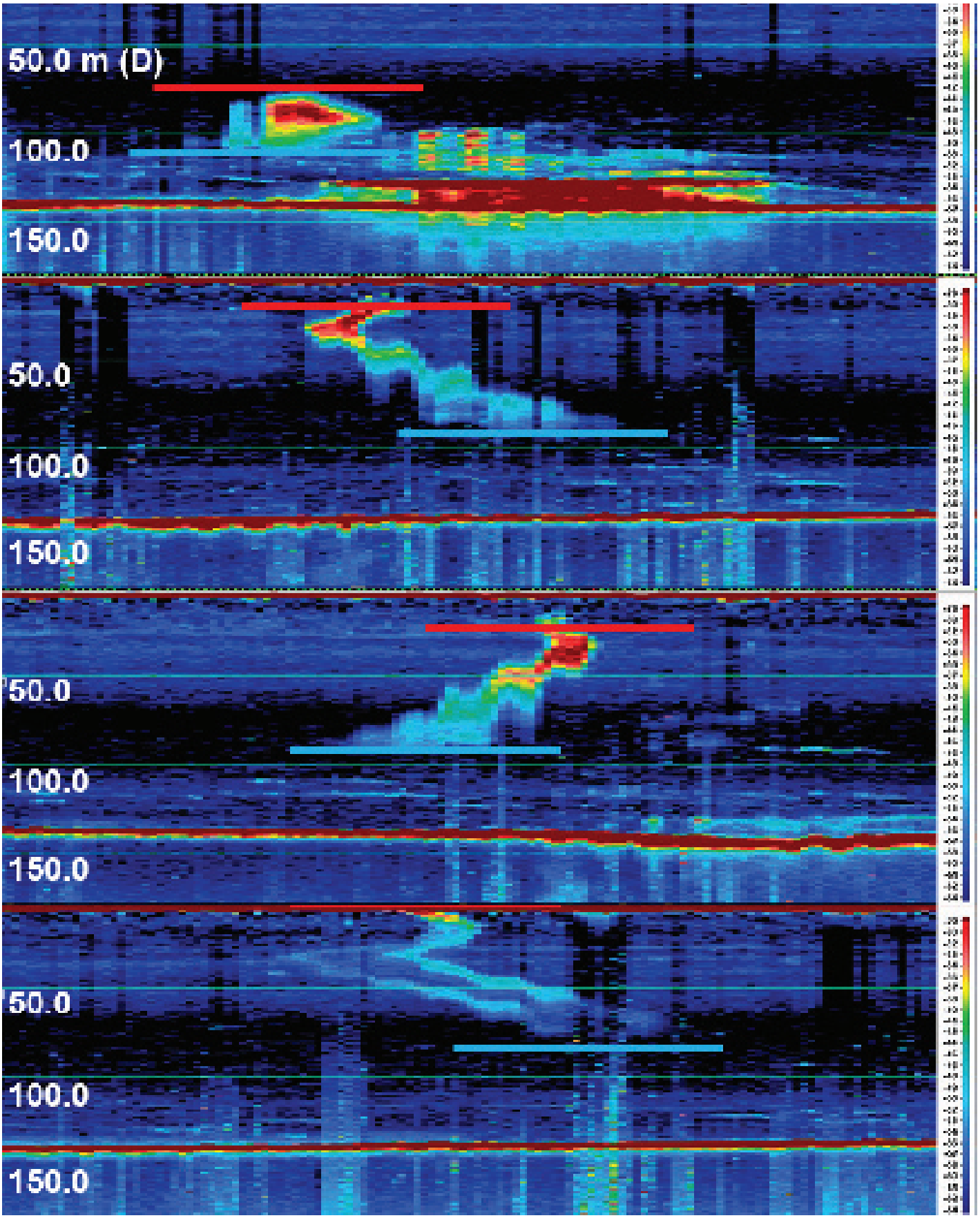

Figure 8.3. Sample echograms showing plume in cross section on successive passes. Seabed is the dark red line at bottom of each panel. Top panel shows jacket structure. Blue horizontal line represents marks for lower portion of plume representing slow rising. Red line marks upper portion and faster rising component of plume.

Flux Rates

The depths were exported with their respective geographic coordinates (Figure 8.4). The distance to each of these points was measured from the seabed source. ADCP horizontal current velocities in depth bins corresponding to the upper and lower components of the plume corrected for lateral advection. Rise rates measured from the echogram ranged from 6.3-7.2 cm/s on the lower portion and 18.5-23.1 cm/s in the upper portion. These estimates correspond well with theoretical measures of Zheng and Yapa (2000). Parameters for estimating oil flux using the above equations are presented in Appendix E (Table E.1).

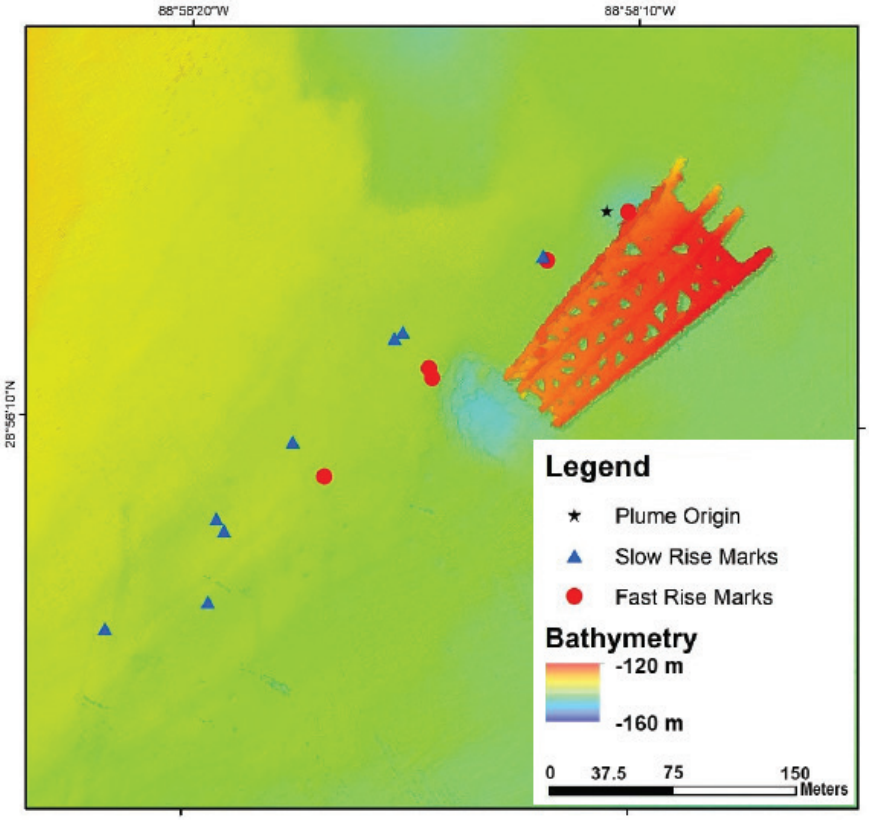

Figure 8.4. Map of mark locations for lower (blue) and upper (red) components of the plume along perpendicular transects.

Eighteen simulations were run assuming three bubble sizes, three proportions of oil:gas in the plume (centered on the proportion calculated from the bubblometer), and two rise velocity methods. Appendix E provides derivations and equations used in simulations, including consideration of scattering properties for small bubbles.

8.3 RESULTS AND DISCUSSION

8.3.1 Flux Estimates From Visual Sampling

Three dimensional distribution of the bubbles reflected the two areas where ROV imaging sonar documented hydrocarbons being discharged within the erosional crater; the two streams of bubbles were more or less distinct throughout the vertical range of bubblometer sampling (Figure 8.5). Kernel-based surface-fitting weighted by oil volumes identified the core of each stream for each depth domain (Figure 8.6). Bubbles observed outside these core areas were designated as outliers and were discarded from subsequent analysis. Partitioning the data in this fashion yields six separate sample populations, i.e. oil and gas-oil bubbles observed in the crater, benthic layer, and midwater depth domains. Each of the sample populations was characterized by rise velocity (from Stokes' equation) and mean oil density (L/m^3). Scaling these for the estimated plume cross-sections yields a separate estimate of flux for each domain and bubble type, with the median to mean range indicating the spread of the data (Table 8.1).

Oil flux estimates for any of the depth domains in Table 8.1 would be the sum of the oil bubbles and the gas-oil bubbles within the median to mean range. These results show that the physical constraints on migration of the plume influence fluxes of oil beyond the area of MC20 platform and to the surface. Notably, the increase in the plume cross-section for oil between the crater and the benthic layer reflect lateral diffusion of slow-moving oil bubbles once they emerge from the crater and the accumulation of oil bubbles in the benthic layer (Figure 8.6).

Table 8.1. Flux estimates from visual bubble samples: Domains are defined by depth ranges--crater (>135 m), benthic layer (135-125 m), and midwater (<125 m); Row shading corresponds to the surface colors in Figures 8.5 and 8.6; Plume cross-sectional areas are estimated from the surface-fitting results shown in Figure 8.6; Rise speeds are estimated from the bubble diameters for the respective groups and fluxes are then estimated for the median and mean oil volumes, respectively, for liters and barrels per day.

Domain	Bubble type	Plume cross-section (m^2)	Rise speed (m/s)	Median			Mean		
				Volume (L/m^3)	Flux (L/day)	Flux (Bbl/day)	Volume (L/m^3)	Flux (L/day)	Flux (Bbl/day)
Midwater	oil	38.2	0.015	0.20	256	1.61	0.24	314	1.98
Midwater	gas-oil	29.5	0.092	0.35	2691	16.93	0.63	4890	30.76
Benthic layer	oil	83.1	0.017	0.91	1333	8.37	1.35	1983	12.46
Benthic layer	gas-oil	53.9	0.119	0.67	6906	43.44	1.18	12197	76.73
Crater	oil	60.4	0.031	0.59	1578	9.92	0.94	2524	15.86
Crater	gas-oil	61.1	0.127	0.72	8050	50.64	1.30	14628	92.02

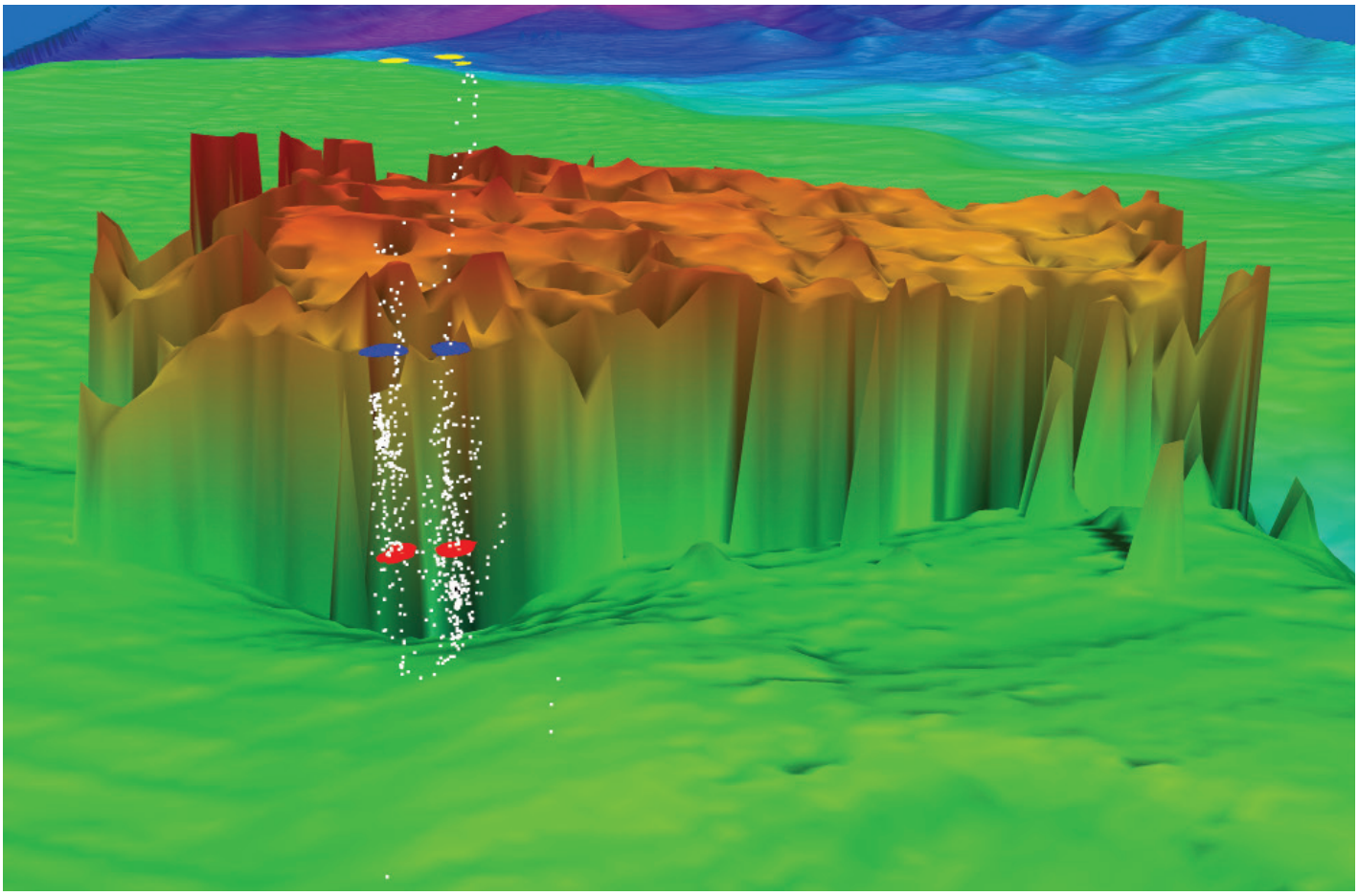

Figure 8.5. Bubble samples and plume cross-sections for image samples of gas-oil bubbles in three depth domains: crater (red), benthic layer (blue), and midwater (yellow).

Flux Rates

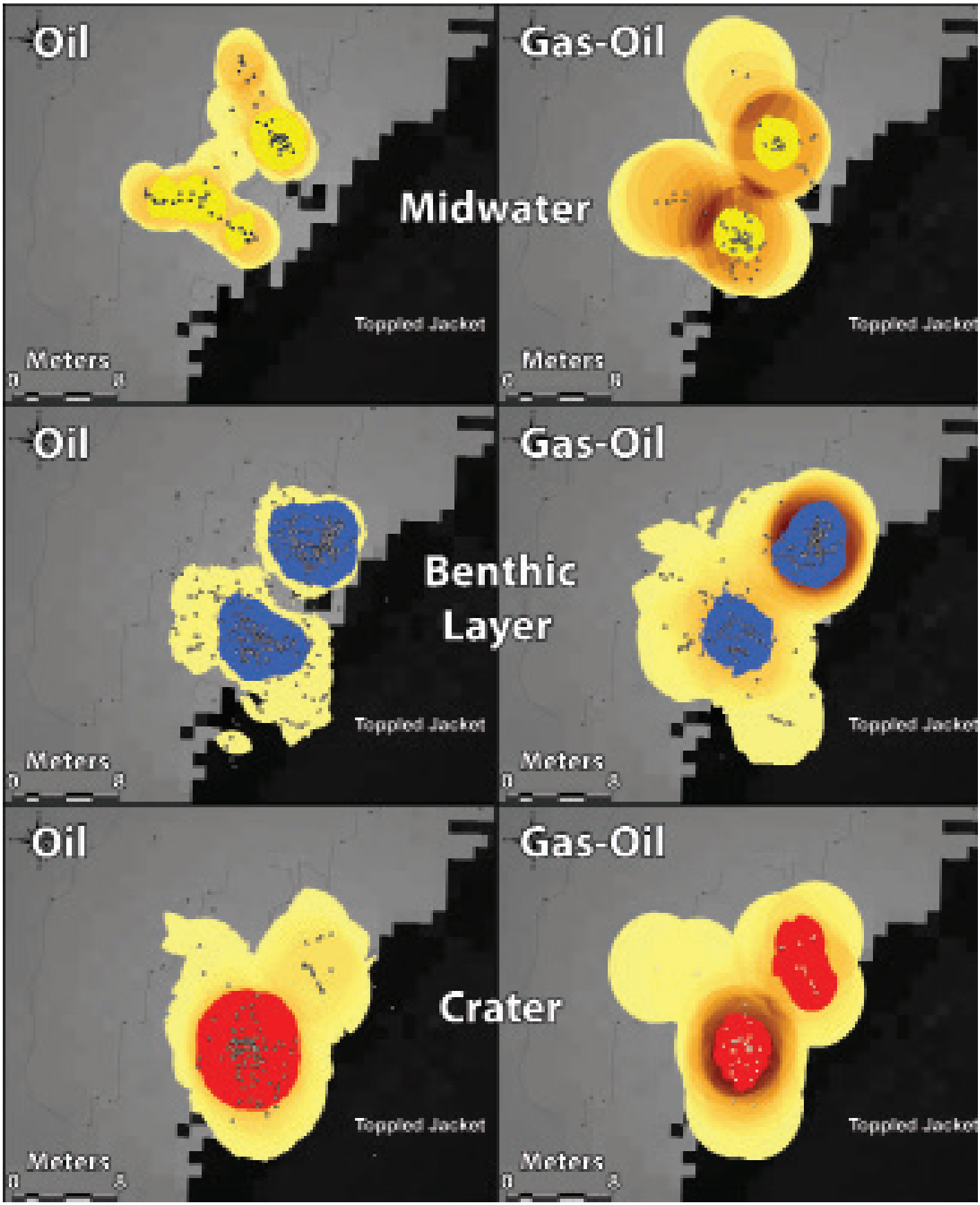

Figure 8.6 Plume cross-sections for two bubble types (oil and gas-oil) and three depth domains (crater, benthic layer, midwater). Dark region in lower right is the well jacket structure. Sample points indicate individual bubblometer images containing multiple bubbles. Colored areas indicate the volume-weighted cross sections used to calculate oil volumes and fluxes. Points in the outer areas of the fitted surfaces were discarded from analysis

The behavior of oil bubbles suggests that capture of the oil by use of a containment dome may be challenged by the low buoyancy of the oil bubbles such that bubble rise alone may not allow the oil drops to be collected into a holding structure. Gas-oil bubbles are contributing more to the flux than oil bubbles because of their greater buoyancy and rise speed. Above the level of the jacket, midwater advection is likely causing the plumes to attenuate, as indicated by the smaller cross-sections and lower oil volumes. Overall, this analysis may underestimate the total flux because observations of bubbles beyond the central core of the plume indicates that turbulent mixing does disperse some of the hydrocarbons into alternate rise paths; therefore the true plume cross-sections would be larger, albeit with lower oil densities in the outer margins, but with an overall increase in flux.

8.3.2 Acoustic Flux Results

Flux of oil through the water column was calculated assuming three proportions of oil:gas bubbles for the cross-sectional area, and assuming three radii size distributions depending on the mean, the maximum, median, and minimum radii extracted from the ROV's images (Table 8.2). It is estimated that the proportion in area of gas bubbles and oil droplets is 4:21, equivalent to 16% of the echogram's volume due to gas bubbles and 84% of the volume due to oil droplets. The rows of Table 8.2 correspond to the percentages of the cross-sectional area (σ). As the proportion of gas bubbles decreases, the flux in barrels per day (bbl/day) increases because more of the scattered signal is attributed to the oil droplets. The columns correspond to different radii (*a*) and different rise rate estimation methods. The maximum number of barrels per day is obtained if the minimum radius distribution is used. If the targets are assumed to be smaller, the number of targets would necessarily increase to achieve the total volume backscatter measured over the plume; and since the flux is proportional to the number of targets, then it increases. The minimum and maximum radii give the two extremes of the flux for that specific gas-oil proportion. Acoustic-based estimates of the flux of oil through the water column range from 9 bbl/day for large bubbles and low proportion of oil to 47 bbl/d for small bubbles and relatively higher proportions of oil in the plume.

Table 8.2. Estimates of oil flux in barrels per day assuming three proportions of oil versus gas and droplet sizes, and assuming rise rates as measured empirically by echograms and currents and theoretical values predicted from Zheng and Yappa (2000).

		Barrels/day					
Rise rate equation		Radii based			Echogram based		
Radii distribution, Gauss mean [mm]		*a* = 1.8	*a* = 1.4	*a* = 1.2	*a* = 1.8	*a* = 1.4	*a* = 1.2
Proportion gas-oil	20 gas – 80 oil	9.04	15.93	27.78	13.57	23.9	41.72
	16 gas – 84 oil	9.46	16.68	29.07	14.2	25.02	43.67
	10 gas – 90 oil	10.17	17.93	31.25	15.26	26.89	46.94

8.4 CONCLUSIONS

Estimates of flux using visual and acoustic backscatter likely represent the lower end of a range of values and several sources of uncertainty may contribute to underestimates of the number and volume of gas bubbles and oil. In order to detect oil and gas over the noise floor of the echosounder system, the signal should exceed noise by approximately 6 dB. Very low concentrations of oil (and gas) on the outer periphery of the plume may pose challenges for detection by echosounding in the water column. Backscatter properties of a gas bubble that contains oil may present different scattering properties and may result in lower backscatter than pure gas bubbles. Further theoretical modeling is needed to refine the sound scattering properties and models relating bubbles and backscatter. Another source of uncertainty in estimating the quantity of oil may be in a collection of oil that is too dense and remains at the seabed and does not rise with the oil that is emitted from the seabed as we observed in the plume. Chapter 7 of this document addresses the fact that a certain portion of the High Molecular Weight (HMW) PAHs along with the relatively long chain *n*-alkanes that are found in

the sediments at the perimeter of the erosional pit are not observed in the water column oil samples and therefore point toward rapid partitioning out of these portions potentially onto the ocean floor. Additionally, Chapter 7 notes that oil-related compounds measured in mid-water column samples where no bulk oil was visible were consistent with free oil droplets in the water and not dissolved oil further pointing towards a portion of the plume that may be small enough to fall outside of the detection limits of the echosounders and visual methods. Other oil may also remain contained within the sediment with a quantity in the environment not considered as part of our estimates. Rise rates were not measured directly, but estimated indirectly by either theoretical models or indirect empirical measures of vertical position of the plume. Further research is still needed to constrain many of these parameters, account for the biases and sensitivities in model derived estimates, and reduce the uncertainty in estimates of flux at the MC20 site.

This project has yielded novel results using a methodology for assessing plumes of oil and gas rising through the water column by incorporating cutting-edge acoustic and visual techniques. Further analysis of current results and/or repeating some of the measurements with improvements in methodology based on previous experience would solidify these approaches and improve any future assessments of accidental or natural hydrocarbon releases in the ocean. Results give insights into how a mixed plume of oil and gas can separate during transit through the water column and the role that gas bubbles can play in promoting the transport of oil as mixed gas-oil bubbles. Both methods (acoustic and visual) were calibrated with the use of a novel computer vision technique that classified bubbles as oil or gas-oil and measured their individual sizes. Further refinement and calibration of these algorithms would increase confidence in future projects. Analysis of the acoustic results deployed a revised method of estimating rise rates of buoyant bubbles in seawater (Zheng and Yappa, 2000) and applied a range of assumptions for the gas/oil ratio of the plume. Assessing the totality of the plume, oil and gas, these methods estimate an overall flux of 9 to 47 barrels per day. The results are sensitive to bubble sizes as this drives the interpretation from backscatter to bubble numbers. Analysis of visual results used a classical method for estimating bubble rise speed (Stokes' Law) and considered the three dimensional distribution of bubble observations, the constraints of the topography of the site, and bubble emission occurring within an approximately 4 m deep crater immediately adjacent to the massive structure of the collapsed well jacket. Clustering of bubbles corresponded closely to the delineation of release points observed by the ROV-mounted imaging sonar (see Chapter 3).

The visual assessment agrees most closely to the acoustic results in the midwater domain. Previous estimates of oil flux at the site used satellite or aerial imagery and models of the extent and thickness of the oil slick to derive flux rates. Comparison with flux estimates reported in this chapter show that the acoustic method is midrange of many satellite derived estimates, but several orders of magnitude higher than flux reported by TEC (Figure 8.7). It is important to note that neither the acoustic nor visual method presented here fully resolves how much oil reaches the surface of the ocean as lateral advection may diminish the vertical fluxes to a degree that is not well-

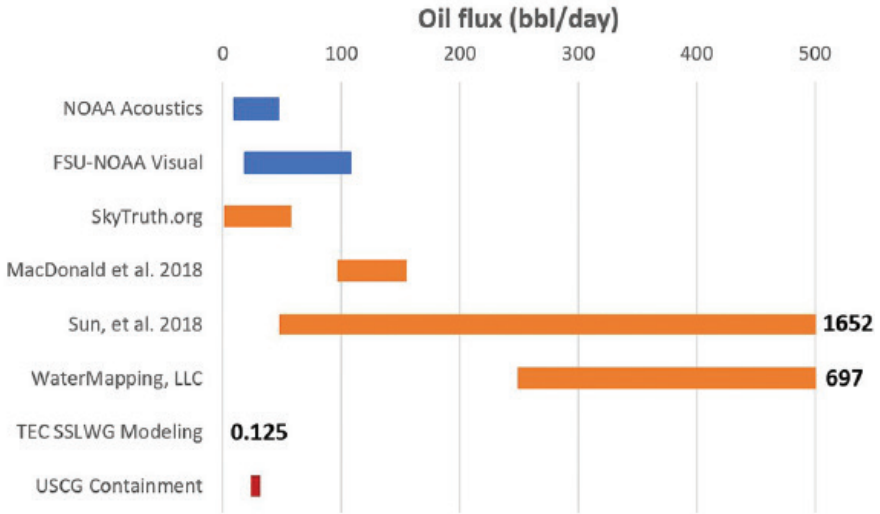

Figure 8.7. Comparison of oil flux estimates at the TEC MC20 site using acoustic and visual methods (blue, this report) to model-based and satellite image derived estimates and TEC model based estimates (0.125 bbl/d). US Coast Guard containment of 1,000 to 1,300 gal/d shown for reference (red). Data sources: Skytruth.org (2017); MacDonald et al. (2018); Sun et al. 2018; WaterMapping, LLC (US Department of Justice, (2018); TEC SSLWG Modeling (BSEE Internal Documents); USCG Containment: US Coast Guard Unified Command.

resolved by the present observational methods. Most recently, a containment system installed immediately over the erosional pit was reported collecting 30,000 gallons of oil in about 30 days, equating to 1,000-1,300 gallons or about 24 to 31 bbl/day, which falls midway in the range of estimates produced using the acoustic method described here, and at the low end of the range estimated using the visual method. Visual assessments from the base of the plume indicate that capture of some oil by passive containment structures will be challenging for small oil bubbles or heavy oil with low buoyancy.

8.5 REFERNCES

Camilli, R., C.M. Reddy, D.R. Yoerger, B.A.S. Van Mooy, M.V. Jakuba, J.C. Kinsey, C.P. McIntyre, S.P. Sylva, and J.V. Maloney. 2010. Tracking hydrocarbon plume transport and biodegradation at Deepwater Horizon. Science 330(6001): 201-204. doi: https://doi.org/10.1126/science.1195223

Camilli, R., D. Di Iorio, A. Bowen, C.M. Reddy, A.H. Techet, D.R. Yoerger, L.L. Whitcomb, J.S. Seewald, S.P. Sylva, and J. Fenwick. 2012. Acoustic measurement of the *Deepwater Horizon* Macondo well flow rate. Proceedings of the National Academy of Sciences 109(50): 20235-20239. doi: https://doi.org/10.1073/pnas.1100385108

Fabregat, A., W.K. Dewar, T.M. Özgökmen, A.C. Poje, and N. Wienders. 2015. Numerical simulations of turbulent thermal, bubble and hybrid plumes. Ocean Modelling 90: 16-28. doi: https://doi.org/10.1016/j.ocemod.2015.03.007

Johansen, C., A.C. Todd, and I.R. MacDonald. 2017. Time series video analysis of bubble release processes at natural hydrocarbon seeps in the northern Gulf of Mexico. Marine and Petroleum Geology 82: 21-34. doi: https://doi.org/10.1016/j.marpetgeo.2017.01.014

Leifer, I., and R.K. Patro. 2002. The bubble mechanism for methane transport from the shallow sea bed to the surface: A review and sensitivity study. Continental Shelf Research 22(16): 2409-2428. doi: https://doi.org/10.1016/S0278-4343(02)00065-1

Leifer, I., and I. MacDonald. 2003. Dynamics of the gas flux from shallow gas hydrate deposits: interaction between oily hydrate bubbles and the oceanic environment. Earth Planet Sc Lett 210(3): 411-424. doi: https://doi.org/10.1016/S0012-821X(03)00173-0

Loranger, S. 2019. Acoustic detection and quantification of crude oil. Dissertation to the Oceanography Department, University of New Hampshire. 140 pp.

MacDonald, I.R., Daneshgar Asl, S., 2018. Remote sensing of persistent oil slicks in Mississippi Canyon 20. Gulf of Mexico Oil Spill and Ecosystem Conference 5-8 Feb 2018, New Orleans

Riedel, M., and M. Scherwath, M. Römer, M. Veloso, M. Heesemann, and G.D. Spence. 2018. Distributed natural gas venting offshore along the Cascadia margin. Nature Communications 9: 3264. 14 pp. doi: https://doi.org/10.1038/s41467-018-05736-x

Römer, M., H. Sahling, T. Pape, G. Bohrmann, and V. Spieß. 2012. Quantification of gas bubble emissions from submarine hydrocarbon seeps at the Makran continental margin (offshore Pakistan). Journal of Geophysical Research: Oceans 117(C10): 19 pp. doi: https://doi.org/10.1029/2011JC007424

Römer, M., S. Wenau, S. Mau, M. Veloso, J. Greinert, M. Schlüter, and G. Bohrmann. 2017. Assessing marine gas emission activity and contribution to the atmospheric methane inventory: A multidisciplinary approach from the Dutch Dogger Bank seep area (North Sea). Geochemistry, Geophysics, Geosystems 18(7): 2617-2633. doi: https://doi.org/10.1002/2017GC006995

SkyTruth.org. 2017. https://skytruth.org/2017/12/taylor-energy-site-23051-cumulative-spill-report-2017-update. Last accessed 12 June 2019.

Sun, S., C. Hu, O. Garcia-Pineda, V.H. Kourafalou, M. Le Hénaff, and Y. Androulidakis. 2018. Remote sensing assessment of oil spils near a damaged platform in the Gulf of Mexico. Marine Pollution Bulletin 136: 141-151. doi: https://doi.org/10.1016/j.marpolbul.2018.09.004

US Department of Justice. 2018. Exhibit 3. Expert Report of Oscar Garcia, PhD. Taylor Energy Company, LLC v. The United States. Case 1:16-cv-00012-NBF Document 81-3, Filed 09/14/18.

Weber, T.C., A. De Robertis, S.F. Greenaway, S. Smith, L. Mayer, and G. Rice. 2012. Estimating oil concentration and flow rate with calibrated vessel-mounted acoustic echo sounders. Proceedings of the National Academy of Sciences 109(50): 20240-20245. doi: https://doi.org/10.1073/pnas.1108771108

Weber, T.C., L. Mayer, K. Jerram, K. Beaudoin, Y. Rzhanov, and D. Lovalvo. 2014. Acoustic estimates of methane gas flux from the seabed in a 6000 km^2 region in the Northern Gulf of Mexico. Geochemistry, Geophysics, Geosystems Volume 15(5): 1671-2094. doi: https://doi.org/10.1002/2014GC005271

Zheng, L., and P.D. Yapa. 2000. Buoyant Velocity of Spherical and Nonspherical Bubbles/Droplets. Journal of Hydraulic Engineering 126(11): 852-854. doi: https://doi.org/10.1061/(ASCE)0733-9429(2000)126:11(852)

Appendix A: Assessment Event Log

Event	Date - Time (UTC)	Ship Latitude	Ship Longitude	Equipment	Equipment Latitude	Equipment Longitude	Equipment Depth (m)
Box corer test cast 1	8/24/18 17:32	N28 56.8591	W095 19.7086	Box Corer	N28 56.8584	W095 19.7012	Not available
Box corer test cast 2	8/28/18 11:27	N28 41.7812	W091 25.3002	Box Corer	N28 41.9079	W092 43.0529	Not available
Box corer test cast 3	8/30/18 7:39	N30 21.4899	W089 05.6731	Box Corer	N28 39.3374	W092 17.9171	Not available
Box corer test cast 4	8/30/18 10:23	N30 21.4901	W089 05.6737	Box Corer	N28 39.3374	W092 17.9171	Not available
Arrive at CTD test site	9/1/18 13:01	N28 57.1454	W088 56.4038	Box Corer	N30 23.4312	W089 01.3711	-18.3
CTD test cast bottle 2 trip	9/1/18 17:44	N28 57.1450	W088 56.4029	CTD Rosette	N28 57.1428	W088 56.4044	-111.0
CTD test cast bottle 3 trip	9/1/18 17:45	N28 57.1449	W088 56.4022	CTD Rosette	N28 57.1407	W088 56.4026	-103.4
CTD test cast bottle 4 trip	9/1/18 17:46	N28 57.1469	W088 56.4003	CTD Rosette	N28 57.1437	W088 56.4008	-91.4
CTD test cast bottle 6 trip	9/1/18 17:47	N28 57.1472	W088 56.4005	CTD Rosette	N28 57.1461	W088 56.3994	-81.4
CTD test cast bottle 8 trip	9/1/18 17:48	N28 57.1428	W088 56.4084	CTD Rosette	N28 57.1469	W088 56.4003	-63.9
CTD test cast bottle 9 trip	9/1/18 17:48	N28 57.1428	W088 56.4060	CTD Rosette	N28 57.1429	W088 56.4006	-52.8
CTD test cast bottle 11 trip	9/1/18 17:49	N28 57.1444	W088 56.3981	CTD Rosette	N28 57.1448	W088 56.3904	-30.4
CTD test cast bottle 12 trip	9/1/18 17:51	N28 57.1452	W088 56.4103	CTD Rosette	N28 57.1482	W088 56.4018	-14.8
USBL in water	9/1/18 18:17	N28 57.1430	W088 56.4000	Calibration	N28 57.1051	W088 56.3944	0
Location of beacon release	9/1/18 18:34	N28 57.1511	W088 56.4059	Calibration	N28 57.1488	W088 56.4323	-135.1
Calibration start	9/1/18 18:58	N28 57.1340	W088 56.4253	Calibration	N28 57.1289	W088 56.4229	-134.2
South Calibration	9/1/18 19:08	N28 57.1068	W088 56.4249	Calibration	N28 57.1300	W088 56.4184	-131.9
End South Calibration	9/1/18 19:13	N28 57.1049	W088 56.4228	Calibration	N28 57.1287	W088 56.4185	-134.5
East Calibration	9/1/18 19:16	N28 57.1300	W088 56.3921	Calibration	N28 57.1358	W088 56.4206	-134.1
End North Calibration	9/1/18 19:30	N28 57.1606	W088 56.4269	Calibration	N28 57.1291	W088 56.4269	-133.9
Start West Calibration	9/1/18 19:34	N28 57.1389	W088 56.4539	Calibration	N28 57.1264	W088 56.4239	-134.2
End West Calibration	9/1/18 19:43	N28 57.1392	W088 56.4543	Calibration	N28 57.1259	W088 56.4239	-134.3
Start Reciprocal Calibration	9/1/18 19:47	N28 57.1169	W088 56.4484	Calibration	N28 57.1273	W088 56.4214	-134.4
End Reciprocal Calibration	9/1/18 19:49	N28 57.1262	W088 56.3972	Calibration	N28 57.1341	W088 56.4191	-132.1
Beacon on board	9/1/18 20:26	N28 57.1008	W088 56.4443	Calibration	N28 57.0943	W088 56.4193	0
Acoustic plume detected 1	9/2/18 0:04	N28 56.1979	W088 58.1979	N/A	-	-	-
Acoustic plume detected 2	9/2/18 0:37	N28 56.1399	W088 58.2950	N/A	-	-	-
Acoustic plume detected 3	9/2/18 0:49	N28 56.2011	W088 58.3492	N/A	-	-	-
Acoustic plume detected 4	9/2/18 1:03	N28 56.2726	W088 58.2648	N/A	-	-	-
Acoustic plume detected 5	9/2/18 1:04	N28 56.1868	W088 58.2566	N/A	-	-	-
Acoustic plume detected 6	9/2/18 1:16	N28 56.1469	W088 58.3179	N/A	-	-	-
Acoustic plume detected 7	9/2/18 1:17	N28 56.2594	W088 58.3161	N/A	-	-	-
Acoustic plume detected 8	9/2/18 1:33	N28 56.1134	W088 58.3775	N/A	-	-	-
Acoustic plume detected 9	9/2/18 2:02	N28 56.0962	W088 58.4051	N/A	-	-	-
End of transect	9/2/18 2:28	N28 56.2552	W088 58.1512	N/A	-	-	-
Secondary acoustic plume detected	9/2/18 2:53	N28 56.2806	W088 58.2329	N/A	-	-	-
Surface oil slick observed starboard	9/2/18 12:27	N28 56.1862	W088 58.2352	N/A	-	-	-

Appendices

Appendix A: Assessment Event Log

Event	Date - Time (UTC)	Ship Latitude	Ship Longitude	Equipment	Equipment Latitude	Equipment Longitude	Equipment Depth (m)
Acoustic plume detected A	9/2/18 12:55	N28 56.2342	W088 58.1872	N/A	-	-	-
Acoustic plume detected B	9/2/18 13:11	N28 56.2110	W088 58.2182	N/A	-	-	-
Acoustic plume detected C	9/2/18 13:25	N28 56.1741	W088 58.2633	N/A	-	-	-
Acoustic plume detected D	9/2/18 13:38	N28 56.1488	W088 58.3317	N/A	-	-	-
Acoustic plume detected E	9/2/18 13:47	N28 56.1146	W088 58.3580	N/A	-	-	-
Surface slick pictures taken	9/2/18 17:23	N28 56.1781	W088 58.2954	N/A	-	-	-
ROV Launch	9/2/18 18:18	N28 56.2657	W088 58.1878	ROV	N28 42.1840	W088 36.8289	0.0
ROV in water	9/2/18 18:23	N28 56.2716	W088 58.1820	ROV	N28 56.2713	W088 58.1828	-32.6
Subsurface bubbles viewed	9/2/18 19:29	N28 56.2670	W088 58.1752	ROV	N28 56.2323	W088 58.1731	-133.5
Subsurface bubbles viewed 2	9/2/18 19:43	N28 56.2673	W088 58.1777	ROV	N28 56.2288	W088 58.1817	-123.5
ROV on deck	9/2/18 22:30	N28 56.2158	W088 58.2324	ROV	N28 56.2117	W088 58.2384	0
Plume surfacing location 1	9/3/18 1:45	N28 56.1918	W088 58.2014	N/A	-	-	-
Plume surfacing location 2	9/3/18 2:27	N28 56.1541	W088 58.2894	N/A	-	-	-
CTD Cast 1 in water	9/3/18 3:19	N28 56.2437	W088 58.1764	CTD Rosette	N28 56.0540	W088 58.5941	0
CTD cast 1 at 102 m	9/3/18 3:23	N28 56.2430	W088 58.1731	CTD Rosette	N28 56.2427	W088 58.1641	-103.3
CTD Cast 1 Bottle 2 tripped	9/3/18 3:29	N28 56.2409	W088 58.1649	CTD Rosette	N28 56.2416	W088 58.1571	-79.7
CTD Cast 1 Bottle 3 tripped	9/3/18 3:34	N28 56.2335	W088 58.1989	CTD Rosette	N28 56.2307	W088 58.1872	-80.9
Visible slick at surface	9/3/18 3:35	N28 56.2195	W088 58.2152	CTD Rosette	N28 56.2167	W088 58.2028	-74.8
CTD Cast 1 at 40 m	9/3/18 3:38	N28 56.2081	W088 58.2227	CTD Rosette	N28 56.2106	W088 58.2144	-41.7
CTD Cast 1 Bottle 4 tripped	9/3/18 3:42	N28 56.2243	W088 58.2030	CTD Rosette	N28 56.2268	W088 58.1931	-41.1
CTD Cast 1 Bottle 6 tripped	9/3/18 3:43	N28 56.2231	W088 58.2114	CTD Rosette	N28 56.2239	W088 58.1990	-35.5
CTD Cast 1 Bottle 9 tripped	9/3/18 3:44	N28 56.2158	W088 58.2217	CTD Rosette	N28 56.2123	W088 58.2091	-25.9
CTD Cast 1 Bottle 10 tripped	9/3/18 3:45	N28 56.2095	W088 58.2317	CTD Rosette	N28 56.2047	W088 58.2200	-20.2
CTD Cast 1 Bottle 11 tripped	9/3/18 3:46	N28 56.2029	W088 58.2421	CTD Rosette	N28 56.1976	W088 58.2321	-15.8
CTD Cast 1 Bottle 12 tripped	9/3/18 3:47	N28 56.1960	W088 58.2543	CTD Rosette	N28 56.1937	W088 58.2515	0
ROV Launch 2	9/3/18 13:52	N28 56.2557	W088 58.1855	ROV	N28 52.4196	W089 08.7184	-19.0
ROV Beacon on	9/3/18 13:55	N28 56.2489	W088 58.1854	ROV	N28 56.2502	W088 58.1807	-61.0
Subsurface oil plume	9/3/18 15:46	N28 56.2214	W088 58.2241	ROV	N28 56.2274	W088 58.1760	-132.7
Subsurface visible gas bubbles	9/3/18 15:52	N28 56.2259	W088 58.2149	ROV	N28 56.2304	W088 58.1705	-117.8
Subsurface visible oil	9/3/18 15:59	N28 56.2205	W088 58.2189	ROV	N28 56.2297	W088 58.1724	-114.7
ROV Dive 2 on deck	9/3/18 16:53	N28 56.1790	W088 58.2378	ROV	N28 56.1840	W088 58.2580	0
ROV in water	9/3/18 19:08	N28 56.2451	W088 58.1762	ROV	N28 55.8520	W088 58.9068	0
Subsurface ADCP in water	9/3/18 21:09	N28 56.2436	W088 58.1818	ADCP	N28 56.2532	W088 58.2134	-7.3
Subsurface ADCP on bottom	9/3/18 21:21	N28 56.2549	W088 58.1746	ADCP	N28 56.2517	W088 58.1730	-134.5
Subsurface ADCP reposition	9/3/18 21:23	N28 56.2524	W088 58.1769	ADCP	N28 56.2553	W088 58.1733	0
Acoustic Plume A detection	9/5/18 13:17	N28 56.2442	W088 58.1731	ROV	N28 56.2320	W088 58.1737	0
Acoustic Plume B detection	9/5/18 13:38	N28 56.1846	W088 58.2405	ROV	N28 56.2320	W088 58.1737	0

Appendix A: Assessment Event Log

Event	Date - Time (UTC)	Ship Latitude	Ship Longitude	Equipment	Equipment Latitude	Equipment Longitude	Equipment Depth (m)
ROV Dive 4	9/5/18 15:59	N28 56.2868	W088 58.2349	ROV	N28 56.2320	W088 58.1737	0
Plume surfacing location	9/5/18 23:42	N28 56.1792	W088 58.2392	N/A	-	-	-
CTD Cast 2 in water	9/6/18 0:20	N28 56.2355	W088 58.2117	CTD Rosette	N28 55.2873	W089 01.7198	-17.7
CTD Cast 2 at lowest point	9/6/18 0:27	N28 56.2339	W088 58.2090	CTD Rosette	N28 56.2253	W088 58.2158	-125.7
CTD Cast 2 Bottle 2 fired	9/6/18 1:00	N28 56.2420	W088 58.1624	CTD Rosette	N28 56.2330	W088 58.1714	-101.0
CTD Cast 2 Bottle 3 fired	9/6/18 1:01	N28 56.2449	W088 58.1645	CTD Rosette	N28 56.2359	W088 58.1711	-85.0
CTD Cast 2 Bottle 4 fired	9/6/18 1:02	N28 56.2430	W088 58.1668	CTD Rosette	N28 56.2340	W088 58.1748	-75.2
CTD Cast 2 Bottle 6 fired	9/6/18 1:03	N28 56.2471	W088 58.1670	CTD Rosette	N28 56.2353	W088 58.1735	-60.3
CTD Cast 2 Bottle 9 fired	9/6/18 1:05	N28 56.2443	W088 58.1712	CTD Rosette	N28 56.2348	W088 58.1771	-50.9
CTD Cast 2 Bottle 10 fired	9/6/18 1:08	N28 56.2253	W088 58.1865	CTD Rosette	N28 56.2185	W088 58.1968	-40.0
CTD Cast 2 Bottle 11 fired	9/6/18 1:09	N28 56.2183	W088 58.1854	CTD Rosette	N28 56.2091	W088 58.1945	-25.2
CTD Cast 2 Bottle 12 fired	9/6/18 1:11	N28 56.2197	W088 58.1837	CTD Rosette	N28 56.2064	W088 58.1880	-11.5
CTD Cast 3 In Water	9/6/18 1:46	N28 56.2437	W088 58.1638	CTD Rosette	N28 56.8482	W088 57.7790	0
CTD Cast 3 Bottle 1 fired	9/6/18 1:52	N28 56.2416	W088 58.1682	CTD Rosette	N28 56.2330	W088 58.1743	-110.2
CTD Cast 3 Bottle 2 fired	9/6/18 1:54	N28 56.2433	W088 58.1636	CTD Rosette	N28 56.2352	W088 58.1737	-90.7
CTD Cast 3 Bottle 3 fired	9/6/18 1:55	N28 56.2448	W088 58.1654	CTD Rosette	N28 56.2351	W088 58.1712	-80.0
CTD Cast 3 Bottle 4 fired	9/6/18 1:56	N28 56.2420	W088 58.1664	CTD Rosette	N28 56.2324	W088 58.1760	-69.8
CTD Cast 3 Bottle 6 fired	9/6/18 1:58	N28 56.2418	W088 58.1696	CTD Rosette	N28 56.2312	W088 58.1757	-55.6
CTD Cast 3 Bottle 9 fired	9/6/18 2:00	N28 56.2352	W088 58.1747	CTD Rosette	N28 56.2254	W088 58.1776	-35.2
CTD Cast 3 Bottle 10 fired	9/6/18 2:02	N28 56.2272	W088 58.1856	CTD Rosette	N28 56.2172	W088 58.1917	-20.9
CTD Cast 3 Bottle 11 fired	9/6/18 2:03	N28 56.2201	W088 58.1919	CTD Rosette	N28 56.2103	W088 58.1989	-10.3
CTD Cast 3 Bottle 12 fired	9/6/18 2:04	N28 56.2117	W088 58.1984	CTD Rosette	N28 56.2075	W088 58.2014	0
BC13 in the water	9/6/18 3:59	N28 55.2620	W088 59.6271	Box Corer	N28 55.2546	W088 59.6375	-20.3
BC13 on bottom	9/6/18 4:02	N28 55.2625	W088 59.6240	Box Corer	N28 55.2625	W088 59.6240	-133.7
Acoustic detection at Dome A	9/6/18 12:30	N28 56.3581	W088 58.3480	N/A	-	-	-
Main plume acoustic detection	9/6/18 12:34	N28 56.2062	W088 58.1775	N/A	-	-	-
Acoustic detection at Dome A 2	9/6/18 12:46	N28 56.3175	W088 58.2582	N/A	-	-	-
ROV Dive 5 in water	9/6/18 14:07	N28 56.2878	W088 58.2382	N/A	-	-	-
ROV visible bubbles	9/6/18 14:46	N28 56.2781	W088 58.2283	ROV	N28 56.2939	W088 58.2465	-114.0
ROV visible bubbles 2	9/6/18 14:58	N28 56.2773	W088 58.2261	ROV	N28 56.2995	W088 58.2424	-131.3
ROV lots of bubbles visible	9/6/18 15:07	N28 56.2772	W088 58.2268	ROV	N28 56.3014	W088 58.2380	-135.8
Surface water sampling	9/6/18 15:40	N28 56.2628	W088 58.2117	ROV	N28 56.2687	W088 58.2120	-87.1
ROV visible oil and bubble mix	9/6/18 16:04	N28 56.2538	W088 58.1745	ROV	N28 56.2371	W088 58.1672	0
ROV visible oil droplets and bubbles	9/6/18 16:20	N28 56.2540	W088 58.1763	ROV	N28 56.2367	W088 58.1666	-127.6
ROV Dive 5 on deck	9/6/18 17:25	N28 56.2496	W088 58.1737	ROV	N28 56.2511	W088 58.1849	0
ROV Dive 6 in water	9/6/18 22:34	N28 56.2623	W088 58.1813	ROV	N28 55.8412	W088 58.7254	0
Subsurface ADCP Hooked	9/6/18 23:13	N28 56.2610	W088 58.1752	ROV	N28 56.2555	W088 58.1738	-133.2

Appendices

Appendix A: Assessment Event Log

Event	Date - Time (UTC)	Ship Latitude	Ship Longitude	Equipment	Equipment Latitude	Equipment Longitude	Equipment Depth (m)
Subsurface ADCP on deck	9/6/18 23:20	N28 56.2595	W088 58.1699	ROV	N28 56.2557	W088 58.1775	-30.2
ROV on deck	9/6/18 23:24	N28 56.2587	W088 58.1760	ROV	N28 56.2485	W088 58.1747	0
BC12 on bottom	9/7/18 0:21	N28 55.5909	W088 59.1462	Box Corer	N28 55.5892	W088 59.1458	-139.1
BC11 on bottom	9/7/18 0:49	N28 55.9226	W088 58.6599	Box Corer	N28 55.9217	W088 58.6603	-132.5
BC10 on bottom	9/7/18 1:12	N28 55.9533	W088 58.6123	Box Corer	N28 55.9524	W088 58.6124	-131.6
BC09 on bottom	9/7/18 1:39	N28 55.9875	W088 58.5633	Box Corer	N28 55.9869	W088 58.5614	-131.6
BC08 on bottom	9/7/18 2:09	N28 56.0186	W088 58.5130	Box Corer	N28 56.0181	W088 58.5141	-131.4
BC07 on bottom	9/7/18 2:54	N28 56.0535	W088 58.4651	Box Corer	N28 56.0524	W088 58.4664	-128.7
BC06 on bottom	9/7/18 3:15	N28 56.0878	W088 58.4200	Box Corer	N28 56.0843	W088 58.4159	-131.9
BC05 on bottom	9/7/18 3:44	N28 56.1196	W088 58.3685	Box Corer	N28 56.1174	W088 58.3690	-132.3
BC04 on bottom	9/7/18 4:04	N28 56.1494	W088 58.3155	Box Corer	N28 56.1477	W088 58.3158	-133.9
BC03 on bottom	9/7/18 4:27	N28 56.1844	W088 58.2670	Box Corer	N28 56.1842	W088 58.2685	-134.1
BC02 on bottom	9/7/18 4:58	N28 56.2189	W088 58.2210	Box Corer	N28 56.2176	W088 58.2181	-134.6
BC01 on bottom	9/7/18 5:29	N28 56.2583	W088 58.1724	Box Corer	N28 56.2560	W088 58.1714	-135.4
BC14 on bottom	9/7/18 6:08	N28 56.5842	W088 57.6907	Box Corer	N28 56.5811	W088 57.6889	-129.6
BC15 on bottom	9/7/18 6:47	N28 56.9139	W088 57.2058	Box Corer	N28 56.9134	W088 57.2063	-133.7
Bubbles visible at surface	9/7/18 13:30	N28 56.2436	W088 58.1669	N/A	-	-	-
Tracer raft anchor deployed	9/7/18 14:39	N28 56.2446	W088 58.1643	N/A	-	-	-
Tracer raft anchor on bottom	9/7/18 14:40	N28 56.2423	W088 58.1734	N/A	-	-	-
Tracer raft deployed	9/7/18 14:42	N28 56.2399	W088 58.2003	N/A	-	-	-
Tracer raft on deck	9/7/18 14:53	N28 56.2404	W088 58.4019	N/A	-	-	-
Tracer raft anchor on board	9/7/18 15:06	N28 56.3107	W088 58.5798	N/A	-	-	-
Tracer raft 2 anchor on bottom	9/7/18 16:09	N28 56.2907	W088 58.2798	N/A	-	-	-
Tracer raft 2 deployed	9/7/18 18:30	N28 56.3660	W088 58.2798	N/A	-	-	-
Tracer raft 2 on deck	9/7/18 18:33	N28 56.3528	W088 58.2757	N/A	-	-	-
Surface water sampled near bubbles	9/7/18 20:09	N28 56.2384	W088 58.1579	N/A	-	-	-

Appendix B: Analyte Method Detection Limits

PAHs

CAS Registry	Compound	Sediment 15g Conc. (ng/g)	Water 1L Conc. (ng/L)	Product (oil) NA Conc. (ng/mg)
91-17-8	cis/trans Decalin	0.13	1.1	10.0
	C1-Decalins	0.26	2.3	10.0
	C2-Decalins	0.26	2.3	10.0
	C3-Decalins	0.26	2.3	10.0
	C4-Decalins	0.26	2.3	10.0
91-20-3	Naphthalene	0.34	2.9	10.0
	C1-Naphthalenes	1.03	1.4	10.0
	C2-Naphthalenes	0.68	5.8	10.0
	C3-Naphthalenes	0.68	5.8	10.0
	C4-Naphthalenes	0.68	5.8	10.0
95-15-8	Benzothiophene	0.09	1.3	10.0
	C1-Benzothiophenes	0.18	2.6	10.0
	C2-Benzothiophenes	0.18	2.6	10.0
	C3-Benzothiophenes	0.18	2.6	10.0
	C4-Benzothiophenes	0.18	2.6	10.0
92-52-4	Biphenyl	0.29	5.1	10.0
208-96-8	Acenaphthylene	0.04	1.2	10.0
83-32-9	Acenaphthene	0.10	1.4	10.0
132-64-09	Dibenzofuran	0.20	1.2	10.0
86-73-7	Fluorene	0.18	0.8	10.0
	C1-Fluorenes	0.37	1.6	10.0
	C2-Fluorenes	0.37	1.6	10.0
	C3-Fluorenes	0.37	1.6	10.0
86-74-8	Carbazole	0.15	0.8	10.0
120-12-7	Anthracene	0.12	0.8	10.0
85-01-8	Phenanthrene	0.21	2.3	10.0
	C1-Phenanthrenes/Anthracenes	0.08	0.7	10.0
	C2-Phenanthrenes/Anthracenes	0.29	3.0	10.0
	C3-Phenanthrenes/Anthracenes	0.29	3.0	10.0
	C4-Phenanthrenes/Anthracenes	0.29	3.0	10.0
132-65-0	Dibenzothiophene	0.12	0.8	10.0
	C1-Dibenzothiophenes	0.06	0.7	10.0
	C2-Dibenzothiophenes	0.23	1.3	10.0
	C3-Dibenzothiophenes	0.23	1.3	10.0
	C4-Dibenzothiophenes	0.23	1.3	10.0
206-44-0	Fluoranthene	0.33	1.1	10.0
129-00-0	Pyrene	0.14	1.4	10.0
	C1-Fluoranthenes/Pyrenes	0.47	2.5	10.0
	C2-Fluoranthenes/Pyrenes	0.47	2.5	10.0
	C3-Fluoranthenes/Pyrenes	0.47	2.5	10.0
	C4-Fluoranthenes/Pyrenes	0.47	2.5	10.0

Appendix B: Analyte Method Detection Limits

PAHs

CAS Registry	Compound	Sediment 15g Conc. (ng/g)	Water 1L Conc. (ng/L)	Product (oil) NA Conc. (ng/mg)
239-35-0	Naphthobenzothiophene	0.13	1.0	10.0
	C1-Naphthobenzothiophenes	0.26	2.1	10.0
	C2-Naphthobenzothiophenes	0.26	2.1	10.0
	C3-Naphthobenzothiophenes	0.26	2.1	10.0
	C4-Naphthobenzothiophenes	0.26	2.1	10.0
56-55-3	Benz(a)anthracene	0.19	0.7	10.0
218-01-9/217-59-4	Chrysene/Triphenylene	0.12	0.8	10.0
	C1-Chrysenes	0.23	1.6	10.0
	C2-Chrysenes	0.23	1.6	10.0
	C3-Chrysenes	0.23	1.6	10.0
	C4-Chrysenes	0.23	1.6	10.0
205-99-2	Benzo(b)fluoranthene	0.20	2.4	10.0
207-08-9/205-82-3	Benzo(k,j)fluoranthene	0.10	2.5	10.0
203-33-8	Benzo(a)fluoranthene	0.10	2.5	10.0
192-97-2	Benzo(e)pyrene	0.18	2.7	10.0
50-32-8	Benzo(a)pyrene	0.10	1.9	10.0
198-55-0	Perylene	1.27	0.6	10.0
193-39-5	Indeno(1,2,3-c,d)pyrene	0.05	1.4	10.0
53-70-3	Dibenzo(a,h)anthracene	0.06	1.1	10.0
	C1-Dibenzo(a,h)anthracenes	0.13	2.3	10.0
	C2-Dibenzo(a,h)anthracenes	0.13	2.3	10.0
	C3-Dibenzo(a,h)anthracenes	0.13	2.3	10.0
191-24-2	Benzo(g,h,i)perylene	0.09	2.5	10.0
91-57-6	2-Methylnaphthalene	1.30	1.1	10.0
90-12-0	1-Methylnaphthalene	0.55	1.4	10.0
581-42-0	2,6-Dimethylnaphthalene	0.26	0.7	10.0
2245-38-7	1,6,7-Trimethylnaphthalene	0.13	0.7	10.0
1730-37-6	1-Methylfluorene	0.19	1.5	10.0
7372-88-5	4-Methyldibenzothiophene	0.09	1.0	10.0
20928-02-3/16587-52-3	2/3-Methyldibenzothiophene	0.09	1.0	10.0
31317-07-4	1-Methyldibenzothiophene	0.09	1.0	10.0
832-71-3	3-Methylphenanthrene	0.10	0.9	10.0
2531-84-2	2-Methylphenanthrene	0.10	0.9	10.0
613-12-7	2-Methylanthracene	0.10	0.9	10.0
832-64-4/719-02-2	4/9-Methylphenanthrene	0.10	0.9	10.0
832-69-9	1-Methylphenanthrene	0.10	0.9	10.0
1576-67-6	3,6-Dimethylphenanthrene	0.11	1.7	10.0
483-65-8	Retene	0.23	1.6	10.0
33543-31-6	2-Methylfluoranthene	0.22	1.1	10.0
243-17-4	Benzo(b)fluorene	0.12	1.4	10.0
53584-60-4	C29-Hopane	0.57	8.2	10.0

Appendix B: Analyte Method Detection Limits

PAHs

CAS Registry	Analyte	Sediment 15g Conc. (ng/g)	Water 1L Conc. (ng/L)	Product (oil) NA Conc. (ng/mg)
30759-92-3	18a-Oleanane	0.57	8.2	10.0
13849-96-2	C30-Hopane	0.57	8.2	10.0
81943-50-2	C20-TAS	0.57	2.6	10.0
	C21-TAS	0.57	2.6	10.0
	C26(20S)-TAS	0.57	2.6	10.0
80382-29-2	C26(20R)/C27(20S)-TAS	0.57	2.6	10.0
	C28(20S)-TAS	0.57	2.6	10.0
	C27(20R)-TAS	0.57	2.6	10.0
80382-33-8	C28(20R)-TAS	0.57	2.6	10.0

Saturate

CAS Registry	Analyte	Water 1 L Conc. (µg/L)	Sediment 15 g Conc. (µg/g)	Product (oil) 40 mg Conc. (ug/mg)
111-84-2	n-C9 - n-nonane	0.288	0.012	0.350
124-18-5	n-C10 - n-decane	0.252	0.021	0.350
1120-21-4	n-C11 - n-undecane	0.251	0.016	0.350
112-40-3	n-C12 n-dodecane	0.266	0.019	0.350
629-50-5	n-C13 - n-tridecane	0.258	0.045	0.350
3891-98-3	i-C15 - 2,6,10-Trimethyldodecane	0.256	0.016	0.350
629-59-4	n-C14 - n-tetradecane	0.277	0.013	0.350
3891-99-4	i-C16 - 2,6,10-Trimethyltridecane	0.234	0.004	0.350
629-62-9	n-C15 - n-pentadecane	0.256	0.016	0.350
544-76-3	n-C16 - n-hexadecane	0.234	0.004	0.350
3892-00-0	i-C18 - Norpristane - 2,6,10-Trimethylpentadecane	0.100	0.004	0.350
629-78-7	n-C17 - n-heptadecane	0.174	0.003	0.350
1921-70-6	i-C19 - Pristane - 2,6,10,14-Tetramethylpentadecane	0.190	0.003	0.350
593-45-3	n-C18 - n-octadecane	0.100	0.004	0.350
638-36-8	i-C20 - Phytane - 2,6,10,14-Tetramethylhexadecane	0.201	0.006	0.350
629-92-5	n-C19 - n-nonadecane	0.073	0.005	0.350
112-95-8	n-C20 - n-eicosane	0.077	0.012	0.350
629-94-7	n-C21 - n-heneicosane	0.081	0.004	0.350
629-97-0	n-C22 - n-docosane	0.150	0.003	0.350
638-67-5	n-C23 - n-tricosane	0.117	0.008	0.350
643-31-1	n-C24 - n-tetracosane	0.069	0.005	0.350
629-99-2	n-C25 - n-pentacosane	0.066	0.007	0.350
630-01-3	n-C26 - n-hexacosane	0.070	0.008	0.350
593-49-7	n-C27 - n-heptacosane	0.069	0.011	0.350
630-02-4	n-C28 - n-octacosane	0.077	0.011	0.350
630-03-5	n-C29 - n-nonacosane	0.087	0.021	0.350

Appendix B: Analyte Method Detection Limits

Saturate

CAS Registry	Analyte	Water 1 L Conc. (µg/L)	Sediment 15 g Conc. (µg/g)	Product (oil) 40 mg Conc. (ug/mg)
638-68-6	n-C30 - n-triacontane	0.081	0.013	0.350
630-04-6	n-C31 - n-hentriacontane	0.126	0.015	0.350
544-85-4	n-C32 - n-dotriacontane	0.083	0.012	0.350
630-05-7	n-C33 - n-tritriacontane	0.282	0.021	0.350
14167-59-0	n-C34 - n-tetratriacontane	0.106	0.016	0.350
630-07-9	n-C35 - n-pentatriacontane	0.112	0.015	0.350
630-06-8	n-C36 - n-hexatriacontane	0.113	0.016	0.350
7194-84-5	n-C37 - n-heptatriacontane	0.148	0.017	0.350
7194-85-6	n-C38 - n-octatriacontane	0.127	0.019	0.350
7914-86-7	n-C39 - n-nonatriacontane	0.160	0.019	0.350
4181-95-7	n-C40 - n-tetracontane	0.144	0.019	0.350

Appendix C: Chemistry Data

Oil Aliphatic Data - Target Compounds

Sample ID	WAT05 Replicate 1		WAT05 Replicate 2		WAT05 Replicate 3		WAT05 mean	
Sample date	9/3/2018		9/3/2018		9/3/2018			
Units	µg/mg		µg/mg		µg/mg		µg/mg	
Target Compound								
n-C9	0.970		1.029		0.999		0.999	
n-C10	1.117		1.063		1.206		1.129	
n-C11	1.207		1.181		1.208		1.199	
n-C12	1.433		1.509		1.459		1.467	
n-C13	1.469		1.535		1.508		1.504	
i-C15	1.472		1.532		1.503		1.502	
n-C14	1.405		1.467		1.445		1.439	
i-C16	1.974		2.049		2.002		2.008	
n-C15	1.287		1.366		1.339		1.331	
n-C16	1.340		1.367		1.348		1.352	
i-C18	1.093		1.095		1.093		1.094	
n-C17	0.791		0.726		0.779		0.765	
Pristane	1.665		1.670		1.841		1.725	
n-C18	0.472	J	0.469	J	0.479	J	0.473	J
Phytane	1.321		1.336		1.338		1.332	
n-C19	0.380	J	0.388	J	0.389	J	0.386	J
n-C20	0.479	J	0.517	J	0.481	J	0.492	J
n-C21	0.235	J	0.239	J	0.241	J	0.238	J
n-C22	0.291	J	0.287	J	0.290	J	0.289	J
n-C23	0.212	J	0.207	J	0.220	J	0.213	J
n-C24	0.182	J	0.171	J	0.175	J	0.176	J
n-C25	0.146	J	0.168	J	0.152	J	0.155	J
n-C26	0.130	J	0.134	J	0.133	J	0.132	J
n-C27	0.100	J	0.086	J	0.099	J	0.095	J
n-C28	0.112	J	0.108	J	0.115	J	0.112	J
n-C29	0.140	J	0.127	J	0.119	J	0.129	J
n-C30	0.084	J	0.087	J	0.047	J	0.073	J
n-C31	0.086	J	0.088	J	0.086	J	0.087	J
n-C32	0.098	J	0.092	J	0.085	J	0.092	J
n-C33	0.119	J	0.114	J	0.114	J	0.116	J
n-C34	0.128	J	0.129	J	0.105	J	0.121	J
n-C35	<0.644	U	<0.644	U	<0.644	U	0	U
n-C36	<0.644	U	<0.644	U	<0.644	U	0	U
n-C37	<0.644	U	<0.644	U	<0.644	U	0	U
n-C38	<0.644	U	<0.644	U	<0.644	U	0	U
n-C39	<0.644	U	<0.644	U	<0.644	U	0	U
n-C40	<0.644	U	<0.644	U	<0.644	U	0	U
Total Alkanes	**21.9**		**22.3**		**22.4**		**22.2**	
Total Petroleum Hydrocarbons	475		471		467		471	
Total Resolved Hydrocarbons	57		56		49		54	
Unresolved Complex Mixture	417		415		418		417	

Note: J = less than 3x the MDL, U = below the MDL

Appendix C: Chemistry Data

Water Aliphatic Data - Target Comounds

Sample ID	WAT Atmosphere Blank	WAT09 Atmosphere Blank 1	WAT08 A (Surface)	WAT08 B (Surface)	WAT11 B (Surface)
Sample date	09/07/18	09/06/18	09/06/18	09/06/18	09/07/18
Units	ng/container	ng/container	ng/L	ng/L	ng/L
Target Compound					
n-C9	<0.288 U	<0.288 U	<0.288 U	<0.288 U	<0.288 U
n-C10	<0.252 U	<0.252 U	0.070 J	<0.252 U	0.634
n-C11	<0.251 U	<0.251 U	0.218 J	0.096 J	2.494
n-C12	<0.266 U	<0.266 U	2.140	0.193 J	5.422
n-C13	<0.258 U	<0.258 U	8.128	0.749	9.025
i-C15	<0.256 U	<0.256 U	14.189	4.358	21.111
n-C14	<0.277 U	<0.277 U	15.818	2.740	16.652
i-C16	<0.234 U	<0.234 U	29.847	12.736	41.417
n-C15	<0.256 U	<0.256 U	28.421	11.401	18.583
n-C16	<0.234 U	<0.234 U	22.376	8.710	17.090
i-C18	<0.1 U	<0.1 U	21.949	11.134	24.421
n-C17	<0.174 U	<0.174 U	15.048	5.756	10.702
Pristane	<0.19 U	<0.19 U	35.151	18.458	38.679
n-C18	<0.1 U	<0.1 U	9.741	3.628	7.473
Phytane	<0.201 U	<0.201 U	27.187	15.665	31.719
n-C19	<0.073 U	<0.073 U	8.222	2.162	3.381
n-C20	<0.077 U	<0.077 U	11.220	5.139	10.604
n-C21	<0.081 U	<0.081 U	6.004	2.153	4.666
n-C22	<0.15 U	<0.15 U	6.122	2.711	6.111
n-C23	<0.117 U	<0.117 U	4.163	1.833	3.645
n-C24	<0.069 U	<0.069 U	4.201	1.582	3.266
n-C25	<0.066 U	<0.066 U	3.213	1.248	1.355
n-C26	<0.07 U	<0.07 U	2.538	1.143	2.314
n-C27	<0.069 U	<0.069 U	2.104	0.695	1.575
n-C28	<0.077 U	<0.077 U	1.905	0.984	1.608
n-C29	<0.087 U	<0.087 U	2.127	<0.087 U	1.939
n-C30	<0.081 U	<0.081 U	1.193	<0.081 U	0.867
n-C31	<0.126 U	<0.126 U	1.289	<0.126 U	1.089
n-C32	<0.083 U	<0.083 U	1.881	<0.083 U	1.922
n-C33	<0.282 U	<0.282 U	1.904	<0.282 U	2.316
n-C34	<0.106 U	<0.106 U	3.249	<0.106 U	1.258
n-C35	<0.112 U	<0.112 U	<0.112 U	<0.112 U	<0.112 U
n-C36	<0.113 U	<0.113 U	<0.113 U	<0.113 U	<0.113 U
n-C37	<0.148 U	<0.148 U	<0.148 U	<0.148 U	<0.148 U
n-C38	<0.127 U	<0.127 U	<0.127 U	<0.127 U	<0.127 U
n-C39	<0.16 U	<0.16 U	<0.16 U	<0.16 U	<0.16 U
n-C40	<0.144 U	<0.144 U	<0.144 U	<0.144 U	<0.144 U
Total Alkanes	**0 U**	**0 U**	**291.6**	**115.3**	**293.3**
Total Petroleum Hydrocarbons	<13 U	<13 U	11894	7153	14329
Total Resolved Hydrocarbons	<13 U	<13 U	1368	678	1624
Unresolved Complex Mixture	<13 U	<13 U	10526	6475	12704

Note: J = less than 3x the MDL, U = below the MDL

Appendix C: Chemistry Data

Water Aliphatic Data - Target Compounds

Sample ID	WAT11 A (Surface)	WAT01 (Midwater)	WAT02 (Midwater)	WAT Atmosphere Blank 2	WAT Blank (tubing)
Sample date	09/07/18	09/02/18	09/02/18	09/05/18	09/05/18
Units	ng/L	ng/L	ng/L	ng/container	ng/L
Target Compound					
n-C9	1.691	15.039	<1.029 U	<0.288 U	0.837 J
n-C10	5.960	79.641	<0.898 U	<0.252 U	2.380
n-C11	9.115	147.510	<0.896 U	<0.251 U	6.686
n-C12	13.982	205.944	<0.951 U	<0.266 U	17.765
n-C13	16.955	213.264	<0.923 U	<0.258 U	27.007
i-C15	33.511	324.144	<0.916 U	<0.256 U	37.000
n-C14	16.758	195.680	<0.988 U	<0.277 U	37.286
i-C16	62.495	434.953	<0.836 U	<0.234 U	64.358
n-C15	28.636	286.992	<0.916 U	<0.256 U	52.837
n-C16	22.858	157.138	<0.836 U	<0.234 U	37.154
i-C18	35.102	240.570	<0.358 U	<0.1 U	52.098
n-C17	20.409	113.480	<0.62 U	<0.174 U	30.180
Pristane	53.846	379.984	<0.678 U	<0.19 U	82.661
n-C18	9.881	73.568	<0.358 U	<0.1 U	19.985
Phytane	47.925	288.541	<0.716 U	<0.201 U	65.766
n-C19	6.872	46.326	<0.262 U	<0.073 U	15.837
n-C20	15.328	96.725	<0.276 U	<0.077 U	21.805
n-C21	7.419	44.001	<0.288 U	<0.081 U	13.628
n-C22	9.415	60.203	<0.535 U	<0.15 U	14.881
n-C23	5.034	50.971	<0.418 U	<0.117 U	10.030
n-C24	4.652	36.284	<0.245 U	<0.069 U	8.677
n-C25	3.305	23.641	<0.234 U	<0.066 U	6.498
n-C26	3.924	27.687	<0.251 U	<0.07 U	6.185
n-C27	2.561	20.027	<0.245 U	<0.069 U	4.889
n-C28	3.451	29.586	<0.275 U	<0.077 U	5.191
n-C29	3.660	32.737	<0.312 U	<0.087 U	6.447
n-C30	1.858	9.379	<0.289 U	<0.081 U	<0.368 U
n-C31	1.982	11.069	<0.45 U	<0.126 U	<0.572 U
n-C32	2.559	17.723	<0.296 U	<0.083 U	<0.376 U
n-C33	3.490	19.692	<1.007 U	<0.282 U	<1.281 U
n-C34	2.983	30.715	<0.38 U	<0.106 U	<0.483 U
n-C35	1.915	15.518	<0.399 U	<0.112 U	<0.507 U
n-C36	<0.113 U	<0.808 U	<0.404 U	<0.113 U	<0.514 U
n-C37	<0.148 U	<1.057 U	<0.528 U	<0.148 U	<0.673 U
n-C38	<0.127 U	<0.908 U	<0.454 U	<0.127 U	<0.578 U
n-C39	<0.16 U	<1.146 U	<0.573 U	<0.16 U	<0.729 U
n-C40	<0.144 U	<1.026 U	<0.513 U	<0.144 U	<0.653 U
Total Alkanes	**459.5**	**3728.7**	**0 U**	**0 U**	**648.1**
Total Petroleum Hydrocarbons	21933	146498	<46.429 U	<13 U	39039
Total Resolved Hydrocarbons	2275	17053	<46.429 U	<13 U	3613
Unresolved Complex Mixture	19659	129446	<46.429 U	<13 U	35426

Note: J = less than 3x the MDL, U = below the MDL

Appendix C: Chemistry Data

Sediment Aliphatic Data - Target Compounds

Sample ID	BC01	BC02	BC03	BC04	BC05	BC06	BC07
Sample date	09/07/18	09/06/18	09/06/18	09/06/18	09/06/18	09/06/18	09/06/18
Units	µg/dry g	µg/dry g	µg/dry g	µg/dry g	µg/dry g	µg/dry g	µg/dry g
Target Compound							
n-C9	0.025	0.022	<0.012 U	<0.012 U	<0.012 U	0.022	0.022
n-C10	0.021 J	0.017 J	<0.021 U	0.017 J	0.022	0.012 J	0.016 J
n-C11	0.070	0.025	<0.016 U	0.024	0.028	0.016 J	0.024
n-C12	0.164	0.032	0.018 J	0.028	0.023	0.015 J	0.022
n-C13	0.482	0.046	0.039 J	0.055	0.047	0.038 J	0.045
i-C15	0.232	0.183	0.058	0.051	0.039	0.031	0.036
n-C14	0.639	0.157	0.051	0.068	0.045	0.033	0.037
i-C16	1.052	0.188	0.072	0.071	0.073	0.038	0.048
n-C15	0.490	0.085	0.036	0.063	0.063	0.051	0.089
n-C16	0.479	0.047	0.023	0.037	0.023	0.021	0.029
i-C18	0.089	0.011	0.025	0.024	0.029	0.011	0.026
n-C17	0.372	0.144	0.117	0.131	0.116	0.114	0.126
Pristane	0.647	0.105	0.052	0.060	0.070	0.056	0.074
n-C18	0.842	0.225	0.203	0.206	0.206	0.202	0.209
Phytane	0.832	0.138	0.046	0.062	0.051	0.042	0.044
n-C19	0.343	0.094	0.075	0.086	0.083	0.086	0.089
n-C20	0.085	0.050	0.024	0.028	0.030	0.019	0.026
n-C21	0.371	0.418	0.403	0.483	0.449	0.494	0.434
n-C22	0.113	0.142	0.072	0.071	0.050	0.052	0.052
n-C23	0.263	0.146	0.100	0.103	0.090	0.090	0.089
n-C24	0.391	0.105	0.106	0.095	0.080	0.075	0.070
n-C25	0.382	0.195	0.192	0.179	0.173	0.141	0.137
n-C26	0.119	0.142	0.106	0.086	0.073	0.079	0.065
n-C27	0.610	0.373	0.335	0.344	0.335	0.339	0.304
n-C28	0.133	0.211	0.152	0.151	0.145	0.136	0.140
n-C29	1.095	0.931	0.856	0.820	0.794	0.805	0.722
n-C30	0.057	0.166	0.143	0.150	0.192	0.187	0.157
n-C31	0.464	1.434	1.358	1.447	2.012	1.953	2.106
n-C32	0.446	0.267	0.213	0.218	0.239	0.234	0.245
n-C33	0.561	0.412	0.392	0.466	0.462	0.443	0.625
n-C34	0.124	0.173	0.159	0.167	0.203	0.169	0.197
n-C35	0.940	0.328	0.243	0.267	0.247	0.256	0.211
n-C36	0.231	0.087	0.108	0.099	0.061	0.057	0.063
n-C37	0.134	0.255	0.126	0.164	0.176	0.141	0.155
n-C38	0.029	0.107	0.031	0.054	0.021	0.023	0.027
n-C39	0.049	0.011 J	<0.019 U	0.091	0.049	0.040	0.043
n-C40	0.038	0.027	<0.019 U	<0.019 U	<0.019 U	<0.019 U	<0.019 U
Total Alkanes	**13.4**	**7.5**	**5.9**	**6.5**	**6.8**	**6.5**	**6.8**
Total Petroleum Hydrocarbons	3889	902	437	327	237	214	195
Total Resolved Hydrocarbons	145	54	41	41	41	37	38
Unresolved Complex Mixture	3744	848	397	285	196	177	157

Note: J = less than 3x the MDL, U = below the MDL

Appendix C: Chemistry Data

Sediment Aliphatic Data - Target Compounds

Sample ID	BC13	BC14	BC15	SED Blank 1	SED Blank 2	SED Blank 3
Sample date	09/05/18	09/07/18	09/07/18	09/07/18	09/06/18	09/05/18
Units	µg/dry g	µg/dry g	µg/dry g	µg/container	µg/container	µg/container
Target Compound						
n-C9	0.021	<0.012 U	0.022	<1.25 U	<1.25 U	<1.25 U
n-C10	0.015 J	<0.021 U	0.018 J	<1.25 U	<1.25 U	<1.25 U
n-C11	0.015 J	0.024	0.018	<1.25 U	<1.25 U	<1.25 U
n-C12	0.017 J	0.021	0.019	<1.25 U	<1.25 U	<1.25 U
n-C13	0.047	0.051	0.040 J	<1.25 U	<1.25 U	<1.25 U
i-C15	0.033	0.028	0.021	<1.25 U	<1.25 U	<1.25 U
n-C14	0.027	0.031	0.026	<1.25 U	<1.25 U	<1.25 U
i-C16	0.026	0.023	0.051	<1.25 U	<1.25 U	<1.25 U
n-C15	0.064	0.078	0.050	<1.25 U	<1.25 U	<1.25 U
n-C16	0.020	0.032	0.018	<1.25 U	<1.25 U	<1.25 U
i-C18	0.012	0.010	0.015	<1.25 U	<1.25 U	<1.25 U
n-C17	0.146	0.122	0.133	<1.25 U	<1.25 U	<1.25 U
Pristane	0.056	0.050	0.044	<1.25 U	<1.25 U	<1.25 U
n-C18	0.234	0.217	0.244	<1.25 U	<1.25 U	<1.25 U
Phytane	0.032	0.028	0.033	<1.25 U	<1.25 U	<1.25 U
n-C19	0.126	0.110	0.103	<1.25 U	<1.25 U	<1.25 U
n-C20	0.026	0.024	0.028	<1.25 U	<1.25 U	<1.25 U
n-C21	0.433	0.424	0.496	<1.25 U	<1.25 U	<1.25 U
n-C22	0.042	0.052	0.047	<1.25 U	<1.25 U	<1.25 U
n-C23	0.097	0.091	0.089	<1.25 U	<1.25 U	<1.25 U
n-C24	0.074	0.074	0.069	<1.25 U	<1.25 U	<1.25 U
n-C25	0.152	0.140	0.147	<1.25 U	<1.25 U	<1.25 U
n-C26	0.074	0.067	0.063	<1.25 U	<1.25 U	<1.25 U
n-C27	0.347	0.318	0.319	<1.25 U	<1.25 U	<1.25 U
n-C28	0.135	0.132	0.131	<1.25 U	<1.25 U	<1.25 U
n-C29	0.798	0.823	0.799	<1.25 U	<1.25 U	<1.25 U
n-C30	0.163	0.154	0.152	<1.25 U	<1.25 U	<1.25 U
n-C31	2.775	2.102	2.644	<1.25 U	<1.25 U	<1.25 U
n-C32	0.277	0.233	0.219	<1.25 U	<1.25 U	<1.25 U
n-C33	0.517	0.585	0.430	<1.25 U	<1.25 U	<1.25 U
n-C34	0.186	0.157	0.155	<1.25 U	<1.25 U	<1.25 U
n-C35	0.250	0.184	0.257	<1.25 U	<1.25 U	<1.25 U
n-C36	0.054	0.066	0.063	<1.25 U	<1.25 U	<1.25 U
n-C37	0.179	0.118	0.147	<1.25 U	<1.25 U	<1.25 U
n-C38	0.057	0.041	0.035	<1.25 U	<1.25 U	<1.25 U
n-C39	0.081	0.052	0.023	<1.25 U	<1.25 U	<1.25 U
n-C40	<0.019 U	0.068	<0.019 U	<1.25 U	<1.25 U	<1.25 U
Total Alkanes	**7.6**	**6.7**	**7.2**	0	0	0
Total Petroleum Hydrocarbons	167	247	263	<20 U	<20 U	<20 U
Total Resolved Hydrocarbons	43	41	39	<20 U	<20 U	<20 U
Unresolved Complex Mixture	124	205	224	<20 U	<20 U	<20 U

Note: J = less than 3x the MDL, U = below the MDL

Appendix C: Chemistry Data

Oil PAH Data - Target Compounds

Sample ID	WAT05 A	WAT05 B	WAT05 C	WAT05 mean
Sample date	09/03/18	09/03/18	09/03/18	
Units	ng/mg	ng/mg	ng/mg	ng/mg
Target Compound				
cis/trans Decalin	882	995	995	957
C1-Decalins	1649	1630	1655	1645
C2-Decalins	1846	1826	1865	1846
C3-Decalins	1626	1497	1432	1518
C4-Decalins	1361	1255	1327	1315
Naphthalene	87.0	88.0	88.4	87.8
C1-Naphthalenes	292	295	295	294
C2-Naphthalenes	1122	1134	1137	1131
C3-Naphthalenes	1360	1290	1301	1317
C4-Naphthalenes	1099	1086	1074	1086
Benzothiophene	19.3	19.2	19.6	19.4
C1-Benzothiophenes	67.9	68.5	74.3	70.2
C2-Benzothiophenes	61.1	58.4	57.7	59.1
C3-Benzothiophenes	89.9	84.0	85.1	86.3
C4-Benzothiophenes	63.7	70.0	71.0	68.2
Biphenyl	37.1	37.3	37.4	37.3
Acenaphthylene	7.84 J	8.09 J	7.93 J	7.95 J
Acenaphthene	22.8	23.1	22.9	22.9
Dibenzofuran	11.6	11.3	11.4	11.4
Fluorene	95.6	96.3	96.8	96.2
C1-Fluorenes	285	273	291	283
C2-Fluorenes	460	480	444	461
C3-Fluorenes	347	378	396	374
Carbazole	6.04 J	5.64 J	5.80 J	5.83 J
Anthracene	3.49 J	3.13 J	3.74 J	3.45 J
Phenanthrene	180	180	180	180
C1-Phenanthrenes/ Anthracenes	548	546	548	547
C2-Phenanthrenes/ Anthracenes	825	849	829	834
C3-Phenanthrenes/ Anthracenes	677	683	702	687
C4-Phenanthrenes/ Anthracenes	318	283	321	307
Dibenzothiophene	37.2	37.1	37.2	37.2
C1-Dibenzothiophenes	139	138	139	139
C2-Dibenzothiophenes	267	257	254	259
C3-Dibenzothiophenes	223	209	214	215
C4-Dibenzothiophenes	106	103	111	107

Table continued on next column

Sample ID	WAT05 A	WAT05 B	WAT05 C	WAT05 mean
Sample date	09/03/18	09/03/18	09/03/18	
Units	ng/mg	ng/mg	ng/mg	ng/mg
Fluoranthene	6.66 J	6.66 J	6.60 J	6.64 J
Pyrene	10.7	10.5	10.6	10.6
C1-Fluoranthenes/Pyrenes	83.1	75.3	74.1	77.5
C2-Fluoranthenes/Pyrenes	109	104	94	103
C3-Fluoranthenes/Pyrenes	124	119	119	121
C4-Fluoranthenes/Pyrenes	95.7	98.6	103	99
Naphthobenzothiophene	19.8	20.5	21.7	20.7
C1-Naphthobenzothiophenes	58.2	60.7	60.3	59.7
C2-Naphthobenzothiophenes	93.9	85.5	92.0	90.5
C3-Naphthobenzothiophenes	86.2	79.5	86.8	84.2
C4-Naphthobenzothiophenes	31.2	29.6	35.1	32.0
Benz(a)anthracene	3.91 J	4.07 J	3.82 J	4 J
Chrysene/Triphenylene	24.3	23.8	23.2	23.8
C1-Chrysenes	87.1	81.3	82.7	83.7
C2-Chrysenes	141	136	141	140
C3-Chrysenes	91.7	91.6	93.3	92.2
C4-Chrysenes	78.2	78.5	73.9	76.9
Benzo(b)fluoranthene	4.15 J	4.17 J	4.15 J	4.16 J
Benzo(k,j)fluoranthene	0.583 J	0.506 J	0.547 J	0.545 J
Benzo(a)fluoranthene	<10 U	<10 U	<10 U	0 U
Benzo(e)pyrene	5.02 J	4.86 J	4.87 J	4.91 J
Benzo(a)pyrene	2.33 J	2.57 J	2.52 J	2.47 J
Perylene	132	134	133	133
Indeno(1,2,3-c,d)pyrene	0.786 J	0.940 J	1.20 J	0.98 J
Dibenzo(a,h)anthracene	<10 U	<10 U	<10 U	0 U
C1-Dibenzo(a,h)anthracenes	<10 U	<10 U	<10 U	0 U
C2-Dibenzo(a,h)anthracenes	<10 U	<10 U	<10 U	0 U
C3-Dibenzo(a,h)anthracenes	<10 U	<10 U	<10 U	0 U
Benzo(g,h,i)perylene	1.42 J	1.43 J	1.43 J	1.43 J
Total PAHs	**17515**	**17252**	**17399**	**17388.84**

Note: J = less than 3x the MDL, U = below the MDL

Appendix C: Chemistry Data

Oil PAH Data - Individual Alkyl Isomers and Hopanes

Sample ID	WAT05 A	WAT05 B	WAT05 C	WAT05 mean
Sample date	09/03/18	09/03/18	09/03/18	
Units	ng/mg	ng/mg	ng/mg	ng/mg
Individual Alkyl Isomers and Hopanes				
2-Methylnaphthalene	245	247	248	247
1-Methylnaphthalene	193	195	196	195
2,6-Dimethylnaphthalene	227	225	232	228
1,6,7-Trimethylnaphthalene	141	140	142	141
1-Methylfluorene	180	183	184	182
4-Methyldibenzothiophene	95.3	95.4	95.5	95.4
2/3-Methyldibenzothiophene	41.1	40.7	41.0	41.0
1-Methyldibenzothiophene	36.8	36.8	36.6	36.7
3-Methylphenanthrene	167	166	166	166
2-Methylphenanthrene	171	170	171	170
2-Methylanthracene	1.97 J	1.96 J	1.93 J	1.95 J
4/9-Methylphenanthrene	220	220	221	220
1-Methylphenanthrene	144	144	145	144
3,6-Dimethylphenanthrene	62.4	62.2	65.5	63.4
Retene	17.9	18.8	18.0	18.2
2-Methylfluoranthene	4.67 J	4.95 J	5.14 J	4.92 J
Benzo(b)fluorene	11.4	11.4	11.4	11.4
C29-Hopane	46.8	46.5	46.2	46.5
18a-Oleanane	<10 U	<10 U	<10 U	0 U
C30-Hopane	113	115	116	114
C20-TAS	48.1	50.2	49.7	49.3
C21-TAS	51.5	53.4	54.1	53.0
C26(20S)-TAS	42.0	44.0	43.2	43.1
C26(20R)/C27(20S)-TAS	147	152	147	149
C28(20S)-TAS	110	112	113	112
C27(20R)-TAS	88.0	87.4	87.5	87.6
C28(20R)-TAS	89.7	91.3	92.5	91.2

Note: J = less than 3x the MDL, U = below the MDL

Appendix C: Chemistry Data

Water PAH Data - Target Compounds

Sample ID	WAT Atmosphere Blank	WAT09 Atmosphere Blank 1	WAT08 A (Surface)	WAT08 B (Surface)	WAT11 B (Surface)	WAT11 A (Surface)	WAT01 (Midwater)	WAT02 (Midwater)	WAT Atmospheric Blank 2	WAT Blank (tubing)
Sample date	09/07/18	09/06/18	09/06/18	09/06/18	09/07/18	09/07/18	09/02/18	09/02/18	09/05/18	09/05/18
Units	ng/container	ng/container	ng/L	ng/L	ng/L	ng/L	ng/L	ng/L	ng/container	ng/L
Target Compound										
cis/trans Decalin	<1.1 U	<1.1 U	85.9	<1.1 U	1744	7148	87851	<4.1 U	<1.1 U	3824
C1-Decalins	<2.3 U	<2.3 U	311	<2.3 U	4336	15978	208895	<8.2 U	<2.3 U	9809
C2-Decalins	<2.3 U	<2.3 U	2099	<2.3 U	10499	31153	320271	<8.2 U	<2.3 U	21715
C3-Decalins	<2.3 U	<2.3 U	6140	<2.3 U	15361	40008	340326	<8.2 U	<2.3 U	28653
C4-Decalins	<2.3 U	<2.3 U	12558	<2.3 U	15316	35384	235314	<8.2 U	<2.3 U	32722
Naphthalene	<2.9 U	<2.9 U	98	18.2	634	1183	19698	<10.4 U	<2.9 U	2480
C1-Naphthalenes	<1.4 U	<1.4 U	1482	190	2448	5327	59440	<4.9 U	<1.4 U	8629
C2-Naphthalenes	<5.8 U	<5.8 U	13107	4327	17961	34491	266496	<20.8 U	<5.8 U	28929
C3-Naphthalenes	<5.8 U	<5.8 U	24835	11421	29310	50747	364289	<20.8 U	<5.8 U	38510
C4-Naphthalenes	<5.8 U	<5.8 U	23493	11972	26219	45561	285084	<20.8 U	<5.8 U	36184
Benzothiophene	<1.3 U	<1.3 U	31.3	4.48	149	417	3564	<4.6 U	<1.3 U	252
C1-Benzothiophenes	<2.6 U	<2.6 U	431	65.4	968	2385	16511	<9.2 U	<2.6 U	1480
C2-Benzothiophenes	<2.6 U	<2.6 U	694	235	1075	2008	16308	<9.2 U	<2.6 U	1442
C3-Benzothiophenes	<2.6 U	<2.6 U	1345	548	1936	2991	21708	<9.2 U	<2.6 U	2546
C4-Benzothiophenes	<2.6 U	<2.6 U	1530	651	1711	3188	18072	<9.2 U	<2.6 U	2000
Biphenyl	<5.1 U	<5.1 U	335	111	525	1307	6229	<18.2 U	<5.1 U	1207
Acenaphthylene	<1.2 U	<1.2 U	124	42.3	159	301	2392	<4.2 U	<1.2 U	260
Acenaphthene	<1.4 U	<1.4 U	381	126	435	807	6225	<5.1 U	<1.4 U	856
Dibenzofuran	<1.2 U	<1.2 U	158	93.5	261	499	4493	<4.2 U	<1.2 U	353
Fluorene	<0.8 U	<0.8 U	1738	1025	2142	4517	18301	<2.9 U	<0.8 U	3480
C1-Fluorenes	<1.6 U	<1.6 U	5945	4201	7872	15777	62402	<5.8 U	<1.6 U	10125
C2-Fluorenes	<1.6 U	<1.6 U	12012	7350	13699	29072	123221	<5.8 U	<1.6 U	16832
C3-Fluorenes	<1.6 U	<1.6 U	11638	5485	11266	26225	114750	<5.8 U	<1.6 U	14698
Carbazole	<0.8 U	<0.8 U	109.8	58.8	119	257	1381	<3 U	<0.8 U	206
Anthracene	<0.8 U	<0.8 U	109	69.8	126	240	649	<2.7 U	<0.8 U	180
Phenanthrene	<2.3 U	<2.3 U	3609	2741	4645	9761	33737	9.62	<2.3 U	6476
C1-Phenanthrenes/Anthracenes	<0.7 U	<0.7 U	12143	8912	15266	32020	122130	<2.5 U	<0.7 U	19215
C2-Phenanthrenes/Anthracenes	<3 U	<3 U	18536	12323	23082	46391	198959	<10.8 U	<3 U	28605
C3-Phenanthrenes/Anthracenes	<3 U	<3 U	16432	9498	18548	35859	158368	<10.8 U	<3 U	22565
C4-Phenanthrenes/Anthracenes	<3 U	<3 U	7787	4305	10499	19159	97743	<10.8 U	<3 U	14423
Dibenzothiophene	<0.8 U	<0.8 U	774	551	964	2005	7184	<2.9 U	<0.8 U	1398
C1-Dibenzothiophenes	<0.7 U	<0.7 U	2969	2063	3643	7489	30280	<2.4 U	<0.7 U	4667
C2-Dibenzothiophenes	<1.3 U	<1.3 U	6330	3714	6629	13909	60436	<4.8 U	<1.3 U	8414
C3-Dibenzothiophenes	<1.3 U	<1.3 U	5139	2912	5407	11344	54145	<4.8 U	<1.3 U	7265
C4-Dibenzothiophenes	<1.3 U	<1.3 U	2618	1454	2972	6428	29904	<4.8 U	<1.3 U	3568
Fluoranthene	<1.1 U	<1.1 U	188	83.0	187	329	1976	<3.9 U	<1.1 U	258
Pyrene	1.39	1.19 J	284	181	331	672	2939	5.91	1.25 J	426
C1-Fluoranthenes/Pyrenes	<2.5 U	<2.5 U	1715	1031	1925	4033	18947	<8.8 U	<2.5 U	2567
C2-Fluoranthenes/Pyrenes	<2.5 U	<2.5 U	2382	1647	2944	6249	24797	<8.8 U	<2.5 U	3278
C3-Fluoranthenes/Pyrenes	<2.5 U	<2.5 U	2772	1936	3488	7646	29076	<8.8 U	<2.5 U	3997
C4-Fluoranthenes/Pyrenes	<2.5 U	<2.5 U	2264	1410	2785	5218	22069	<8.8 U	<2.5 U	3201
Naphthobenzothiophene	<1 U	<1 U	580	321	587	1171	5193	<3.7 U	<1 U	729
C1-Naphthobenzothiophenes	<2.1 U	<2.1 U	1297	876	1752	3532	13881	<7.4 U	<2.1 U	1861
C2-Naphthobenzothiophenes	<2.1 U	<2.1 U	2079	1323	2462	5355	22820	<7.4 U	<2.1 U	3077
C3-Naphthobenzothiophenes	<2.1 U	<2.1 U	1898	1118	2222	4398	20142	<7.4 U	<2.1 U	2660
C4-Naphthobenzothiophenes	<2.1 U	<2.1 U	886	390	1067	1600	5863	<7.4 U	<2.1 U	988
Benz(a)anthracene	<0.7 U	<0.7 U	94.1	62.4	94	181	725	<2.6 U	<0.7 U	107

Table continued on next page

Note: J = less than 3x the MDL, U = below the MDL

Appendix C: Chemistry Data

Water PAH Data - Target Compounds Continued

Sample ID	WAT Atmosphere Blank	WAT09 Atmosphere Blank 1	WAT08 A (Surface)	WAT08 B (Surface)	WAT11 B (Surface)	WAT11 A (Surface)	WAT01 (Midwater)	WAT02 (Midwater)	WAT Atmospheric Blank 2	WAT Blank (tubing)
Sample date	09/07/18	09/06/18	09/06/18	09/06/18	09/07/18	09/07/18	09/02/18	09/02/18	09/05/18	09/05/18
Units	ng/container	ng/container	ng/L	ng/L	ng/L	ng/L	ng/L	ng/L	ng/container	ng/L
Chrysene/Triphenylene	<0.8 U	<0.8 U	556	431	753	1440	4864	<2.9 U	<0.8 U	719
C1-Chrysenes	<1.6 U	<1.6 U	1749	1313	2112	4813	19508	<5.7 U	<1.6 U	2443
C2-Chrysenes	<1.6 U	<1.6 U	2872	1986	4015	7437	28687	<5.7 U	<1.6 U	3954
C3-Chrysenes	<1.6 U	<1.6 U	2281	1259	2743	5151	24439	<5.7 U	<1.6 U	2959
C4-Chrysenes	<1.6 U	<1.6 U	1750	662	1927	3134	18168	<5.7 U	<1.6 U	2048
Benzo(b)fluoranthene	<2.4 U	<2.4 U	91	52.3	117	239	990	<8.5 U	<2.4 U	134
Benzo(k,j)fluoranthene	<2.5 U	<2.5 U	48	24.6	39.5	72.9	373	<9 U	<2.5 U	46.2
Benzo(a)fluoranthene	<2.5 U	<2.5 U	18.9	<2.5 U	17.0	41	164	<9 U	<2.5 U	<11.4 U
Benzo(e)pyrene	<2.7 U	<2.7 U	116	89.2	154	340	1103	<9.6 U	<2.7 U	192
Benzo(a)pyrene	<1.9 U	2.33	71.9	36.2	78	139	745	16.6	2.81	108
Perylene	<0.6 U	<0.6 U	3456	1286	3079	5509	36009	8.35	<0.6 U	3878
Indeno(1,2,3-c,d)pyrene	<1.4 U	<1.4 U	42.9	<1.4 U	39.1	34.4	165	<5 U	<1.4 U	27.9
Dibenzo(a,h)anthracene	<1.1 U	<1.1 U	28.0	<1.1 U	27.8	57.3	157	<4.1 U	<1.1 U	28.2
C1-Dibenzo(a,h)anthracenes	<2.3 U	<2.3 U	<4.5 U	<2.3 U	<4.5 U	<9.1 U	<64.9 U	<8.1 U	<2.3 U	<10.3 U
C2-Dibenzo(a,h)anthracenes	<2.3 U	<2.3 U	<4.5 U	<2.3 U	<4.5 U	<9.1 U	<64.9 U	<8.1 U	<2.3 U	<10.3 U
C3-Dibenzo(a,h)anthracenes	<2.3 U	<2.3 U	<4.5 U	<2.3 U	<4.5 U	<9.1 U	<64.9 U	<8.1 U	<2.3 U	<10.3 U
Benzo(g,h,i)perylene	<2.5 U	<2.5 U	37.5	16.0	37.3	69	374	<9 U	<2.5 U	40.5
Total PAHs	**1.39**	**3.52**	**226684**	**114003**	**292906**	**610198**	**3700932**	**40.5**	**4.06**	**423697**

Water PAH Data - Individual Alkyl Isomers and Hopanes

Sample ID	WAT Atmosphere Blank	WAT09 Atmosphere Blank 1	WAT08 A (Surface)	WAT08 B (Surface)	WAT11 B (Surface)	WAT11 A (Surface)	WAT01 (Midwater)	WAT02 (Midwater)	WAT Atmospheric Blank 2	WAT blank (tubing)
Sample date	09/07/18	09/06/18	09/06/18	09/06/18	09/07/18	09/07/18	09/02/18	09/02/18	09/05/18	09/05/18
Units	ng/container	ng/container	ng/L	ng/L	ng/L	ng/L	ng/L	ng/L	ng/container	ng/L
Individual Alkyl Isomers and Hopanes										
2-Methylnaphthalene	<1.1 U	<1.1 U	1133	135	1765	4215	43261	<3.9 U	<1.1 U	7010
1-Methylnaphthalene	<1.4 U	<1.4 U	1117	153	1951	3870	46980	<5.1 U	<1.4 U	6061
2,6-Dimethylnaphthalene	<0.7 U	<0.7 U	2277	719	3463	6137	59061	<2.5 U	<0.7 U	6042
1,6,7-Trimethylnaphthalene	<0.7 U	<0.7 U	2916	1218	3180	5343	40616	<2.4 U	<0.7 U	4415
1-Methylfluorene	<1.5 U	<1.5 U	4052	2632	4959	10004	41363	<5.3 U	<1.5 U	6311
4-Methyldibenzothiophene	<1 U	<1 U	2058	1413	2496	5133	21034	<3.4 U	<1 U	3219
2/3-Methyldibenzothiophene	<1 U	<1 U	888	682	1141	2355	8980	<3.4 U	<1 U	1460
1-Methyldibenzothiophene	<1 U	<1 U	815	542	979	2001	8351	<3.4 U	<1 U	1283
3-Methylphenanthrene	<0.9 U	<0.9 U	3571	2565	4487	9344	35871	<3.4 U	<0.9 U	5559
2-Methylphenanthrene	<0.9 U	<0.9 U	3614	2803	4817	10132	36343	<3.4 U	<0.9 U	5694
2-Methylanthracene	<0.9 U	<0.9 U	45.8	35.9	65.5	150	496	<3.4 U	<0.9 U	70.2
4/9-Methylphenanthrene	<0.9 U	<0.9 U	4865	3382	6046	12525	49506	<3.4 U	<0.9 U	7424
1-Methylphenanthrene	67.37	<0.9 U	3543	2506	4246	9090	35084	<3.4 U	<0.9 U	5597
3,6-Dimethylphenanthrene	<1.7 U	<1.7 U	1357	927	1655	2901	13825	<6 U	<1.7 U	2112
Retene	<1.6 U	<1.6 U	541	222	565	888	7595	<5.7 U	<1.6 U	695
2-Methylfluoranthene	<1.1 U	<1.1 U	118.3	60.7	118	223	1187	<4.1 U	<1.1 U	153
Benzo(b)fluorene	<1.4 U	<1.4 U	254	169	313	630	2536	<4.9 U	<1.4 U	361
C29-Hopane	<8.2 U	<8.2 U	1489	685	1464	2739	16003	<29.3 U	<8.2 U	3166
18a-Oleanane	<8.2 U	<8.2 U	66.9	<8.2 U	103.6	103	947	<29.3 U	<8.2 U	130
C30-Hopane	<8.2 U	<8.2 U	2972	1331	2902	5505	29878	<29.3 U	<8.2 U	6098
C20-TAS	<2.6 U	<2.6 U	1455	699	1600	3138	15394	<9.3 U	<2.6 U	2071
C21-TAS	<2.6 U	<2.6 U	1618	756	1735	3428	17216	<9.3 U	<2.6 U	2207
C26(20S)-TAS	<2.6 U	<2.6 U	1301	548	1299	2458	13696	<9.3 U	<2.6 U	2101
C26(20R)/C27(20S)-TAS	<2.6 U	<2.6 U	3391	1337	3470	5983	35825	<9.3 U	<2.6 U	5309
C28(20S)-TAS	<2.6 U	<2.6 U	3687	1459	3721	7099	39219	<9.3 U	<2.6 U	5945
C27(20R)-TAS	<2.6 U	<2.6 U	2795	1175	2878	5352	30985	<9.3 U	<2.6 U	4578
C28(20R)-TAS	<2.6 U	<2.6 U	3027	1279	3087	5452	32305	<9.3 U	<2.6 U	4663

Note: J = less than 3x the MDL, U = below the MDL

Appendix C: Chemistry Data

Sediment PAH Data - Target Compounds

Sample ID	BC01	BC02	BC03	BC04	BC05	BC06	BC07	BC13	BC14	BC15	SED Blank 1	SED Blank 2	SED Blank 3
Sample date	09/07/18	09/06/18	09/06/18	09/06/18	09/06/18	09/06/18	09/06/18	09/05/18	09/07/18	09/07/18	09/07/18	09/06/18	09/05/18
Units	µg/dry g	µg/dry g	µg/dry g	µg/dry g	µg/dry g	µg/dry g	µg/dry g	µg/dry g	µg/dry g	µg/dry g	µg/ container	µg/ container	µg/ container
Target Compound													
cis/trans Decalin	72.4	12.7	8.88	10.5	8.89	6.39	8.12	9.80	9.45	9.91	<10 U	<10 U	<10 U
C1-Decalins	61.5	2.38	2.32	2.32	4.75	2.15	5.09	3.13	4.39	2.41	<10 U	<10 U	<10 U
C2-Decalins	1128	56.9	9.61	15.9	22.7	13.5	17.4	7.68	10.8	4.11	<10 U	<10 U	<10 U
C3-Decalins	3117	208	48.9	49.7	57.3	33.9	35.6	17.6	26.4	13.0	<10 U	<10 U	<10 U
C4-Decalins	3308	290	59.5	48.5	45.3	33.1	20.8	13.1	20.3	<0.3 U	<10 U	<10 U	<10 U
Naphthalene	7.07	6.68	6.58	7.32	6.40	6.08	6.71	6.99	7.29	7.33	<10 U	<10 U	<10 U
C1-Naphthalenes	8.43	7.85	7.74	8.73	7.74	7.35	7.82	8.49	8.30	7.97	<10 U	<10 U	<10 U
C2-Naphthalenes	29.1	16.3	15.9	15.6	18.0	15.8	16.5	15.7	15.49	14.4	<10 U	<10 U	<10 U
C3-Naphthalenes	81.2	19.4	16.9	17.7	24.4	18.0	23.0	18.7	18.01	15.9	<10 U	<10 U	<10 U
C4-Naphthalenes	82.4	14.2	10.2	11.4	23.4	13.5	19.8	12.4	16.10	8.62	<10 U	<10 U	<10 U
Benzothiophene	<0.7 U	0.399	<0.1 U	<0.1 U	<0.1 U	<0.1 U	<0.1 U	0.153	<0.1 U	<0.1 U	<10 U	<10 U	<10 U
C1-Benzothiophenes	<1.4 U	<0.2 U	<0.2 U	<0.2 U	<0.2 U	<0.2 U	<0.2 U	<0.2 U	<0.2 U	<0.2 U	<10 U	<10 U	<10 U
C2-Benzothiophenes	<1.4 U	<0.2 U	<0.2 U	<0.2 U	<0.2 U	<0.2 U	<0.2 U	<0.2 U	<0.2 U	<0.2 U	<10 U	<10 U	<10 U
C3-Benzothiophenes	<1.4 U	<0.2 U	<0.2 U	<0.2 U	<0.2 U	<0.2 U	<0.2 U	<0.2 U	<0.2 U	<0.2 U	<10 U	<10 U	<10 U
C4-Benzothiophenes	<1.4 U	<0.2 U	<0.2 U	<0.2 U	<0.2 U	<0.2 U	<0.2 U	<0.2 U	<0.2 U	<0.2 U	<10 U	<10 U	<10 U
Biphenyl	4.03	3.30	3.14	3.80	3.23	2.89	3.13	3.20	3.23	3.14	<10 U	<10 U	<10 U
Acenaphthylene	13.1	7.37	5.48	5.89	4.90	4.65	4.89	5.01	4.77	4.68	<10 U	<10 U	<10 U
Acenaphthene	4.88	2.66	2.34	2.73	2.21	2.06	0.57	2.22	0.872	2.31	<10 U	<10 U	<10 U
Dibenzofuran	3.79	3.39	3.29	4.28	3.52	3.21	3.47	3.55	3.34	3.26	<10 U	<10 U	<10 U
Fluorene	7.09	5.18	5.01	6.03	5.89	5.05	5.04	5.14	5.00	4.89	<10 U	<10 U	<10 U
C1-Fluorenes	<2.9 U	13.1	7.02	8.33	9.70	6.47	7.69	5.92	6.16	5.07	<10 U	<10 U	<10 U
C2-Fluorenes	<2.9 U	<0.4 U	<0.4 U	16.6	26.6	14.5	16.0	10.8	11.8	10.4	<10 U	<10 U	<10 U
C3-Fluorenes	<2.9 U	<0.4 U	<0.4 U	30.0	32.2	23.9	23.6	13.1	14.7	13.1	<10 U	<10 U	<10 U
Carbazole	37.6	6.44	2.88	2.75	2.11	1.89	1.72	1.61	1.60	1.48	<10 U	<10 U	<10 U
Anthracene	<0.9 U	6.69	6.06	6.77	5.94	5.47	5.53	5.94	5.55	5.73	<10 U	<10 U	<10 U
Phenanthrene	22.2	13.5	13.3	15.1	14.4	12.1	13.5	14.2	13.0	11.9	<10 U	<10 U	<10 U
C1-Phenanthrenes/ Anthracenes	49.4	17.2	16.0	17.0	24.2	16.0	20.6	17.7	17.7	14.1	<10 U	<10 U	<10 U
C2-Phenanthrenes/ Anthracenes	337	51.4	30.7	33.2	54.2	34.6	43.0	30.8	33.8	26.0	<10 U	<10 U	<10 U
C3-Phenanthrenes/ Anthracenes	812	103	44.1	62.4	68.8	48.8	51.7	27.6	33.8	26.4	<10 U	<10 U	<10 U
C4-Phenanthrenes/ Anthracenes	1612	252	100	83.3	60.5	48.0	42.4	23.0	26.5	25.1	<10 U	<10 U	<10 U
Dibenzothiophene	14.0	3.44	2.19	2.68	2.80	2.07	1.94	1.93	1.77	1.53	<10 U	<10 U	<10 U
C1-Dibenzothiophenes	14.0	5.09	4.21	4.82	6.80	4.37	5.10	3.58	3.79	2.87	<10 U	<10 U	<10 U
C2-Dibenzothiophenes	119	14.2	7.00	11.5	17.7	8.76	12.0	6.98	8.23	5.74	<10 U	<10 U	<10 U
C3-Dibenzothiophenes	287	31.7	14.0	27.7	21.7	15.9	14.8	7.98	10.6	8.25	<10 U	<10 U	<10 U
C4-Dibenzothiophenes	392	49.5	20.0	27.7	17.6	14.8	11.5	6.48	8.97	6.96	<10 U	<10 U	<10 U
Fluoranthene	39.8	20.8	20.9	23.7	20.3	19.4	20.1	22.6	19.8	19.7	<10 U	<10 U	<10 U
Pyrene	193	40.4	27.9	27.9	22.8	21.9	22.0	23.8	21.6	21.6	<10 U	<10 U	<10 U
C1-Fluoranthenes/Pyrenes	515	68.5	31.9	31.3	23.0	22.1	21.2	19.9	18.7	17.4	<10 U	<10 U	<10 U
C2-Fluoranthenes/Pyrenes	993	126	50.0	42.3	26.7	26.7	22.7	15.2	18.1	18.6	<10 U	<10 U	<10 U
C3-Fluoranthenes/Pyrenes	1187	140	57.1	38.1	27.1	23.4	19.9	9.43	12.7	13.6	<10 U	<10 U	<10 U
C4-Fluoranthenes/Pyrenes	1137	132	50.8	30.2	20.0	19.2	19.2	7.48	8.91	9.19	<10 U	<10 U	<10 U
Naphthobenzothiophene	114	18.8	11.9	10.1	7.61	7.43	7.14	7.17	6.54	6.83	<10 U	<10 U	<10 U
C1-Naphthobenzothiophenes	413	67.7	28.8	26.5	15.8	14.2	13.8	9.75	11.2	10.0	<10 U	<10 U	<10 U

Table continued on next page

Note: J = less than 3x the MDL, U = below the MDL

Appendix C: Chemistry Data

Sediment PAH Data - Target Compounds

Sample ID	BC01	BC02	BC03	BC04	BC05	BC06	BC07	BC13	BC14	BC15	SED Blank 1	SED Blank 2	SED Blank 3
Sample date	09/07/18	09/06/18	09/06/18	09/06/18	09/06/18	09/06/18	09/06/18	09/05/18	09/07/18	09/07/18	09/07/18	09/06/18	09/05/18
Units	µg/dry g	µg/dry g	µg/dry g	µg/dry g	µg/dry g	µg/dry g	µg/dry g	µg/dry g	µg/dry g	µg/dry g	µg/ container	µg/ container	µg/ container
C2-Naphthobenzothiophenes	1039	155	58.2	45.9	26.8	23.6	21.9	12.4	16.5	15.0	<10 U	<10 U	<10 U
C3-Naphthobenzothiophenes	969	160	60.6	38.4	23.3	21.8	22.1	11.3	14.2	12.1	<10 U	<10 U	<10 U
C4-Naphthobenzothiophenes	494	78.6	29.5	17.8	11.5	11.3	9.57	5.36	6.29	5.01	<10 U	<10 U	<10 U
Benz(a)anthracene	18.7	12.9	12.9	13.7	11.4	10.9	11.1	13.0	11.6	11.8	<10 U	<10 U	<10 U
Chrysene/Triphenylene	141	34.0	26.1	24.4	20.4	17.8	18.4	18.3	17.0	16.5	<10 U	<10 U	<10 U
C1-Chrysenes	663	127	53.3	41.9	29.9	<0.2 U	26.3	17.4	19.3	17.7	<10 U	<10 U	<10 U
C2-Chrysenes	1721	286	98.8	69.1	36.8	<0.2 U	32.4	19.5	23.7	21.2	<10 U	<10 U	<10 U
C3-Chrysenes	1575	263	83.5	57.1	30.6	<0.2 U	31.8	14.2	19.1	14.8	<10 U	<10 U	<10 U
C4-Chrysenes	842	139	52.6	38.6	18.3	<0.2 U	18.4	7.70	11.7	<0.2 U	<10 U	<10 U	<10 U
Benzo(b)fluoranthene	82.3	30.7	23.6	25.7	20.4	20.7	21.0	22.2	20.4	19.8	<10 U	<10 U	<10 U
Benzo(k,j)fluoranthene	24.9	17.4	16.9	18.0	15.8	15.3	15.9	17.4	15.5	15.8	<10 U	<10 U	<10 U
Benzo(a)fluoranthene	29.7	3.94	6.20	6.05	4.72	4.93	4.81	4.78	4.34	4.31	<10 U	<10 U	<10 U
Benzo(e)pyrene	115	30.1	20.0	20.2	15.9	15.8	16.4	16.9	15.5	15.2	<10 U	<10 U	<10 U
Benzo(a)pyrene	48.2	21.1	17.0	18.6	15.0	14.6	14.4	13.2	13.8	14.9	<10 U	<10 U	<10 U
Perylene	920	315	257	289	247	259	173	99.8	143	255	<10 U	<10 U	<10 U
Indeno(1,2,3-c,d)pyrene	25.2	16.2	15.2	16.5	14.2	14.0	14.3	16.4	14.9	14.5	<10 U	<10 U	<10 U
Dibenzo(a,h)anthracene	16.7	6.09	4.61	4.88	4.03	3.93	3.12	4.59	4.14	3.9	<10 U	<10 U	<10 U
C1-Dibenzo(a,h) anthracenes	<1 U	<0.1 U	<0.1 U	<0.1 U	<0.1 U	<0.1 U	<0.1 U	<0.1 U	<0.1 U	<0.1 U	<10 U	<10 U	<10 U
C2-Dibenzo(a,h) anthracenes	<1 U	<0.1 U	<0.1 U	<0.1 U	<0.1 U	<0.1 U	<0.1 U	<0.1 U	<0.1 U	<0.1 U	<10 U	<10 U	<10 U
C3-Dibenzo(a,h) anthracenes	<1 U	<0.1 U	<0.1 U	<0.1 U	<0.1 U	<0.1 U	<0.1 U	<0.1 U	<0.1 U	<0.1 U	<10 U	<10 U	<10 U
Benzo(g,h,i)perylene	30.8	17.1	16.4	17.8	15.1	15.0	15.3	17.5	16.2	16.0	<10 U	<10 U	<10 U
Total PAHs	**24972**	**3552**	**1605**	**1553**	**1329**	**1028**	**1065**	**758**	**856**	**857**	**0**	**0**	**0**

Note: J = less than 3x the MDL, U = below the MDL

Appendix C: Chemistry Data

Sediment PAH Data - Individual Alkyl Isomers and Hopanes

Sample ID	BC01	BC02	BC03	BC04	BC05	BC06	BC07	BC13	BC14	BC15	SED Blank 1	SED Blank 2	SED Blank 3
Sample date	09/07/18	09/06/18	09/06/18	09/06/18	09/06/18	09/06/18	09/06/18	09/05/18	09/07/18	09/07/18	09/07/18	09/06/18	09/05/18
Units	µg/dry g	µg/dry g	µg/dry g	µg/dry g	µg/dry g	µg/dry g	µg/dry g	µg/dry g	µg/dry g	µg/dry g	µg/ container	µg/ container	µg/ container
Individual Alkyl Isomers and Hopanes													
2-Methylnaphthalene	7.63 J	7.36	7.20	8.11	7.15	6.78	7.19	7.80	7.68	7.35	<10 U	<10 U	<10 U
01/00/00	5.51	4.87	4.87	5.50	4.93	4.67	5.01	5.44	5.26	5.07	<10 U	<10 U	<10 U
2,6-Dimethylnaphthalene	9.28	7.96	7.61	8.29	8.94	7.86	8.45	7.62	8.17	8.22	<10 U	<10 U	<10 U
1,6,7-Trimethylnaphthalene	2.97	2.57	2.63	2.78	3.94	2.61	3.76	2.97	2.92	2.40	<10 U	<10 U	<10 U
1-Methylfluorene	<1.5 U	4.67	3.70	3.83	5.92	3.43	4.04	2.79	3.02	2.44	<10 U	<10 U	<10 U
4- Methyldibenzothiophene	12.7	3.59	2.71	3.13	4.75	2.94	3.47	2.38	2.56	1.88	<10 U	<10 U	<10 U
2/3-Methyldibenzothiophene	4.31	2.97	2.12	2.38	2.82	1.96	2.36	1.80	1.85	1.50	<10 U	<10 U	<10 U
1-Methyldibenzothiophene	1.90	0.32	0.86	1.01	1.63	1.00	1.07	0.66	0.71	0.50	<10 U	<10 U	<10 U
3-Methylphenanthrene	12.4	4.70	4.68	4.97	7.16	4.75	6.07	5.14	5.06	4.33	<10 U	<10 U	<10 U
2-Methylphenanthrene	11.2	6.22	5.74	5.90	7.40	5.38	6.96	6.33	6.06	5.02	<10 U	<10 U	<10 U
2-Methylanthracene	11.1	3.51	2.27	2.40	2.14	1.98	1.98	1.80	1.90	1.82	<10 U	<10 U	<10 U
4/9-Methylphenanthrene	20.2	5.38	5.17	5.74	9.68	5.61	7.50	6.37	6.44	4.53	<10 U	<10 U	<10 U
1-Methylphenanthrene	12.4	3.55	3.91	4.07	6.54	4.04	5.50	4.47	4.57	3.44	<10 U	<10 U	<10 U
3,6-Dimethylphenanthrene	35.6	4.79	2.54	3.13	4.93	3.35	3.85	2.43	2.77	2.07	<10 U	<10 U	<10 U
Retene	92.4	35.5	14.2	13.4	9.70	8.75	11.3	7.21	6.45	7.48	<10 U	<10 U	<10 U
2-Methylfluoranthene	50.3	8.50	4.18	4.03	3.18	2.93	2.97	2.92	2.76	2.72	<10 U	<10 U	<10 U
Benzo(b)fluorene	60.1	7.25	5.66	6.22	4.81	4.65	4.44	4.47	4.31	4.65	<10 U	<10 U	<10 U
C29-Hopane	605	122	71.2	54.6	48.6	48.0	49.6	41.4	35.02	36.9	<10 U	<10 U	<10 U
18a-Oleanane	<4.6 U	<0.6 U	<0.6 U	<0.6 U	<0.6 U	<0.6 U	<0.6 U	4.06	<0.6 U	<0.6 U	<10 U	<10 U	<10 U
C30-Hopane	1077	214	113	105	78.9	80.7	76.6	62.1	62.7	55.6	<10 U	<10 U	<10 U
C20-TAS	656	100	33.9	22.6	12.0	11.1	10.2	3.44	1.55	3.48	<10 U	<10 U	<10 U
C21-TAS	807	129	41.7	27.6	14.5	11.5	11.2	3.82	6.14	3.83	<10 U	<10 U	<10 U
C26(20S)-TAS	531	85.4	31.8	24.2	16.9	16.9	14.7	11.2	11.3	11.0	<10 U	<10 U	<10 U
C26(20R)/C27(20S)-TAS	1773	298	102	70.1	41.0	37.3	37.8	18.0	24.1	17.3	<10 U	<10 U	<10 U
C28(20S)-TAS	1456	258	91.8	63.2	38.3	35.7	36.9	18.1	23.7	17.9	<10 U	<10 U	<10 U
C27(20R)-TAS	1105	194	71.6	52.3	37.0	34.3	40.1	28.0	28.0	13.4	<10 U	<10 U	<10 U
C28(20R)-TAS	1169	203	72.9	49.8	28.3	26.8	27.6	12.9	17.3	13.4	<10 U	<10 U	<10 U

Note: J = less than 3x the MDL, U = below the MDL

Appendix C: Chemistry Data

Sediment Carbon

Sample ID	BC01	BC02	BC03	BC04	BC05	BC06	BC07	BC13	BC14	BC15
Sample date	09/07/18	09/06/18	09/06/18	09/06/18	09/06/18	09/06/18	09/06/18	09/05/18	09/07/18	09/07/18
Target Analyte	mg Carbon	mg Carbon	mg Carbon	mg Carbon	mg Carbon	mg Carbon	mg Carbon	mg Carbon	mg Carbon	mg Carbon
Total Carbon (TC)	6.16	5.14	4.82	4.59	4.84	4.72	4.95	5.05	4.55	5.04
Total Organic Carbon (TOC)	4.75	4.02	3.58	3.39	4.34	4.08	4.44	3.33	3.95	2.38
Total Inorganic Carbon (TIC)	1.41	1.11	1.24	1.21	0.50	0.63	0.51	1.72	0.60	2.66
	% Carbon	% Carbon	% Carbon	% Carbon	% Carbon	% Carbon	% Carbon	% Carbon	% Carbon	% Carbon
Total Carbon (TC)	2.53	2.08	1.88	1.85	1.91	1.86	1.97	1.94	1.89	1.94
Total Organic Carbon (TOC)	1.77	1.57	1.44	1.25	1.76	1.56	1.78	1.32	1.57	0.94
Total Inorganic Carbon (TIC)	0.76	0.51	0.44	0.60	0.16	0.30	0.19	0.62	0.32	1.01

Sediment Grain Size

Sample ID	BC01	BC02	BC03	BC04	BC05	BC06	BC07	BC13	BC14	BC15
Sample date	09/07/18	09/06/18	09/06/18	09/06/18	09/06/18	09/06/18	09/06/18	09/05/18	09/07/18	09/07/18
% GRAVEL	0.00	0.00	0.00	0.00	0.00	0.00	0.00	0.00	0.00	0.00
% SAND	6.71	3.85	4.36	7.05	3.89	6.91	6.66	4.38	6.61	3.03
% SILT	79.13	54.65	57.43	47.49	65.06	68.27	81.90	83.07	81.79	83.77
% CLAY	14.16	41.50	38.21	45.46	31.05	24.82	11.44	12.55	11.60	13.20

Appendix D: Historical MC20 Oil Data

Identification	n-C3 (%)	n-C4 (%)	n-C5 (%)	n-C6 (%)	n-C7 (%)	n-C8 (%)	n-C9 (%)	n-C10 (%)	n-C11 (%)	n-C12 (%)	i-C13 (%)	i-C14 (%)
MC20 Well #9	1.05184	3.79414	3.15552	2.40421	1.91585	6.49887	3.04282	1.91585	1.31480	2.25394	4.99624	5.07137
MC20 Well #2 A	0.66075	2.03889	3.49254	5.39928	6.06003	6.60751	5.04059	4.92732	4.75741	4.22881	2.03889	2.07665
MC20 Well #2 B	0.51453	2.07393	2.51722	2.58054	2.58054	3.23755	2.63595	2.68345	2.58054	3.05549	1.03697	0.95781

Identification	n-C13 (%)	i-C15 (%)	n-C14 (%)	i-C16 (%)	n-C15 (%)	n-C16 (%)	i-C18 (%)	n-C17 (%)	i-C19 (%)	n-C18 (%)	i-C20 (%)	n-C19 (%)
MC20 Well #9	0.45079	5.03381	7.77611	6.38618	4.47032	2.21638	5.70999	2.51690	9.61683	2.06612	4.35763	3.68144
MC20 Well #2 A	6.06003	2.20880	4.79517	3.20936	5.15386	3.90787	2.35983	3.70021	4.00227	3.22824	2.02001	3.49254
MC20 Well #2 B	3.32463	0.98947	3.22172	1.50400	2.81010	2.23225	1.17153	2.05810	2.03435	1.70189	0.92615	1.71772

Identification	n-C20 (%)	n-C21 (%)	n-C22 (%)	n-C23 (%)	n-C24 (%)	n-C25 (%)	n-C26 (%)	n-C27 (%)	n-C28 (%)	n-C29 (%)	n-C30 (%)	n-C31 (%)
MC20 Well #9	2.17881	1.69046	1.31480	0.86401	0.71375	0.75131	0.26296	0.18783	0.07513	0.03757	0.07513	0.07513
MC20 Well #2 A	2.43534	1.81235	1.37814	0.90617	0.58524	0.64187	0.28318	0.22654	0.13215	0.05664	0.01888	0.03776
MC20 Well #2 B	1.17945	0.89448	0.72825	0.46703	0.37204	0.34038	0.15832	0.12665	0.07916	0.04749	0.02375	0.02375

Identification	n-C32 (%)
MC20 Well #9	0.07513
MC20 Well #2 A	0.01888
MC20 Well #2 B	0.00792

Note: MC20 Well #2 A reservoir depth = 8,668 ft; Well #2 B reservoir depth = 10,016 ft.

Appendix E: Acoustic Flux Rate Methods

Estimating Concentration of Bubbles

Estimation of concentration of bubbles considered both gas and oil provided in the following equation as a sum:

$$Flux_{total} = \frac{4\pi}{3} \sum_{i=1}^{M} N_i * a_i^3 * A_i * \omega_i \quad (1)$$

Since it is a linear summation, it can be split in two fluxes, one for the gas bubbles and one for the oil bubbles (interchangeably called oil droplets)

$$Flux_{total}[ab, ad, \rho d, f] = Flux_{bubbles} + Flux_{droplets}$$

$$= \frac{4\pi}{3} A_i \left[\sum_{i=1}^{M} \left(Nb_i * ab_i^3 * \omega b_i \right) + \sum_{i=1}^{M} \left(Nd_i * ad_i^3 * \omega d_i \right) \right] \quad (2)$$

$$Nb_i(ab, f) = \frac{\sigma b_i}{\sigma b_{bs}} \quad (3)$$

$$Nd_i(ab, f) = \frac{\sigma d_i}{\sigma d_{bs}} \quad (4)$$

where suffixes *b* and *d* represent quantities related to gas bubbles or oil droplets, respectively; a_i is the mean radius of the bubble or droplet; A_i is the vertical cross-sectional plume area; ω_i is the rise rate; N_i is the number of targets inside a specific bin volume; and the subscript *i* denotes the depth bin counted from the surface in 1 m steps.

The total backscatter cross-sectional area σ is derived from the volume scattering, Sv, as

$$\sigma = 10^{\frac{Sv}{10}} \quad (5)$$

and it is also the summation of the relative backscatter cross-sectional areas of each target. It is a quantity that is added linearly; it can be split in the backscatter cross-sectional area due to bubbles σ*b* and the one due to droplets σ*d*, as in (6).

$$\sigma = \sigma b_i + \sigma d_i = \sigma_i(p) + \sigma_i(1 - p) \quad (6)$$

The proportionality factor *p* was based on evidence from the bubblometer. An estimate of *p* was obtained by counting and calculating relative proportions of surface area of the bubbles and droplets from the ROV's images and comparing them with the total acoustic area. Proportions about 10% higher and 10% lower were also considered.

The average backscatter cross-sectional area $\underline{\sigma}_{bs}$ is the average of all the target's relative backscatter cross-sectional areas (Loranger, 2019). Since all targets, bubbles and droplets, are assumed as spheres, $\underline{\sigma}_{bs}$ is then the relative backscatter cross-sectional area, σ_{bs}, calculated on the average radius.

Appendix E: Acoustic Flux Rate Methods

Consideration of Rayleigh scattering properties

The relative cross-sectional area (σ_{bs}) is the cross-sectional area of an individual target (Loranger, 2019). All targets, bubbles and droplets, were assumed to be spheres for simplicity and equivalent spherical dimensions were calculated from the video images. Depending on the size of the target, the scattering would be in the Rayleigh regime, in a transitional regime, or in the geometrical regime (Medwin and Clay, 1998). Relating backscatter and densities to the size and number of oil and gas particles is highly dependent on the acoustic scattering regime (Figure E.1). To determine the correct regime, the product of the wavenumber and the radius of the sphere (*ka*) must be calculated. An average radius for each depth bin and its distribution is shown in Chapter 4 and repeated here. In the case of bubbles, if the product of the wavenumber *k* and the radius of the sphere *a* is less than one, then the cross-sectional areas would be (7). For an oil droplet, if *ka*<<1, effectively *ka*<0.5, the cross-sectional area is (8).

$$\sigma b_{bs}(ab,f) = \frac{4\pi a^2}{\left[\left(\frac{f_R}{f}\right)-1\right]^2+\delta^2},\ ka<1, \tag{7}$$

$$\sigma d_{bs}(ad,f) = \frac{a^2 25(ka)^4}{36},\ ka \ll 1, \tag{8}$$

The wavenumber is $k=\frac{2\pi f}{c}$; $g=\frac{\rho_1}{\rho_o}$ is a ratio of the sphere's and medium's density; $f_R=\frac{0.0136c}{2\pi a}$;

is the resonance frequency for gas bubbles; and the damping coefficient is

$$\delta = \delta_r = ka \tag{9}$$

The thermal damping δ_t and the viscosity damping δ_v were ignored from (9).

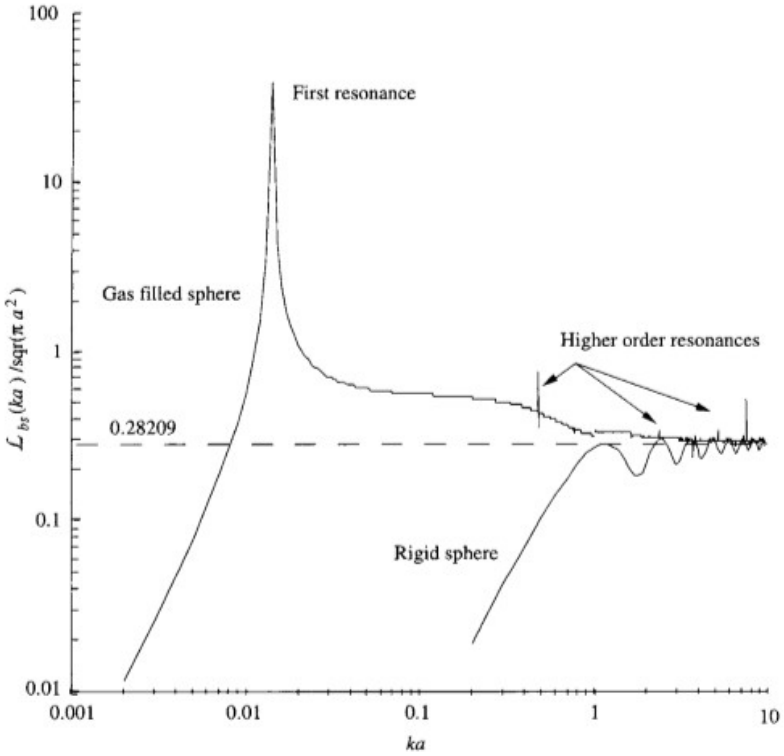

Figure E.1. Relative backscattering length of a spherical air bubble at sea level compared with the rigid sphere solution. We are assuming a rigid sphere in the case of an oil droplet (from Medwin and Clay, 1998).

Appendix E: Acoustic Flux Rate Methods

If the product *ka*>>1, effectively *ka*>10, the target starts to act as a plane boundary with respect to the small wavelength. The cross-sectional area is then approximately the geometrical cross-sectional area (10). In this case the dependence on the frequency is negligible

$$\sigma_{bs}(a) = \pi a^2, \; ka \gg 1,$$

(Medwin and Clay, 1998) (10)

When 1<*ka*<10, the cross-sectional area is in a transitional state between Rayleigh regime and geometrical regime. In that case the general form of the cross-sectional area is used

$$\sigma_{bs}(ka) = \frac{4\pi a^2}{(ka)^2} \sum_{m=0}^{M-1} \frac{2m+1}{1+C_m^2}, \; 1 < ka < 10,$$

(Medwin and Clay, 1998) (11)

Sizes of gas bubbles and oil droplets were estimated from the ROV's images. Gaussian distributions based on the mean radii per depth of the ROV's images were generated and used as the estimated radii of the echogram's spherical targets. The depths of the ROV's images and plume's echogram did not correspond directly; therefore, the radii distributions are just an approximation, but a reasonable assumption since oil droplets will not change measurably in shape with depth. The plume's echogram is shallower than the analyzed images, so the radii of the bubbles and droplets inside the plume should be closer to the shallower parts of the ROV distributions. In Figure E.2 and Figure E.3, Rayleigh and geometrical regimes are denoted with green and red lines, respectively; cyan lines mark values of *ka*=[2,3] in the transition zone. It can be seen that the radii of the bubbles oscillate around *ka*=0.85, and most of the mean radii are in the Rayleigh regime. It is then a fair assumption to approximate the scattering of gas bubbles to (7).

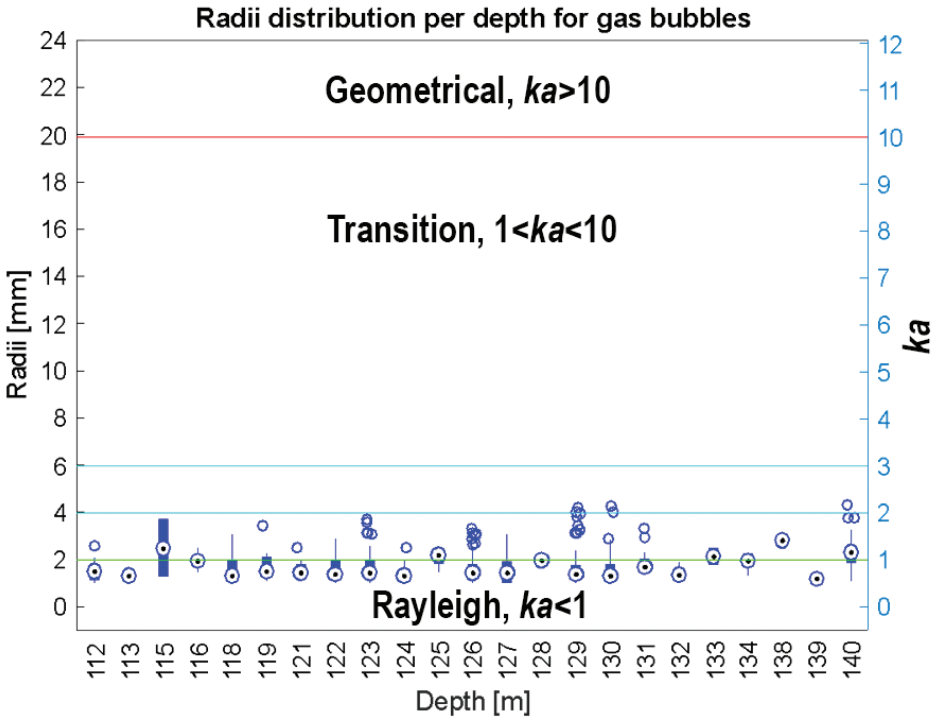

Figure E.2. Radii distribution at depth for gas bubbles as measured in the bubblometer images.

Appendix E: Acoustic Flux Rate Methods

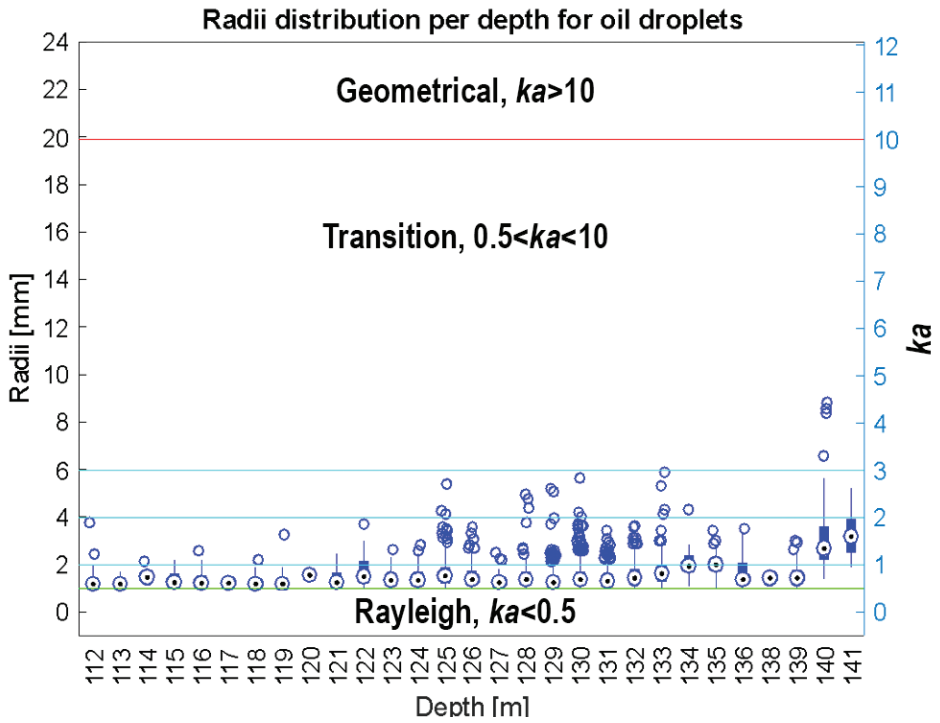

Figure E3. Radii distribution at depth for oil bubbles measured in the ROV video images.

For the oil droplet distribution shown, the relative backscattering length oscillates around *ka*=0.7. At shallower depths, the radii approach 1 mm and *ka*≈0.5. The Rayleigh approximation is a fair assumption since, as seen in Figure 8A.1, the relative backscattering length of a rigid sphere is close to linear for values between 0.5<*ka*<1 and most of the nonlinear values take place for 1<*ka*<10.

REFERENCES

Loranger, S. 2019. Acoustic detection and quantification of crude oil. Dissertation to the Oceanography Department, University of New Hampshire. 140 pp.

Medwin, H., and C.S. Clay. 1998. Fundamentals of Acoustical Oceanography. Academic Press, Elsevier, Inc. New York. 712 pp. doi: https://doi.org/10.1016/B978-0-12-487570-8.X5000-4

Appendix E: Acoustic Flux Rate Methods

Table E.1. Parameter values used in equations and model simulations to estimate oil flux from acoustic backscatter.

Parameter	Value	
Sv	-53.41 [dB] (average, depends on depth)	
Gas bubble radii	Mean: 1.8, Max: 2.8, Min: 1.2 [mm]	
Oil droplets radii	Mean: 1.4, Max: 1.8, Min: 1.2 [mm]	
Water sound speed (average)	1542 [m/s] (constant)	
Frequency	20 [kHz] (constant)	
Water density	1029 [kg/m^3] (constant)	
Crude density	899 [kg/m^3] (constant)	
Water viscosity	0.0019 [Pa/s] (constant)	
Seep area	295.46 [m^2] (average, depends on echogram)	
Backscattering cross-sectional area (σ)	1.84 x 10^{-5} [m^2] (average, depends on echogram)	
Gas Relative backscattering cross-sectional area (σb_{bs})	2.23 x 10^{-5} [m^2] (average, depends on radii)	
Oil Relative backscattering cross-sectional area (σd_{bs})	4.48 x 10^{-7} [m^2] (average, depends on radii)	
Gas number of targets (Nb)	0.13 per m^3	
Oil number of targets (Nd)	37.17 per m^3	
	Based on radii	Based on echogram
Gas Maximum Rise Rate (ωb)	0.24 [m/s]	0.19 [m/s]
Gas Minimum Rise Rate (ωb)	0.22 [m/s]	0.065 [m/s]
Oil Maximum Rise Rate (ωd)	0.14 [m/s]	0.19 [m/s]
Oil Minimum Rise Rate (ωd)	0.06 [m/s]	0.065 [m/s]

Appendices

Appendix F: Final Report Memo

To: David Fish, Chief of Environmental Compliance Division
From: Andrew Mason, Chief Scientist for NOAA/BSEE MC20 Survey
Date: 3 June 2019
RE: Delivery of Final NOAA/BSEE Survey Report

The attached Technical Memorandum titled, "An Integrated Assessment of Oil and Gas Release into the Marine Environment at the Former Taylor Energy MC20 Site" is delivered in partial fulfillment of the requirements of Inter Agency Agreement (IAA) E18PG00016 between the National Oceanic and Atmospheric Administration (NOAA) and the Bureau of Safety and Environmental Enforcement (BSEE). This version is not the final publicly published version of this report as review by BSEE is required as part of E18PG00016 prior to any publication. Any changes between this version and the final published and publicly available version are believed to be minor and editorial only in nature. The major findings of this survey are final as of the signing of this memo and are detailed in brief in the Executive Summary.

The authors of this report undertook specific peer review steps during the creation of this final product. In the spirit of transparency and for clarity in the rigorous review process for these data products, the technical reviewers beyond the individual chapter authors for the attached report are listed below with their affiliations. This signed memorandum will be included in the final publicly available report in the Appendices.

Technical Reviewers
Chapter 1: Introduction and Background Conditions at the Former Taylor Energy MC20 Site in September 2018
Lisa DiPinto – NOAA, Office of Response and Restoration (ORR)
Dr. Dennis Apeti – NOAA, National Centers for Coastal Ocean Science (NCCOS)
Dr. David Whitall – NOAA, National Centers for Coastal Ocean Science (NCCOS)

Chapter 2: Characterization of the Observed Physical Characteristics of the Water Column at MC20
Dr. Dennis Apeti – NOAA, National Centers for Coastal Ocean Science (NCCOS)
Andrew Mason – NOAA, National Centers for Coastal Ocean Science (NCCOS)
Dr. J. Christopher Taylor – NOAA, National Centers for Coastal Ocean Science (NCCOS)

Chapter 3: Surface and ROV Acoustic Mapping of the MC20 Oil and Gas Leak in the Northern Gulf of Mexico
Dr. Avery Paxton – NOAA, National Centers for Coastal Ocean Science (NCCOS)
Mike Bollinger – NOAA, National Centers for Coastal Ocean Science (NCCOS)
Andrew Mason – NOAA, National Centers for Coastal Ocean Science (NCCOS)

Chapter 4: Quantitative Imaging of Oil and Gas Bubbles Discharged at MC20
Dr. Jeff Chanton – Florida State University (FSU)
Andrew Mason – NOAA, National Centers for Coastal Ocean Science (NCCOS)
Dr. J. Christopher Taylor – NOAA, National Centers for Coastal Ocean Science (NCCOS)

Chapter 5: Surface Methane Measurements and Flux at the MC20 Oil and Gas Leak in the Northern Gulf of Mexico
Dr. W. Edward Johnson – NOAA, National Centers for Coastal Ocean Science (NCCOS)
Dr. David Whitall – NOAA, National Centers for Coastal Ocean Science (NCCOS)
Andrew Mason – NOAA, National Centers for Coastal Ocean Science (NCCOS)

Appendix F: Final Report Memo

Chapter 6: Chemical Analysis of Gas Samples Collected from the MC20 Leak in the Northern Gulf of Mexico
Megan Konarik – TDI Brooks International
Dr. Kimani Kimbrough – NOAA, National Centers for Coastal Ocean Science (NCCOS)
Andrew Mason – NOAA, National Centers for Coastal Ocean Science (NCCOS)

Chapter 7: An Assessment of Oil-related Chemical Contaminants in Sediment, Water, and Oil from the MC20 Site in the Northern Gulf of Mexico
Dr. Scott Stout – NewFields
Dr. Thomas McDonald – Texas A&M University
Dr. Dennis Apeti - NOAA, National Centers for Coastal Ocean Science (NCCOS)
Dr. W. Edward Johnson - NOAA, National Centers for Coastal Ocean Science (NCCOS)
Dr. Anthony Pait - NOAA, National Centers for Coastal Ocean Science (NCCOS)
Dr. Kimani Kimbrough - NOAA, National Centers for Coastal Ocean Science (NCCOS)

Chapter 8: Estimates of Oil Flux to the Ocean using Optical and Acoustical Methods
Dr. Jeffrey Chanton – Florida State University (FSU)
Dr. Geir Pedersen – Norwegian Research Center
Andrew Mason – NOAA, National Centers for Coastal Ocean Science (NCCOS)

Respectfully,

Andrew Mason

Signature: Date:

06/03/2019

Andrew L Mason
Physical Scientist, NOAA National Ocean Service
Chief Scientist for NOAA/BSEE MC20 Survey

U.S. Department of Commerce

Wilbur L. Ross, Jr., *Secretary*

National Oceanic and Atmospheric Administration

Neil A. Jacobs, *Under Secretary*

National Ocean Service

Nicole LeBoeuf, *Assistant Administrator, Acting*

The mission of the National Centers for Coastal Ocean Science is to provide managers with scientific information and tools needed to balance society's environmental, social and economic goals. For more information, visit: https://coastalscience.noaa.gov/